1-1-2013

Surface Modification and Transport Modeling of Micron- and Nano-Sized Materials

Erick Salvador Vasquez Guardado

Surface modification and transport modeling of micron- and nano-sized materials

By

Erick S. Vasquez Guardado

A Dissertation
Submitted to the Faculty of
Mississippi State University
in Partial Fulfillment of the Requirements
for the Degree of Doctor of Philosophy
in Chemical Engineering
in the Dave C. Swalm School of Chemical Engineering

Mississippi State, Mississippi

August 2013

Surface modification and transport modeling of micron- and nano-sized materials

By

Erick S. Vasquez Guardado

Approved:

Keisha B. Walters Associate Professor and Graduate Coordinator Chemical Engineering (Committee Chair)	D. Keith Walters Associate Professor Mechanical Engineering (Committee Member)
Hossein Toghiani Associate Professor Chemical Engineering (Committee Member)	W. Todd French Associate Professor Chemical Engineering (Committee Member)
Oliver J. Myers Assistant Professor Mechanical Engineering (Committee Member)	Billy B. Elmore Associate Professor Chemical Engineering (Committee Member)

Royce O. Bowden
Interim Dean of the Bagley College of Engineering

Name: Erick S. Vasquez Guardado

Date of Degree: August 17, 2013

Institution: Mississippi State University

Major Field: Chemical Engineering

Director of Dissertation: Dr. Keisha B. Walters

Title of Study: Surface modification and transport modeling of micron- and nano-sized materials

Pages in Study: 238

Candidate for Degree of Doctor of Philosophy

Nanoparticle-based technologies are an emerging field with the promise to impact a wide range of application areas. However, that potential is somewhat married to a host of research questions that remain to be answered. This work explores the surface modification of magnetic nanoparticles in a controlled fashion to produce hybrid nanoparticle (metal/polymer) systems with different morphologies, understand *in-situ* behavior of stimuli-responsive polymers grafted to a substrate, and obtain better computational methods for particle-tracking and -deposition. Nanoparticle surface modification was performed using ATRP, obtaining homo-, block-*co*-, and 'two-faced/biphasic' polymer structures on the nanoparticle surfaces. Biphasic Janus nanoparticles (JPs) were formed using a magnetic nanoparticle core and an innovative technique combining non-covalent solid protection with sequential controlled radical polymerization to form the two surface-grafted polymer phases. Surface-confined polymerizations were conducted using pH- and thermo-responsive materials. Poly(methacrylic acid) (PMAA) and a series of (aminoalkyl) methacrylate polymers were used as pH responsive polymers. Additionally, poly(N-isopropylacrylamide) (PNIPAM)

was selected as the thermo-responsive material for this study. *In-situ* characterization techniques, including atomic force microscopy (AFM), dynamic light scattering (DLS), and ellipsometry, were used to evaluate the thermo- and pH-responsiveness of these stimuli responsive materials. A new general-oscillator (GENOSC) model was used to determine swelling ratio, thickness, and optical constant changes in the polymer brush as pH was changed *in-situ*. AFM was used to study morphological changes due to changes in pH and temperature. Nanoparticle temperature responsiveness was investigated using DLS. A related effort involved the use of computational fluid dynamic (CFD) methods to track (micron-sized) particles in certain geometries, including a human lung morphology. Predicted particle transport and deposition was compared to Lagrangian computational approaches and available experimental data. The Eulerian particle phase modeling method developed resulted in the accurate prediction of both near-wall particle tracking and wall deposition. This Eulerian-Eulerian model is a new tool that has potential for particle tracking in physiological morphologies. This combination of experimental and computational research has led to new nano- and micro-particle surface modification methods and particle transport modeling.

DEDICATION

This work is dedicated to my family, especially to my parents, Sara and Salvador for the unconditional support provided under any circumstance. Thank you for all your encouragement throughout all these years away from home.

ACKNOWLEDGEMENTS

I would like to principally acknowledge my advisor Dr. Keisha B. Walters for the tremendous assistance, patience, encouragement, and time that she dedicated to bring this document to fruition. All the research ideas, projects, results and contributions were spurred on by her guidance. Thank you for helping me to become a better researcher, writer, mentor, and leader.

My most sincere gratitude is expressed to my dissertation committee members for their input and counseling during the development of this work. Dr. Keith Walters provided tremendous help on the computational developments of this study. I am greatly appreciative of Dr. Hossein Toghiani's encouragement to continue working hard when days were especially tough and for providing additional lab space. I extend my gratitude to Dr. Todd French for also providing access to equipment and lab space. I would also like to thank Dr. Oliver Myers for his information and guidance on smart materials. Lastly, I give special recognition to Dr. Bill Elmore for his incredible inspiration to excel as a great person and to always help those willing to learn.

This work was funded through the National Science Foundation Mississippi EPSCoR program [EPS-0903787 and EPS-100688]. The EPSCoR program more than provided financial resources; it provided an outlet to present my findings and receive technical feedback at the regional level. I also was able to meet and work with students and faculty from a wide range of disciplines through this program. These interactions

and the leadership opportunities had a impacted my professional development as a graduate student and really helped me to stay motivated. The Mississippi State University (MSU) Bagley College of Engineering Ph.D. Fellowship provided supplemental funding and allowed me to present at my research at AIChE 2009 and 2010. The availability of different instrument grants was possible due to the following grants: CBET-0933493, CBET-0923474 for AFM, DSC, and SDT. Lastly, HR TEM access is acknowledged as it was possible due to grant DBI-1126743.

Thank you to all of those who have had an impact on the results of this work, including Dr. I-Wei Chu for her help and assistance in microscopy (AFM, TEM, SEM). The I^2AT center and staff, especially Amanda Lawrence and Bill Monroe, was gracious in providing access to great sample characterization equipment and techniques. They were patient in training me and sharing their expertise while preparing and analyzing samples. Thanks to: (1) Eric Bowman of SemiSouth (Starkville, MS) for providing access to equipment to cut silicon chips for the surface modification work, (2) Vu Le, Chemistry graduate student at MSU, and (3) Eric Burden and Dr. McCormick at USM for providing DLS equipment access.

I am appreciative of the undergraduate students who helped me in the lab over the years: Matthew Gresham, Nicole Stein, Matthew Young, Brad Nicholson, Mariana Lemus, Gavin Barnett, Marquita Jones, Liza Nalley, Kate Bush, Kenneth Newton, Jasmine Young, Gerald Nail, Caitie O'Horo, Julia Mattson, Bo Portillo, John Tomlinson, and NSF REU student Louise Stewart. All of these undergraduate researchers helped me to collect great data and to practice my supervisory skills, which has helped me develop as a mentor. In particular, I would like to acknowledge Bo Portillo. In addition to his

help as an undergraduate researcher, he is now a current graduate student in Dr. Walters' PolySEL (Polymer and Surface Engineering Laboratory) research group who provided tremendous assistance editing this work. I am thankful for the PolySEL group members with whom I have shared many highs and lows, including Dr. Matthew Rowe, Caitlin Naske, Ashley Cornell, Zach Wynne, Ersan Eyiler, Maryam Dadgarmoghaddan, and Emily Smith.

Many thanks to the Chemical Engineering Graduate Student Association and its members who allowed me to serve as their president for two years, the MSU Society of Hispanic Professional Engineers chapter, and the MSU Hispanic Student Association for becoming a part of my journey. I would like to heartfully thank all the great people and friends from around the world I met at MSU for sharing their unique experiences with a Salvadoran student. Special gratitude is given to Dr. Monica Nárvaez-Rivas for providing me with strength and motivation to finish this work. Thanks to everybody I met while at MSU for sharing great moments in life that will stay with me forever.

I deeply appreciate my parents who encouraged me every step of the way and who were great role models, showing me strength, dedication, and perseverance. Thanks to my sisters for making me laugh during difficult times and for providing help generating some great illustrations in this work. Finally, thanks to my grandparents for their wisdom and support.

.

TABLE OF CONTENTS

LIST OF TABLES

LIST OF FIGURES

ABBREVIATIONS

AFM: Atomic force microscope

ATRP: Atom Transfer Radical Polymerization

CFD: computational fluid dynamics

DLS: Dynamic light scattering

Dn: Dean number

FTIR: Fourier transform infrared spectroscopy

JPs: Janus Particles

MFM: magnetic force microscopy

PMAA: Poly(methacrylic) acid

PNIPAM: Poly(N-Isopropyl) acrylamide

PDMAEMA: Poly((2-dimethylamino) ethyl methacrylate)

PDEAEMA: Poly((2-diethylamino) ethyl methacrylate)

PDMAEA: Poly((2-dimethylamino) ethyl acrylate)

PTBAEMA: Poly(*tert*-butylamino) ethyl methacrylate

Re: Reynolds number

SEM: Scanning electron microscopy

SRPs: Stimuli responsive polymers

Si: Silicon substrate

St: Stokes number

SRPs: Stimuli responsive polymers

TEM: Transmission electron microscope

XPS: X-ray photoelectron spectroscopy

CHAPTER I

INTRODUCTION TO MICRO- AND NANO-PARTICLES MATERIALS: PERSPECTIVES, PAST EFFORTS AND FUTURE TRENDS FOR NEW APPLICATION DEVELOPMENTS

1.1 Nanotechnology: Background, definitions and applications

Nanotechnology has received much attention over the last few decades since the visionary insight of Richard Feynman back in the sixties: "There's plenty room at the bottom" (Feynman, 1960). Since then, scientists and researchers around the world have made tremendous strides in developing new nano-sized materials, nano-robots, and nano-characterization techniques. These advances have made nanotechnology such a promising field that it has been called the new industrial revolution (Drexler and Minsky, 1990; Stix, 2001). However, there is some controversy as the effects of nano-scale materials, especially long-term, are not well understood or even yet identified, including health, environment, ethics and quality of life improvements (Drexler et al., 1991; Baird, 2006). Nanomaterials and related nanotechnologies must be further explored in order to design and create new applications that can positively impact society on a daily basis.

Nanoparticles are one example of a nanotechnology system, composed of any one or more solid/soft materials. Nanoparticles are often inorganic, and gold, cadmium, platinum, titanium, iron, and copper nanoparticles are available in different commercial products including sunscreen lotions, cosmetics, and pharmaceuticals (Li et al., 2000; Ni

et al., 2002; Perez-Juste et al., 2005; Jung et al., 2006; Latham and Williams, 2008; Rangappa et al., 2008; Kumfer et al., 2010; Yuan et al., 2010; Wang et al., 2012). Moreover, nanoparticles can also be made of organic matter, such as polymers, allowing the design of molecular building blocks at the nano-level (El-Sherbiny and Smyth, 2010; Trzebicka et al., 2013). Organic and inorganic materials can be combined at the nano-level, producing hybrid nanomaterials in which the inorganic and organic phases are part of a nanocomposite, forming a hybrid nanoparticle. Current fundamental challenges in the field of nanoparticles relies on controlling the size and shape of the nanoparticles during synthesis/production, forming stable and uniform systems, and developing methods to characterize these systems *in situ* such that the true structure and behavior can be accessed without the measurement itself inducing changes or artifacts in the samples.

Nanoparticles are capable to carry a variety of materials such as drugs, genes, DNA, and/or metals, and are called nanocarriers (Baldi et al., 2007). These type of nanoparticles are candidates for biomedical research, and exist in a variety of forms including liposomes,(Allen et al., 1995), biodegradable polymers (Jeong et al., 1997; Jain, 2000), hydrogels (Papaphilippou et al., 2010), magnetic nanocarriers (Kumar and Mohammad, 2011; Mahmoudi et al., 2011), etc. In particular, stimuli-responsive polymers (SRPs) are one of the most attractive options to produce nanocarriers with specific targeting characteristics due to their responsiveness to pH-, temperature and different stimuli conditions (Onaca et al., 2009). In fact, nanotechnology has already been related with SRPs to produce nanocarriers that have potential as nanocarriers for drug delivery applications and gene therapy (Ganta et al., 2008). As an example, SRPs synthesized at the nano-scale level are called polymersomes (Lo et al., 2009) , however,

when polymerized on the surface of a metal-nanoparticle, a hybrid polymer-metal nanocomposites with highly active properties is produced (Hsu et al., 2011; Lyer et al., 2011). For instance, magnetic nanoparticles are potential drug carriers, allowing controlled-manipulation, and targeting specific organs within a certain specimen. Thus, the surface modification of magnetic nanoparticles is still on-going, and is a promising field of investigation.

Predicting the particle transport and deposition of nanoparticles in a certain host/morphology can aid to avoid *in vivo* experiments that analyze nanoparticles behavior. As an example, magnetic nanoparticles aerosol transport and deposition has been studied under the effects of different magnetic fields, and particle sizes using computational fluid dynamics (CFD) (Xie et al., 2010). This is possible due to improvements in computational power and the fast-growing development of experimental techniques to characterize nano-scale materials, opening new opportunities to explore the nanoworld. Over the last two decades, there has been a tremendous increase in the number of publications related to nanotechnology, nanoparticles, surface modification, and CFD (Figure 1.1), therefore, new investigations are needed to fully understand the behavior of nanoparticle systems (Scifinder, 2013). Based on the widespread research interest and the impact to-date on industrial processes, the study of nanoparticle materials will dominate nanotechnology research over the next decade and beyond.

The overall aims of this work are to: (1) extend current knowledge of hybrid inorganic/organic nanoparticle synthetic routes, (2) analyze possible new *in-situ* characterization techniques for nano/micro particulates, and (3) utilize computational fluid dynamics to predict the fate/transport of micron-sized particles. This chapter will

serve to introduce the topics and provide a context for the work performed. First, an introduction to surface modification on flat (planar) substrates and the relationship with nanoparticle surface modification is presented. Next, stimuli-responsive polymers and nanoparticle surface modification techniques are discussed. A comparison of microparticles with nanoparticles is then presented. Finally, computational fluid dynamics is introduced along with an Eulerian method for particle tracking in a two-phase flow system. The last section of this chapter provides a summary of the main goals of this dissertation and a brief description of each chapter.

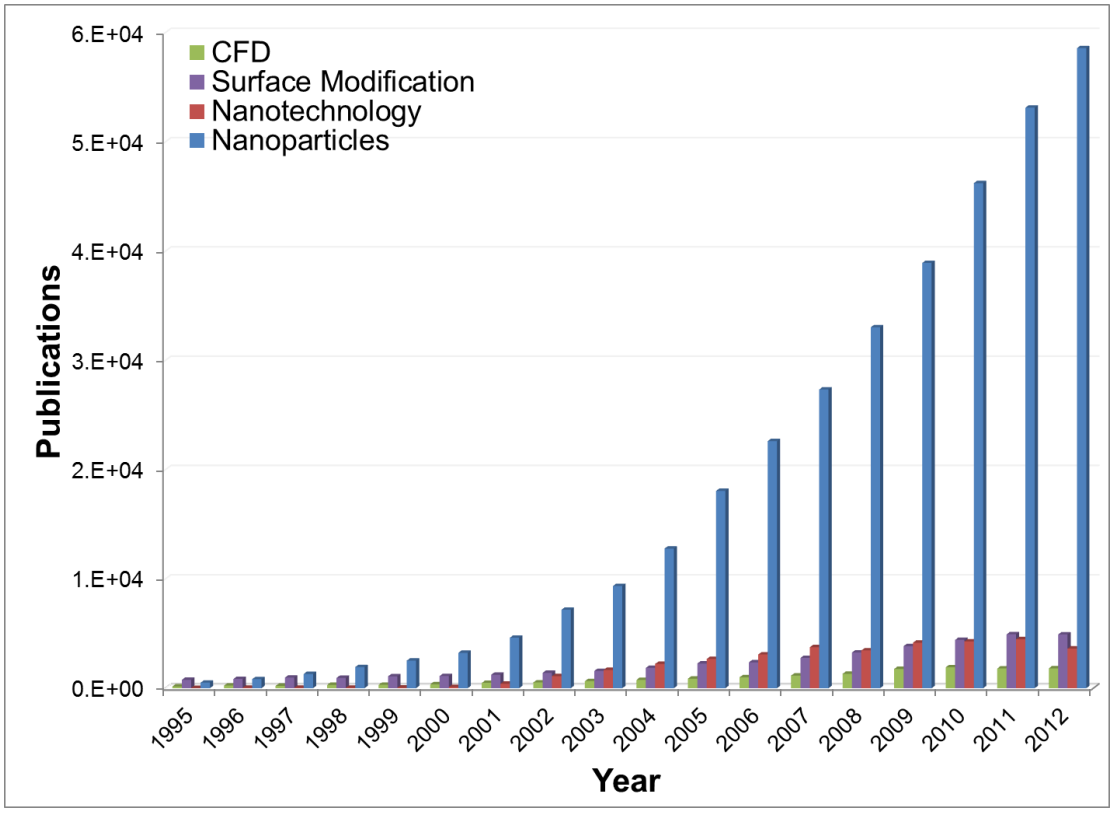

Figure 1.1 Number of publications by year related to different technological fields including computational fluid dynamics (CFD), surface modification, nanotechnology and nanoparticles (Scifinder, 2013).

1.1 Surface modification: Applications and current work

Surface modification had a major impact on technological development during the 21st century and it is believed to be a precursor of nanotechnology and "smart materials" due to molecular building block (Yerushalmi et al., 2005). Surfaces are modified to improve properties such as adhesion, wettability, biocompatibility and many other properties which are sensitive to the surface chemistry (Utsugi, 1973; Schonhorn, 1976; Uyama et al., 1998; Sastry et al., 1999; Ma et al., 2007). New technologies such as micro-chip designs, micro-channels, drug delivery, biomedical applications, adsorption of materials, electrodes, and membranes are examples of surface modified applications. Physical and chemical modifications exist and chemical surface modifications can be achieved using inorganic and/or organic 'coatings'.

There are a number of methods that are used for the surface modification of substrates. This work will focus on the addition of polymer chains to a substrate. The methods described herein are ubiquitous, but are often applied to flat (planar) substrates, and often this is done even if the ultimate goal is to modify a non-planar substrate as often it is easier to characterize the polymer attachment and properties of the modified substrate when flat. It is also often helpful to use reflective substrates, as they allow for interrogation of the surface by reflective techniques. In this work, silicon wafers, gold-coated silicon wafers, and mica substrates will be used, in addition to nano- and micro-particles, for surface modification. The polymers used for surface modification are stimuli-responsive polymers (SRPs), specifically pH and temperature sensitive polymers. These are of interest as they can be used to change the size, shape, roughness, adhesion, agglomeration, and charge of the substrates, and have significant application potential.

Typically to covalently attach a polymer chain to a surface, there are two basic classes of techniques: “grafting to” and “grafting from”. “Grafting to” approaches consist of attaching a preformed polymer with some specific length and molecular weight to a flat/spherical surface, through a reactive functional group on the polymer chain end and/or the substrate. Polymer brushes formed using the “grafting to” approach have some drawbacks due to low grafting density due to steric hindrance involved in a new chain adding an already populated surface (Bittrich et al., 2012). The “grafting from” approach consists of growing a polymer from a reactive/initiated surface. This technique is utilized to create polymeric brushes with desired thickness and molecular weight (Xie et al., 2008; Babu and Dhamodharan, 2009). It has been demonstrated that higher values of grafting density are achieved with this technique (Yim et al., 2006). Main drawbacks of these techniques are related with air-sensitive/anhydrous environments for polymer synthesis. Non-covalent material adsorption has also been used to modify surfaces creating physisorbed films. One example is a layer-by-layer polymer deposition which involves alternating layers of materials with opposite charges using electrostatic interactions (Zhou et al., 2010). Other film deposition technique, such as spin coating and solvent-casting, are well known and established in literature and outside the scope of this work (LeBaron et al., 1999; Siemann, 2005; Krebs, 2009).

Grafting-from approaches, one of the most promising techniques for uniform coating of materials, is the approach used in this study. In particular, atom transfer radical polymerization (ATRP), one of the most versatile and utilized controlled radical polymerization for surface-confined polymerizations, is used in this study. First, the substrate is modified with a self-assembled monolayer (SAM). For example, on a gold

substrate a thiol with an end-functionalized group can be used as the building block for the SAM; due to the formation of the Au-S bond. (Kim et al., 2000). Silanes are also a preferred SAM building block for silicon substrates, and the siloxane (Si-O-Si) bond formed is much more stable than the Au-S bond (Ito et al., 2009). To use the SAM as a reactive substrate, either the terminal group of the SAM, as deposited, is a reactive group (e.g., alkene, halogen) or a reactive group must be formed at the SAM terminus after the SAM is deposited. For surface-confined polymerization, these terminal functional groups are reacted with an initiator. In the case of surface-confined ATRP, a tethered polymer brush can then be formed by adding the monomer in combination with the catalyst/ligand complex in solution. By controlling the concentration of monomer and the reaction time, the desired polymer brush thickness is achieved. A representative illustration of this process is shown below (Figure 1.2).

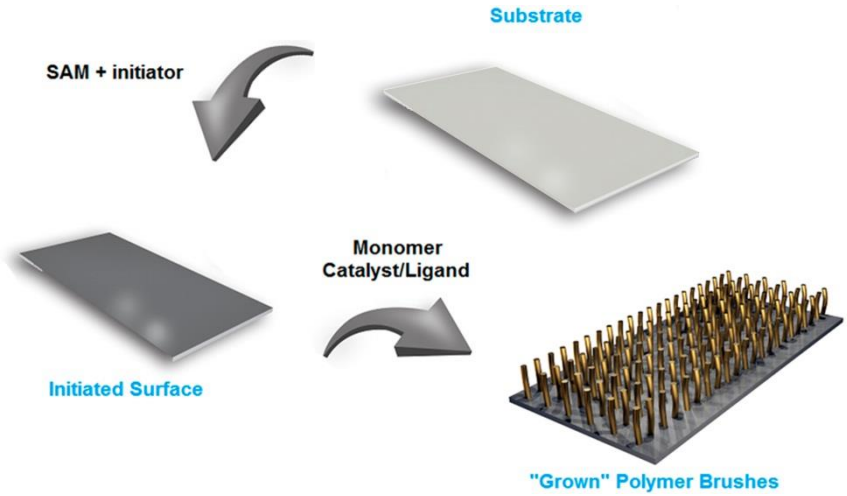

Figure 1.2 Surface-confined ATRP scheme to modify surface of a flat substrate.

In this work, the synthesis and characterization of polymer brushes formed from stimuli-responsive polymers (SRP) is carried out using ATRP on a variety of substrates, including flat silicon wafers and magnetic nanoparticles. SRP were selected due to the significant changes in size and shape when triggered by stimuli's in their surrounding environment including temperature, pH, ionic strength, and UV-light. Briefly, Section 1.2 describes the principles of stimuli responsive polymers and applications and fields of study.

1.2 Stimuli-responsive polymer: An overview

Stimuli responsive polymers are materials that are triggered by a change in an external response such as light, temperature, pH, ionic strength, mechanical deformations, etc (Alarcon et al., 2005; Mendes, 2008; Lee et al., 2010). SRPs were first studied in the form of polymer gel backs in the 1980's, volume phase transitions and responsiveness to pH and temperature changes were explained as a balance between hydrophobic and hydrophilic interactions at the molecular level (Tanaka et al., 1980; Ilavsky, 1982; Stauffer et al., 1982; Hirokawa and Tanaka, 1984; Hirotsu et al., 1987; Khokhlov et al., 1993). Then, polymers in solution, block-*co*-polymers, surface tethered SRPs, and cross-linked gels were analyzed and investigated for several applications including drug delivery and inorganic materials encapsulation (Jeong and Gutowska, 2002; Nath and Chilkoti, 2002a). These materials found inspiration in nature, becoming promising in a variety a fields such as drug delivery, self-healing materials, encapsulation of metals, and many other fields (Nath and Chilkoti, 2002b; Ionov et al., 2003; Granville et al., 2004; Brittain et al., 2006; Motornov et al., 2007).

SRPs have also found a place in nanotechnology. As previously discussed, SRPs nanoparticles can be used for targeting, diagnostics, and delivery carriers to specific organs in the human body (Onaca et al., 2009; Mishra et al., 2010). A variety of polymers have already been characterized, synthesized and demonstrated responsiveness behavior to different external triggers. Some examples of polymers that present a switching behavior to certain stimuli, and their main characteristics, are shown on Table 1.1. Additionally, pH and temperature responsive SRPs are the most common triggers that are studied for the development of polymers, becoming a demanding field for the synthesis, dry/*in-situ* characterization, and *in-vitro/in-vivo* applications (Nath and Chilkoti, 2002a; Gil and Hudson, 2004).

Table 1.1 Examples SRPs and descriptions of their responses to different stimuli.

Stimuli	Example Polymer(s)	Description	Reference(s)
Temperature	Poly(N-isopropyl acrylamides) and/or poly(N-substituted acrylamides)	Polymer collapsed at a lower critical solution temperature (e.g. PNIPAM at 32 °C in water)	(Hoffman and Stayton, 2004; Kizhakkedathu et al., 2004; Plunkett et al., 2006; Patra et al., 2011)
pH	Poly(cationic/anionic) polymers, e.g. poly(2-dimethylaminoethyl methacrylate) (PDMAEMA)	Polymeric-based delivery vehicles for therapeutics	(Veron et al., 2004; Chen et al., 2011; Truong et al., 2011)
UV/light	Photo-responsive polymers, e.g. poly(N,N-dimethylacrylamide-co-methacryloyloxyazobenzene)	Polymer chains dissociate upon UV-interactions	(Deshmukh, 2008)
Deformation/stress, self-repairing materials	Shape-memory alloys, e.g. poly(ε-caprolactone)	Return to original shape after deformation effects	(Zhu et al., 2003)
Ultrasound	1,2 disubstituted bezocyclobutene mechanophore incorporated on polymethacrylate chain	Polymer change in color as ultrasound effects are present	(Potisek et al., 2007)

For instance, SRPs combined with nanoparticles is a promising field in biomedicine, allowing researchers to produce materials with drug delivery characteristics capable of release/entrap materials, and a variety of studies are the emphasis of this work. Due to the vast literature in this subject area, each chapter involving SRPs and surface modification of nanoparticles/flat substrates, and prior efforts for each particular type of polymer will include a detailed discussion. Peculiar responses to pH and/or temperature will also be discussed in conjunction with previous findings for each polymer analyzed on each chapter of this work.

1.3 Polymeric and surface-modified metallic nanoparticles for drug delivery applications

Nanoparticles, as documented earlier, are currently one of the most published topics for research. While many different inorganic and nanoparticles have been synthesized and characterized with an aim towards new drug delivery devices (Pankhurst et al., 2003; McCarthy and Weissleder, 2008; Namdeo et al., 2008), few reports are available in the literature where the surfaces of nanoparticles are modified in a controlled fashion with SRP (Ayres et al., 2007; Motornov et al., 2007; Robinson et al., 2007; Chuang et al., 2010).

The main purposes in modifying the surfaces of nanoparticles are to attach a moiety for be 'delivered' and/or to control nanoparticle interactions with one another and their environment. Pharmacokinetics and particle fate in a living system are affected by the external coating on the surface of nanoparticles influencing the internal transport, partitioning, cellular interactions and uptake. For example, breviscapine, a drug to treat cerebrovascular diseases, has poor bioavailability as orally administered; but, when

combined with poly(L-lactic acid), nano-particles carriers were able to pass across the blood brain barrier, acting as a drug-targeting/delivery material (Liu et al., 2008). Different examples illustrate applications in which drug-loaded micro/nano-particles has improved bio-distribution, pharmacokinetics, dispersion or sensor properties using different drug encapsulation methods.

Micro-beads and –particles were studied earlier than nanoparticles as powders, dispersants, lubricants, micro-droplets, two-phase flows and drug carriers (DiStefano, 2007; Prata et al., 2010). One of the major early uses of microparticles was for drug delivery that relied on fast absorption in the gastrointestinal tract, due to a high-surface area with respect to volume ratio. These drug delivery methods were usually accompanied with biodegradable/biocompatible polymers such as poly(ethylene glycol) and poly(lactic acid) (Jain, 2000). Other drug delivery mechanisms consist of aerosols with micro-sized droplets which deliver certain drugs to the lungs causing a rapid absorption through alveolar epithelium and into the bloodstream. Different examples of encapsulation and/or preparation methods are shown in Table 1.2, where a polymer is loaded with a drug in a micro-scale design.

Table 1.2 Different methods for drug encapsulation using polymer carrier.

Synthesis Method	Polymer(s)	Drug	Reference
Solvent displacement	PEO-PCL	Tamoxifen	(Jeong et al., 2005)
Co-precipitation	P(Esu-co-PAd) Polyesters	Raloxifene HCL	(Bikiaris et al., 2009a)
Suspension Polymerization	P(HEMA)	5-Fluorouracil	(Chouhan and Bajpai, 2009)
Miniemulsion/solvent displacement	Nylon 6	--------	(Crespy and Landfester, 2007)
Emulsion-solvent evaporation	Chitosan/PEG PLGA	Plasminogen activators	(Chung et al., 2008)
Emulsion solvent diffusion	PLGA and PLA	------	(Murakami et al., 1999)
Emulsion-solvent evaporation	PLGA	DNA	(Wang et al., 1999)
Oil-in-water emulsion	PLGA	TNBS	(Lamprecht et al., 2001)
Ring opening polymerization	Chitosan	Peptides	(Batista et al., 2006)
Polycondensation	Poly(propylene succinate)	Fluvastatin	(Bikiaris et al., 2009b)
Direct-write inject technique	Calcium alginate	Rodamine 6G	(Desai et al., 2010)
Incubation	Chitosan/PAA/PNIPAM	Doxycycline	(Chuang et al., 2009)
Grafting to approach	Chitosan	Phenylalanine	(Yoksan and Akashi, 2009)

ATRP, a technique previously discussed for the surface-modification of flat substrates, has also been used to "grow" polymer brushes from the surface of nanoparticles using different types of monomers such as methyl methacrylate (Marutani et al., 2004), acrylic acid (Rutnakornpituk et al., 2011), ethylene glycol (Kang et al., 2009), and styrene (Garcia et al., 2007). Despite the different reports available in literature for the surface modification of nanoparticles, to this author's knowledge there is only few reports in the literature of homogeneous and heterogeneous SRPs covalently bonded coated on the surface of magnetic nanoparticles (Shim and Kwon, 2012).

Therefore, one of the objectives of this work is to evaluate the synthesis of pH- and thermo-responsive polymers from the surface of magnetic nanoparticles using ATRP.

Additionally, biological design at the micron-scale and micro-scale manipulation can provide a foundation upon which to understand the nano-scale behavior of materials. Thus, the transport behavior of micron-sized particles is critical in drug-delivery applications. Having a way to know *a priori* where and how much of a drug will be taken up by the body would be vital to developing patient-specific treatments and evaluation of new drug delivery methods. Moreover, by understanding the transport properties of microparticles, predictions can be made for nanoparticle transport models, in a similar way as compared to drug loading microparticles being a model for the design of nanoparticle carriers. For this reason, current efforts for the transport and deposition studies of micron-sized particles in different morphologies, that later could be potentially use for the analysis of nanoparticle systems, are discussed next.

1.4 Transport modeling of micron-sized particles

Micron-sized particles have been utilized in a variety of processes (see Section 1.3). Therefore, predicting the fate and transport properties of these materials becomes a practical tool for drug synthesis as properties such as size and shape behavior can be optimized for improved delivery. Previously two-phase flow systems have been modeled using a well-known Lagrangian approach in which particles are followed individually until they reach their final destination (Breuer et al., 2006; Kuan et al., 2007). A tracking method involving an Eulerian approach in which coordinate systems/planes are used to track particles rather than following the trajectory of each individual particle has been developed and studied (Heistracher and Hofmann, 1995; Longest and Xi, 2007; Pilou et

al., 2011). Eulerian tracking-methodology provides a better framework and applicability where a large number of particles will be present as occurs in the case of nanoparticle size materials distributions. Thus, by developing and validating a Eulerian tracking method on micron-sized particle the model for utilization with nanoparticles could be improved and lead to further applications in the prediction of nanoparticle fate and transport.

In this work, two main grids: a 90-degree bend and a physiological realistic model (PRB) are used to validate the developed method. More information about this work is presented in chapter 5 and 6 of this dissertation.

1.5 Summary

Nanoparticle-based technologies are an emerging field with the promise to impact a wide range of application areas. However, that potential is somewhat married to a host of research questions that remain to be answered. This work attempts to answer the surface modification of magnetic nanoparticles in a controlled fashion to produce hybrid nanoparticle systems with different morphologies, understand *in situ* behavior of SRPs, and obtain a better idea for the particle-tracking and -deposition in certain defined grids; it is organized to discuss particle surface modification, a novel method of forming 'two-faced' nanoparticles, use of stimuli-responsive polymers to modify (planar) surfaces and analyze *in situ* characterization techniques, and use computational methods(CFD) to track particulate flows and deposition in human lung morphologies. Specifically, Chapter 2 describes efforts to modify the surface modification of magnetic nanoparticles with two different stimuli-responsive polymers, poly(N-isopropyl acrylamide) (PNIPAM) and poly(methacrylic acid) (PMAA). Chapter 3 presents a novel method to produce a hybrid

biphasic polymer-metal nanoparticle, known as 'Janus nanoparticle", where two dissimilar polymers are grafted on opposite sides. Chapter 4 describes how *in-situ* characterization techniques were used to evaluate the responsiveness of surface grafted polymer brushes. Chapters 5 and 6 carry the work towards looking at particle fate—particularly in the human lung—and detail the use of computational fluid dynamics (CFD) to accurately predict particle transport and fate of micron-sized nanoparticles in a 90-degree bend (Chapter 5) and in a human physiological realistic bifurcation (PRB) (Chapter 6). Lastly, a summary of the main conclusions and current efforts in the synthesis and characterization techniques are briefly summarized and put in context of possible future directions in this field in Chapter 7.

1.6 References

Al-Rawashdeh, N. A. F. and W. Azzam (2011). "Gold nanoparticles chemisorbed by a terphenyldithiol self-assembled monolayer for fabrication of a protein biosensor." Res. Chem. Intermed. **37**: 759-770.

Alarcon, C. d. l. H., S. Pennadam and C. Alexander (2005). "Stimuli responsive polymers for biomedical applications." Chemical Society Reviews **34**: 276-285.

Allen, T. M., C. B. Hansen and M. D. E. L. de (1995). "Pharmacokinetics of long-circulating liposomes." Adv. Drug Delivery Rev. **16**: 267-284.

Ayres, N., S. G. Boyes and W. J. Brittain (2007). "Stimuli-Responsive Polyelectrolyte Polymer Brushes Prepared via Atom-Transfer Radical Polymerization." Langmuir **23**: 182-189.

Babu, K. and R. Dhamodharan (2009). "Synthesis of polymer grafted magnetite nanoparticle with the highest grafting density via controlled radical polymerization." Nanoscale Res. Lett. **4**: 1090-1102.

Baird, D. (2006). Nanotechnology challenges: implications for philosophy, ethics and society, World Scientific.

Baldi, G., D. Bonacchi, M. C. Franchini, D. Gentili, G. Lorenzi, A. Ricci and C. Ravagli (2007). "Synthesis and coating of cobalt ferrite nanoparticles: a first step toward the obtainment of new magnetic nanocarriers." Langmuir **23**: 4026-4028.

Batista, M. K. S., L. F. Pinto, C. A. R. Gomes and P. Gomes (2006). "Novel highly-soluble peptide-chitosan polymers: Chemical synthesis and spectral characterization." Carbohydrate Polymers **64**: 299-305.

Bikiaris, D., V. Karavelidis and E. Karavas (2009a). "Novel Biodegradable Polyesters. Synthesis and Application as Drug Carriers for the Preparation of Raloxifene HCl Loaded Nanoparticles." Molecules **14**: 2410-2430.

Bikiaris, D. N., G. Z. Papageorgiou, S. A. Papadimitriou, E. Karavas and K. Avgoustakis (2009b). "Novel Biodegradable Polyester Poly(Propylene Succinate): Synthesis and Application in the Preparation of Solid Dispersions and Nanoparticles of a Water-Soluble Drug." AAPS PharmSciTech **10**: 138-146.

Bittrich, E., S. Burkert, M. Müller, K.-J. Eichhorn, M. Stamm and P. Uhlmann (2012). "Temperature-Sensitive Swelling of Poly(N-isopropylacrylamide) Brushes with Low Molecular Weight and Grafting Density." Langmuir **28**: 3439-3448.

Breuer, M., H. T. Baytekin and E. A. Matida (2006). "Prediction of aerosol deposition in 90˚ bends using LES and an efficient Lagrangian tracking method." Journal of Aerosol Science **37**: 1407-1428.

Brittain, W. J., S. G. Boyes, A. M. Granville, M. Baum, B. K. Mirous, B. Akgun, et al.M. D. Foster (2006). "Surface rearrangement of diblock copolymer brushes-stimuli responsive films." Adv. Polym. Sci. **198**: 125-147.

Chen, J.-K., B.-J. Bai and F.-C. Chang (2011). "Diagnosis of breast cancer recurrence using a microfluidic device featuring tethered cationic polymers." Appl. Phys. Lett. **99**: 013701-013703.

Chouhan, R. and A. K. Bajpai (2009). "An in vitro release study of 5-fluoro-uracil (5-FU) from swellable poly-(2-hydroxyethyl methacrylate) (PHEMA) nanoparticles." Journal of Materials Science-Materials in Medicine **20**: 1103-1114.

Chuang, C.-Y., T.-M. Don and W.-Y. Chiu (2010). "Synthesis and characterization of stimuli-responsive porous/hollow nanoparticles by self-assembly of chitosan-based graft copolymers and application in drug release." J. Polym. Sci., Part A: Polym. Chem. **48**: 2377-2387.

Chuang, C. Y., T. M. Don and W. Y. Chiu (2009). "Synthesis and Properties of Chitosan-Based Thermo- and pH-Responsive Nanoparticles and Application in Drug Release." Journal of Polymer Science Part a-Polymer Chemistry **47**: 2798-2810.

Chung, T. W., S. S. Wang and W. J. Tsai (2008). "Accelerating thrombolysis with chitosan-coated plasminogen activators encapsulated in poly-(lactide-co-glycolide) (PLGA) nanoparticles." Biomaterials **29**: 228-237.

Crespy, D. and K. Landfester (2007). "Preparation of nylon 6 nanoparticles and nanocapsules by two novel miniemulsion/solvent displacement hybrid techniques." Macromolecular Chemistry and Physics **208**: 457-466.

Desai, S., J. Perkins, B. S. Harrison and J. Sankar (2010). "Understanding release kinetics of biopolymer drug delivery microcapsules for biomedical applications." Materials Science and Engineering: B **168**: 127-131.

Deshmukh, S. (2008). Responsive polymers for dynamic modulation of bio-macromolecular transport properties, Massachusetts Institute of Technology.

DiStefano, F. V. (2007). Use of 2,3-dihydroxynaphthalene-6-sulfonic acid salts as dispersants, Air Products and Chemicals, Inc., USA . 11 pp.

Drexler, K. E. and M. L. Minsky (1990). Engines of creation (pp. 171-190), Fourth Estate.

Drexler, K. E., C. Peterson and G. Pergamit (1991). Unbounding the future: the Nanotechnology Revolution. G. Pergamit (Ed.). William Morrow.

El-Sherbiny, I. M. and H. D. Smyth (2010). "Biodegradable nano-micro carrier systems for sustained pulmonary drug delivery: (I) self-assembled nanoparticles encapsulated in respirable/swellable semi-IPN microspheres." International Journal of Pharmaceutics **395**: 132-141.

Feynman, R. P. (1960). "There's plenty of room at the bottom." Engineering and Science **23**: 22-36.

Ganta, S., H. Devalapally, A. Shahiwala and M. Amiji (2008). "A review of stimuli-responsive nanocarriers for drug and gene delivery." Journal of Controlled Release **126**: 187-204.

Garcia, I., A. Tercjak, N. E. Zafeiropoulos, M. Stamm and I. Mondragon (2007). "Self-assembling nanomaterials using magnetic nanoparticles modified with polystyrene brushes." Macromol. Rapid Commun. **28**: 2361-2365.

Gil, E. S. and S. M. Hudson (2004). "Stimuli-responsive polymers and their bioconjugates." Progress in Polymer Science **29**: 1173-1222.

Granville, A. M., S. G. Boyes, B. Akgun, M. D. Foster and W. J. Brittain (2004). "Synthesis and Characterization of Stimuli-Responsive Semifluorinated Polymer Brushes Prepared by Atom Transfer Radical Polymerization." Macromolecules **37**: 2790-2796.

Gravano, S. M., R. Dumas, K. Liu and T. E. Patten (2005). "Methods for the surface functionalization of γ-Fe2O3 nanoparticles with initiators for atom transfer radical polymerization and the formation of core-shell inorganic-polymer structures." J. Polym. Sci., Part A: Polym. Chem. **43**: 3675-3688.

Heistracher, T. and W. Hofmann (1995). "Physiologically realistic models of bronchial airway bifurcations." Journal of Aerosol Science **26**: 497-509.

Hirokawa, Y. and T. Tanaka (1984). "Volume phase transition in a nonionic gel." The Journal of Chemical Physics **81**: 6379-6380.

Hirotsu, S., Y. Hirokawa and T. Tanaka (1987). "Volume-phase transitions of ionized N-isopropylacrylamide gels." Journal of Chemical Physics **87**: 1392.

Hoffman, A. S. and P. S. Stayton (2004). "Bioconjugates of smart polymers and proteins: synthesis and applications." Macromol. Symp. **207**: 139-151.

Hsu, L., C. Weder and S. J. Rowan (2011). "Stimuli-responsive, mechanically-adaptive polymer nanocomposites." J. Mater. Chem. **21**: 2812-2822.

Ilavsky, M. (1982). "Phase transition in swollen gels. 2. Effect of charge concentration on the collapse and mechanical behavior of polyacrylamide networks." Macromolecules **15**: 782-788.

Ionov, L., S. Minko, M. Stamm, J.-F. Gohy, R. Jerome and A. Scholl (2003). "Reversible Chemical Patterning on Stimuli-Responsive Polymer Film: Environment-Responsive Lithography." J. Am. Chem. Soc. **125**: 8302-8306.

Ito, Y., A. A. Virkar, S. Mannsfeld, J. H. Oh, M. Toney, J. Locklin and Z. Bao (2009). "Crystalline ultrasmooth self-assembled monolayers of alkylsilanes for organic field-effect transistors." J Am Chem Soc **131**: 9396-9404.

Jain, R. A. (2000). "The manufacturing techniques of various drug loaded biodegradable poly(lactide-co-glycolide) (PLGA) devices." Biomaterials **21**: 2475-2490.

Jeong, B., Y. H. Bae, D. S. Lee and S. W. Kim (1997). "Biodegradable block copolymers as injectable drug-delivery systems." Nature (London) **388**: 860-862.

Jeong, B. and A. Gutowska (2002). "Lessons from nature: stimuli-responsive polymers and their biomedical applications." Trends Biotechnol. **20**: 305-311.

Jeong, Y. I., S. J. Seo, I. K. Park, H. C. Lee, I. C. Kang, T. Akaike and C. S. Cho (2005). "Cellular recognition of paclitaxel-loaded polymeric nanoparticles composed of poly(gamma-benzul L-glutamate) and poly(ethylene glycol) diblock copolymer endcapped with galactose moiety." International Journal of Pharmaceutics **296**: 151-161.

Jung, J., K. W. Kim, K. Na, M. Kaholek, S. Zauscher and J. Hyun (2006). "Fabrication of micropatterned gold nanoparticle arrays as a template for surface-initiated polymerization of stimuli-responsive polymers." Macromol. Rapid Commun. **27**: 776-780.

Kang, S. M., I. S. Choi, K.-B. Lee and Y. Kim (2009). "Bioconjugation of poly(poly(ethylene glycol) methacrylate)-coated iron oxide magnetic nanoparticles for magnetic capture of target proteins." Macromol. Res. **17**: 259-264.

Khokhlov, A., S. Starodubtzev and V. Vasilevskaya (1993). Conformational transitions in polymer gels: Theory and experiment

Responsive Gels: Volume Transitions I. K. Dušek, Springer Berlin / Heidelberg. **109:** 123-171.

Kim, J.-B., M. L. Bruening and G. L. Baker (2000). "Surface-Initiated Atom Transfer Radical Polymerization on Gold at Ambient Temperature." J. Am. Chem. Soc. **122**: 7616-7617.

Kizhakkedathu, J. N., R. Norris-Jones and D. E. Brooks (2004). "Synthesis of well-defined environmentally responsive polymer brushes by aqueous ATRP." Macromolecules **37**: 734-743.

Kolodziejczyk, L., D. Martinez-Martinez, T. C. Rojas, A. Fernandez and J. C. Sanchez-Lopez (2007). "Surface-modified Pd nanoparticles as a superior additive for lubrication." J. Nanopart. Res. **9**: 639-645.

Krebs, F. C. (2009). "Fabrication and processing of polymer solar cells: A review of printing and coating techniques." Sol. Energy Mater. Sol. Cells **93**: 394-412.

Kuan, B., W. Yang and M. P. Schwarz (2007). "Dilute gas-solid two-phase flows in a curved 90 degrees duct bend: CFD simulation with experimental validation." Chemical Engineering Science **62**: 2068-2088.

Kumar, C. S. S. R. and F. Mohammad (2011). "Magnetic nanomaterials for hyperthermia-based therapy and controlled drug delivery." Adv. Drug Delivery Rev. **63**: 789-808.

Kumfer, B. M., K. Shinoda, B. Jeyadevan and I. M. Kennedy (2010). "Gas-Phase Flame Synthesis and Properties of Magnetic Iron Oxide Nanoparticles with Reduced Oxidation State." Journal of Aerosol Science **41**: 257-265.

Lamprecht, A., N. Ubrich, H. Yamamoto, U. Schafer, H. Takeuchi, P. Maincent, et al.C. M. Lehr (2001). "Biodegradable nanoparticles for targeted drug delivery in treatment of inflammatory bowel disease." Journal of Pharmacology and Experimental Therapeutics **299**: 775-781.

Latham, A. H. and M. E. Williams (2008). "Controlling transport and chemical functionality of magnetic nanoparticles." Accounts of Chemical Research **41**: 411-420.

LeBaron, P. C., Z. Wang and T. J. Pinnavaia (1999). "Polymer-layered silicate nanocomposites: an overview." Appl. Clay Sci. **15**: 11-29.

Lee, H.-i., J. Pietrasik, S. S. Sheiko and K. Matyjaszewski (2010). "Stimuli-responsive molecular brushes." Prog. Polym. Sci. **35**: 24-44.

Li, G., C. Li and Y. Zhu (2000). "Surface modification of nanometer titania particles used as ultraviolet absorbent in cosmetics." Huaxue Shijie **41**: 59-63.

Liu, M., H. Li, G. Luo, Q. Liu and Y. Wang (2008). "Pharmacokinetics and biodistribution of surface modification polymeric nanoparticles." Arch. Pharmacal Res. **31**: 547-554.

Lo, P. C., H. Lomas, M. Massignani, T. Smart and G. Battaglia (2009). "Polymersomes: nature inspired nanometer sized compartments." J. Mater. Chem. **19**: 3576-3590.

Longest, P. W. and J. X. Xi (2007). "Effectiveness of direct Lagrangian tracking models for simulating nanoparticle deposition in the upper airways." Aerosol Science and Technology **41**: 380-397.

Lyer, S., E. Schreiber, R. Tietze, J. Mann, T. Struffert, T. Engelhorn, et al.C. Alexiou (2011). "Nanotechnology and Cancer Treatment: Magnetic Nanoparticles for a New and Innovative Drug Delivery System." Anticancer Research **31**: 1991-1992.

Ma, Z., Z. Mao and C. Gao (2007). "Surface modification and property analysis of biomedical polymers used for tissue engineering." Colloids Surf., B **60**: 137-157.

Mahmoudi, M., S. Sant, B. Wang, S. Laurent and T. Sen (2011). "Superparamagnetic iron oxide nanoparticles (SPIONs): Development, surface modification and applications in chemotherapy." Adv. Drug Delivery Rev. **63**: 24-46.

Marutani, E., S. Yamamoto, T. Ninjbadgar, Y. Tsujii, T. Fukuda and M. Takano (2004). "Surface-initiated atom transfer radical polymerization of methyl methacrylate on magnetite nanoparticles." Polymer **45**: 2231-2235.

McCarthy, J. R. and R. Weissleder (2008). "Multifunctional magnetic nanoparticles for targeted imaging and therapy." Adv. Drug Delivery Rev. **60**: 1241-1251.

Mendes, P. M. (2008). "Stimuli-responsive surfaces for bio-applications." Chem. Soc. Rev. **37**: 2512-2529.

Mishra, B., B. B. Patel and S. Tiwari (2010). "Colloidal nanocarriers: a review on formulation technology, types and applications toward targeted drug delivery." Nanomedicine-Nanotechnology Biology and Medicine **6**: 9-24.

Motornov, M., R. Sheparovych, R. Lupitskyy, E. MacWilliams, O. Hoy, I. Luzinov and S. Minko (2007). "Stimuli-responsive colloidal systems from mixed brush-coated nanoparticles." Adv. Funct. Mater. **17**: 2307-2314.

Murakami, H., M. Kobayashi, H. Takeuchi and Y. Kawashima (1999). "Preparation of poly(-lactide-co-glycolide) nanoparticles by modified spontaneous emulsification solvent diffusion method." International Journal of Pharmaceutics **187**: 143-152.

Namdeo, M., S. Saxena, R. Tankhiwale, M. Bajpai, Y. M. Mohan and S. K. Bajpai (2008). "Magnetic nanoparticles for drug delivery applications." J. Nanosci. Nanotechnol. **8**: 3247-3271.

Nath, N. and A. Chilkoti (2002b). "Creating “Smart” Surfaces Using Stimuli Responsive Polymers." Advanced Materials **14**: 1243-1247.

Ni, T., D. K. Nagesha, J. Robles, N. F. Materer, S. Mussig and N. A. Kotov (2002). "CdS nanoparticles modified to chalcogen sites: new supramolecular complexes, butterfly bridging, and related optical effects." J Am Chem Soc **124**: 3980-3992.

Onaca, O., R. Enea, D. W. Hughes and W. Meier (2009). "Stimuli-responsive polymersomes as nanocarriers for drug and gene delivery." Macromol. Biosci. **9**: 129-139.

Pankhurst, Q. A., J. Connolly, S. K. Jones and J. Dobson (2003). "Applications of magnetic nanoparticles in biomedicine." J. Phys. D: Appl. Phys. **36**: R167-R181.

Papaphilippou, P. C., A. Pourgouris, O. Marinica, A. Taculescu, G. I. Athanasopoulos, L. Vekas and T. Krasia-Christoforou (2010). "Fabrication and characterization of superparamagnetic and thermoresponsive hydrogels based on oleic-acid-coated Fe3O4 nanoparticles, hexa(ethylene glycol) methyl ether methacrylate and 2-(acetoacetoxy)ethyl methacrylate." J. Magn. Magn. Mater. **323**: 557-563.

Patra, L., A. Vidyasagar and R. Toomey (2011). "The effect of the Hofmeister series on the deswelling isotherms of poly(N-isopropylacrylamide) and poly(N,N-diethylacrylamide)." Soft Matter **7**: 6061-6067.

Perez-Juste, J., I. Pastoriza-Santos, L. M. Liz-Marzan and P. Mulvaney (2005). "Gold nanorods: Synthesis, characterization and applications." Coord. Chem. Rev. **249**: 1870-1901.

Perez-Lopez, B. and A. Merkoci (2011). "Magnetic Nanoparticles Modified with Carbon Nanotubes for Electrocatalytic Magnetoswitchable Biosensing Applications." Adv. Funct. Mater. **21**: 255-260.

Pilou, M., S. Tsangaris, P. Neofytou, C. Housiadas and Y. Drossinos (2011). "Inertial particle deposition in a 90 laminar flow bend: An eulerian fluid particle approach." Aerosol Science and Technology **45**: 1376-1387.

Plunkett, K. N., X. Zhu, J. S. Moore and D. E. Leckband (2006). "PNIPAM Chain Collapse Depends on the Molecular Weight and Grafting Density." Langmuir **22**: 4259-4266.

Potisek, S. L., D. A. Davis, N. R. Sottos, S. R. White and J. S. Moore (2007). "Mechanophore-Linked Addition Polymers." Journal of the American Chemical Society **129**: 13808-13809.

Prata, J. E., T. A. Barth, S. A. Bencherif and N. R. Washburn (2010). "Complex fluids based on methacrylated hyaluronic acid." Biomacromolecules **11**: 769-775.

Rangappa, D., S. Ohara, M. Umetsu, T. Naka and T. Adschiri (2008). "Synthesis, characterization and organic modification of copper manganese oxide nanocrystals under supercritical water." J. Supercrit. Fluids **44**: 441-445.

Robinson, I., C. Alexander, L. T. Lu, L. D. Tung, D. G. Fernig and N. T. K. Thanh (2007). "One-step synthesis of monodisperse water-soluble 'dual-responsive' magnetic nanoparticles." Chem. Commun.: 4602-4604.

Rutnakornpituk, M., N. Puangsin, P. Theamdee, B. Rutnakornpituk and U. Wichai (2011). "Poly(acrylic acid)-grafted magnetic nanoparticle for conjugation with folic acid." Polymer **52**: 987-995.

Sastry, M., V. Patil and K. S. Mayya (1999). Bilayer formation on nanoparticle surfaces. A new strategy for surface modification, Imperial College Press.

Schonhorn, H. (1976). “Surface modification of polymer and practical adhesion.” Polym. Eng. Sci. **17**:440-9.

Scifinder. (2013). "Chemical Abstracts Services." , search by name. Retrieved 04/05/13, from https://scifinder.cas.org/.

Shim, M. S. and Y. J. Kwon (2012). "Stimuli-responsive polymers and nanomaterials for gene delivery and imaging applications." Adv. Drug Delivery Rev. **64**: 1046-1059.

Siemann, U. (2005). "Solvent cast technology - a versatile tool for thin film production." Prog. Colloid Polym. Sci. **130**: 1-14.

Stauffer, D., A. Coniglio and M. Adam (1982). Gelation and critical phenomena. Polymer Networks. K. Dušek, Springer Berlin Heidelberg. **44:** 103-158.

Stix, G. (2001). "Little big science." Scientific American **285**: 26-31.

Tanaka, T., D. Fillmore, S.-T. Sun, I. Nishio, G. Swislow and A. Shah (1980). "Phase Transitions in Ionic Gels." Physical Review Letters **45**: 1636-1639.

Truong, N. P., Z. Jia, M. Burgess, L. Payne, N. A. J. McMillan and M. J. Monteiro (2011). "Self-catalyzed degradable cationic polymer for release of DNA." Biomacromolecules **12**: 3540-3548.

Trzebicka, B., B. Robak, R. Trzcinska, D. Szweda, P. Suder, J. Silberring and A. Dworak (2013). "Thermosensitive PNIPAM-peptide conjugate - Synthesis and aggregation." Eur. Polym. J. **49**: 499-509.

Utsugi, H. (1973). "Surface modification of oxide powders and the properties of the modified surfaces." Hyomen **11**: 591-609; (511), 654-570.

Uyama, Y., K. Kato and Y. Ikada (1998). "Surface modification of polymers by grafting." Adv. Polym. Sci. **137**: 1-39.

Veron, L., A. Ganee, M. T. Charreyre, C. Pichot and T. Delair (2004). "New hydrolyzable pH-responsive cationic polymers for gene delivery: a preliminary study." Macromol Biosci **4**: 431-444.

Wang, D., D. R. Robinson, G. S. Kwon and J. Samuel (1999). "Encapsulation of plasmid DNA in biodegradable poly(D, L-lactic-co-glycolic acid) microspheres as a novel approach for immunogene delivery." Journal of Controlled Release **57**: 9-18.

Wang, M., Q. Sheng, D. Zhang, Y. He and J. Zheng (2012). "TiC nanoparticles-chitosan composite film for the direct electron transfer of myoglobin and its application in biosensing." Bioelectrochemistry **86**: 46-53.

Whitesides, G. M. (2006). "The origins and the future of microfluidics." Nature (London, U. K.) **442**: 368-373.

Xie, M., J. Dang, H. Han, W. Wang, J. Liu, X. He and Y. Zhang (2008). "Well-Defined Brush Copolymers with High Grafting Density of Amphiphilic Side Chains by Combination of ROP, ROMP, and ATRP." Macromolecules **41**: 9004-9010.

Xie, Y., P. Zeng, R. A. Siegel, T. S. Wiedmann, B. E. Hammer and P. W. Longest (2010). "Magnetic deposition of aerosols composed of aggregated superparamagnetic nanoparticles." Pharm Res **27**: 855-865.

Yerushalmi, R., A. Scherz, M. E. van der Boom and H.-B. Kraatz (2005). "Stimuli responsive materials: new avenues toward smart organic devices." Journal of Materials Chemistry **15**: 4480-4487.

Yim, H., M. S. Kent, S. Mendez, G. P. Lopez, S. Satija and Y. Seo (2006). "Effects of grafting density and molecular weight on the temperature-dependent conformational change of poly(N-isopropylacrylamide) grafted chains in water." Macromolecules **39**: 3420-3426.

Yoksan, R. and M. Akashi (2009). "Low molecular weight chitosan-g-l-phenylalanine: Preparation, characterization, and complex formation with DNA." Carbohydrate Polymers **75**: 95-103.

Yuan, J., F. Schacher, M. Drechsler, A. Hanisch, Y. Lu, M. Ballauff and A. H. E. Mueller (2010). "Stimuli-Responsive Organosilica Hybrid Nanowires Decorated with Metal Nanoparticles." Chem. Mater. **22**: 2626-2634.

Zhou, J., G. Romero, E. Rojas, L. Ma, S. Moya and C. Gao (2010). "Layer by layer chitosan/alginate coatings on poly(lactide-co-glycolide) nanoparticles for antifouling protection and Folic acid binding to achieve selective cell targeting." J Colloid Interface Sci.**345**:241-247

Zhu, G., G. Liang, Q. Xu and Q. Yu (2003). "Shape-memory effects of radiation crosslinked poly (ϵ-caprolactone)." Journal of Applied Polymer Science **90**: 1589-1595.

CHAPTER II

SURFACE MODIFICATION OF IRON OXIDE (Fe_3O_4) NANOPARTICLES WITH STIMULI RESPONSIVE POLYMERS

2.1 Abstract

The synthesis of stimuli responsive polymer brushes was carried out using surface-confined atom transfer radical polymerization (ATRP) on iron oxide (Fe_3O_4) nanoparticles. N_2 was used to sparge the solution at all times, providing particle mixing as the different steps were conducted. Amine-modified magnetic nanoparticles, 'as-received' Fe_3O_4/NH_2, (200 nm, 100 nm, and 50 nm nominal d(H)) were modified by first reacting a bromine-based initiator onto the particle surface. After addition of the initiator, poly(methacrylic acid) (PMAA), poly(N-isopropylacrylamide) (PNIPAM), or PMAA-*b*-PNIPAM was grown from the surface of these 'as-received' nanoparticles. ATR-FTIR spectroscopy analysis confirmed the presence of the different polymers. TEM and AFM imaging corroborated the formation of nanocomposites with a magnetic nanoparticle core and silicate shell surrounded by amorphous material(s). DLS measurements on 200 nm Fe_3O_4/NH_2 grafted with PMAA-b-PNIPAM revealed a decrease in the hydrodynamic radius as the solution temperature was increased, revealing the thermoresponsive behavior of Fe_3O_4@PMAA-*b*-PNIPAM. Thus, a new methodology to produce metal-polymer nanocomposites was confirmed, using N_2 to sparge the surface-confined ATRP reaction. Novel hybrid (metal/polymer) nanocomposites with

thermal responsiveness were synthesized and characterized *in-situ* as the main outcome of this work.

2.2 Introduction

As discussed in Chapter 1, nanoparticles are materials that are well-known to have a high surface area to volume ratio and are considered an emerging tool for biomedical applications, electronics, environmental treatments and many other fundamental and applied research areas (Nalwa, 2004; Freitas, 2005; Richtering, 2006). Recently, magnetic nanoparticles (MNPs) have gained more interest due to their inherent magnetic properties which allow manipulation and hyperthermic applications of these particles under the presence of a magnetic field. The ease of manipulation magnetic nanoparticles is widely studied and has been used in electronic device, sensor, catalyst and drug delivery applications (Berry and Curtis, 2003). Their multifunctional nature combined with ease of manipulation and ability to be dispersed in fluids means that magnetic nanoparticles are being more widely studied and considered as material platform in diverse application areas.

Various approaches have been suggested to use magnetic nanoparticles as therapeutic agents, specifically as anticarcinogens. A study in 1996 by Lubbe et al. used epirubicin, a drug to treat breast cancer after surgery, loaded within a ferrofluid to treat cancer cells *in vivo* using rats and mice; however, no information was presented about the size of the magnetic particles, and the transport method of the drug on the ferrofluid (Lubbe et al., 1996). In fact, a response to this paper, (Gallo and Hafeli, 1997) noted that characterization of the drug release (pharmacokinetics), particle size, and/or magnetic stability was not performed; nonetheless, it was one of the pioneer *in vivo* studies using

drug-loaded MNPs. Doxorubicin, a known anticarcinogen, is another example of a drug delivery application that has been tested using a magnetic carrier, this drug was loaded onto the surface of MNPs with the aid of oleic acid and pluronic acid as stabilizers, and showed great efficiency with *in vitro* studies (Jain et al., 2005). In addition to drug-loading, a recent development in medical applications of MNPs is hyperthermia-based therapy where local heat is generated to treat cancer/tumor cells (Kumar and Mohammad, 2011). Despite several advances in this technique during the last two years, the shortcomings of MNPs as therapeutic agents concern the possible effects of non-stable systems in physiological media, effects on the central nervous system, and loss of magnetization, as pointed out recently in the literature (Akbarzadeh et al., 2012; Nunes et al., 2012; Kim et al., 2013).

Stabilization effects can be solved by surface modifying MNPs (Gupta and Gupta, 2005; Garcia et al., 2007; Zhou et al., 2008; Bajpai and Gupta, 2010). One of the focuses of this work is to modify the surface of MNPs with stimuli-responsive polymers (SRPs) (Kim et al., 2003). Stimuli for SRPs include pH, temperature, ionic strength, UV-radiation and many other conditions (Gupta et al., 2002). Here, one of the SRPs most widely studied to-date is poly(N-isopropylacrylamide) (PNIPAM) is used for the surface modification of MNPs. PNIPAM is well-known to have a lower critical solution temperature (LCST) at 32 °C (Liu and Zhang, 2005). Similarly, weak polyacids are often studied as pH-responsive polymer brushes. One example is poly(methacrylic acid) (PMAA), a well-known pH-sensitive polymer with a pKa value around 5, which is chosen for this work as well (Kim and Shin, 2007).

Stimuli responsive polymer-magnetic nanoparticle (SRP-MNP) hybrid materials have been previously synthesized using different techniques such as ultraviolet heat treatments, living radical polymerizations, and emulsion processes (Marutani et al., 2004; Liu et al., 2009). In fact, very few studies have utilized living radical polymerization (LRP), recently named as reversible-deactivation radical polymerization (RDRP), as a method to produce a surface-confined MNPs system despite the wide-spread interest in the scientific community to coat/ modify the surface of MNPs and the expanded use RDRP techniques during the last 20 years (Matyjaszewski et al., 1995; Matyjaszewski, 2012). RDRP allows for the controlled growth of a polymer and when used in concert with surface attachment of the initiator, a well-defined polymer layer (brush) can be 'grown' from the surface (Patten and Matyjaszewski, 1998; Matyjaszewski and Davis, 2002; Matyjaszewski, 2009).

In this chapter, the synthesis and characterization of PNIPAM-Fe_3O_4, PMAA-Fe_3O_4 and Fe_3O_4@PMAA-*b*-PNIPAM nano-composite structures is reported. PNIPAM and PMAA were chosen as the SRP for this study since their selective usage in surface modifying the MNPs will result in hybrid inorganic-organic (metal/polymer) nanocomposite systems with temperature and/or pH responsive functionality. One type of CRDP, atom transfer radical polymerization (ATRP), was used in a surface-confined approach to produce homo- and co-polymer brushes of PNIPAM and PMAA from the surface of the MNPs. Briefly, a bromine initiator was reacted on the surface of 'as-received' Fe_3O_4/NH_2 to finally proceed with the polymerization on the surface of the nanoparticles. Characterization of the morphology, chemistry, and stimuli responsive behavior of the polymer-modified MNPs was performed using TEM, DLS, FTIR, and

atomic/magnetic force microscopy (AFM/MFM) techniques. The synthesis and hybridization methods of this work will combine the capabilities of easy nanoparticle manipulation under a magnetic field, hyperthermic heating, and temperature/pH responsive behavior all in one nano-scale material system resulting in a multifunctional-material that can be used for a variety of applications.

2.3 Experimental

2.3.1 Materials

Fe_3O_4/NH_2 nanoparticles substrates with different nominal diameters: 50nm, 100nm, and 200 nm were used 'as-received' (Chemicell ,GmbH, Berlin, Germany). 5 mg of each substrate diameter were utilized for all the polymerizations carried out in this study, unless otherwise specified. Different reagents utilized in this work were: copper (I) chloride (Aldrich, 97%), triethylamine (Aldrich, 99.5%), Me_6TREN (Aldrich), methacrylic acid (Aldrich, 99%), N-(isopropylacrylamide) (NIPAM; TCI, 98%), ethanol (Fisher Sci., 99.9%), water (Aldrich, HPLC grade), 2-bromoisobutyril bromide (Aldrich, 98%), 2,2'-bipyridyl (bypiridine) (Aldrich, 99%), toluene (Acros, 99.8%), tetrahydrofuran (THF; Fisher Sci., 99.9%), propanol (Aldrich, 99.7%), uranyl acetate (EMS, 98%), and copper (I) bromide (Aldrich, 98%).

2.3.2 Synthesis of Fe_3O_4-initiator

'As-received' Fe_3O_4/NH_2 nanoparticles were placed in 0.12 M triethylamine/THF solution for 10 seconds at ~ 0 °C. Then, a 0.1 M 2-bromopropionyl bromide/THF solution was added to the reaction tube. This initiation reaction was allowed to proceed overnight and was performed under an inert nitrogen atmosphere using a steady flow of

nitrogen, also used to sparge the solution and ensure proper mixing. After completion, the reaction was kept under an inert (nitrogen) atmosphere. The solvent was then removed from the particles by using an external pump, while the particles remained inside by the effect of an external magnet. After solvent removal, the particles were washed thoroughly with methanol or isopropanol three times to remove any physisorbed material. As a result, magnetic particles with surface-confined bromine initiator were obtained. An illustration providing the different steps that were performed is depicted in Figure 2.1.

2.3.3 Synthesis of Fe_3O_4-PMAA/Fe_3O_4-PNIPAM

After attachment of the bromine initiator to the surface of the 'as-received' Fe_3O_4/NH_2 MNPs, the ATRP reaction was started using either NIPAM or MAA monomer. NIPAM ATRP was performed using a 26.6 mM monomer concentration in propanol/water (70/30 %v/v) that had been pre-purged with N_2 for 1 h. Then 2,2-bypiridine (bpy) and Cu(I)Br, ligand and catalyst respectively, were added to start the reaction at a 9.5/2/1 monomer/ligand/catalyst molar ratio. The NIPAM polymerization was allowed to proceed for 12 h under an inert atmosphere at room temperature. ATRP of MAA, either as a homopolymer or the second block, was conducted at a neutral pH (7), where MAA remains on a deprotonated state (Sankhe et al., 2006). A 2 M MAA/HPLC water solution was then prepared and 1 M NaOH was added to neutralize the solution to a pH of~7. This solution was then placed under a stream of nitrogen for ~1 h. To start the polymerization of MAA, a 0.1 mM solution of Me_6TREN and Cu(I)Cl was added to the monomer solution.

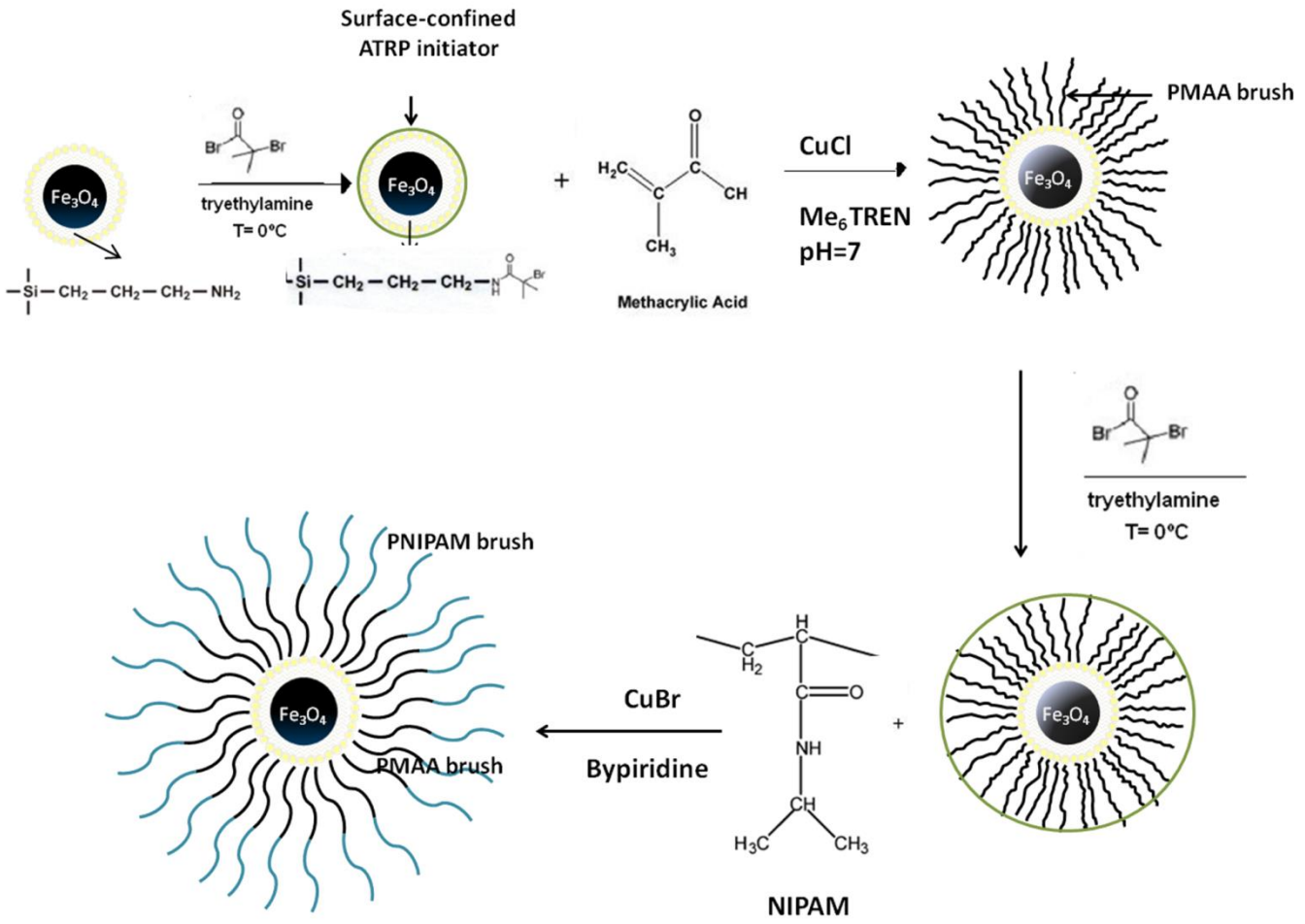

Figure 2.1 ATRP synthetic route for PMAA and then PMAA-*b*-PNIPAM surface grafted to Fe_3O_4 magnetic nanoparticles.

2.3.4 Synthesis of Fe_3O_4-PNIPAM-*b*-PMAA

Fe_3O_4-PNIPAM-*b*-PMAA, block copolymers systems, were obtained by reinitializing the terminal group from the "first" ATRP polymerization, in this case PNIPAM. For this purpose, bromine initiation was repeated in the same manner as described previously. First, NIPAM monomer solution was removed from the reactor using an external pump or a syringe, while the particles were held by an external magnet (particle larger than 100 nm). Then, ATRP of the second monomer (i.e., PMAA) was performed under the reactions conditions described above. Finally, the resultant Fe_3O_4@PMAA-*b*-PNIPAM nanoparticles were cleaned using two methods. For particles larger than 100 nm, an external magnet was located on a side of the test tube where the reaction took place, as depicted in Figure 2.2. For smaller particles (< 100 nm), centrifugation was utilized at 14,500 RPM for 30 min.

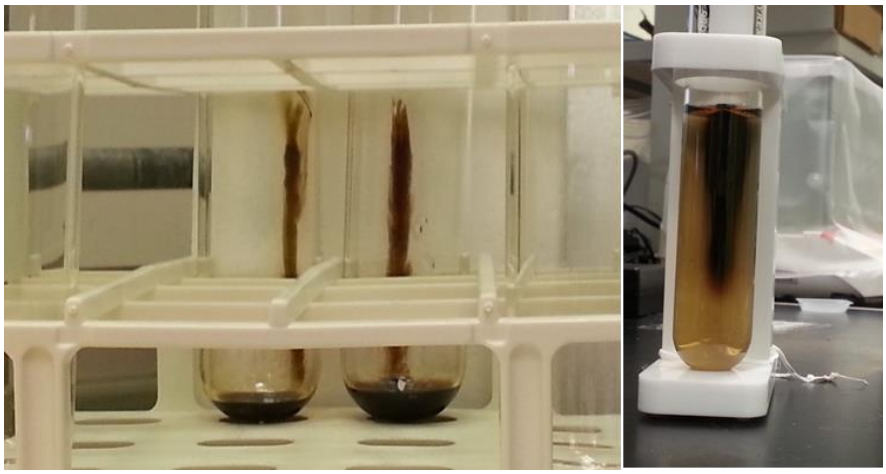

Figure 2.2 Magnetic separation of Fe_3O_4/NH_2 from the as-received solvent (left image) and Fe_3O_4-Br after the addition of the monomer/catalyst/ligand (MAA/Cu(I)Cl/ Me_6TREN) solution (right image).

2.4 Characterization

2.4.1 Fourier transform infrared (FTIR) spectroscopy.

FTIR spectra were obtained using a Miracle-ATR^{TM} accessory (PIKE Technologies) with a diamond-ZnSe crystal. A Nicolet 6700 FTIR with a mercury cadmium telluride (MCT-A*) detector, KBr beamsplitter, and dry gas purging was used to collect the FTIR spectra. Ommic software (v8.1.10) by Thermo Scientific was used for data acquisition and analysis. Nanoparticles were deposited onto the surface of the Zn-Se crystal from solution. The solvent was allowed to evaporate and then another drop was added; at least 5 drops were added to obtain a small dry film of particles on the crystal surface. Spectra were collected from 400 cm^{-1} to 4000 cm^{-1} with a minimum of 256 scans collected at a 4 cm^{-1} resolution.

2.4.2 Dynamic light scattering (DLS) measurements.

A Dynapro Nanostar manufactured by Wyatt was used for DLS measurements, and Wyatt's Dynamics (v7.0.0) software was used to fit the data. A cumulant method was used for the autocorrelation function. A stabilization time of 5 min was allowed prior to data collection. Data were collected at 25 °C and temperature response studies were also performed over the temperature range from 20 °C to 50 °C using a 5 °C step size.

2.4.3 Transmission electron microscopy (TEM).

A JEOL JEM-2000 FE II TEM instrument was used at 100 kV for collecting TEM images. Prior to imaging, particles were deposited from water onto 300 mesh copper grids and allowed to dry at ambient conditions. Uranyl acetate staigning material was added dropwise to the NP samples after they have been deposited and dried on the

grid to identify PNIPAM by negative staining. High resolution TEM images were collected using a JEOL 2100 TEM, with a LaB6 emitter operated at 200kV. The same procedure was used to deposit the samples.

2.4.4 Atomic/magnetic force microscopy

Atomic force microscopy (AFM) data were collected using a Dimension Icon AFM (Bruker) operated in tapping mode with an electrical and magnetic mode to obtain phase magnetic force microscopy (MFM) images. The AFM samples were obtained by applying a drop of MNP in solution onto a silica surface followed by drying in air overnight. MESP probes from Bruker with maximum resonant frequency of 320 kHz and spring constant of 5 N/m,were used for all AFM measurements shown in this chapter.

2.5 Results and discussion

Magnetic nanoparticles (MNPs) were surface-modified with NIPAM and/or MAA to produce surface-confined homo- and block-copolymer brushes. MNPs were reacted with a bromine initiator followed by ATRP to grow chains of PMAA and/or PNIPAM from the surface of the functionalized MNPs. The following sections describe the chemical and morphological characterization of the modified magnetic nanoparticles.

2.5.1 Analysis of the chemical structure of the surface-modified magnetic nanoparticles

ATR-FTIR spectroscopy was performed on the following: 'as-received' Fe_3O_4/NH_2, PMAA-Fe_3O_4, PNIPAM-Fe_3O_4 and PNIPAM-b-PMAA-Fe_3O_4, and the spectra (Figure 2.3) showed the expected chemical functionality for each polymerization step. In particular, Figure 2.3 shows absorption peaks in the wavenumber region from

2900-3000 cm^{-1} that correspond to $-CH_2$ and $-CH_3$/-CH stretching vibrations, and a broader O-H stretch (3300 cm^{-1}) as a result of the acid hydroxyl group present in the PMAA structure (Day and Underwood, 1991). PMAA-Fe_3O_4 nanoparticles have carbonyl (C=O) C-O stretching peaks from the carboxylate anion (C(=O)-O^-) and acid (C(=O)OH) group observed at 1414 cm^{-1} and 1710 cm^{-1}, respectively (Matyjaszewski and Davis, 2002). The presence of the CH_3/CH_2 and the acid/anion carbonyl groups confirmed the presence of PMAA on the surface of the nanoparticles.

As previously mentioned, amine-functionalized magnetic nanoparticles (Fe_3O_4/NH_2) were used as the substrate. For another example of surface-confined modification of silanol-coated magnetic nanoparticles (Fe_3O_4/OH), the reader is referred to APPENDIX A.

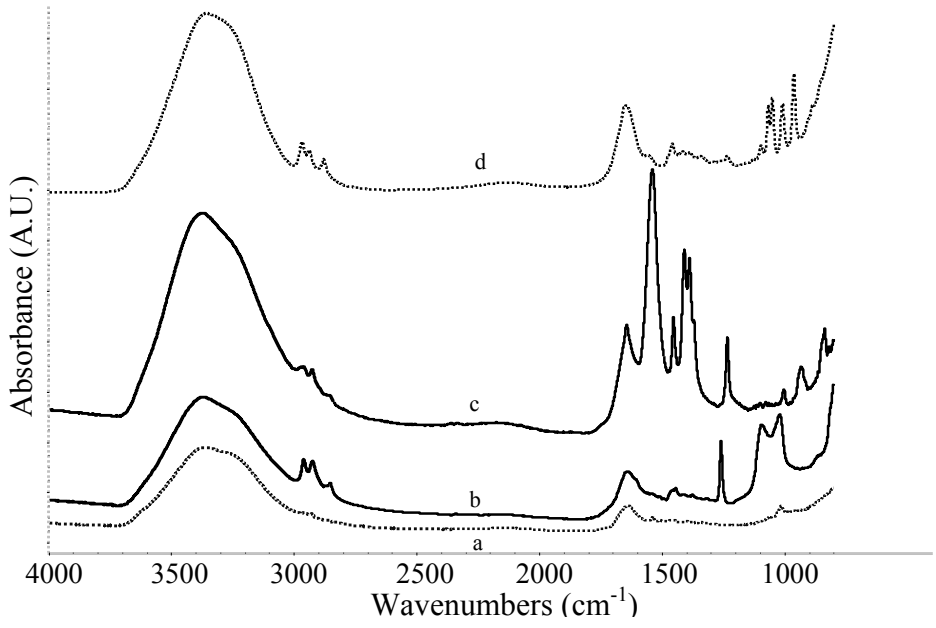

Figure 2.3 ATR-FTIR spectra

a) 'as received' amine- functionalized nanoparticles (Fe3O4/NH_2), b) PNIPAM-modified magnetic nanoparticles (Fe3O4-PNIPAM), c) PMAA-modified magnetic nanoparticles (Fe3O4-PMAA) and d) block copolymer nanoparticle composite (Fe_3O_4@PMAA-*b*-PNIPAM).

Amine-functionalized magnetic nanoparticles (Figure 2.3a) showed N-H stretching peak characteristic of amines at 3300 cm^{-1} (Day and Underwood, 1986). Along with the peaks at 1640 cm^{-1} (O-H bending) and 1063 cm^{-1} (Si-O-Si), the presence of an amine-terminated silicate coating on the 'as received' Fe_3O_4/NH_2 nanoparticles is then confirmed (Day and Underwood, 1986; Pretsch and Zenobi, 2009).

For this particular case, NIPAM monomer was polymerized from the 'as-received' Fe_3O_4/NH_2 substrates following the same reaction conditions described in Section 2.3.3. Two characteristic absorption bands for PNIPAM (Figure 2.3b) are C-N stretching (1446 cm^{-1}) (Mauricio et al., 2009) and the amide-I C=O symmetric stretching (1640 and 1080 cm^{-1}) (Lien and Wu, 2008). These peaks were clearly observed in addition to the symmetric/asymmetric C-H stretching of $-CH_2$ and $-CH_3$ that increased in intensity (in comparison with the 'as-received' Fe_3O_4/NH_2), confirming the surface-confined polymerization of PNIPAM.

PMAA polymer chains were also grown from the 'as-received' Fe_3O_4/NH_2 magnetic nanoparticles surface. Characteristic PMAA absorption peaks are at 3300 cm^{-1} for the broad O-H stretch associated with the carboxylic acid group [C(=O)OH] (Kim and Peppas, 2003), C-O carbonyl stretching from the carboxylate anion [$C(=O)O^-$] at 1645 and 1540 cm^{-1}, and C-O carbonyl stretching from the carboxylic acid [C(=O)OH] at 1710 cm^{-1} (Kim and Peppas, 2003; Dong et al., 2011); (Matyjaszewski and Davis, 2002). The intensity of these PMAA characteristic peaks along with the presence of the typical symmetric/asymmetric C-H stretching of $-CH_2$ and $-CH_3$ around 2900 cm^{-1} confirms the polymerization of a second monomer, MAA, from Fe_3O_4/NH_2 (200 nm) using surface-confined ATRP (Figure 2.3c).

ATR-FTIR characterizations were performed on block-copolymers and results are displayed in Figure 2.3d. Fe_3O_4@PMAA-*b*-PNIPAM has a very broad peak observed at a region within 1500 -1720 cm^{-1} (Figure 2.3d) as compared with PMAA-Fe_3O_4 and PNIPAM-Fe_3O_4 spectra, previously discussed. However, this large region encompasses three main peaks for the two different described polymers. A small peak (1560 cm^{-1}) is actually observed on the copolymer structure, believed to correspond to the C-O carbonyl stretching to [C(=O)O^-] from PMAA. Moreover, a larger peak, but broader as compared with PNIPAM-Fe_3O_4 was observed at 1640 cm^{-1}, including carboxylate anion (PMAA) and amide-I peak (PNIPAM) within this region. Thus, co-polymerization of PMAA-*b*-PNIPAM on the surface of the 'as-received' Fe_3O_4/NH_2 was successfully demonstrated by ATR-FTIR.

2.5.2 Morphological characterization of homo- and block-copolymers grafted from the surface of (200 nm) Fe_3O_4/NH_2

The morphology of an isolated 'as received' Fe_3O_4/NH_2 (200 nm, nominal hydraulic diameter) nanoparticle structure is shown in Figure 2.4, with a dark multi-core/shell structure that can be observed. FTIR and XPS Chemical analysis of the 'as received' Fe_3O_4/NH_2 types of magnetic structures revealed silicon in addition to iron, carbon, and oxygen (more details will be discussed in Chapter 3). A dark muli-core is observed in Figure 2.4, strongly suggesting that these components are the magnetic core. In addition, a shell around the core (lighter color) is also observed, that is believed to be a silica (Si) shell, as demonstrated by the different chemical composition analysis conducted in this work such as XPS, EDS and ATR-FTIR.

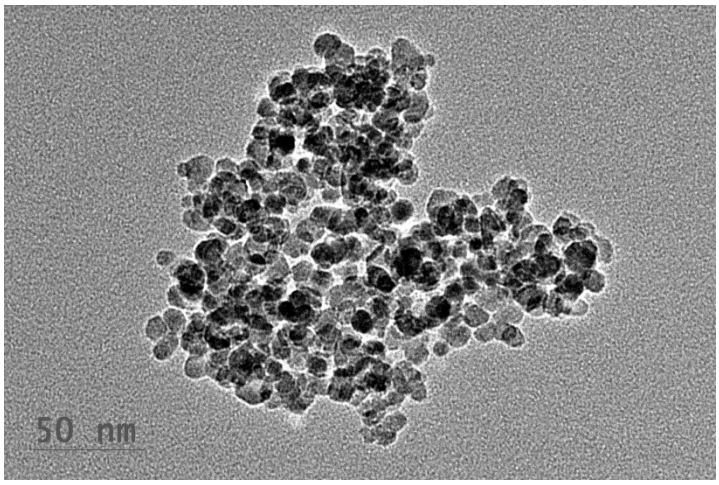

Figure 2.4 High resolution TEM image of 'as received' Fe_3O_4/NH_2 magnetic nanoparticle with a distinctive core/shell structure.

The morphology of the polymer-grafted Fe_3O_4 particles was also examined using TEM. First, homo-polymerized magnetic nanoparticles were characterized (Figure 2.5) and an organic layer surrounding an inorganic core was observed. First, TEM images confirmed the attachment of PMAA to the surface of 200 nm 'as-received' Fe_3O_4/NH_2 magnetic nanoparticles. Because the particles were washed thoroughly prior to characterization, the PMAA is expected to be chemisorbed to the NP surface, not merely physisorbed. Polymer was unfortunately grown in different directions of the nanoparticles surfaces, producing aggregates on which Fe_3O_4 were inside a polymer spherical structure. This effect is probably produced due to poor production of bromine-initiation sites during the ATRP reaction. Current and future work is focusing on developing a new reactor with a sonicator probe inside to guarantee that particles do not precipitate/agglomerate as the polymerization takes place (APPENDIX B). As discussed

earlier, controlling the agglomeration of particles is one of the main challenges when a surface-confined polymerization is undertaken.

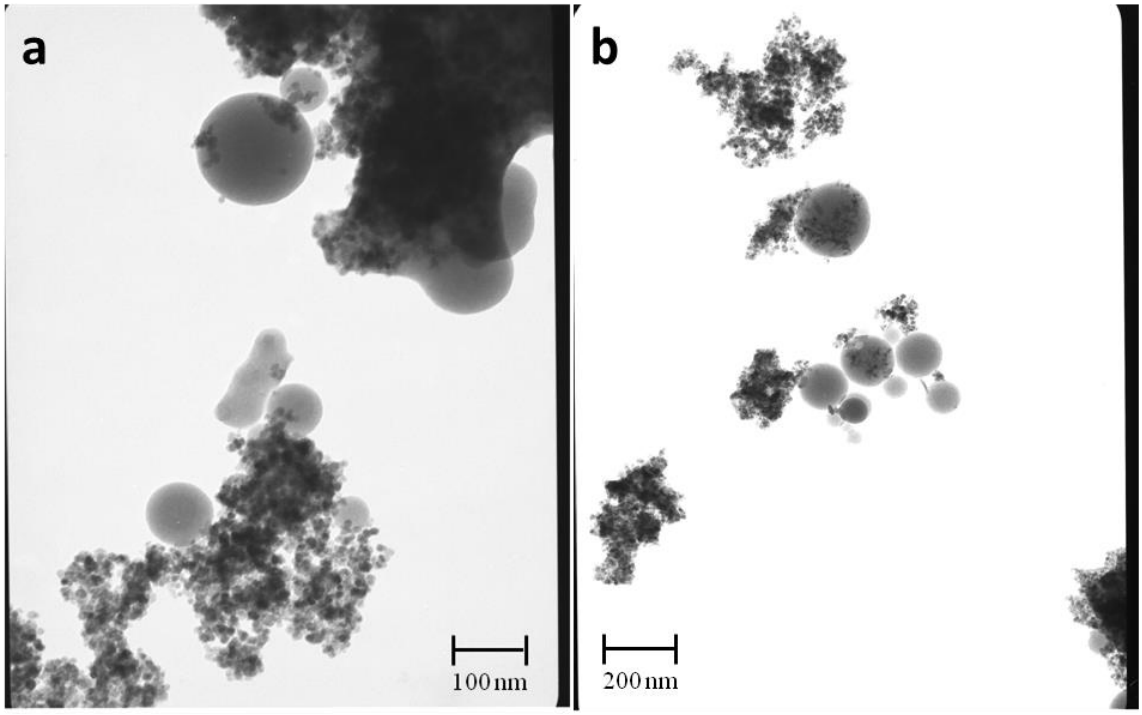

Figure 2.5 TEM images of PMAA-Fe_3O_4 ('as received' 200 nm Fe_3O_4/NH_2) after polymerization

a) Fe_3O_4/NH_2 surrounded by a polymer-shell and b) polymer spherical structures with enclosed Fe_3O_4/NH_2.

A separate reaction using 50 nm nominal size Fe_3O_4/NH_2 'as-received' nanoparticles was also conducted with PNIPAM with a monomer/catalyst/ratio (NIPAM/CuCl/Me_6TREN) of 100/1/1. This particular experiment was performed to see any effect on polymer aggregation on the surface of MNPs for a smaller core. Indeed, results for this polymerization are promising as depicted in TEM, AFM and MFM measurements. However, FTIR and XPS characterization of these materials becomes challenging due to the smaller size particles and difficulties encountered while separating

using an external magnet. HR-TEM shows interesting morphological structures of a polymer with small particles inside as part of a core. To further demonstrate the chemical composition of these particles, TEM/EDS was performed, but quantitative results were not possible with the current equipment set-up due to the significant amount of carbon present on the Cu-grids. (The elemental composition is discussed further in APPENDIX C.)

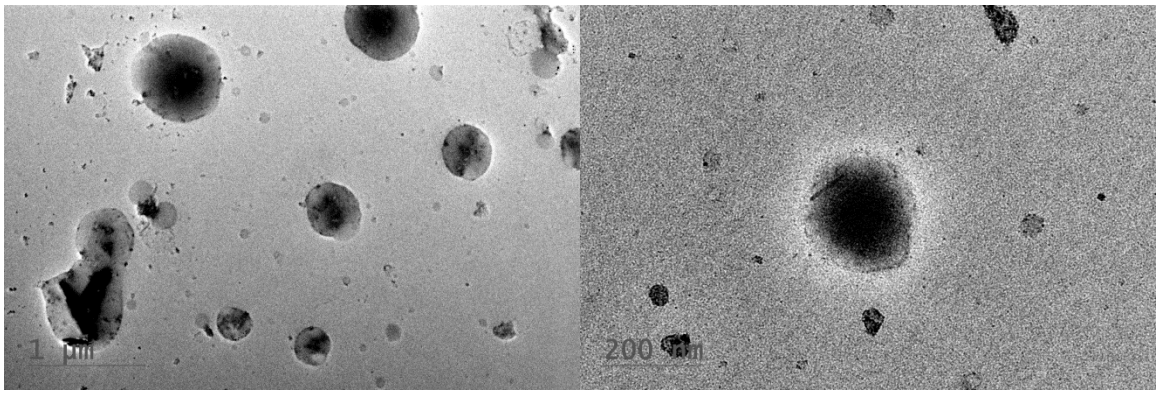

Figure 2.6 HR-TEM images of PNIPAM-Fe_3O_4 ('as received' 50 nm Fe_3O_4/NH_2 substrate) after polymerization showing Fe_3O_4/NH_2 surrounded by a polymer-shell at different levels of magnification.

AFM/MFM images were taken to demonstrate different nanocomposite phases (Figure 1.6). AFM/MFM confirmed the presence of different types of materials on the formed nanocomposite. Height and phase images are shown in Figure 2.7. As observed, a spherical structure was depicted in the Height AFM images. To further examine this morphology, a phase image was also obtained over the same region, showing small nanoparticle inside the shell with a stronger phase angle. The magnetic phase image showed a very small signal of these particles with respect to the polymeric shell, thus, it

is strongly supported that magnetic nanoparticles are completely coated with PNIPAM froming PNIPAM-Fe_3O_4 nanocomposites.

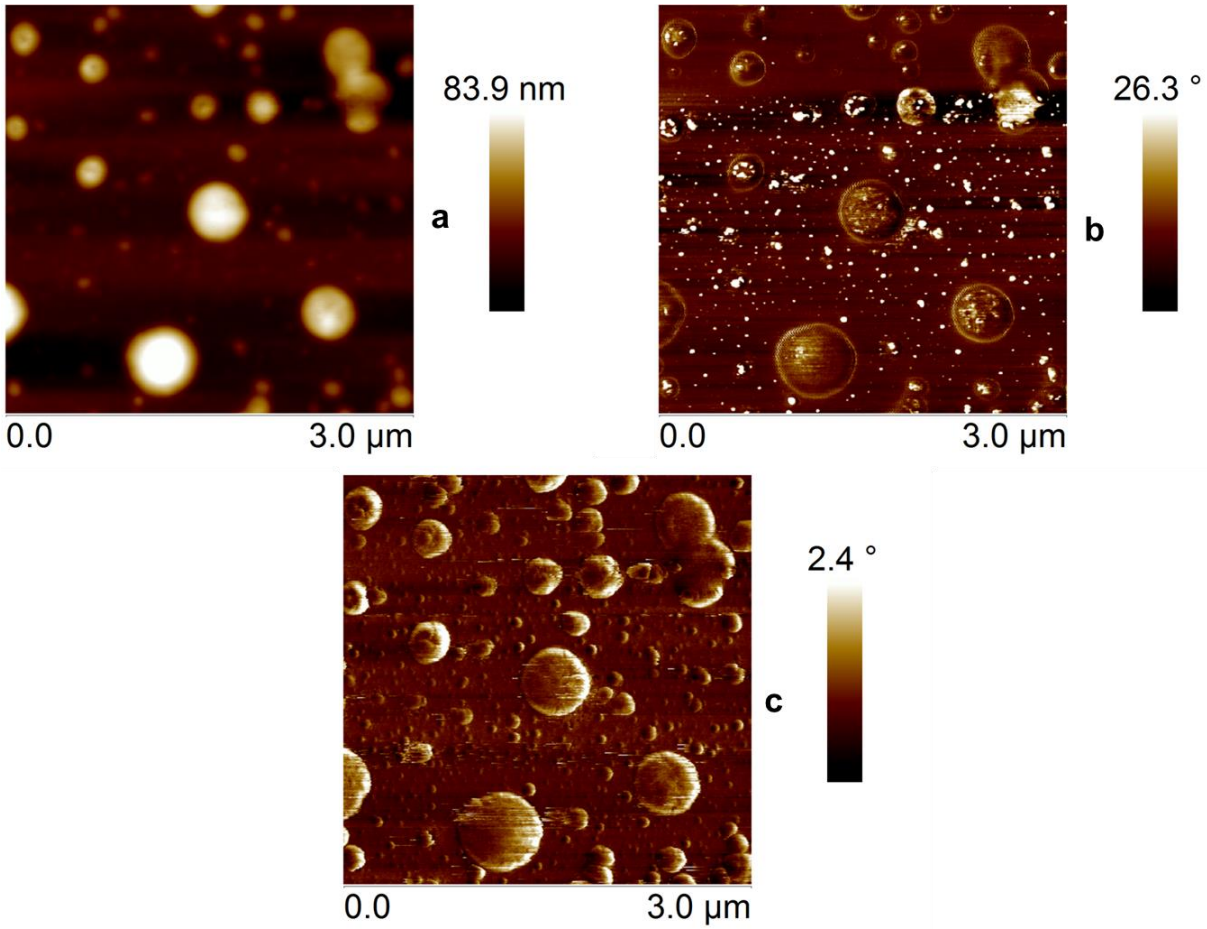

Figure 2.7 AFM/MFM images show a spherical structure after PNIPAM polymerization on 'as-received' Fe_3O_4/NH_2 nanoparticles.

(a) Height image shows spherical morphologies, (b) phase image showed different materials inside the spherical structure, believed to be magnetic nanoparticles, and (c) poor contact was obtained with MFM signal.

For the block copolymers grafted to the Fe_3O_4/NH_2, PNIPAM was polymerized first followed by PMAA on 200 nm 'as-received' Fe_3O_4/NH_2. Figure 2.8 shows the block copolymer structure Fe_3O_4@PMAA-*b*-PNIPAM after completion of both

polymerizations. As observed in Figure 2.8, uranyl acetate stained the PNIPAM structure and a second polymer can be observed outside of the first core layer.

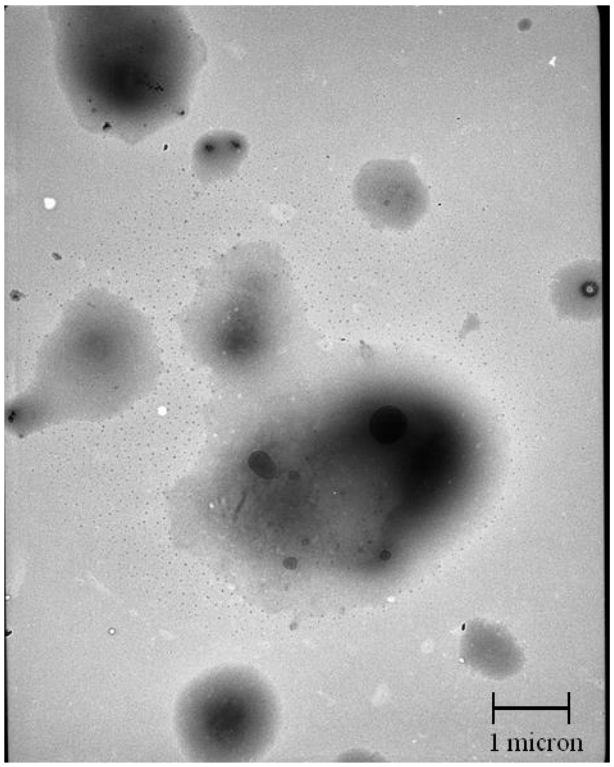

Figure 2.8 TEM image of Fe_3O_4@PMAA-*b*-PNIPAM block copolymer-Fe_3O_4 structure with PNIPAM stained (dark).

2.5.3 Size and thermal response of Fe_3O_4@PMAA-*b*-PNIPAM

The size and thermal response of these SRP surface-modified nanoparticles was studied using dynamic light scattering (DLS) while the particles were dispersed in DI-water. As controls the 'as received' and Br-initiator Fe_3O_4 (Br- Fe_3O_4) were examined using DLS over a 25 °C to 50 °C temperature range (to ensure no thermally induced size fluctuations were observed in the core MNP sample) and look for any discernable size change or agglomeration due to the initiator attachment. At temperatures below 35 °C,

the block copolymer modified MNPs have a baseline *in-situ* size of 500 nm, in comparison with ~ 100 nm for Fe_3O_4 and Fe_3O_4-Br. As temperature was increased, a reduction on the hydrodynamic diameters of the block copolymer was observed, reaching a final in situ size of 300 nm at 50 °C.

Over the temperature range studied, hydrodynamic radius of the Fe_3O_4/NH_2 (refer to APPENDIX D) and Fe_3O_4-Br particles was constant at about 100 nm (Figure 2.9). In contrast, Fe_3O_4@PMAA-*b*-PNIPAM particle size decreased as the temperature was increased (Figure 2.9). This behavior is expected as PNIPAM is a well-known thermo-responsive polymer with a ~32 °C lower critical solution temperature (LCST). Below the LCST, PNIPAM is in a soluble, relaxed state. Above the LCST, PNIPAM brushes tend to become hydrophobic and insoluble in water resulting in a collapsed state. DLS results show the collapse of PNIPAM as the temperature was increased. The addition of both PMAA and PNIPAM allows for the surface chemistry to be controlled and for a polar polymer to be exposed on the perimeter, impacting solubilization, stability, and agglomeration, while providing a thermo-responsive PNIPAM block. (Additionally, the PMAA block will add pH responsiveness to this MNP system, but that was not explored in this study)

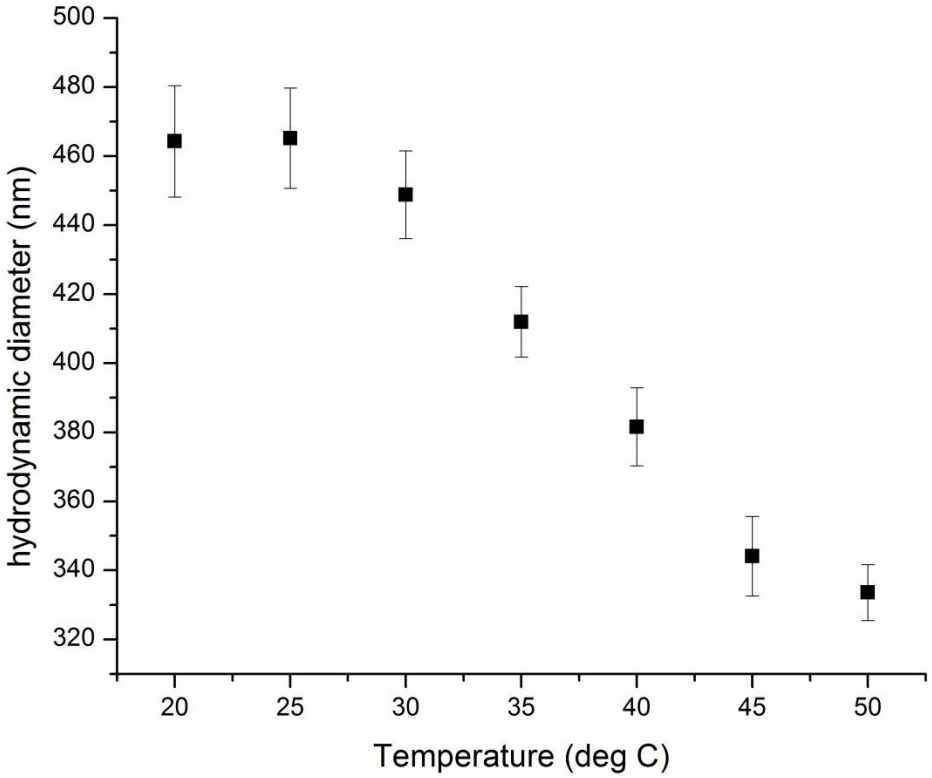

Figure 2.9 Thermo-sensitivity analysis of Fe_3O_4@PMAA-*b*-PNIPAM using dynamic light scattering over a range of 25- 50 °C while nano-composites were dispersed in DI water.

2.6 Conclusions

Two different stimuli responsive polymers (SRP) PMAA and PNIPAM—have been grown, both as homopolymers and block copolymers, from the surface of 'as-received' Fe_3O_4/NH_2 magnetic nanoparticles using surface-confined ATRP polymerization. ATR-FTIR spectroscopy confirmed successful polymerization by monitoring chemical functionality at each reaction step. The size and morphology of the particles was studied using TEM and DLS. The presence of the polymer brushes on the Fe_3O_4 MNP was demonstrated through increased size and an amorphous 'shell' around the metal oxide core. Copolymer structures were clearly observed by TEM as two

different phases using a stain for PNIPAM. The thermo-responsive behavior of these hybrid SRP-MNP systems, including the LCST of PNIPAM, was observed by temperature-dependent DLS measurements. This work describes the synthesis and characterization of PMAA-Fe_3O_4, PNIPAM-Fe_3O_4, and Fe_3O_4@PMAA-*b*-PNIPAM; these three nanocomposites are indeed multifunctional systems displaying morphological changes, chemical composition variations, and responsiveness to temperature changes, using a single nanoparticle substrate.

2.7 References

Akbarzadeh, A., M. Samiei, et al. (2012). "Magnetic nanoparticles: preparation, physical properties and applications in biomedicine." Nanoscale Res. Lett. **7**: **144**, 113 pp.

Bajpai, A. K. and R. Gupta (2010). "Synthesis and Characterization of Magnetite (Fe_3O_4)-Polyvinyl Alcohol-Based Nanocomposites and Study of Superparamagnetism." Polymer Composites **31**(2): 245-255.

Berry, C. C. and A. S. G. Curtis (2003). "Functionalisation of magnetic nanoparticles for applications in biomedicine." Journal of Physics D-Applied Physics **36**(13): R198-R206.

Day, R. A. and A. L. Underwood (1986). Quantitative analysis. Englewood Cliffs, N.J., Prentice-Hall.

Day, R. A. and A. L. Underwood (1991). Quantitative analysis : laboratory manual. Englewood Cliffs, N.J., Prentice-Hall.

Dong, H., J. Huang, R. R. Koepsel, P. Ye, A. J. Russell and K. Matyjaszewski (2011). "Recyclable Antibacterial Magnetic Nanoparticles Grafted with Quaternized Poly(2-(dimethylamino)ethyl methacrylate) Brushes." Biomacromolecules **12**(4): 1305-1311.

Freitas, R. A. (2005). "Current status of nanomedicine and medical nanorobotics." Journal of Computational and Theoretical Nanoscience **2**(1): 1-25.

Gallo, J. M. and U. Hafeli (1997). "A.S. Lubbe et al., Preclinical experiences with magnetic drug targeting: tolerance and efficacy. Cancer Res., 56: 4694-4701, 1996; and Clinical experiences with magnetic drug targeting: a phase I study with 4'-epidoxorubicin in 14 patients with advanced solid tumors. Cancer Res., 56: 4686-4693, 1996." Cancer Research **57**(14): 3063-3065.

Garcia, I., N. E. Zafeiropoulos, A. Janke, A. Tercjak, A. Eceiza, M. Stamm and I. Mondragon (2007). "Functionalization of iron oxide magnetic nanoparticles with poly(methyl methacrylate) brushes via grafting-from atom transfer radical polymerization." Journal of Polymer Science Part A: Polymer Chemistry **45**(5): 925-932.

Gupta, A. K. and M. Gupta (2005). "Synthesis and surface engineering of iron oxide nanoparticles for biomedical applications." Biomaterials **26**: 3995-4021.

Gupta, P., K. Vermani and S. Garg (2002). "Hydrogels: from controlled release to pH-responsive drug delivery." Drug Discovery Today **7**(10): 569-579.

Jain, T. K., M. A. Morales, S. K. Sahoo, D. L. Leslie-Pelecky and V. Labhasetwar. (2005). "Iron oxide nanoparticles for sustained delivery of anticancer agents." Molecular Pharmaceutics **2**(3): 194-205.

Kim, B. and N. A. Peppas (2003). "Analysis of molecular interactions in poly(methacrylic acid-g-ethylene glycol) hydrogels." Polymer **44**(13): 3701-3707.

Kim, B. and Y. Shin (2007). "pH-sensitive swelling and release behaviors of anionic hydrogels for intelligent drug delivery system." Journal of Applied Polymer Science **105**(6): 3656-3661.

Kim, D. J., J. Y. Heo, K. S. Kim and I. S. Choi (2003). "Formation of thermoresponsive poly(n-isopropylacrylamide)/dextran particles by atom transfer radical polymerization." Macromolecular Rapid Communications **24**(8): 517-521.

Kim, E., K. Lee, Y.-M. Huh and S. Haam (2013). "Magnetic nanocomplexes and the physiological challenges associated with their use for cancer imaging and therapy." J. Mater. Chem. B **1**: 729-739.

Kumar, C. S. S. R. and F. Mohammad (2011). "Magnetic nanomaterials for hyperthermia-based therapy and controlled drug delivery." Adv. Drug Delivery Rev. **63**: 789-808.

Lien, Y.-H. and T.-M. Wu (2008). "The application of thermosensitive magnetic nanoparticles in drug delivery." Advanced Materials Research, **47**, 528-531.

Liu, G., H. Wang and X. Yang (2009). "Synthesis of pH-sensitive hollow polymer microspheres with movable magnetic core." Polymer **50**(12): 2578-2586.

Liu, G. and G. Zhang (2005). "Collapse and swelling of thermally sensitive poly(N-isopropylacrylamide) brushes monitored with a quartz crystal microbalance." J. Phys. Chem. B **109**(2): 743-747.

Lubbe, A. S., C. Bergemann, et al. (1996). "Preclinical experiences with magnetic drug targeting: tolerance and efficacy." Cancer Research **56**(20): 4694-4701.

Marutani, E., S. Yamamoto, T. Ninjbadgar, Y. Tsujii, T. Fukuda and M. Takano (2004). "Surface-initiated atom transfer radical polymerization of methyl methacrylate on magnetite nanoparticles." Polymer **45**(7): 2231-2235.

Matyjaszewski (2009). The Matyjaszewski Polymer Group , available at : http://www.cmu.edu/maty/, accessed on 06/01/13

Matyjaszewski, K. (2012). "Atom Transfer Radical Polymerization (ATRP): Current Status and Future Perspectives." Macromolecules **45**(10): 4015-4039.

Matyjaszewski, K., S. Gaynor and J.-S. Wang (1995). "Controlled Radical Polymerizations: The Use of Alkyl Iodides in Degenerative Transfer." Macromolecules **28**: 2093-2095.

Matyjaszewski, K. and T. P. Davis (2002). Handbook of radical polymerization (p. 523). New York: Wiley-Interscience.

Mauricio, M. R., G. M. Carvalho, E. Radovanovic, E. C. Muniz and A. F. Rubira (2009). "Analysis of poly(N-isopropylacrylamide) grafted onto the surface of PET films by SI-ATRP technique." Materials Science & Engineering C-Biomimetic and Supramolecular Systems **29**(2): 594-598.

Nalwa, H. S. (2004). Encyclopedia of nanoscience and nanotechnology. Stevenson Ranch, Calif., American Scientific Publishers.

Nunes, A., K. T. Al-Jamal and K. Kostarelos (2012). "Therapeutics, imaging and toxicity of nanomaterials in the central nervous system." J. Controlled Release **161**: 290-306.

Patten, T. E. and K. Matyjaszewski (1998). "Atom Transfer Radical Polymerization and the Synthesis of Polymeric Materials." Advanced Materials **10**(12): 901-915.

Pretsch, E. and R. Zenobi (2009). "Solution to spectroscopy blog challenge. Capsaicin." Anal Bioanal Chem **393**(2): 407-408.

Richtering, W. (2006). Smart Colloidal Materials. Progress in Colloid and Polymer Science,. Berlin, Heidelberg, Springer-Verlag Berlin Heidelberg.

Sankhe, A. Y., S. M. Husson and S. M. Kilbey (2006). "Effect of Catalyst Deactivation on Polymerization of Electrolytes by Surface-Confined Atom Transfer Radical Polymerization in Aqueous Solutions." Macromolecules **39**(4): 1376-1383.

Zhou, Y., S. X. Wang, B. J. Ding and Z. M. Yang (2008). "Modification of magnetite nanoparticles via surface-initiated atom transfer radical polymerization (ATRP)." Chemical Engineering Journal **138**(1-3): 578-585.

CHAPTER III

STIMULI-RESPONSIVE BIPHASIC-POLYMER JANUS MAGNETIC MANOPARTICLES PREPARED VIA ELECTROSTATIC INTERACTIONS AND SURFACE-CONFINED ATRP

3.1 Abstract

Metal-biphasic polymer core-shell nanocomposites were formed by polymerizing two chemically dissimilar polymers on opposite sides of amine-functionalized magnetic nanoparticles ('as-received' Fe_3O_4/NH_2). The synthesis methodology used to fabricate these amphiphilic three-dimensionally asymmetric Janus magnetic nanoparticles (JPs) combined: (1) particle retention on a solid substrate by electrostatic interactions and (2) surface-confined atom transfer radical polymerization (ATRP). Poly(methacrylic acid) (PMAA) and poly(N-isopropylacrylamide) (PNIPAM) were polymerized from opposite hemispheres of 'as-received' Fe_3O_4/NH_2 using a sequential adsorption/polymerization/release/polymerization method,. AFM, SEM and TEM demonstrated the morphology of the JPs after each reaction step. Chemical compositions were analyzed using attenuated total reflectance Fourier transform infrared spectroscopy (ATR-FTIR) and X-ray photoelectron spectroscopy (XPS). Thus, biphasic PMAA-Fe_3O_4-PNIPAM JPs were formed using a non-covalent solid protection method along with a sequential controlled radical polymerization scheme. This innovative technique does not involve difficult reaction conditions and equipment and can easily be extended

to other particle types, electrostatically charged materials, and biphasic polymer combinations.

3.2 Introduction

Studies of asymmetric particles, also known as Janus particles, have increased in the last two decades because of their potential in material science applications such as photovoltaic cells, electric paper, anti-reflection coatings, optical and optoelectronic displays, drug delivery, micro-rheology probes and sensing devices (Li et al., 2005; Mock et al., 2006; Walther and Muller, 2008; McConnell et al., 2010; Poree et al., 2011; Yang et al., 2012). Janus particles (JPs) are composed of at least two physically and/or chemically distinct surfaces, and can be fabricated by a number of different approaches. P.G. de Gennes (Perro et al., 2005a) introduced "Janus grains" about two decades ago after the experimental efforts of Casagrande et al. (Casagrande et al., 1989) that focused on "Janus beads" made of a glass core and separate hydrophilic and hydrophobic sides. Since then, a variety of experimental/modeling techniques have been reported to produce inorganic and organic asymmetric particles in a variety of research fields. Synthetic routes and the self-assembly behavior of polymeric JPs have been described in several review articles (Perro et al., 2005b; Wurm and Kilbinger, 2009; Du and O'Reilly, 2011; Hu et al., 2012). Some techniques for the fabrication of JPs include surface selective modification (Tanaka et al., 2010), template-assisted self-assembly (Andala et al., 2012), emulsion/phase separation (Wang et al., 2011), surface-controlled nucleation and growth (Lattuada and Hatton, 2007; Berger et al., 2008), and microfluidic methods(Yang et al., 2012). Regardless of the synthetic route for JPs formation, the major advantage of JPs is to provide structures with a duality that can allow for distinct, and even divergent

properties on the same physical system resulting in unique self-assembly, stimuli-response, and stable systems. As an example, properties that might vary using a JP system under different environmental conditions include magnetic, catalytic, optical and electrical responses. In combination, the synthesis methods and the particle materials determine the physicochemical properties and therefore the potential applications. New synthetic routes, characterization methods for chemically distinct areas in close proximity in small size area/volumes, and the resultant dynamic JPs systems are all current areas of study for JPs structures.

JPs can be a composite of inorganic-inorganic, polymer-polymer or inorganic-polymer materials, and at the sub-micron scale are often referred to as a hybrid material (Nogawa and Japanese Technical Information Service., 1988; Gómez-Romero and Sanchez, 2004; Kickelbick, 2007). Silica beads (Li et al., 2005), gold (Lu et al., 2003; Wang et al., 2008; Smith et al., 2009), and/or magnetic nanoparticles (Lattuada and Hatton, 2006; Lattuada and Hatton, 2007) are commonly used as the inorganic (core) material in a JPs structure. Controlled manipulation in the presence of a magnetic field is one of the advantages for using magnetic nanoparticles (MNPs) when an inorganic component is present in JPs. As an example, MNPs have previously been combined with silicon dioxide to form inorganic-inorganic hybrid structures using flame synthetic approaches; however, the JPs resulting from this method were limited to an inorganic hybrid structures (Zhao and Gao, 2009). MNPs have also been used as the inorganic material in inorganic-organic hybrid structures. Recently, Chang and Hatton formed JPs using MNPs as one side of the structure and polystyrene (PS) as the complimentary side. Emulsion droplet solvent vaporization was used to create the hybrid styrene-MNPs Janus

beads (Chang and Hatton, 2012). PS shells were also utilized to encapsulate MNPs, and then these modified particles were combined with silicon dioxide particles using a miniemulsion/sonochemical processes (Teo et al., 2010). Similarly, Qiang et al. formed half-raspberry/snowman structures using silicon dioxide and styrene with the aid of miniemulsion polymerizations (Qiang et al., 2008). Lattuada and Hatton also combined MNPs with charged polymers using a combination of self-assembly and *in-situ* polymerizations of oppositely charged polymers (Lattuada and Hatton, 2007). Therefore, it has been demonstrated that amphiphilic MNPs-polymer structures can be synthesized using different microemulsion techniques to create novel nanostructure systems with different morphology and/or surface chemistry.

Other synthetic approaches can be used for core-shell nanostructures where MNPs act as a core and two dissimilar polymers are grafted on the MNPs surface to act as the shell. Hatton's group used atom transfer radical polymerization (ATRP) for the modification of monodisperse magnetic nanoparticles with charged polymers. For example, surface-confined modification of nanoparticles substrates utilizing 'grafting to' and 'grafting from' approaches were used to produce inorganic-polymeric JPs (Lattuada and Hatton, 2007). Controlled radical polymerization has also been used for the development of polymer-polymer JPs using various nanoparticles as the substrates. Berger et al. worked with stimuli-responsive acrylate polymers that were formed using ATRP and then attached to silica nanoparticles to produce stimuli responsive JPs (Berger et al., 2008). Another study by Li et al. involved "hairy" nanoparticles produced via controlled radical polymerization techniques and hydrolysis to create a mixture of poly(acrylic acid) (PAA) and PS brushes on the surface of silica (Si) nanoparticles to

obtain a PAA-Si-PS hybrid system (Li et al., 2005). A different study used gold (Au) nanoparticles as the substrate combining the well-known grafting-to and grafting-from approaches to create JPs. Au nanoparticles were first immobilized to a thiol-end functionalized single crystal polyethylene oxide (PEO) substrate and then ATRP started on one side of the Au nanoparticles with PAA and/or poly(*tert*-butyl acrylate). This method was found to avoid particle aggregation and result in increased areal density (Wang et al., 2008). Here, electrostatic interactions of amine-functionalized magnetic iron oxide nanoparticles (Fe_3O_4/NH_2) and a negative charge mica surface with $K[Si_3Al]O_{10}Al_2(OH)_2$ chemical structure, are explored as an alternative for producing similar Janus nanostructures. The negative charge in mica is a result of the dissociation of K^+ ions in water that produce a negative outer layer (AlO_2^-), becoming a charged substrate (Liberelle et al., 2008). The partial charge of the amine group NH_3^+ is then analyzed with the negative mica substrate. Additionally, only 'grafting from' approaches are used for polymer grafting to the magnetic nanoparticle surfaces, and desired molecular weight and brush thickness can thus be controlled.

Thus, a new synthetic route for the fabrication of three-dimensionally amphiphilic and asymmetric Janus magnetic nanoparticles is presented. The synthesis involved a combination of two methods: (1) particle retention on a solid substrate by electrostatic interactions and (2) surface-confined ATRP. Additionally, the biphasic surface-grafted polymers were both stimuli-responsive polymers, poly(methacrylic acid) (PMAA) and poly(N-isopropylacrylamide) (PNIPAM), with each grafted onto opposite hemispheres of amine-functionalized magnetic iron oxide nanoparticles (Fe_3O_4/NH_2). The morphological structure of this polymeric-inorganic-polymeric nanohybrid system of 3-D

amphiphilic and asymmetric magnetic JPs was examined using atomic force microscopy (AFM) and transmission electron microscopy (TEM). Additionally, chemical composition and structure were analyzed by attenuated transmitted reflectance Fourier transform infrared spectroscopy (ATR-FTIR), X-ray photoelectron spectroscopy (XPS) and energy-dispersive X-ray spectroscopy (EDS). The formation of surface-grafted biphasic PNIPAM/PMAA Janus MNPs (PMAA- Fe_3O_4-PNIPAM) using a combination of non-covalent solid protection chemistry and surface-confined ATRP was successfully confirmed by the characterization techniques mentioned above. In addition, the novel PMAA-Fe_3O_4-PNIPAM structures described in this work could potentially be used in different scenarios due to the dual response of the two different polymer brushes grafted on each side of the particles and the ease of manipulation of these particles in the presence of a magnetic field.

3.3 Experimental section

3.3.1 Materials

Muscovite mica (Electron Microscopy Sciences, Hatfield, PA, USA) and 50 nm 'as-received' amine-functionalized magnetite nanoparticles (Fe_3O_4/NH_2, Chemicell GmbH, Berlin, Germany) were used as the substrates in this work. Reagents obtained from Sigma-Aldrich included: copper(I) chloride (CuCl; 97%), copper(I) bromide (CuBr; 98%), triethylamine (99.5%), hexamethylated tris(2-aminoethyl)amine (Me_6TREN; 96%), methacrylic acid (MAA; 99%), water (HPLC grade), 2-bromoisobutyryl bromide (98%), and propanol (99.7%). Ethanol (99.9%), tetrahydrofuran (THF, 99.9%), and glacial acetic acid (CH_3COOH, 17.4 N) were obtained from Fisher Scientific. N-

(isopropylacrylamide) (NIPAM, 98%) was received from TCI and toluene (99.8%) was received from Acros. All materials were used as received.

3.3.2 Synthesis

3.3.2.1 Preparation of surface-initiated magnetic nanoparticles (Fe_3O_4-Br)

'As-received' Fe_3O_4/NH_2 nanoparticles were deposited from water onto the surface of mica, previously dried with a stream of N_2, and were allowed to dry overnight at room temperature. After water evaporated, the mica substrate was washed thoroughly with water and dried with a nitrogen gun. This procedure was done to guarantee that the particles remaining on the surface were attached primarily due to the electrostatic interaction between the nanoparticles and the negatively charged mica substrate (Patricio et al., 2010). The mica-Fe_3O_4/NH_2 substrate was then placed in a 5 mL THF solution of 2-bromoisobutyryl bromide (0.01M) and triethylamine (0.012 M) and allowed to react overnight under an inert nitrogen sparge and with sonication. The reaction was quenched by opening the solution to ambient conditions after 12 h, and removing the mica substrate from the solution. The mica with adsorbed brominated Fe_3O_4/NH_2 particles (mica-Fe_3O_4/NH_2-Br) was washed thoroughly with ethanol three times to ensure that only the magnetic particles with a strong electrostatic interaction with the mica surface would remain. The remaining adsorbed nanoparticles contained surface-confined bromine initiator moeties on the terminus of their exposed surface which was used for the next step, polymerization of PNIPAM.

3.3.2.2 Synthesis of mica-Fe_3O_4-PNIPAM

ATRP using NIPAM as the monomer was started immediately after attachment of the bromine initiator to the mica-Fe_3O_4/NH_2 substrate. NIPAM ATRP was performed in propanol/water (70/30% v/v) with a molar ratio of 100/1/1 for the monomer/catalyst/ligand (Ye and Narain, 2009). First, Cu(I)Br (catalyst) and bypiridine (ligand) were placed in 5 mL of propanol and subjected to at least three freeze-pump-thaw cycles (until no gas bubbles were observed during thawing). Afterwards, nitrogen was used to sparge this solution in a sealed test tube for 1 h. Then, the NIPAM monomer solution was prepared in a 70/30 volume ratio solution (water/propanol) and subjected to at least three freeze-pump-thaw cycles. The two resultant solutions (catalyst/ligand and monomer solution) were then combined in a separate dried vessel containing the mica-Fe_3O_4/NH_2-Br. NIPAM polymerization was allowed to proceed for 12 h under an inert atmosphere (N_2 flow) at room temperature and quenched by introducing air to the reaction.

3.3.2.3 Detachment of Fe_3O_4/NH_2-PNIPAM

The electrostatic interaction holding the iron oxide MNPs to the mica can be reversed by the addition of 2M acetic acid to a pH value of ~ 2. At this low pH value the ionic attraction between the carboxylate anion (COO^-) and the NH_3^+ becomes stronger than the electrostatic interaction between the particles and the substrate. In this manner, hemispherical-shaped iron oxides MNPs were released from the mica substrate. Particles in the solution were then subjected to evaporation using a rotovap to remove the solvent and residues from the first polymerization. Then, clean ethanol was added to the dried particles and the solution was placed in a sonicator for three minutes. Particles were

dried again to remove any solvent and/or residue remaining from previous steps using the rotovap. This 'washing' procedure was repeated at least three times to remove residues from the first polymerization step. After these washing cycles, the particles were stored in clean toluene at ~ 4 °C in a refrigerator prior to the final polymerization step.

3.3.2.4 Preparation of Br-Fe_3O_4-PNIPAM nanoparticles

The stored NH_2/Fe_3O_4-PNIPAM nanoparticles were first dried using a rotovap prior to the reaction of the bromine initiator to the unreacted amines. The surface initiation step from the synthesis of surface-initiated magnetic nanoparticles (NH_2/Fe_3O_4-Br) was repeated here. Modified NH_2/Fe_3O_4-PNIPAM particles were placed in a 0.01 M 2-bromoisobutyryl bromide/triethylamine/THF solution and allowed to react for 12 h with the unreacted amines to create a surface-initiated Br-Fe_3O_4-PNIPAM particle system. The resultant particles were then 'washed' using centrifugation and isopropanol addition three times and then transferred to a clean container. Particles were 'washed' with water and rotovap evaporation two more times.

3.3.2.5 Synthesis of Janus (PMAA-Fe_3O_4-PNIPAM) nanoparticles

ATRP of MAA was performed in a similar manner. First, a 2 M solution of MAA/HPLC water was prepared and then NaOH (1 M) was used to neutralize the solution (Sankhe et al., 2006). At a pH of 7, the solution was placed under a stream of nitrogen for about 1 h and submitted to three freeze-pump-thaw cycles. The monomer solution was transferred to the dried and cleaned particles (obtained in step 4) using a syringe under an inert atmosphere. A degassed 0.1 mM solution of Me_6TREN and Cu(I)Cl was added to the MAA/Br-Fe_3O_4-PNIPAM solution to start the ATRP

polymerization on the unprotected hemisphere of the amine-functionalized magnetic nanoparticles and the reaction proceeded for 8 h to obtain the PMAA-Fe_3O_4-PNIPAM JPs. A scheme for all the reaction steps is shown in Figure 3.1.

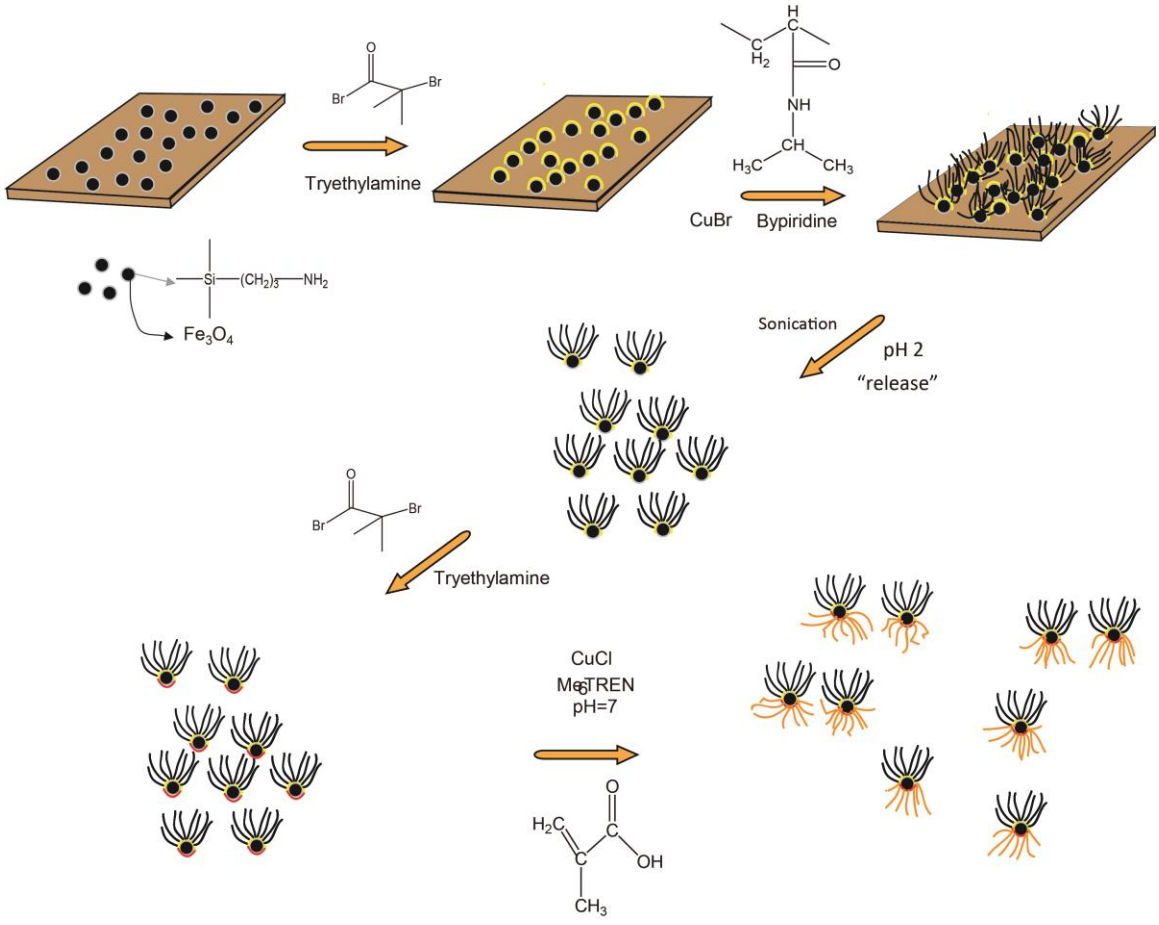

Figure 3.1 Scheme for producing biphasic PMAA-Fe_3O_4-PNIPAM Janus nanoparticles (JPs)

(i) deposition of 'as-received' Fe_3O_4/NH_2MNPs onto mica with reaction of initiator onto the exposed surface, (ii) polymerization of NIPAM monomer by surface-initiated ATRP, (iii) release of modified Fe_3O_4/NH_2-PNIPAM particles from the mica by sonication in an acidic solution, and (iv) initiation and ATRP polymerization of the newly exposed MNP surface using a second monomer, MAA.

3.3.3 Characterization of magnetic nanoparticles

Transmission electron microscopy (TEM) was performed using a JEOL 100CXII at 100 kV. Sample droplets were placed on a Cu grid (Electron Microscopy Science) and the solvent was allowed to evaporate. Atomic force microscopy (AFM) data were collected on a Dimension Icon AFM operated in tapping and ScanAsyst modes. The AFM samples were obtained by applying a drop of MNP in solution onto a mica surface followed by drying in air. NCHV probes from Bruker with resonant frequency 320 kHz, spring constant 42 N/m, and tip radius 10 nm were used for all AFM measurements. A PHI 1600 X-ray photoelectron spectroscopy (XPS) surface analysis system (Physical Electronics, Eden Prairie, MN) with Mg K_α X-ray source operating at 300 W and 15 kV was used to collect XPS data. PHI 10-360 spherical capacitor energy analyzer and an Omni Focus II small-area lens were utilized to focus the incident source. Survey spectra were collected using a minimum of 10 scans with 26.95 eV pass energy across the 1100 to 0 eV range. High-resolution spectra were gathered using a minimum of 15 scans with 23.5 eV pass energy and 0.1 eV step size. Measurements were taken on at least three spots per sample and the average results fitted using Gaussian peaks are reported. ATR-FTIR spectra were collected using a Miracle-ATR™ accessory (PIKE Technologies) with a diamond-ZnSe crystal. Nanoparticles were deposited as a solution droplet which was allowed to dry on the crystal surface until a thin film of particles remained. A minimum total of 800 scans were collected on a Nicolet 6700 FT-IR (Thermo Electron Corporation) with a helium-neon laser, mercury-cadmium-telluride (MCT-A*) detector, and KBr beamsplitter using Omnic software (v8.1.10, ©1992-2009, Thermo Fisher Scientific Inc.). FTIR peak assignments were obtained from selected references unless

otherwise specified (Stuart, 2004; Silverstein et al., 2005). Scanning electron microscopy (SEM) and Energy dispersive X-ray spectroscopy data were collected using a JEOL JSM-6500 field emission scanning electron microscope (FE-SEM) operated at 15 KeV. Samples were deposited on copper tape and allowed to dry in a ventilated hood prior to placement into the FE-SEM chamber.

3.4 Results and discussion

While the 'as-received' Fe_3O_4/NH_2 magnetic nanoparticles (MNPs) were electrostatically adsorbed to the mica surface, the exposed side of the particles was reacted with a bromine initiator followed by ATRP to grow chains of PNIPAM from the surface of the MNPs. Then, the MNPs were released from the mica substrate and a second set of initiation and ATRP reactions were performed to grow PMAA on the newly exposed amine-functionalized MNP surface (hemisphere opposite to the grafted PNIPAM) (Figure 3.1). Prior to characterization, the biphasic PMAA–Fe_3O_4–PNIPAM JPs were washed a minimum of three times using water and rotovap distillation. A discussion of the chemical and physical characterization of these samples follows.

3.4.1 Chemical structure of the biphasic PMAA–Fe_3O_4–PNIPAM Janus magnetic nanoparticles.

After synthesis, the chemical composition of the PMAA-Fe_3O_4-PNIPAM JPs was analyzed by three spectroscopic techniques. ATR-FTIR analysis was performed on 'as-received' Fe_3O_4/NH_2 sample which consists of the Fe_3O_4 magnetic nanoparticles with an amine-terminated silica coating (Figure 3.2a). Absorption bands appeared at 3400 cm^{-1} for Fe_3O_4/NH_2, characteristic of a primary amine examined in a dilute solution. Additionally, a peak was observed at 1625 cm^{-1} which is assigned to the N-H bending

(scissoring) vibrations of primary amines. N-H stretching vibrations have been reported at approximately 2000 cm^{-1} where peaks were observed for the 'as-received' Fe_3O_4/NH_2 magnetic nanoparticles. The peak at 2160 cm^{-1} can also be attributed to NH^+ stretching. Thus, the presence of the amine group on the iron oxide nanoparticle is confirmed. A representative FTIR spectrum of the PMAA-Fe_3O_4-PNIPAM JPs can be seen in Figure 3.2b and confirms the presence of PNIPAM and PMAA grown from the 'as-received' Fe_3O_4/NH_2 surface. First, the N-H peaks associated with primary amines previously discussed, in particular those at ~ 2000 cm^{-1}, were no longer observed. Second, a broad absorption peak over the range 3000-3300 cm^{-1} was attributed to O-H stretching from the PMAA structure (Pretsch et al., 2009). Third, in the range of 1600-1720 cm^{-1} two overlapping peaks match well with the characteristic carbonyl absorbances for PNIPAM and PMAA (1650 and 1710 cm^{-1}, respectively). Lastly, at 1540 cm^{-1} a sharp peak was observed that is related to the carboxylate anion from PMAA related with the doublet at 1710 cm^{-1} (Dean and Lange, 1973).

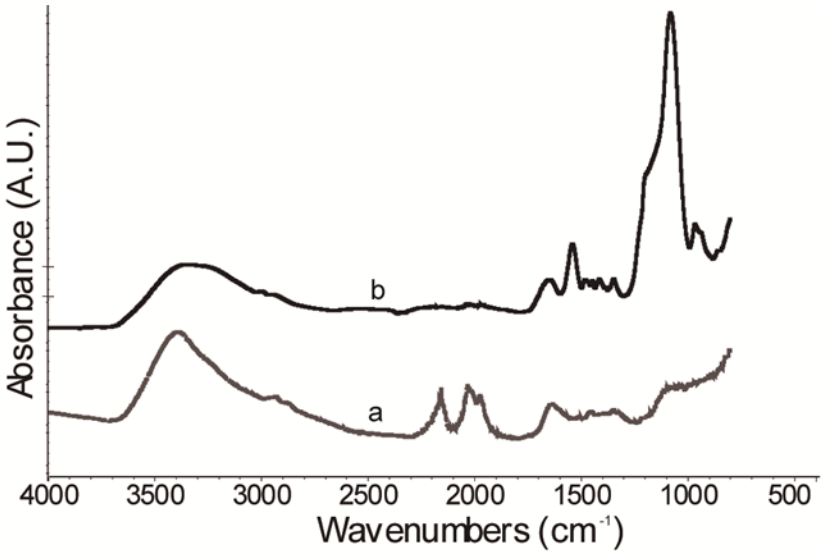

Figure 3.2 ATR-FTIR spectra comparison of the chemical structure

(a) 'as-received' Fe_3O_4/NH_2 magnetic nanoparticles (red line) and the resulting (b) biphasic PMAA-Fe_3O_4-PNIPAM JPs (black line). PNIPAM and PMAA carbonyl (C=O) absorption bands were identified at 1650 and 1710 cm^{-1}, respectively.

While the characteristic spectral signatures for the PNIPAM/PMAA biphasic JPs were observed, an additional unexpected peak was observed at 1082 cm^{-1}. In this region, a very broad and intense peak of -Si-O has been reported in literature (Silverstein et al., 2005). However, analysis of the 'as-received' Fe_3O_4/NH_2 nanoparticles (Figure 3.2a) did not show this peak. [Instead, it shows peaks at 2100 cm^{-1} which is characteristic of R_3SiH, believed to be part of the silicate/amine shell of the as-received amine-modified Fe_3O_4/NH_2 (Figure 3.1)]. Therefore, this unexpected -Si-O peak at ~1100 cm^{-1} in the resulting JP sample is likely to be from the mica. Mica may be present in the JPs solution despite the different separations procedures that were carried out. SEM and energy dispersive X-ray spectroscopy (EDS) analysis (discussed below) supports this claim of mica residues as a minor contaminant in the JP sample. EDS was primarily used as a

qualitative tool to demonstrate that mica elements were indeed present in the PMAA-Fe_3O_4-PNIPAM JP solution.

X-ray photoelectron spectroscopy (XPS) was then performed on the bare particles and the resulting biphasic magnetic JPs. Figure 3.3 shows representative survey scans collected for both a) 'as-received' Fe_3O_4/NH_2 and b) PMAA-Fe_3O_4-PNIPAM JPs. Survey and high resolution scans on the 'as-received' Fe_3O_4/NH_2 nanoparticles confirmed the presence of carbon, oxygen, iron, nitrogen and silica. The average atomic percentage for bare magnetic nanoparticles (Figure 3.3a) was carbon 55.37 ± 1.51%, oxygen 27.96 ± 17%, nitrogen 2.67 ± 2.5%, silica 3.79 ± 1.95% and iron 5.23 ± 9.23 %. XPS survey scan results for the Janus nanoparticles show only carbon and oxygen after formation of PMAA-Fe_3O_4-PNIPAM JPs. Average atomic compositions obtained for Janus nanoparticles (Figure 3.3b) were carbon 73.77 ± 1.59%, oxygen 21.75 ± 1.79%, and nitrogen 4.48 ± 0.37%. Therefore, it is strongly believed that the entire surface of the magnetic nanoparticle has been successfully surface-modified with polymer brushes on both hemispheres. Additionally, the atomic percentage has less variability in the measurements collected for JPs than for the as-received nanoparticles. This is believed to be an effect of the particle sizes of the nanoparticles. Thus, a thicker and homogeneous coating was formed on the surface of the magnetic nanoparticles. For comparison purposes, a 50/50 mix of PNIPAM and PMAA will have a theoretical atomic percentage of carbon 70.8 %, oxygen 22.9 % and nitrogen 6.3%. Elemental composition for carbon and oxygen measured by XPS are close to this theoretical mixture (C 74.4%, O 25.6%), however, nitrogen was not observed in the XPS measurements collected. This might be an effect of the high concentration of carbon and oxygen and equipment sensitivity.

Nitrogen was detected for the bare nanoparticles, however, in very small amounts which confirmed the presence of amine groups on the surface.

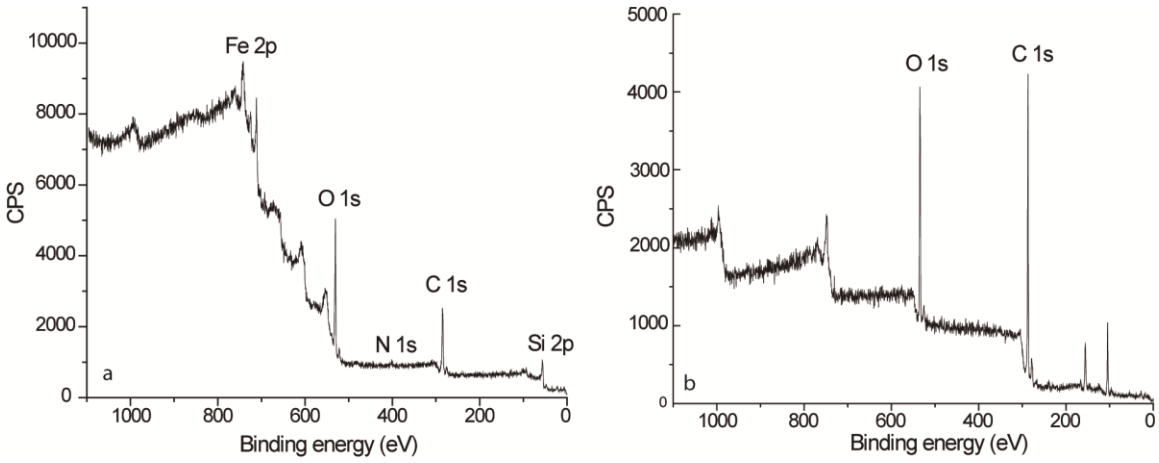

Figure 3.3 Carbon, oxygen, iron, nitrogen and silica content was confirmed for the 'as-received' Fe_3O_4/NH_2 magnetic nanoparticles

(a). XPS survey scan results for the Janus nanoparticles show only carbon and oxygen after formation of PMAA-Fe_3O_4-PNIPAM JPs (b). Average atomic compositions obtained for Janus nanoparticles were 73.77 ± 1.59% for carbon, 21.75 ± 1.79% for oxygen, and 4.48 ± 0.37 for nitrogen which match theoretical concentrations for PMAA/PNIPAM and confirm the successful formation of Janus nanoparticles.

High resolution XPS scans were performed for carbon, silica and iron as shown in Figure 3.4, for both as-received magnetic nanoparticles and PMAA–Fe_3O_4–PNIPAM JPs. A representative carbon 1s high resolution scan is shown (Figure 3.4a) for the as-received magnetic nanoparticles. Four carbon peaks were obtained at 282.3, 285, 286.3 and 289 eV for Si-C, C-H/C-C , C-H-, and N-H, respectively. Comparison with available literature values helped to identify the chemical functionality and bonds of the 'as-received' Fe_3O_4/NH_2 nanoparticles. Previous studies have found at 282.3 eV a peak corresponding to the Si-C bond (Smith and Black, 1984). Thus, it is believed that this peak represents part of the core-shell structure where the core is the magnetic particle

with a silica corona shell. C-H/C-C bonds are generally identified at 285 eV and would be expected for the silicates shell structure of the 'bare' nanoparticles (Clark and Thomas, 1976). Two peaks that demonstrate the presence of an amine on the surface were found at 286.3 and 289 eV. The peak at 286.3 has been previously characterized as C-H-adjacent to N-H group (Tu et al., 2004) and N-H has also been reported at 289.0 eV(Peeling et al., 1978). As a result, the amine functional group was also noticeable in the carbon scan. The chemical composition of the magnetic core was confirmed by a high resolution scan for iron. Previous studies show the presence of two peaks for Fe_3O_4: 710.6eV for Fe $2p_{3/2}$ and 724.1 eV for Fe $2p_{1/2}$ (Yamashita and Hayes, 2008). The two peaks observed for iron at the binding energies reported previously (Figure 3.4b) and the absence of a satellite peak confirmed the presence of magnetite (Fe_3O_4)—instead of Fe_2O_3—as the core. Moreover, Figure 3.4c shows the high resolution scan for silica on the NH_2-modified magnetic nanoparticles, and a peak expected for Si $2p_{3/2}$ was observed at 103 eV(Gonzalez-Elipe et al., 1988; Tu et al., 2004). Additionally, the peak at 94 eV corresponds to Fe_3O_4 and confirms the magnetic behavior of the particles, as previously reported in literature (Mills and Sullivan, 1983). Therefore, XPS analysis of the 'as-received' Fe_3O_4/NH_2 confirmed the presence of a magnetite core surrounded by a polymeric silicate shell with amine groups present.

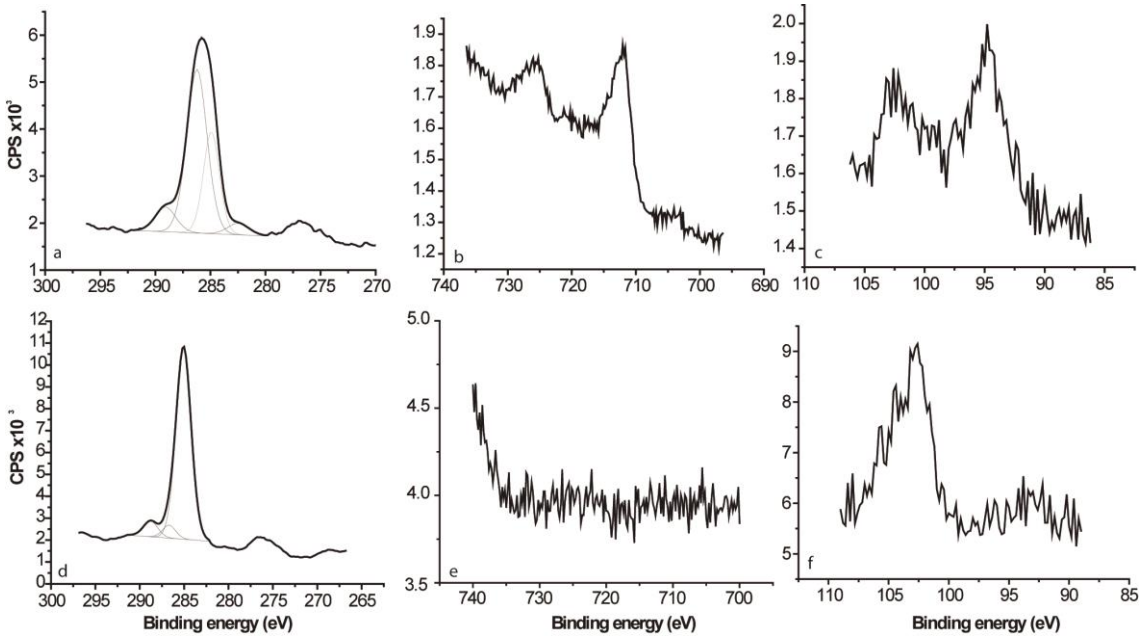

Figure 3.4 XPS high resolutions spectra for 'as-received' Fe_3O_4/NH_2 nanoparticles (a) carbon, (b) iron and (c) silica. PMAA-Fe_3O_4-PNIPAM JP spectra show (d) shifted carbon peaks showing –COOH (288.8 eV), C-O (286.7 eV) and C-C/C-H (285 eV) for PMAA peaks, (e) iron is no longer detected due to the polymer now present over the Fe_3O_4 core and the limited d_p, and (f) different peaks for silica as the silicate from the bare particles is no longer 'visible' due to the polymer but silica from the mica is now present.

Surface-confined modification of the 'as-received' Fe_3O_4/NH_2 with PMAA and PNIPAM to produce biphasic magnetic JPs was also confirmed with XPS data (Figure 3.4[d-f]). A strong carbon 1s peak was located at 285 eV for C-H/C-C which is characteristic of hydrocarbons. Both the polymers in this study and the silicate shell structure of the bare nanoparticles contain C-C linkages. Nonetheless, this peak was dramatically stronger in the PMAA-Fe_3O_4-PNIPAM JPs than in the 'as-received' Fe_3O_4/NH_2, as is expected from the significantly larger number of C-C bonds in the PMAA and PNIPAM structures. Moreover, carboxylic acids typically present two characteristic peaks, –COOH at 288.8 eV (DeKoven and Hagans, 1986) and C-O at 286.7

eV (Beamson et al., 2000), that could confirm the presence of PMAA in the resultant JPs. These two peaks were observed in the high resolution scan of the PMAA–Fe_3O_4–PNIPAM JPs (Figure 3.4d). Due to the close binding energy proximity of the C-N at 285 eV, it is difficult to separate peaks in this region for both PMAA and PNIPAM. In addition, PNIPAM carbon peaks are close to the 285 eV value. For example, Tu et al. analyzed the resulting binding energies of PNIPAM and their results showed that carbon peaks for $–CH_3$, $–CH_2–$, and –CH– in PNIPAM were at 284.9, 285.3, and 286.2 eV, respectively (Tu et al., 2004). Results shown in Figure 3.4d confirm a large peak at 285 eV; however, XPS instrument was unable to resolve a difference in 0.8 eV which is the region that contains the different hybridized carbon peaks mentioned above. Finally, as the sampling depth (d_p) for XPS is at most 10 nm, surface-confined ATRP modification of the 'as-received' Fe_3O_4/NH_2 nanoparticles with polymer brushes was confirmed, as peaks corresponding to the 'bare' system were no longer observed (Figure 3.4[e-f]). Therefore, the surface-confined modification of these particles was achieved. [Note that a strong peak was observed at around 102.5 eV for PMAA–Fe_3O_4–PNIPAM JPs. This peak differs from the Si peaks at 282.3 eV (Si-C) and 103 eV (Si $2p_{3/2}$) eV seen in the 'as-received' Fe_3O_4/NH_2 samples and corresponds to silica in muscovite mica (Wagner et al., 1982), confirming that the slight Si contamination in the sample is from mica, as discussed previously in the IR results.]

SEM and EDS techniques were utilized to confirm the presence of mica sediments with the modified JPs. Figure 3.5(a,c) shows different SEM images on which the JPs particle morphology can be observed, however, another material was also observed as different images were collected Figure 3.5(b,d). The presence of small

circular particles, different in contrast of both materials, seems to appear and confirm the presence and successful creation of JPs with this process. However, Figure 3.5(c,d) showed a second spot on which a different morphological structure was observed. This image has flat small sections (~ 1 micron) near the JPs. Previous spectroscopic (XPS and ATR-FTIR) discussion showed the presence of silica particles perhaps from mica residues. These SEM samples were then analyzed using EDS to determine any possible source of contamination. The chemical structure of mica has elements different from those utilized in the nanostructures in this work, such as aluminum and potassium (Gonzalez-Elipe et al., 1988). Different high carbon and oxygen contents were observed as EDS data were collected on the small circular particles. In addition, the presence of nitrogen (present in PNIPAM) was also shown in some of the EDS scans. Other elements such as aluminum, potassium, and silica also appeared in the elemental analysis confirming that the contaminant material is mica. Despite obtaining different elemental percentages, these are not reported due to the greater depth of penetration using EDS, as compared to surface-sensitive techniques such as XPS, and possible carbon contamination from the SEM grip support. As a summary, EDS confirmed the presence of mica contaminant within the novel biphasic JPs system suspended in water; however, it does not provide a quantitative analysis due to the high beam depth penetration and the small size of the nanoparticles of this study.

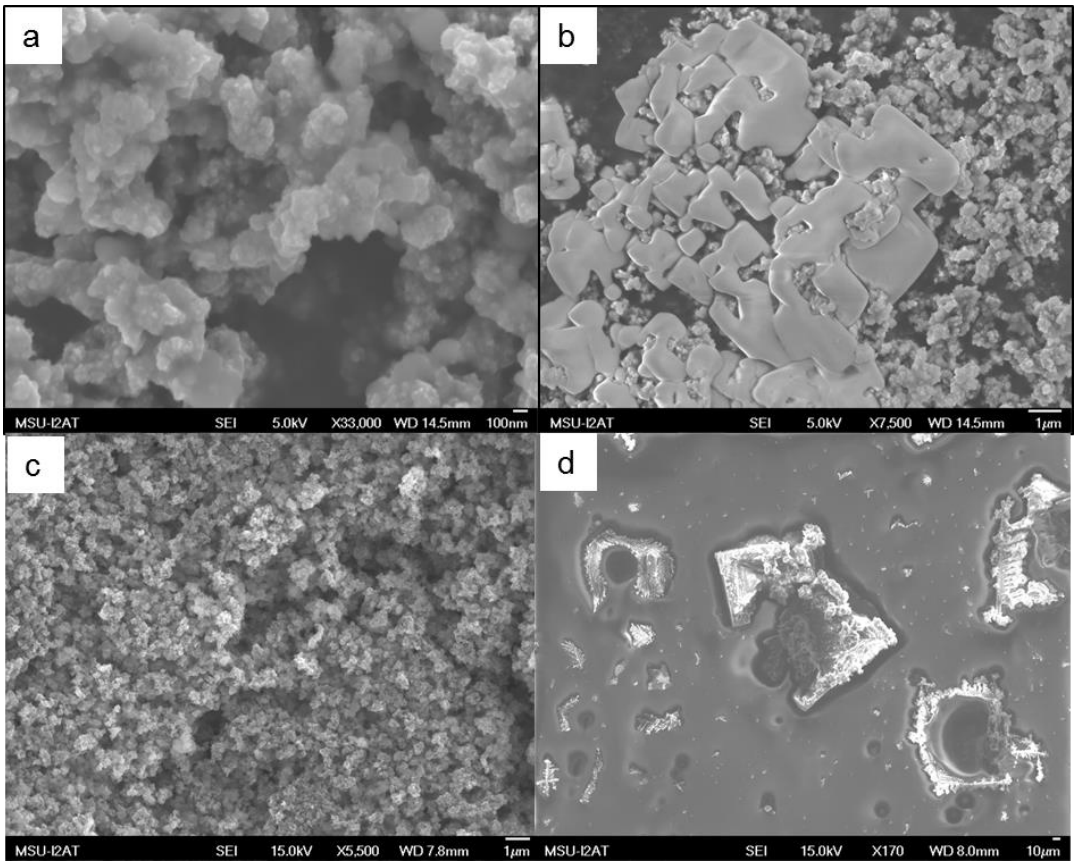

Figure 3.5 SEM images (a,c) shows PMAA-Fe_3O_4-PNIPAM JPs.

Additionally, silica particles from the mica can be seen as contaminants in the JP samples (b,d).

ATR-FTIR and XPS confirmed the formation of PMAA-Fe_3O_4-PNIPAM biphasic systems. Theoretical atomic percentages of NIPAM for carbon, oxygen and nitrogen are 75%, 12.5% and 12.5%, respectively. MAA theoretical atomic percentages for carbon and oxygen are 67% and 33%, respectively. Thus, the average result obtained with XPS (carbon 74.4% and oxygen 25.6%) are within a range of an expected mixed polymer atomic concentration. All structural and chemical composition analyses confirmed the successful formation of hemispherical Fe_3O_4/NH_2-PNIPAM nano-structures and biphasic JPs structures composed of PMAA-Fe_3O_4-PNIPAM.

3.4.2 Morphology of the biphasic PMAA-Fe3O4-PNIPAM Janus nanoparticles.

TEM, SEM and AFM were used to analyze the morphology of the resultant Janus magnetic nanoparticles after the two sequential ATRP reactions were carried out on opposite hemispheres of the'as-received' Fe_3O_4/NH_2 nanoparticles. First, grafting of the first polymer (PNIPAM) on one side of the magnetic nanoparticles using surface-initiated ATRP was confirmed. The expected PNIPAM-Fe_3O_4/NH_2 structure showed a half-moon shape (Figure 3.6[a,b]) with an approximate width of 250 nm. The dark core can be assigned to Fe_3O_4, the thin light-colored shell is the NH_2/silane layer, and the thick grey corona is comprised of the PNIPAM brushes grafted on the surface of the MNPs (Figure 3.6b). This half-moon shaped structure was due to the polymer (PNIPAM) growing on the exposed MNP surface while they were attached to the mica substrate (Figure 3.6a). However, some smaller (~ 10 nm) spherical structures could be observed at the outer edge of the hemispherical PNIPAM polymer brush. Due to the size (much less than the 50 nm MNP), an absence of these smaller size particles in TEM images of the bare MNP, and the strong PNIPAM chain association observed, it is likely that these dark spherical area on the periphery are densely packed PNIPAM. It is obvious that in solution the Fe_3O_4/NH_2-PNIPAM structures self-assemble tail-to-tail with the PNIPAM chains associating after being released from the mica substrate upon the pH shift. This type of behavior can clearly be seen both in the formation of a second spherical PNIPAM–Fe_3O_4 structure observed (Figure 3.6[c,d]) that has also a diameter of approximately 250 nm and also in the dense particulate seen in the interior.

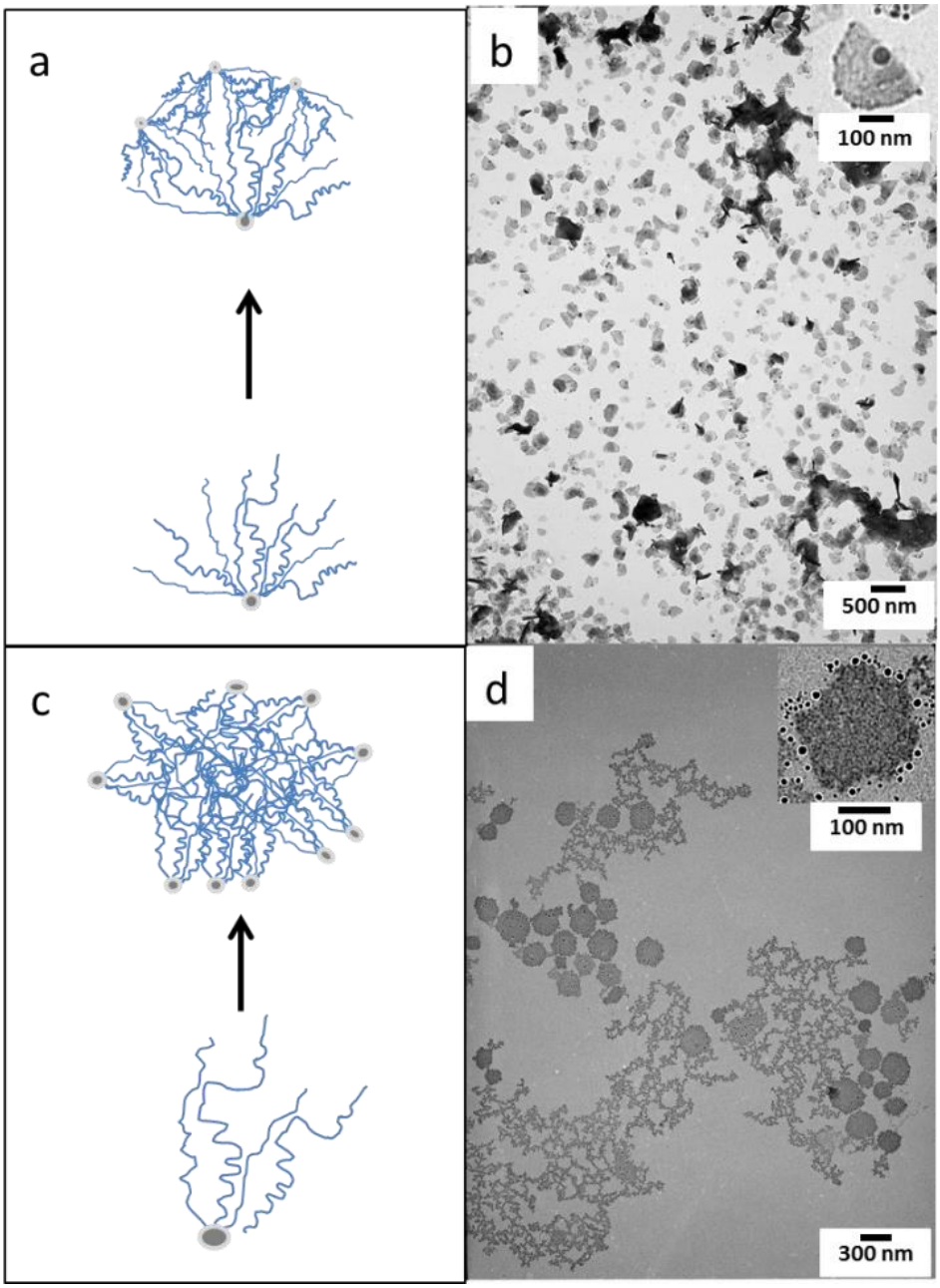

Figure 3.6 The half-moon/hemispherical morphology for Fe_3O_4/NH_2-PNIPAM and secondary (aggregated) structures (a,b) are shown by TEM.

A second aggregate structure comprised of Fe_3O_4/ NH_2-PNIPAM was also identified (c,d). Illustrations (a,c) depict each process theorized for the observed structures. [Note that inset images (b,d) are at higher magnifications.]

At this point, it is not entirely clear whether the PNIPAM chains were associated with one another during the polymerization process or only after the particles were released from the mica substrate. It may be that these dense PNIPAM particulates seen on the periphery in Figure 3.6b and in the center of the structure in Figure 3.6d are free PNIPAM chains than have collapsed on themselves more readily due to not being confined on one end as a polymer brush structure. These free PNIPAM chains could be formed from bromine initiator that was retained in the sample prior to monomer addition. These secondary structures might be controlled by the concentration and removal method for the bromine initiator, the solubility parameter of the solvent used for polymerization and deposition (e.g, for TEM analysis), and by the ambient temperature—as PNIPAM is a thermoresponsive polymer. The initial assembly, structural (re)organization—by multiple triggers, and/or paramagnetic heating in response to a magnetic field is all exciting aspects of these new thermo-responsive biphasic Janus material. Certainly there is potential use of these multifunctional materials in a variety of applications. The expected "half-moon" shapes were the dominant morphology of these Janus nanoparticles, as was confirmed by TEM and AFM studies. Figure 3.7 shows an AFM topography image of the hemispherical shape of PNIPAM-Fe_3O_4/NH_2.

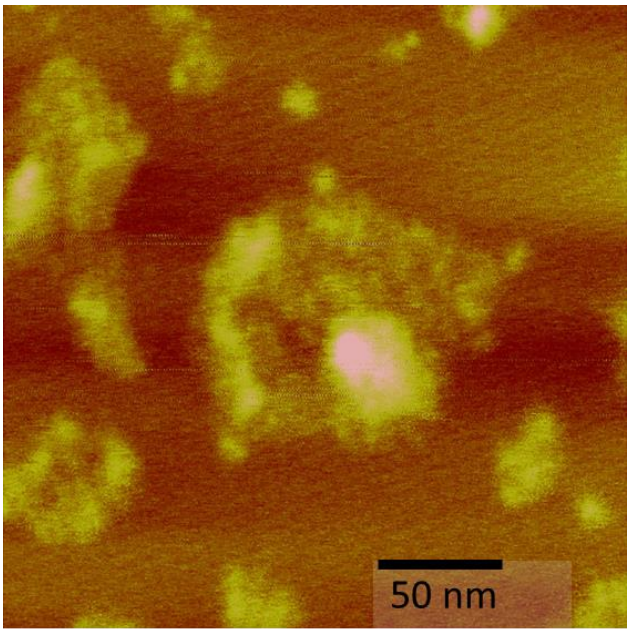

Figure 3.7 AFM phase imaging showed the expected half-moon/hemispherical morphology for Fe_3O_4/ NH_2-PNIPAM that was also documented with TEM (Figure 3.6b inset).

The magnetic core and polymer shell are distinctly visible in this two phase metal/polymer system.

After confirming the desired morphology, the second monomer (MAA) was grown on the opposite side of PNIPAM-Fe_3O_4/NH_2 via ATRP. The PMAA-Fe_3O_4-PNIPAM Janus NPs were found to aggregate at two different length scales (Figure 3.8 and 3.9). The first was the assembly of a few biphasic polymer JPs into defined clusters. Figure 3.8 shows the aggregated PNIPAM as darker large spheres due to the hydrophobic collapse and the more diffuse grey network structure is the hydrophilic PMAA swollen in isopropanol. The second was the aggregation of these clusters into larger scale assemblies. The small PMAA-Fe_3O_4-PNIPAM clusters (~400 nm) and the larger assemblies (~1 micron) of biphasic JPs can be observed in the TEM (Figure 3.8) and AFM images (Figure 3.9) as tertiary structures at very different length scales.

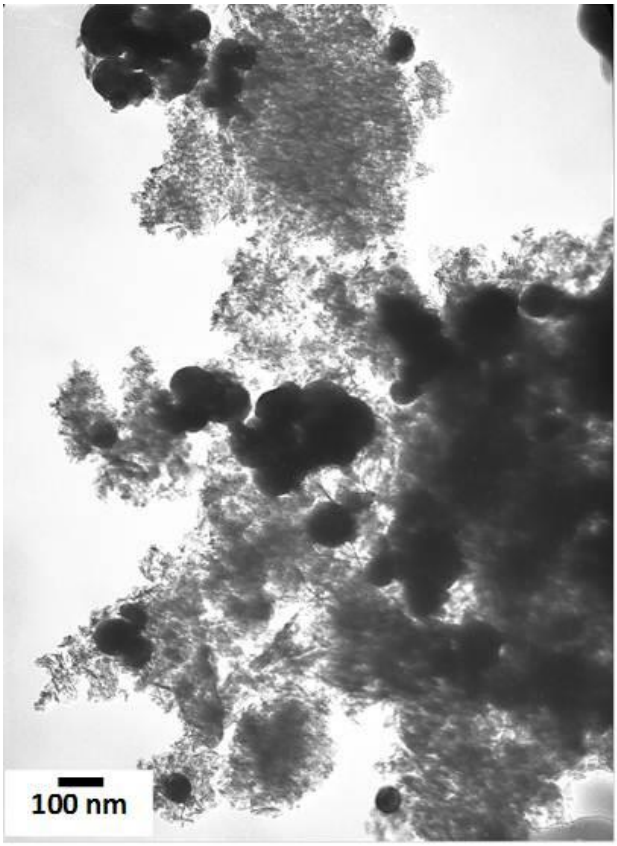

Figure 3.8 TEM image of 3D asymmetric Janus magnetic nanoparticles deposited from isopropanol

The darker clustered particles are comprised of agglomerated PNIPAM due to hydrophobic collapse, and PMAA chains are more diffuse (lighter grey color) as they are expanded due to the hydrophilic environment.

Recently, Walther et al. suggested that solvent selectivity is sufficient to induce particle self-assembly into defined discrete clusters of JPs (Walther and Muller, 2008). Thus, PMAA–Fe_3O_4–PNIPAM aggregation is dependent on the type of solvent used for the dispersion of the nanoparticle composites. In this work, this self-assembly further demonstrated the presence of two amphiphilic polymers in the JPs structure as confirmed by TEM, AFM and SEM.

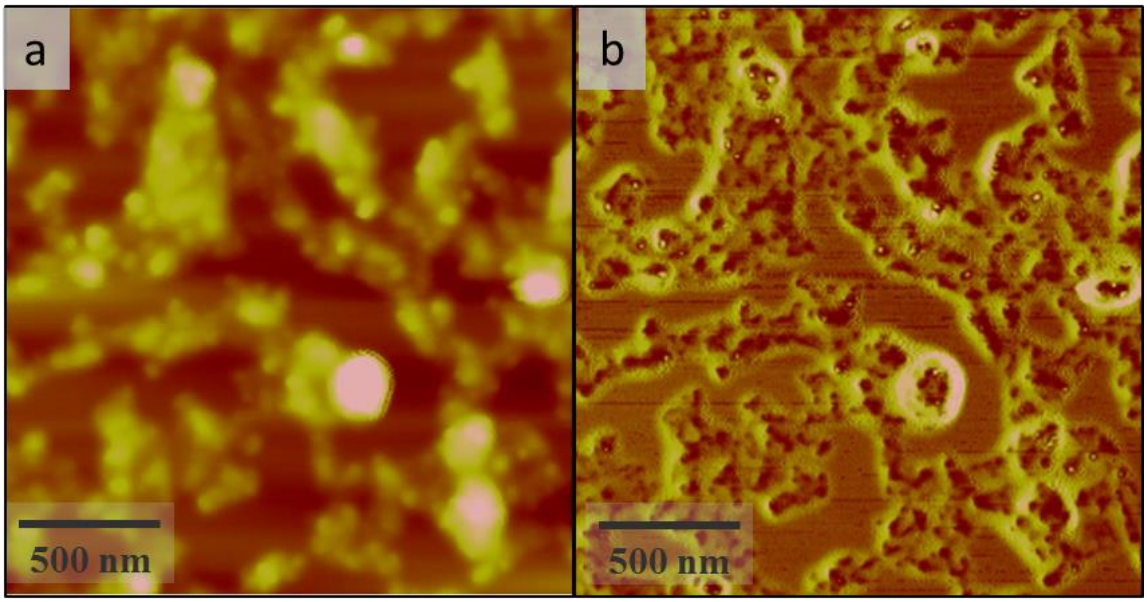

Figure 3.9 AFM (a) height and (b) phase images of 3D asymmetric Janus magnetic nanoparticles.

Long polymer chains are attached to the magnetic core and the PMAA–Fe_3O_4–PNIPAM JPs are aggregated into assemblies > 1 micron

3.5 Conclusions

Three-dimensionally amphiphilic and asymmetric magnetic Janus nanoparticles (JPs), PMAA-Fe_3O_4-PNIPAM, were synthesized by combining two methods (1) electrostatic surface-binding interactions and (2) surface-confined reversible-deactivation radical polymerization technique (ATRP). Chemical composition was analyzed using attenuated total reflectance Fourier transform infrared spectroscopy (ATR-FTIR) and X-ray photoelectron spectroscopy (XPS). These techniques demonstrated the successful bi-phasic polymer modification of the amine-functionalized magnetic nanoparticles. ATR-FTIR showed that post-polymerization the N-H peaks associated with primary amines of the 'as-received' Fe_3O_4/NH_2 nanoparticles were no longer observed. In addition, characteristic carbonyl absorbances for PNIPAM and PMAA were observed for the

PMAA-Fe_3O_4-PNIPAM JP system. Lastly, FTIR doublet peaks for the carboxylate anion seen in from PMAA was clearly present. Using the sequential adsorption/polymerization/release/polymerization method, two different polymers were polymerized from opposite sides of iron oxide magnetic nanoparticles to form bi-polymer Janus nanoparticles.

Morphological structure and structural changes were monitored by TEM, SEM, and AFM and further supported the chemical composition results. The successful grafting of the first polymer (PNIPAM) on one side of the magnetic nanoparticles using surface-confined ATRP with the particles electrostatically deposited on the mica surface was demonstrated clearly in AFM and TEM images by the formation of a half-moon/hemispherical morphology in the Fe_3O_4/ NH_2-PNIPAM samples. The resulting PMAA-Fe_3O_4-PNIPAM JPs system was formed only after the particles were released from the mica surface by lowering the pH. ATRP was then performed on the newly released amine functional groups of the magnetic nanoparticles. The final bi-polymeric Janus nanoparticle structure with Fe_3O_4 core was confirmed through spectroscopy and microscopy. The morphologies at each synthesis step agreed with the expected and observed chemical composition changes and support the formation of a PMAA-Fe_3O_4-PNIPAM JPs system. These thermo-responsive biphasic Janus nanostructures have tremendous potential due to their multifunctional nature and the inherent dynamic control over their size, shape, and spacing.

This study provides a framework for a methodology to create spatially and chemically amphiphilic Janus nanoparticles in a facile manner. The strategy was monitored and confirmed by multiple chemical composition and morphological

experimental techniques. This approach has the potential to be extended to the synthesis of other types of biphasic polymer systems, particle types, and other electrostatically charged materials.

3.6 References

Andala, D. M., S. H. R. Shin, H.-Y. Lee and K. J. M. Bishop (2012). "Templated Synthesis of Amphiphilic Nanoparticles at the Liquid–Liquid Interface." ACS Nano **6**: 1044-1050.

Beamson, G., D. Briggs and SurfaceSpectra Ltd. (2000). The XPS of polymers database. Manchester, SurfaceSpectra: 1 CD-ROM.

Berger, S., A. Synytska, L. Ionov, K. J. Eichhorn and M. Stamm (2008). "Stimuli-Responsive Bicomponent Polymer Janus Particles by "Grafting from"/"Grafting to" Approaches." Macromolecules **41**: 9669-9676.

Casagrande, C., P. Fabre, E. Raphaël and M. Veyssié (1989). ""Janus Beads": Realization and Behaviour at Water/Oil Interfaces." EPL (Europhysics Letters) **9**: 251.

Chang, E. P. and T. A. Hatton (2012). "Membrane Emulsification and Solvent Pervaporation Processes for the Continuous Synthesis of Functional Magnetic and Janus Nanobeads." Langmuir **28**: 9748-9758.

Clark, D. T. and H. R. Thomas (1976). "Applications of ESCA to polymer chemistry. X. Core and valence energy levels of a series of polyacrylates." Journal of Polymer Science: Polymer Chemistry Edition **14**: 1671-1700.

Dean, J. A. and N. A. Lange (1973). Lange's handbook of chemistry. New York, McGraw-Hill: v.

DeKoven, B. M. and P. L. Hagans (1986). "XPS studies of metal/polymer interfaces — Thin films of Al on polyacrylic acid and polyethylene." Applied Surface Science **27**: 199-213.

Du, J. and R. K. O'Reilly (2011). "Anisotropic particles with patchy, multicompartment and Janus architectures: preparation and application." Chemical Society Reviews **40**: 2402-2416.

Gómez-Romero, P.; Sanchez, C., Functional hybrid materials. Wiley-VCH; John Wiley distributor: Weinheim. Chichester, 2004; pp. xvii, 417.Gonzalez-Elipe, A. R., J. P. Espinos, G. Munuera, J. Sanz and J. M. Serratosa (1988). "Bonding-state characterization of constituent elements in phyllosilicate minerals by XPS and NMR." The Journal of Physical Chemistry **92**: 3471-3476.

Hu, J., S. Zhou, Y. Sun, X. Fang and L. Wu (2012). "Fabrication, properties and applications of Janus particles." Chemical Society Reviews **41**: 4356-4378.

Kickelbick, G. (2007). Hybrid materials : synthesis, characterization, and applications. Weinheim, Wiley - VCH.

Lattuada, M. and T. A. Hatton (2006). "Functionalization of Monodisperse Magnetic Nanoparticles." Langmuir **23**: 2158-2168.

Lattuada, M. and T. A. Hatton (2007). "Preparation and controlled self-assembly of janus magnetic nanoparticles." Journal of the American Chemical Society **129**: 12878-12889.

Li, D. J., X. Sheng and B. Zhao (2005). "Environmentally responsive "Hairy" nanoparticles: Mixed homopolymer brushes on silica nanoparticles synthesized by living radical polymerization techniques." Journal of the American Chemical Society **127**: 6248-6256.

Liberelle, B., X. Banquy and S. Giasson (2008). "Stability of Silanols and Grafted Alkylsilane Monolayers on Plasma-Activated Mica Surfaces." Langmuir **24**: 3280-3288.

Lu, Y., H. Xiong, X. Jiang, Y. Xia, M. Prentiss and G. M. Whitesides (2003). "Asymmetric Dimers Can Be Formed by Dewetting Half-Shells of Gold Deposited on the Surfaces of Spherical Oxide Colloids." Journal of the American Chemical Society **125**: 12724-12725.

McConnell, M. D., M. J. Kraeutler, S. Yang and R. J. Composto (2010). "Patchy and Multiregion Janus Particles with Tunable Optical Properties." Nano Letters **10**: 603-609.

Mills, P. and J. L. Sullivan (1983). "A study of the core level electrons in iron and its three oxides by means of X-ray photoelectron spectroscopy." Journal of Physics D: Applied Physics **16**: 723.

Mock, E. B., H. De Bruyn, B. S. Hawkett, R. G. Gilbert and C. F. Zukoski (2006). "Synthesis of Anisotropic Nanoparticles by Seeded Emulsion Polymerization." Langmuir **22**: 4037-4043.

Nogawa, H. and Japanese Technical Information Service. (1988). Hybrid materials : concepts and case studies. Metals Park, Ohio, ASM International.

Patricio, S., A. I. Cruz, K. Biernacki, J. Ventura, P. Eaton, A. L. Magalhaes, et al.C. Freire (2010). "Novel Layer-by-Layer Interfacial [Ni(salen)]-Polyelectrolyte Hybrid Films." Langmuir **26**: 10842-10853.

Peeling, J., F. E. Hruska and N. S. McIntyre (1978). "ESCA spectra and molecular charge distributions for some pyrimidine and purine bases." Canadian Journal of Chemistry **56**: 1555-1561.

Perro, A., S. Reculusa, S. Ravaine, E. Bourgeat-Lami and E. Duguet (2005a). "Design and synthesis of Janus micro- and nanoparticles." Journal of Materials Chemistry **15**: 3745-3760.

Poree, D. E., M. D. Giles, L. B. Lawson, J. He and S. M. Grayson (2011). "Synthesis of amphiphilic star block copolymers and their evaluation as transdermal carriers." Biomacromolecules **12**: 898-906.

Pretsch, E., P. Bühlmann, M. Badertscher and Knovel (Firm) (2009). Structure determination of organic compounds tables of spectral data. Berlin, Springer: xv, 433 p.

Qiang, W., Y. Wang, P. He, H. Xu, H. Gu and D. Shi (2008). "Synthesis of Asymmetric Inorganic/Polymer Nanocomposite Particles via Localized Substrate Surface Modification and Miniemulsion Polymerization." Langmuir **24**: 606-608.

Sankhe, A. Y., S. M. Husson and S. M. Kilbey (2006). "Effect of Catalyst Deactivation on Polymerization of Electrolytes by Surface-Confined Atom Transfer Radical Polymerization in Aqueous Solutions." Macromolecules **39**: 1376-1383.

Silverstein, R. M., F. X. Webster and D. J. Kiemle (2005). Spectrometric identification of organic compounds. Hoboken, NJ, John Wiley & Sons.

Smith, A. E., X. W. Xu, T. U. Abell, S. E. Kirkland, R. M. Hensarling and C. L. McCormick (2009). "Tuning Nanostructure Morphology and Gold Nanoparticle "Locking" of Multi-Responsive Amphiphilic Diblock Copolymers." Macromolecules **42**: 2958-2964.

Smith, K. L. and K. M. Black (1984). "Characterization of the treated surfaces of silicon alloyed pyrolytic carbon and SiC." Journal of Vacuum Science & Technology A: Vacuum, Surfaces, and Films **2**: 744-747.

Tanaka, T., M. Okayama, Y. Kitayama, Y. Kagawa and M. Okubo (2010). "Preparation of "Mushroom-like" Janus Particles by Site-Selective Surface-Initiated Atom Transfer Radical Polymerization in Aqueous Dispersed Systems." Langmuir **26**: 7843-7847.

Teo, B. M., S. K. Suh, T. A. Hatton, M. Ashokkumar and F. Grieser (2010). "Sonochemical Synthesis of Magnetic Janus Nanoparticles." Langmuir **27**: 30-33.

Tu, H., C. E. Heitzman and P. V. Braun (2004). "Patterned Poly(N-isopropylacrylamide) Brushes on Silica Surfaces by Microcontact Printing Followed by Surface-Initiated Polymerization." Langmuir **20**: 8313-8320.

Walther, A. and A. H. E. Muller (2008). "Janus particles." Soft Matter **4**: 663-668.

Wang, B., B. Li, B. Zhao and C. Y. Li (2008). "Amphiphilic Janus Gold Nanoparticles via Combining “Solid-State Grafting-to” and “Grafting-from” Methods." Journal of the American Chemical Society **130**: 11594-11595.

Wang, Y., C. Zhang, C. Tang, J. Li, K. Shen, J. Liu, et al.Z. Yang (2011). "Emulsion Interfacial Synthesis of Asymmetric Janus Particles." Macromolecules **44**: 3787-3794.

Wurm, F. and A. F. Kilbinger (2009). "Polymeric janus particles." Angew Chem Int Ed Engl **48**: 8412-8421.

Yamashita, T. and P. Hayes (2008). "Analysis of XPS spectra of Fe2+ and Fe3+ ions in oxide materials." Applied Surface Science **254**: 2441-2449.

Yang, S., F. Guo, B. Kiraly, X. Mao, M. Lu, K. W. Leong and T. J. Huang (2012). "Microfluidic synthesis of multifunctional Janus particles for biomedical applications." Lab on a Chip **12**: 2097-2102.

Ye, J. D. and R. Narain (2009). "Water-Assisted Atom Transfer Radical Polymerization of N-Isopropylacrylamide: Nature of Solvent and Temperature." Journal of Physical Chemistry B **113**: 676-681.

Zhao, N. and M. Gao (2009). "Magnetic Janus Particles Prepared by a Flame Synthetic Approach: Synthesis, Characterizations and Properties." Advanced Materials **21**: 184-187.

CHAPTER IV

A STUDY OF THE PH- AND THERMO-RESPONSIVE BEHAVIOR OF A SERIES OF AMINO (METH)ACRYLATE POLYMER BRUSHES ON SILICON SUBSTRATES

4.1 Abstract

Surface-confined ATRP and/or SET radical polymerizations have been used to synthesize a series of surface-tethered poly(amino (meth)acrylates) brushes from silicon substrates that were modified with silane self-assembled monolayers (SAM). The following polymers were synthesized: poly((2-dimethylamino) ethyl methacrylate) (PDMAEMA), poly((2-diethylamino) ethyl methacrylate) (PDEAEMA), poly((2-dimethylamino) ethyl acrylate) (PDMAEA), and poly ((*tert*-butylamino) ethyl methacrylate) (PTBAEMA). *In-situ* characterization techniques, including AFM and ellipsometry, were used to evaluate the thermo- and pH-responsiveness of these materials. A new general-oscillator (GENOSC) model was used to determine swelling ratio, thickness, and optical constant changes in the polymer brush as pH was changed *in-situ*. AFM was used to study morphological changes due to changes in pH and temperature, and results were compared with the traditional Cauchy layer model. A new method for evaluating optical constants of surface-tethered polymer brushes as pH and temperature are changed is the main outcome of this work.

4.2 Introduction

Stimuli-responsive polymers (SRP) can expand and collapse as a response to an external effect in different configurationally structured shapes. Polymer brushes that are tethered on a substrate are called "smart surfaces" due to the responsiveness as an external stimulus is applied. Surfaces such as flat wafers (Alarcon et al., 2005), nanoparticles (Bi et al., 2008; Tagliazucchi et al., 2012), membranes (Wandera et al., 2010), microfluidic-devices, and many others (Kikuchi and Okano, 2002; Nath and Chilkoti, 2002; Gil and Hudson, 2004; Twaites et al., 2004; Azzaroni, 2012) are of interest to find a variety of different applications. Nonetheless, these polymer brushes are limited in motion as one end of the polymer is attached, physically or covalently, to the surface of the desired substrate. Polymer brushes can be covalently grafted on a particular substrate by using a "grafting-to" or a "grafting-from" approach as introduced in Chapter 1. Briefly, in a "grafting-to" approach the polymer is already formed and is then covalently attached to the surface of the substrate, generally by using a reactive group often located on the chain terminus. Conversely, for a "grafting-from" approach the polymer is "grown" up from the substrate, allowing for more precise control over the polymer brush structure and density. In addition, controlled layer thickness and/or chain molecular weights can be obtained by using reversible-deactivation radical polymerization (RDRP), also known as controlled radical polymerization (CRP) (Matyjaszewski, 2012). Different studies have used RDRP approach for the synthesis of polymer brushes including surface-confined atom transfer radical polymerization (SC-ATRP) (Yoon et al., 2008), supplemental activators and reducing agents (SARA-ATRP) (Mendonça et al., 2011), electrochemical ATRP (eATRP) (Matyjaszewski et al., 2001),

initiators for continuous activator regeneration (ICAR), and reversible addition-fragmentation chain-transfer polymerization (RAFT) (Bouchekif and Narain, 2007). Characterization techniques of grafted polymers are important to determine grafting density, thickness, and evaluate responses to environmental changes such as light, pH, temperature, ionic strength, etc. Many SRP are charge-based and thus are responsive only in a liquid environment. Therefore, novel characterization techniques are required to evaluate the properties of tethered SRP brushes under different *in-situ* conditions.

Amino (meth)acrylates polymers have been well-studied because of their medical and biological application potential. These are weak base SRPs that are triggered by pH changes due to their capability to accept and donate protons and hence extend or collapse under acidic or basic conditions respectively. The most studied methacrylate polymer is poly(2-(dimethylamino)ethyl methacrylate) (PDMAEMA), which has been characterized as a pH- and thermo-responsive polymer with a pKa of 7.0-7.3 (Li et al., 2011) and a lower critical solution temperature (LCST) in the range of 32-52 °C, depending on the molecular weight and polydispersity (Munoz-Bonilla et al., 2007). Poly(2-dimethylamino) ethyl acrylate (PDEAEMA) is similar to PDMAEMA in that it contains a tertiary amine group on the pendant group. PDEAEMA is a weak (basic) polyelectrolyte and has been characterized as a pH-sensitive polymer with a pKa of 7.3 (Liu et al., 2002). Other (meth)acrylate polymers have been studied as potential pH- or thermo-responsive materials, including poly(2-(dimethyl amino)ethyl acrylate) (PDMAEA), poly(3-(dimethylamino)propyl methacrylate) (PDMAPMA), poly(tert-(butylamino)ethyl methacrylate) (PTBAEMA), and others (van de Wetering et al., 1999). The pH-responsiveness of these materials is caused by the protonation or deprotonation of the

pendant tertiary amine. When tethered to a surface, the responsive behaviors of these polymers have been evaluated *in-situ* using a variety of techniques including ellipsometry (Xue et al., 2011; Bittrich et al., 2012), neutron reflectivity (Sanjuan et al., 2007), atomic force microscopy (AFM) (Sui et al., 2011), gravimetric methods (Chang et al., 2011), and ATR-FTIR (Rakhmatullina et al., 2007; Rowe-Konopacki and Boyes, 2007; Sanjuan et al., 2007; Bittrich et al., 2012). Other techniques have been used to evaluate the pH and thermal response when polymeric chains are dispersed in solution. The pH and temperature response of amino (meth)acrylate polymers in solution has been studied using dynamic light scattering (DLS), turbidity measurements, and potentiometric methods, to determine for example the critical transition pH of these polymers where collapse/expansion occurs (Vamvakaki et al., 2004; Wu et al., 2005; Li et al., 2009). The focus of this chapter is to study the pH- and thermo-responsive properties of polymer brushes; however, these properties can change for free polymer chains in solution. In addition to the polymer chemistry, structural parameters, such as molecular weight and grafting density, affect the responsive behavior of these polymer brushes and they need to be considered when analyzing *in-situ* data.

In-situ characterization techniques have been used to examine the real pH- and thermo-responsiveness of SRP. For example, Hartmann and coworkers (Naini et al., 2011) studied the temperature-dependent response rates of PNIPAM brushes grafted on silica using a novel optical microscope configuration. They measured micro- to the millisecond response time scales by using a microfocused continuous wave laser beam to obtain a particular temperature value (between ambient to 48 °C) by adjusting the laser intensity. The thermal response of PNIPAM brushes was studied with *in-situ*

ellipsometry using a dedicated temperature-control cell by Kooij et al. (Kooij et al., 2012) and at different heating rates in pH buffer solution by Uhlmann and coworkers (Bittrich et al., 2012). In this chapter, the responsiveness of a series of surface-tethered amino (meth)acrylate polymer brushes was evaluated using *in-situ* spectroscopic ellipsometry with different pH phosphate buffer solutions (PBS) with constant ionic strength.

The goal of this chapter is to describe *in-situ* analytical methods and the *in-situ* behavior of stimuli responsive polymer brushes. In this work *in-situ* ellipsometry measurements were used to evaluate the response of polymer layer thickness and corresponding optical properties were evaluated at different pH and temperature conditions for four different polymers: PDEAEMA, PDMAEMA, PDMAEA and PTBAEMA. A general oscillator layer (GENOSC) model was used to determine the thickness and optical properties of the polymer brush. GENOSC layers have different oscillator options, such as Gaussian, Lorentz, Cody-Laurent, etc., and are Kramers-Kronig (K-K) consistent, where polymer light absorption is taken into consideration (Tompkins and McGahan, 1999); this feature is not possible with the Cauchy layer model that is traditionally used for polymer brushes thickness determination. The GENOSC model was recently utilized for determining polymer/nanoparticles ratio using an effective media approach (Schädel et al., 2012). However, evaluation of the pH- and/or thermo-responsive properties of polymer brushes with a GENOSC layer model have not been previously reported. Moreover, *in-situ* AFM was performed to examine topographical and phase segregation polymer morphology changes as a function of pH and temperature. Finally, contact angle measurements were conducted on each polymer brush characterized on this study. Understanding the behavior of amino(meth)acrylate

polymer brushes as a function of ionic strength, temperature, and pH will have significant impacts on the development of drug release mechanisms and gene delivery technologies based on these SRPs (van de Wetering et al., 1999).

4.3 Experimental section

4.3.1 Materials

The following chemicals were used as received from Aldrich: (3-aminopropyl)dimethylethoxysilane (99%), 2-bromoisobutyril bromide (BIB, 98%), 2-bromopropionyl bromide (BPB, 97%), 2,2'-bipyridine (> 99 %), 2-(diethylamino)ethyl methacrylate (DEAEMA, 99%), 2-(dimethylamino)ethyl methacrylate (DMAEMA, 98%), 2-(dimethylamino) ethyl acrylate (DMAEA, 98%), 2-(tert-butylamino)ethylmethacrylate (TBAEMA, 97%), tris(2-amino-ethyl)amine (97%), 1,1,4,7,10,10-hexamethyltriethylenetetramine (HMTETA, 97%), copper (I) bromide (CuBr, 98%), copper (II) bromide ($CuBr_2$, 99.999%), copper powder (Cu (0), 99%), formic acid (>95%), formaldehyde (37 wt%), sodium hydroxide (99.5%), dichloromethane (>99.5%), toluene (anhydrous), methanol (>99.8%), dimethyl sulfoxide (DMS, >99.9%), isopropyl alcohol (IPA, 70% aq), and water (HPLC grade). Hexamethylated tris(2-aminoethyl)amine (Me_6TREN) was prepared as described elsewhere (Queffelec et al., 2000). Silicon wafers (<1 1 1>, 1-5 Ohm, 475-575 micron thick) were purchased pre-diced (1x1.2 cm) from SiliQUEST International (Reno, NV). Certified pH phosphate buffer solutions (PBS) with pH values ranging from pH 2 to 12 were obtained and used as received from Fisher Scientific (Fisher Chemical); these PBS solutions had salt concentration of approximately 0.05 M and additional information regarding the ionic species present in these PBS is given in APPENDIX E (Section E.2,

Table E.1). In addition to the purchased, certified PBS, other pH solutions were prepared and used to assess pH responsiveness of the polymer brushes: pH 2 solution (hydrochloric acid and potassium chloride), pH 7 solution (sodium phosphate and potassium phosphate) and pH 10 solution (sodium bicarbonate and carbonate). In addition, the different polymers characterized in this work have different pKa dissociation constants. Table 4.1 shows the pKa of different polyelectrolytes including the ones studied in this work.

Table 4.1 pKa of different polyelectrolytes in solution

Material	pKa	Reference
Poly(acrylic acid)	4.7	Richter et al., 2008
poly (l-glutamic acid)	4.9	Zhou et al., 2008
PDMAEMA	8.44	Sutani et al., 2002
PDMAEA	7.5	Laurienzo et al., 2006
PDEAEMA	7-7.3	Amalvy et al.,2004

4.3.2 Synthesis and surface modification of silicon substrates

4.3.2.1 Monolayer preparation

Silicon (Si) wafers were cleaned using a two-step procedure. First, Si wafers were sonicated in clean isopropyl alcohol/water solution (IPA, 70% v/v) two times for 30 min each cycle. Next, the Si wafers were immersed in a piranha solution (70/30 v/v H_2SO_4 (30%)/H_2O_2 (35%)) for 1 h. (Caution!! Piranha solution is highly reactive and appropriate personal protective equipment must be used at all times.) The Si wafers were

then rinsed three times in clean water, placed in clean water for 30 min, and then dried with N_2. Silanization was carried out by immersing the wafers in a 10 mM solution of 3-aminopropyldimethylethoxysilane in anhydrous toluene for 24 h. The terminal primary amine on the SAM will be used to attach the initiator for polymerization. After the SAM deposition, sonication was performed at least three times in clean toluene to remove any physisorbed material. The amine-functionalized Si wafers (Si-NH_2) wafers were then rinsed in ethanol and dried with N_2.

4.3.2.2 Initiator immobilization.

Initiated surfaces were prepared by immersing the Si-NH_2 wafers in 3% v/v toluene solutions of either the BPB or BIB initiator. This reaction was carried out overnight. The initiated surfaces (Si-Br) were then rinsed and sonicated at least three times with clean toluene, dried with a N_2 stream, and placed under an inert atmosphere to await polymerization.

4.3.2.3 Surface-confined ATRP for Poly-(amino (meth) acrylates).

Four different amino(meth)acrylate homopolymers—DMAEMA, DEAEMA, DMAEA, and TBAEMA—were grown from these bromo-initiated substrates by ATRP under an inert N_2 atmosphere. Details of the DMAEMA ATRP polymerization are provided as an example. The same polymerization steps were followed for the the synthesis of other homopolymers. Briefly, DMAEA (3 mL), Me_6TREN (22.8 mg), CuCl (9.7 mg) and $CuCl_2$ (1.4 mg) were added to a flask and purged with nitrogen for about 2 h. Then, five freeze-pump-thaw cycles were used to degas the flask. The degased monomer/ligand/catalyst solution was added to a flask containing the Si-Br substrate and

the reaction was allowed to proceed for 72 h. This reaction was carried out using bulk monomer solution with a molar ratio of 200/10/10/1 of DMAEA/CuCl/$CuCl_2$/Me_6Tren. Other reaction times, temperatures and solvents were utilized for the different surface-confined polymerizations on this work, and are depicted in APPENDIX E, Section E.3.

4.3.3 Characterization techniques

4.3.3.1 Ellipsometry measurements: Dry and *in-situ* characterization.

A Woolam-M spectroscopic ellipsometer with a 220–1000 nm wavelength range was used with a fixed 70° angle liquid cell for data collection. Data were collected on a custom-build liquid cell able to resist abrupt changes in pH and temperature. A peristaltic pump was used to control volumetric flow rates and switch different pH solutions. Additionally, pH values were checked before and after each experiment, using a pH-meter outside the cell, to ensure constant solution pH values. Proper adjustments, such as liquid-cell windows effects, were considered for variations on data acquisition and correct GENOSC modeling. Data presented in this work represents the average of at least two measurements on each polymer-brush sample, unless otherwise specified. A general oscillator model (GENOSC) was used for polymer layer modeling (Schädel et al., 2012) in order to determine the precise layer thickness and optical constants, and guarantee Kramers-Kronig (K-K) consistency. The same GENOSC model was used to characterize the swelling behavior of the polymer brushes using CompletEASE software (v.4.68, J.A. Woollam Co., Inc.). The software also allowed for the thermal variations and windows effects to be accounted for data fitting. Gaussian oscillator(s) were used for fitting polymer brush thickness, accounting for amplitude, broadening, and energy

position as the main fitting parameters as recommended elsewhere(Tompkins and McGahan, 1999; Hinrichs et al., 2008) (Fujiwara, 2007).

4.3.3.2 AFM: *In-situ* measurements

To obtain the *in situ* morphology of the tethered polymer brushes, a Dimension Icon AFM (Veeco-Bruker, Santa Barbara, CA) with Scanasyst model was used. Scanasyst-fluid nitride tips (T: 0.5-0.7 μm, a frequency of 120-180 KHz; K=0.7 N/m) were utilized for the *in-situ* measurements with different pH solutions inside a fluid cell. Sample preparation consisted of depositing a drop of PBS solution on top of the Si wafer. Then, a drop of the same pH solution was deposited on the nitride tip while aligning the instrument. Carefully, both drops were put in contact as the cantilever head was lowered to the polymer brush surface. Once the drops were in contact, alignment of the scanning head was checked, and a calibration mark (scratch) was located and scanned to determine the height of the polymer brush with respect to the Si surface. Topography and phase segregation of the polymer brushes was also observed as the pH of the surrounding solution was changed.

4.4 Results and discussion

PDMAEMA, PDEAEMA, PDMAEA, and PTBAEMA were polymerized from Si substrates were characterized to demonstrate their pH and temperature responsiveness. Figure 4.1 shows the chemical structure of the corresponding monomers. Three of these polymers have tertiary amine pendant groups (PDMAEMA, PDMAEA and PDEAEMA) and the fourth polymer contains a secondary amine pendant group (PTBAEMA). The secondary amines can hydrogen bond, while the tertiary amine cannot. Conversely, the

tertiary amine is able to protonate more readily. These chemical differences are expected to alter intramolecular bonding, transition temperatrures, and charge, and these will be moderated by the local pH and temperature. These polymer brushes were analyzed using *in-situ* ellipsometry, for pH changes, and *in-situ* AFM while examining their behavior at different pH and temperature conditionss.

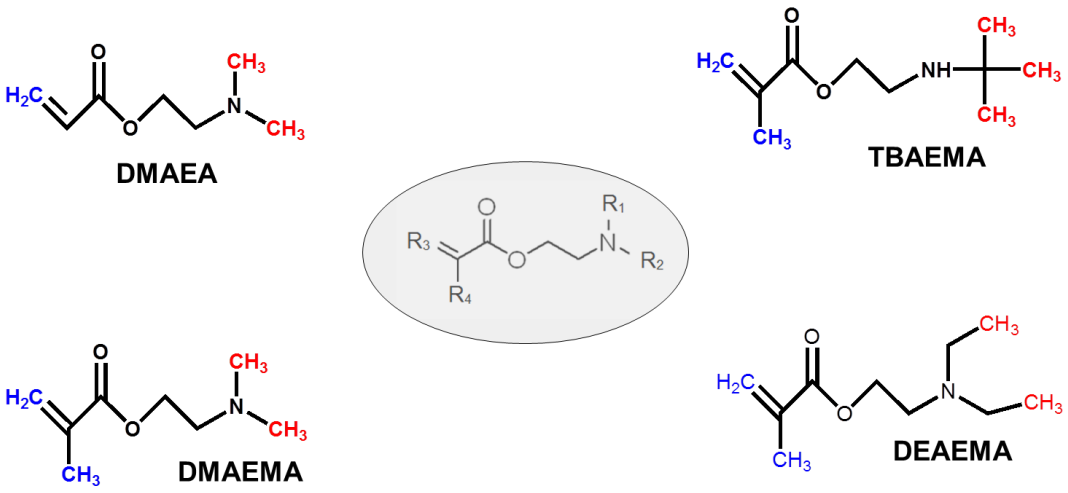

Figure 4.1 Amino(meth)acrylate monomer structures

Homopolymer brushes were grown using surface-confined ATRP from Si and the pH- and thermo-responsiveness evaluated.

4.4.1 Analysis of the pH response of polymer brushes

The pH response of each polymer brush grafted on Si substrates was characterized by thickness and the swelling ratio percentage. The swelling ratio percentage is calculated using the formula

$$Swelling\ ratio(\%) = \left(\frac{Wet\ thickness - Dry\ thickness}{Dry\ thickness}\right) * 100 \qquad (4.1)$$

where *wet thickness* indicates the thickness of the solvated polymer brush and *dry thickness* represents the polymer brush thickness obtained under non-solvated, ambient conditions. Each polymer was evaluated using the GENOSC model as a function of pH. All the results shown in this chapter were conducted at ambient temperature (~ 23 °C), unless otherwise specified.

4.4.2 Poly(2-dimethylamino)ethyl methacrylate (PDMAEMA)

Poly((2-dimethylamino)methyl acrylate) (PDMAEMA) is a well-known polymer that responds to pH and temperature fluctuations (Ayres et al., 2007; Rowe-Konopacki and Boyes, 2007). Figure 4.2 shows the swelling ratio results obtained for PDMAEMA as a function of time as pH was changed from 4 to 6 three times at ambient temperature. Interestingly, PDMAEMA , a polymer with a pKa value ranging between 7 and 7.3, demonstrated a swelling ratio increase as pH increased. These experiments are consistent with previous findings that demonstrated the pH-sensitive behavior of PDMAEMA in solution (Zhang et al., 2007; Zhou et al., 2007; Chen et al., 2008); however, results contradict earlier reports where thickness decreased as pH increased due to the protonation occurring in the polymer backbone. For example, PDMAEMA/PEG mixed polymers were studied at pH 9.2 showing an average hydrodynamic diameter of 214 nm, expanding at a lower pH ~ 5 to 272 nm (Chen et al., 2008). Zhang et al. performed DLS experiments on PDMAEMA as it was grafted on the surface of styrene, results in a thickness decrease from 124 to 65 nm. Additional experiments were performed using NaCl, a salt that influence the hydration properties of the polymer chains (Zhang et al., 2007). Swelling and collapse transitions have also been explored as different electrolytes interacts with PDMAEMA as grafted on the surface of Au-coated Si wafers. However, it

was demonstrated that a low concentrations of electrolytes does not affect the swelling ratio of PDMAEMA using electrochemical impedance methods (Zhou et al., 2007). It is expected that at low pH values the PDMAEMA chains become protonated and swelling occurs. As the pH increases, the PDMAEMA chains will deprotonate and the chains collapse. In the present study, while each pH PBS used in the *in-situ* ellipsometry experiments had the same 0.05 M ionic strength, each PBS contained different salt species. Therefore, it is theorized that the salt species used at pH 4 and pH 6 affected the swelling behavior of PDMAEMA, due to the association-dissociation on the polymer brush depends on pH, salt types and concentration (Zhou et al., 2007). PBS buffer solutions were selected due to their constant salt concentration of 0.05 at pH value. Previous studies have confirmed the interesting results obtained in this work, where a polymer brush expands at small salt concentrations as a result of electrostatic interactions (Biesalski et al., 2002). Moreover, 'weak polyelectrolytes' such as PDMAEMA grafted on a planar surface are difficult to understand due to the need of having dense polymer layers on well-defined surfaces. In an effort to better understand interactions of PBS buffer solutions with the different amino methacrylates polymers, contact angle measurements and AFM imaging experiments were conducted.

Water static contact angle(WCA) measurements for PDMAEMA resulted in 77.8° ± 13.7°. This value is above the reported on literature for PDMAEMA on Si/SiO2 surface that was 48° ± 3° (Yu et al., 2003). In fact, advancing and receding contact angles for PDMAEMA can be as low as 35° and 10°, respectively (Sha et al.,2000). Thus, a hydrophilic surface is expected; however, results obtained in this work showed a much larger WCA. In order to see the effect of uncoated areas, a Si-SAM wafer was

examined and results showed a WCA of 77.8° ± 13.7°. Thus, it is strongly believed that PDMAEMA is not homogeneously distributed over the surface of the Si-SAM wafer. A table with different WCA for the samples characterized in this work is shown in Table E.3 (APPENDIX E).

Over the course of different pH 4-6 cycles, the swelling ratio at all pH values was very consistent. However, after the second full cycle, the swelling ratio at pH 4 seems to increase as compared from the first two cycles. These unforeseen results were demonstrated to be an effect on salt deposition on the recirculating tubing; thus, pH values were slightly affected to the point that the polymer swell/contract. To further examine these results, a different experiment was conducted to demonstrate the effects of slight pH changes on the swelling behavior of PDMAEMA. APPENDIX E provides a study on the influence of switching pH solutions *in-situ,* demonstrating the sensitivity of the grafted PDMAEMA brushes to slight pH changes.

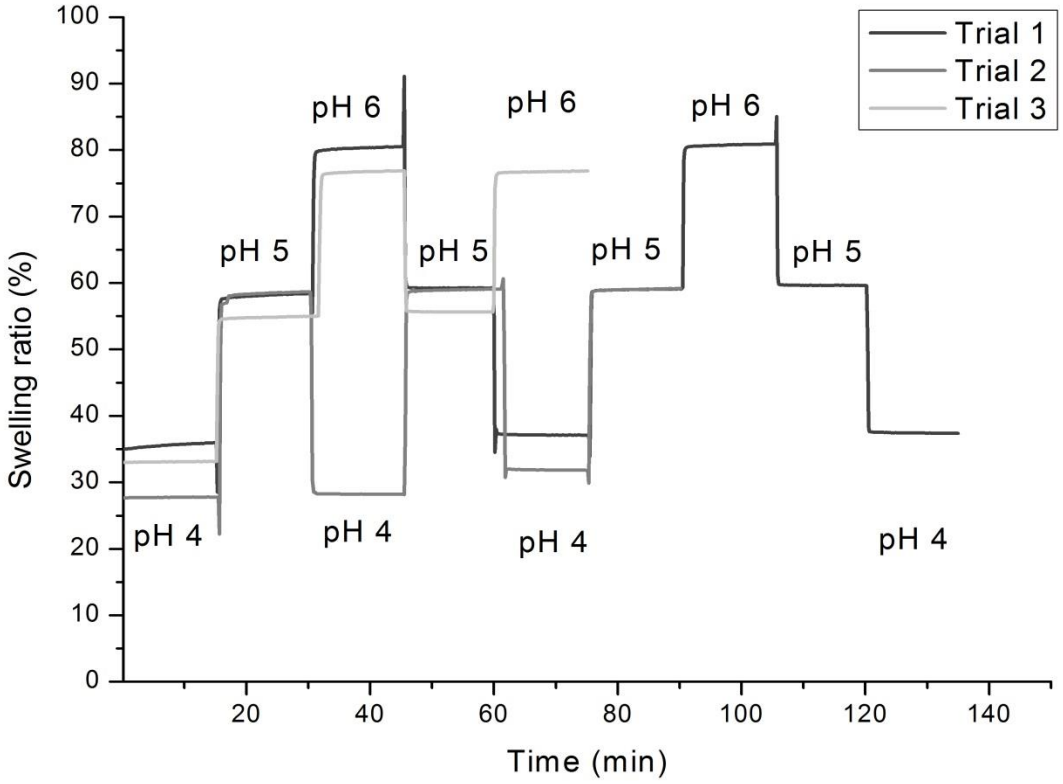

Figure 4.2 Swelling ratio of a PDMAEMA polymer brush as a function of time with three cycles of shifting pH from 4 to 6.

The effect of ionic species, from PBS solutions, on protonation/deprotonation on PDMAEMA was further evaluated using the custom pH solutions described in APPENDIX E. Again, *in-situ* ellipsometry was used and the brush thickness was evaluated using the novel GENOSC model. This experiment was performed to evaluate the consistency of the previous results using the exact same sample. Figure 4.3 shows the swelling ratio of PDMAEMA as pH is changed from 2, to 4, to 7, and finally to 10. At a very low pH (2), the PDMAEMA brushes were fully protonated and extended, showing a large thickness as expected, and as reported in the literature. As the pH was switched to 4, the polymer brushes deprotonated, and the thickness decreased. The polymer brush

swelled when the pH was increased to 7, and then to 10. These findings fit well with the experimental data shown in Figure 4.2 where only pH 4 and 6 were examined and confirm that the PBS directly affects the deprotonating/protonation of the polymer brushes grafted on Si substrates. In addition to proton accept/donor changes, electrostatic interactions of the polymer chain and counterions need to be considered to fully understand the behavior and changes of the polymer brush at different pH conditions (Rahane et al., 2008). One goal of this work is directed toward obtaining a general oscillator model that is capable of characterizing the absorption effects of polymer brushes as they are grafted on Si substrates, resulting in the in-situ characterization of these materials. Thus, future studies on which different pH solutions are used are recommended to compare salt-types effects on the pH-responsiveness properties of these polymers.

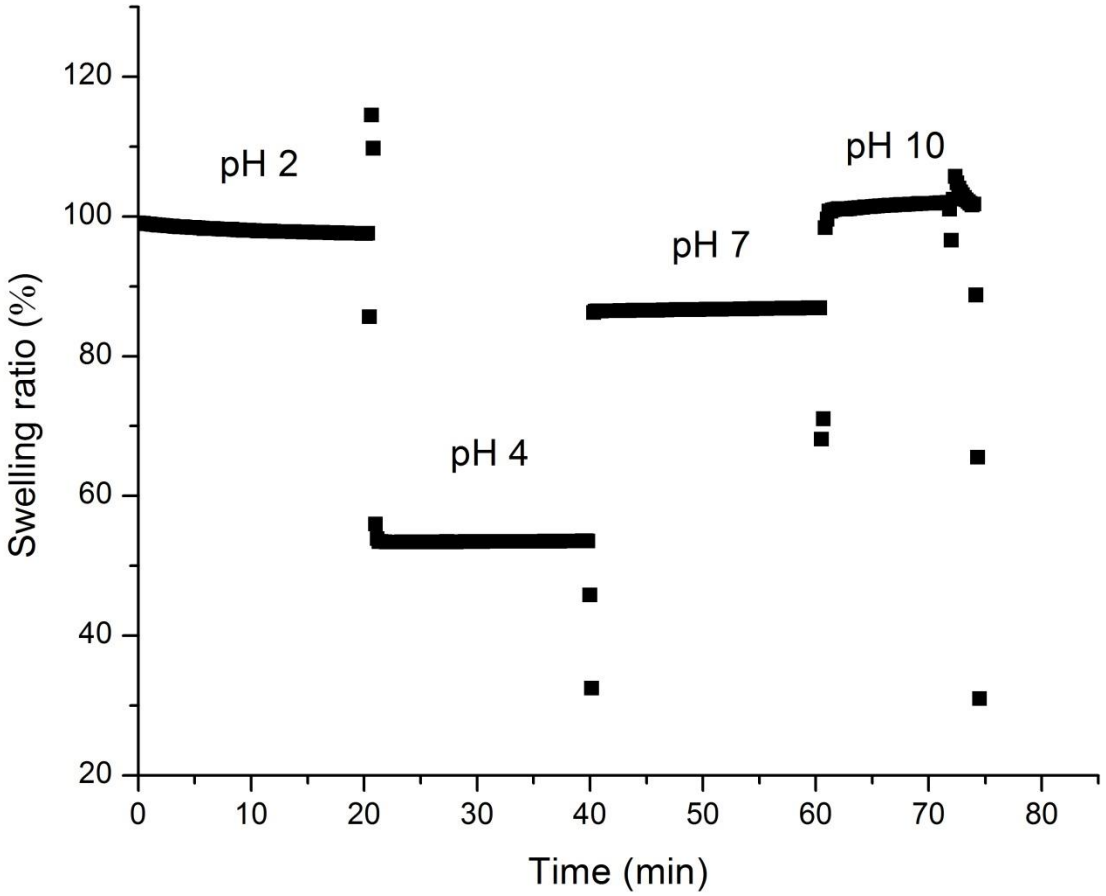

Figure 4.3 PDMAEMA swelling ratio as a function of time obtained for different PBS solutions at different pH values.

PDMAEMA morphology was examined using AFM height and phase images at different pH conditions. Figure 4.4(a-c) shows representative images of the PDMAEMA polymer brush and its configurations at different pH conditions. As the pH increased, swelling behavior was observed, matching ellipsometry measurements and data fitting. High swelling areas and non-uniform polymer zones were observed at the different pH values. Certain "globular" swelling configurations were observed at each pH condition (Figure 4.4), demonstrating the partial effect of swelling as increasing pH. Particle size analysis was used to determine the height of the polymer brushes at different pH

conditions. This analysis was performed to obtain an average height which could be later compared with ellipsometry characterization. Using AFM, selected areas of 10 micrometers that contained the polymer brush were analyzed for height determination. Polymer brushes were not homogeneous in size with high variability in small areas observed. Figure 4.4(d) shows an example of a selected area for particle height determination at a pH 10 for PDMAEMA. AFM swelling ratios were calculated using equation 1, however, dry thickness and wet thickness were obtained from the different AFM measurements. Results showed swelling ratios of 27.5%, 73.1%, and 95% for pH 4, 7, and 10, respectively. The average height obtained for each picture was used for these calculations; variability was high for all the samples. As discussed, AFM measurements provide a second option for the analysis of change in swelling ratio but reveal great variability within the small sample areas. AFM correlates well with ellipsometry data, showing an increase in swelling ratio of PDMAEMA as pH increases.

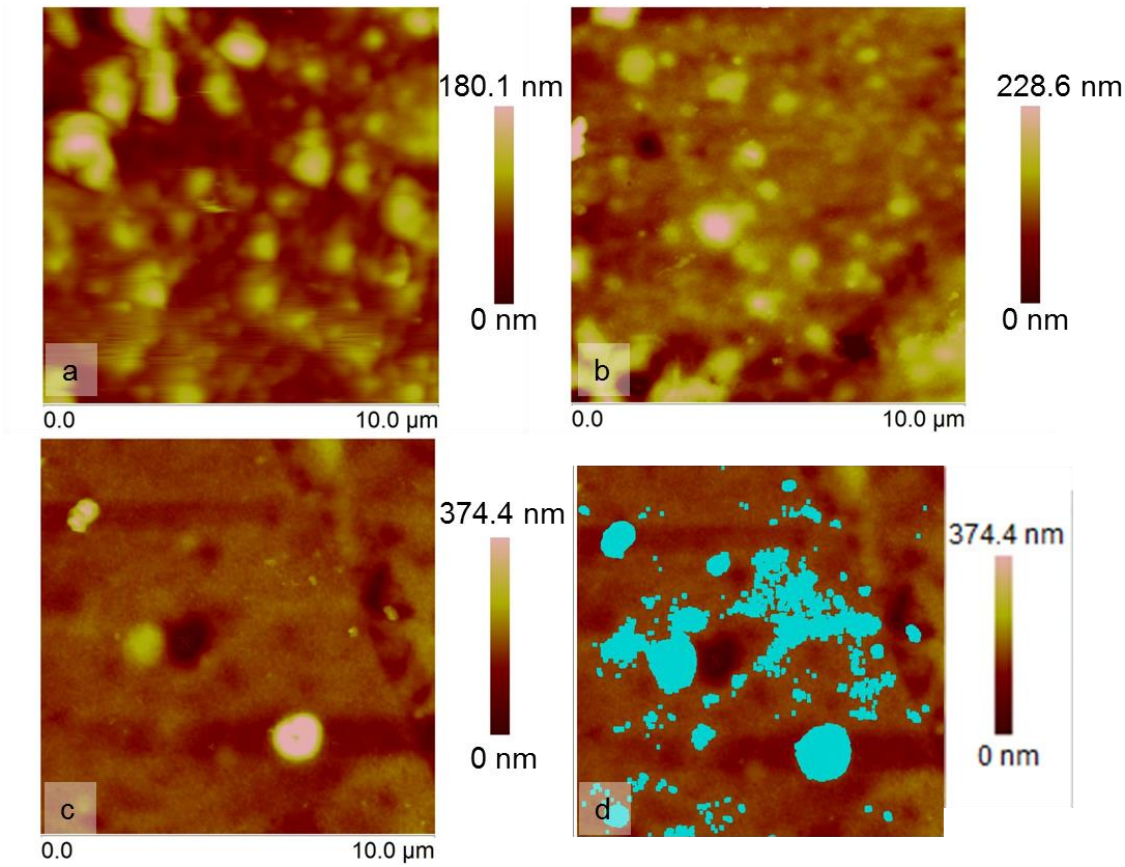

Figure 4.4 Height AFM images for PDMAEMA

a) pH 4, b) pH 7, c) pH 10, and d) particle height calculations based on data selection.

4.4.3 Poly(2-dimethylamino-ethyl) acrylate (PDMAEA)

Poly(2-dimethylamino-ethyl) acrylate (PDMAEA) has been characterized as a pH responsive polymer. The pKa of the monomer is 8.3 (Kim et al., 2012) with a pKa in solution ranging from 8.1-8.6 (Suchao-in et al., 2009; Kim et al., 2012). At pH values below the pKa, this polymer becomes protonated, and the positive charges repel each other due to the internal electrostatic interactions, producing a swelling behavior of the polymer chains. In this section, a discussion of PDMAEA grafted on silicon substrates is presented. The experiments were conducted at different pH values, demonstrating the stability of these polymer brushes while switching pH. Different pH PBS solutions, 4, 6,

7, 8, and 10, were evaluated to demonstrate any particular change on the polymer brush as a function of pH. As expected, the polymer brush was fully expanded below the pKa and high swelling ratios were detected by ellipsometry, shown in Figure 4.5. These results show a deprotonation effect occuring at pH values above 7, resulting in collapsed polymer chains on the Si substrates. These values are particularly important due to promising applications of PDMAEA in drug delivery applications. For example, Troung et al. demonstrated the release of SiRNA and DNA from PDMAEA as pH was changed. Moreover, PDMAEA is a nontoxic polymer that undergoes degradation and does not alter cellular behavior, making it attractive for drug delivery applications (Truong et al., 2011a; Truong et al., 2011b).

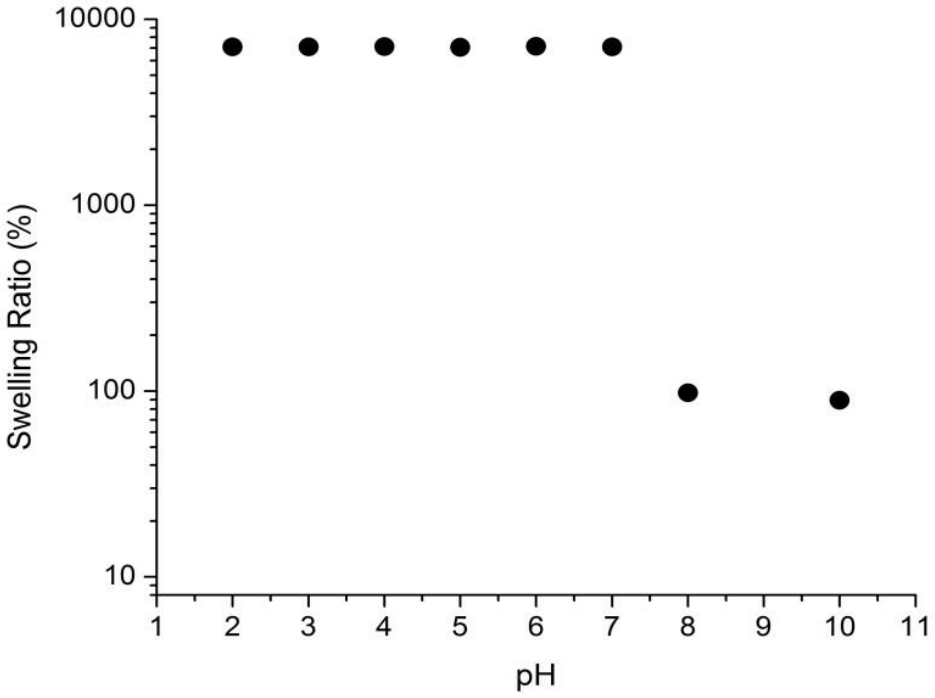

Figure 4.5 Swelling ratio of PDMAEA as a function of pH.

PDMAEA optical properties were obtained using the GENOSC layer characterization model presented and discussed previously. The optical properties of PDMAEA-grafted polymer on the Si wafer changed as a response to pH. A low refractive index was obtained below the critical pH (~8) where the polymer was fully extended and protonated, whereas a high refractive index was obtained above the critical pH. GENOSC layers provide the advantage of considering absorbing regions of the polymer films, allowing for refractive index model calculations as a function of pH transitions. Results for the analyzed optical properties, refractive index, and the extinction coefficient are shown in Figure 4.6. Absorption peaks occurring below 600 nm wavelength were observed, improving the model as compared to Cauchy layer calculations. Similarly, PBS solutions become absorbing at wavenumbers below 315 nm. Data were fitted on wavenumbers above 315 nm to avoid errors when fitting the data.

PDMAEA morphology was examined using *in-situ* AFM at different pH values. A pH of 4 was chosen because this value is below the pKa of DMAEA monomer and in the expanded region as shown by ellipsometry results. A drop of pH 10 PBS buffer solution was deposited on PDMAEA-Si wafers to analyze any change in morphology. Figure 4.7 shows the AFM topography image results for different pH conditions. Topological changes were observed in the sample as pH was switched. At pH 10, the polymer brush was in a collapsed state repelling the positive charges; however, the polymer is in an extended configuration at pH 4. PDMAEA configurational state at pH 10 can also be observed on peak force error images, as shown in Figure 4.7 (c,d), where the polymer seems to be oriented in different directions on the surface of the Si wafer. Polymer brush configuration on the Si wafers and grafting density were not consistent

despite the interesting results shown on topological changes at different pH values. AFM confirms the structural changes reported previously by ellipsometry measurements, becoming a potential tool for future examination of surface-tethered polymers.

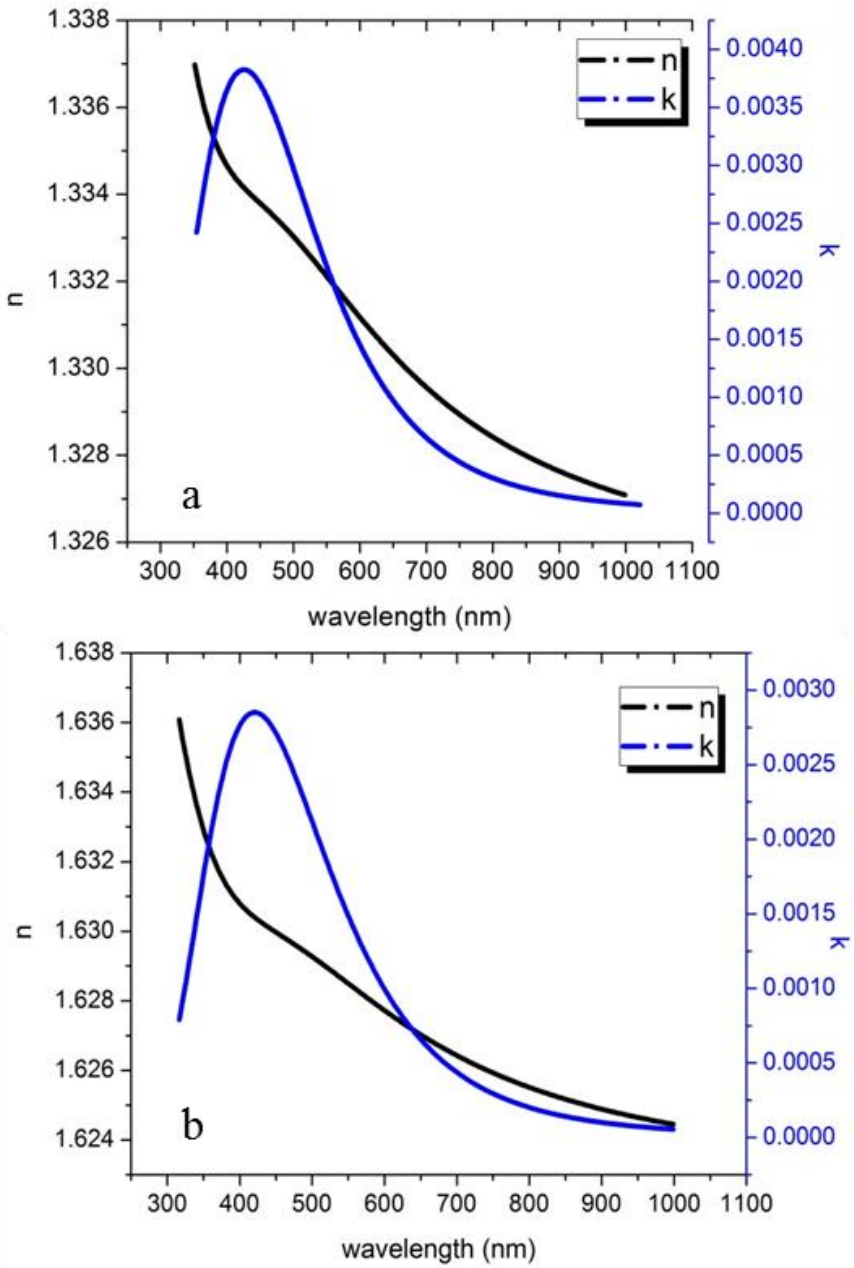

Figure 4.6 Optical properties (n,k) of PDMAEA at pH values a) below and b) above the critical pH

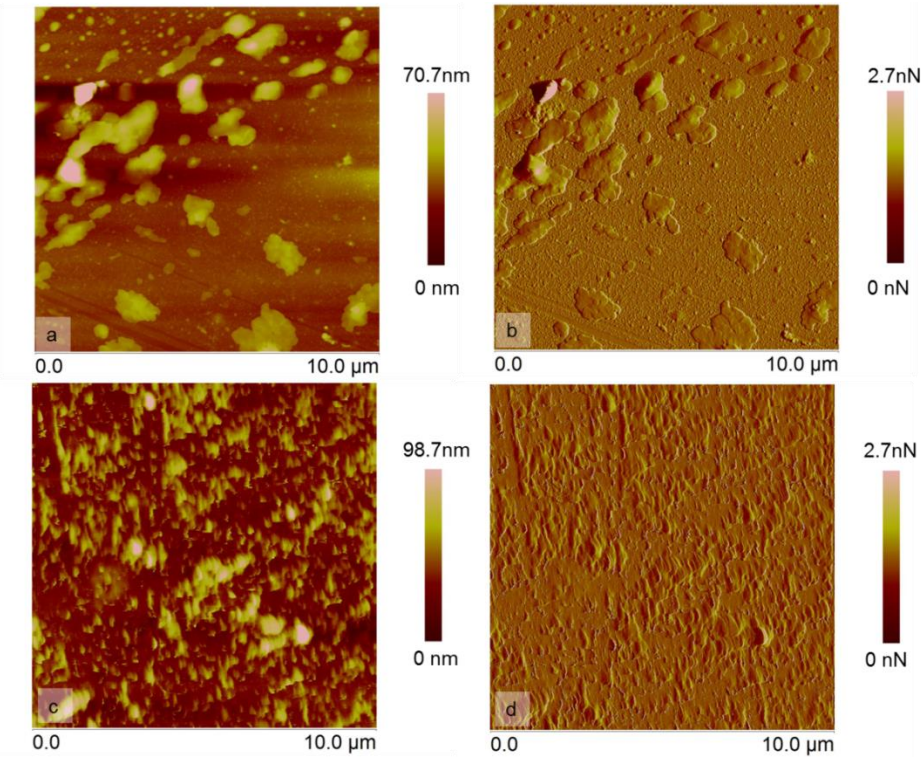

Figure 4.7 Height and peak force error AFM images of PDMAEA at a,b) pH 4 and c,d) pH 10, respectively

4.4.4 Poly(2-diethylamino-ethyl) methacrylate (PDEAEMA)

Ellipsometry results demonstrating the swelling behavior of PDEAEMA brushes are shown in Figure 4.8. In this particular case, swelling ratio increased rapidly as a response to change in pH and was constant, but different, for each pH. Conversely, results in literature indicate a collapse of PDEAEMA polymer brushes, comparable with PDMAEMA, as pH is increased. For example, Sun et al. demonstrated extended polymer chains at low pH values due to the protonation occurring in their internal structure (Sun et al., 2010). Similarly, Liu et al. confirmed that at pH values greater than 8, PDEAEMA chains becomes hydrophobic due to the deprotonation occurring on the amine groups (Liu et al., 2008). In contrast, the results of this work at high pH (10) showed an increase

in thickness with respect to acidic pH values, revealing additional features that have not been previously reported. This particular effect may be a result of salts diffusing through the different polymer brushes and producing an effect on the thickness of the polymer brush. This particular response could be exploited for controlling the release and or capture of physisorbed materials trapped within the polymer brush when concentration/salts present in solution are known.

Different applications can be obtained by using PDEAEMA with PBS buffer solution. For instance, nanoparticles dispersion and aggregation effects could be exploited with PDEAEMA surface modified materials, and carbon-walled nanotubes surface-modified with PDEAEMA show aggregation as the pH is increased at values above 7 (Li et al., 2005). Results from this work contrast this theory, and could lead to better dispersion of nanotubes in basic pH solutions when phosphate buffer solutions are present. Thus, a plethora of applications at the nanoscale level could potentially be explored using SRPs like PDEAMEA, PDMAEMA and PDMAEA in PBS solutions.

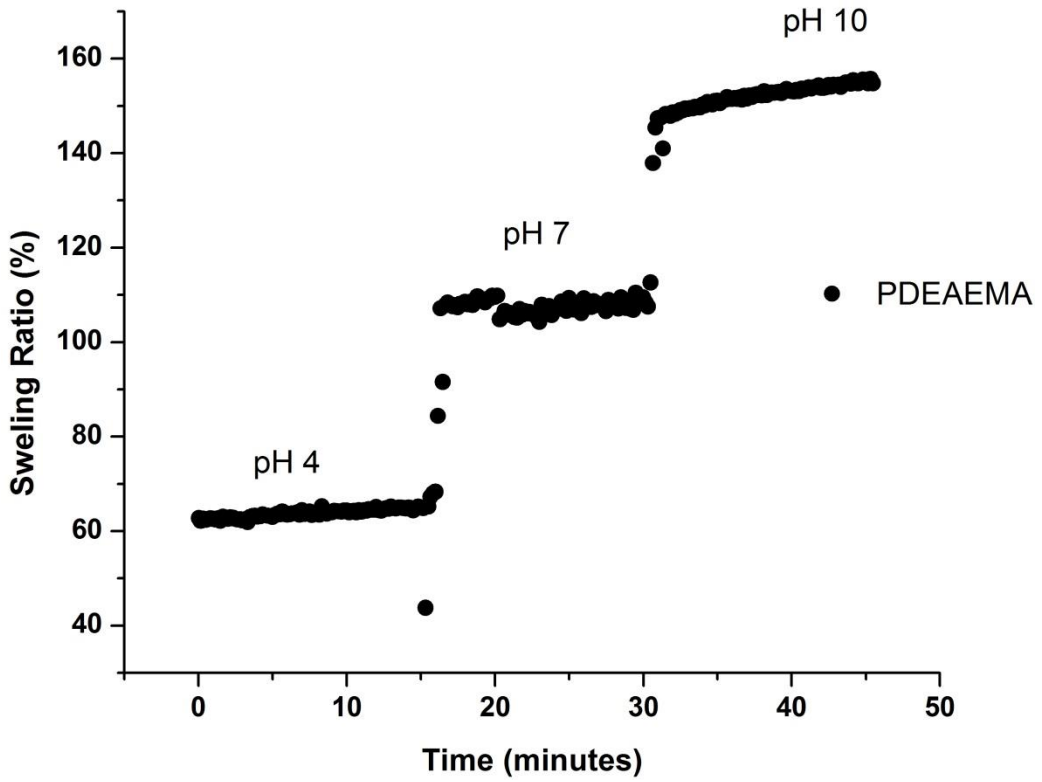

Figure 4.8 Swelling ratio (%) of PDEAEMA at different pH conditions and constant temperature (ambient)

The morphology of PDEAEMA was also analyzed by AFM *in-situ* characterization. Previous AFM studies on PDEAEMA have been reported in literature for dry-state conditions, but to the author's knowledge no swollen/hydrated AFM characterization has been carried out on this polymer (Feng et al., 2009). In this work, the *in-situ* characterization while the polymer is tethered to a surface and the pH changes is presented, analyzed, and discussed. A comparison of PDEAMEA in dry and hydrated state is shown in Figure 4.9. PDEAMEA chains are hydrated (pH 4, 6) with respect to the dry height image. This result confirmed the protonation/deprotonation that takes place as the polymer is characterized *in-situ*. Interestingly, different morphological

features were observed as pH was switched from 4 to 6. This result can be associated with the different protonation effect that occurs when the polymer is in solution, confirming the response obtained by ellipsometry measurements.

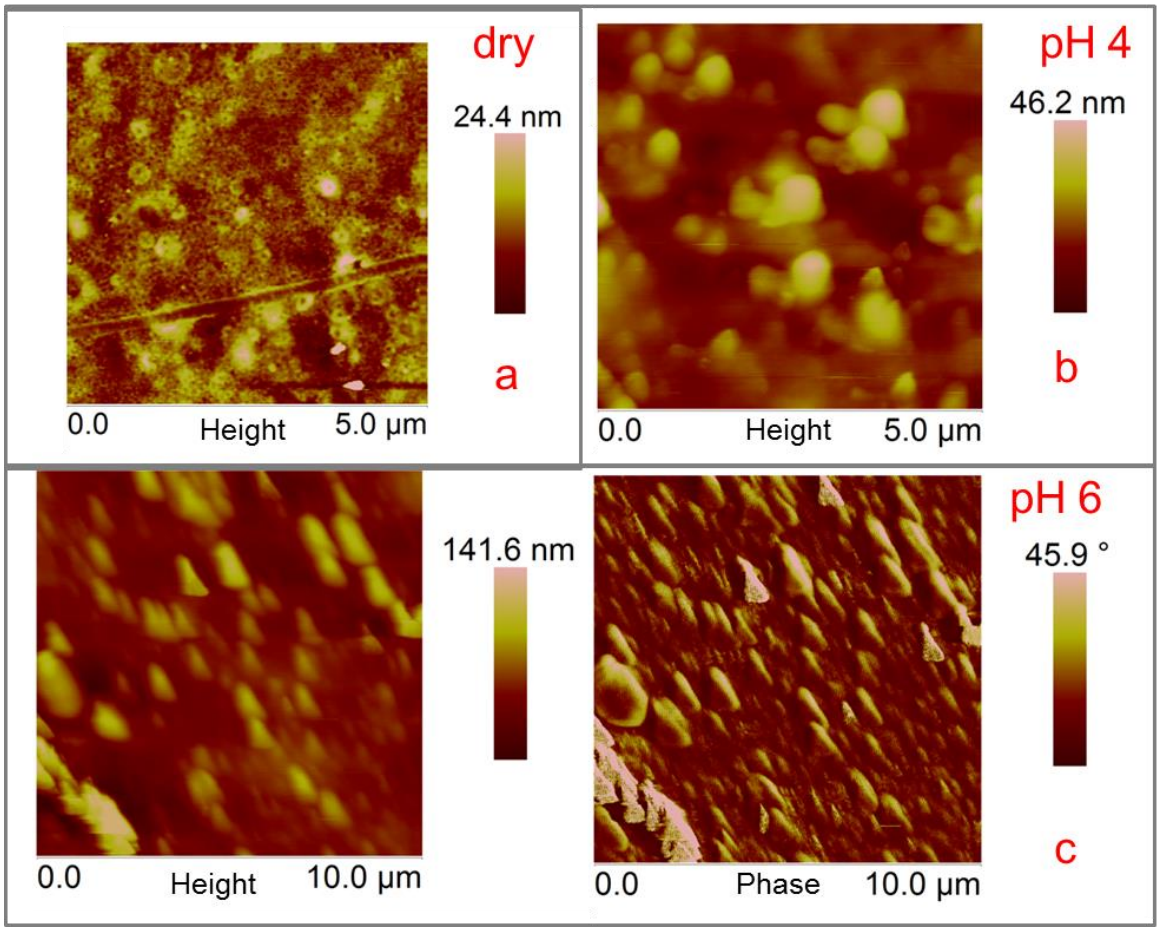

Figure 4.9 PDEAEMA phase and height images

a) dry conditions, b) pH of 4 and c) pH of 6

4.4.5 Poly (*tert*-butylamino) ethyl methacrylate (PTBAEMA)

The last polymer analyzed in this section is PTBAEMA, a polycationic polymer with secondary amines and a backbone structure comparable to PDMAEMA and PDEAEMA. However, PTBAEMA has a *tert*-butyl substituent group interfering with the

protonation effect and pH responsiveness of the material. PTBAEMA has been used as a biocide and for the formation of antifouling paint and coatings (Lenoir et al., 2005; Thomassin et al., 2007; Compagnoni et al., 2012). Recently, it was demonstrated that linear PTBAEMA dissolves in acidic solutions when the polymer is at low pH conditions. Thus, a necessary level of crosslinking was required create a stable polymer and produce a pH responsive material (Morse et al., 2012). This work examines PTBAEMA tethered to a Si surface in an effort to analyze any pH responsiveness under PBS solutions at different pH values. Figure 4.10 shows the response of PTBAEMA as a function of pH. PTBAEMA thickness on dry conditions (~6 nm) was relatively small as compared with the polymers previously analyzed. The responsiveness of this polymer brush was evaluated using a simplified Cauchy model (600-1000nm wavenumber range), due to poor fitting of optical constants for polymer films below 10 nm (Fujiwara, 2007). Results showed PTBAEMA protonates at acidic pH causing a swelling behavior with respect to the dry state. Once the polymer was fully protonated and the pH gradually increased, a controlled decrease in thickness was observed, resulting in a collapse of the polymer chains. These results demonstrate that PTBAEMA is a pH responsive polymer despite the bulky *tert*-butyl groups present on the backbone of the polymer, which is in agreement with the results shown in previous findings (Morse et al., 2012). Cauchy layer modeling verified the changes in thickness of PTBAEMA as a function of pH, though fitted optical properties for PTBAEMA at this low thickness were not possible. Analysis of thicker PTBAEMA brushes grafted on the surface of Si substrates are strongly recommended for future *in-situ* characterization since this polymer has potential uses as

an antimicrobial agent and/or resin combinations for dental fixtures (Paleari et al., 2011; Compagnoni et al., 2012; Marra et al., 2012).

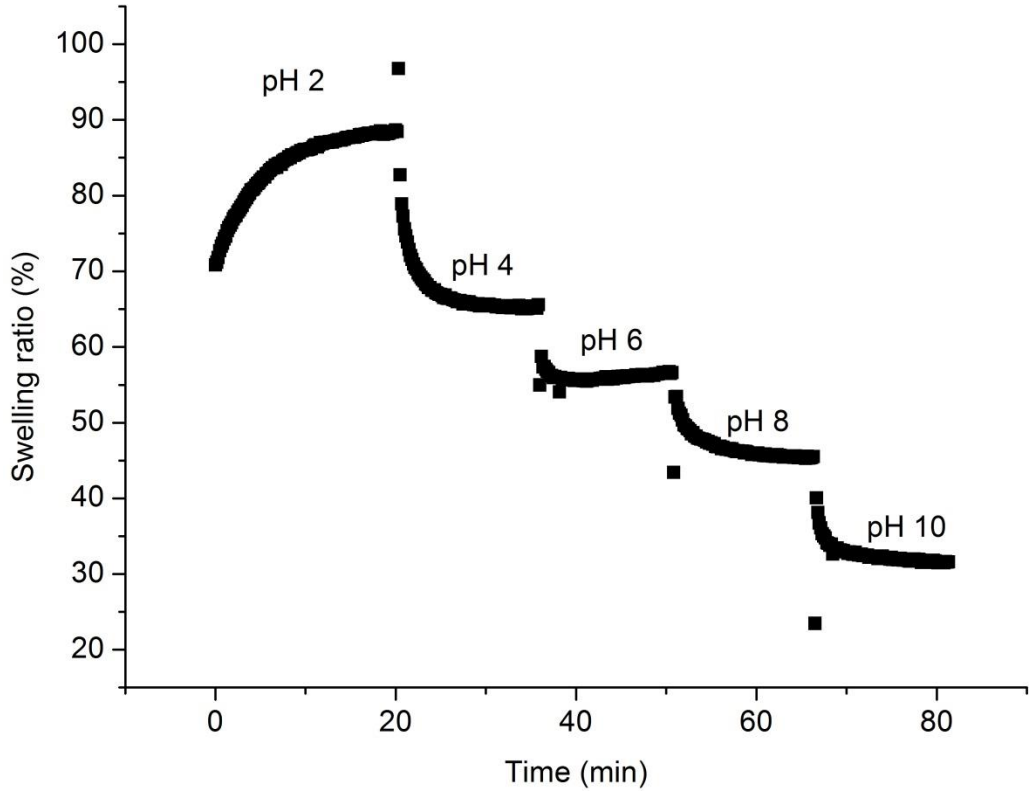

Figure 4.10 Temporal PTBAEMA thickness response to change in pH

AFM pictures were also collected for PTBAEMA (Figure 4.11) despite the small thickness. Similar morphology was obtained for the different pH conditions analyzed and as pH was switched compared with a dry state topography image. Due to the small difference in thickness and non-homogenous polymer brush presence on the PTBAEMA-Si surface, difficulties arose to calculate and estimate the pH responsiveness of this material. Further analysis was conducted on the surface of this material using a

temperature response liquid cell stage installed on the AFM instrument as discussed in the following section.

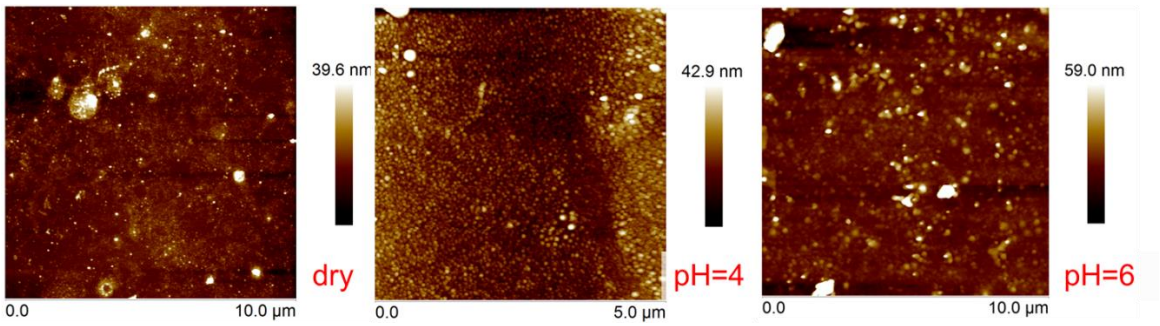

Figure 4.11 AFM height images of PTBAEMA at different dry and pH solutions

4.4.7 Summary: pH responsiveness and temperature evaluation of amino (meth)acrylate polymers grafted on Si surfaces

All four polymers demonstrated pH responsiveness, an expected result caused by the protonation that occurred in the amine groups of the polymer backbone. Moreover, PTBAEMA and PDMAEA followed the traditional and expected trend: as pH solution changes from acidic to basic conditions, chain collapse occurs as the polymer behavior changes from hydrophilic to hydrophobic. These results are confirmed with literature values and the different analysis previously discussed in this chapter. Conversely, PDEAEMA and PDMAEMA displayed different, unexpected swelling behavior as the pH was increased. Despite the fact that PDMAEMA demonstrated a collapse as pH increased from 2 to 4, it swelled as pH was increased from 4 to 7. These results invite further studies and investigations regarding the collapse observed for the polymer chains when PBS solutions are used. Other parameters to consider that could potentially affect

this behavior include grafting density and chain length, and need to be examined as possible triggers/causes.

In an effort to understand the temperature behavior of the different polymers analyzed in this work, AFM was run at different temperatures. Due to the non-homogeneity of the polymer brushes, these studies were performed using an average value for the observed height at the different pH conditions evaluated. Significant changes in thickness with respect to temperature could not be observed for the different polymers of this work (Figure 4.12). Thus, the temperature responsiveness of these materials was not detected with *in-situ* AFM measurements. Other studies such as neutron reflectivity and ellipsometry might be better tools due to their sensitivity with change in thicknesses. However, using these techniques requires the utilization of more complex models and equipment for the correct fitting of the polymer changes. Swelling ratios plots were not obtained due to the small difference obtained with respect to wet vs. swollen thickness. Nonetheless, **Error! Reference source not found.** (APPENDIX E) has different individual images on which temperature responses for each polymer can be observed.

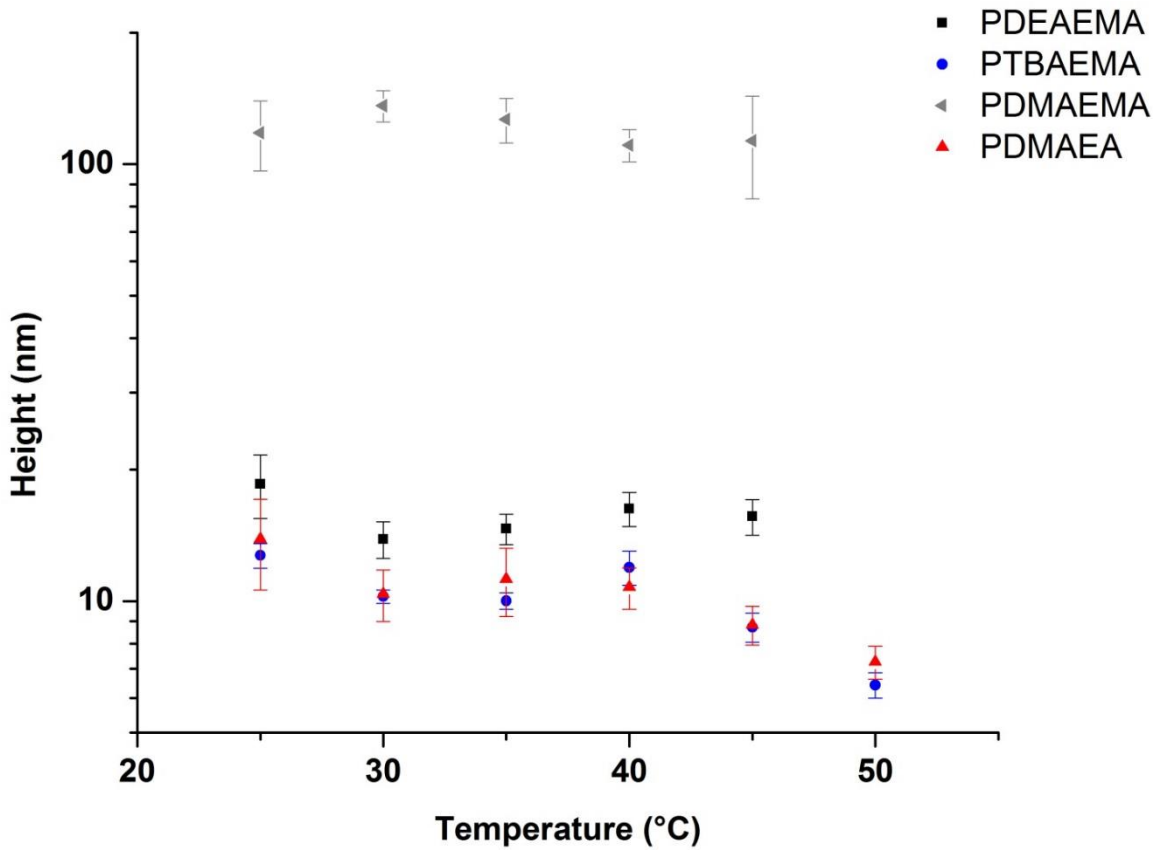

Figure 4.12 Thermo-responsive behavior for the different poly(meth)acrylate polymers evaluated ranging from 25 to 50 °C

4.5 Conclusions

Different amino(meth)acrylate polymer brushes grafted on silicon wafers have been evaluated as potential pH sensitive materials that could be used for drug delivery application, biomedical treatments, and/or biocides. A new model that includes a general oscillator layer (GENOSC) has been implemented and used to obtain the optical properties of these polymer brushes as pH changes. However, parameters such as non-uniform thicknesses, roughness, and low grafting density affected the results presented in this chapter. Despite these variances in morphology, PDMAEA and PTBAEMA have

been demonstrated to be pH responsive materials as expected due to the protonation of the amine groups at low pH values. PDEAEMA and PDMAEMA are affected in pH ranges from 4-10. In these conditions, the polymer chains swell rather than contract, producing the opposite effect reported in literature (swell as pH decreases). Thus, it is concluded that phosphate buffer solutions (PBS) interact with the polymer chains opening new applications and possible studies with salt interactions and charges within the polymer backbone. Temperature changes were observed but were not statistically conclusive at this point. Future work will analyze other types of polymers to confirm the results obtained by the GENOSC modeling in this work.

4.6 References

Alarcon, C. d. l. H., S. Pennadam and C. Alexander (2005). "Stimuli responsive polymers for biomedical applications." Chemical Society Reviews **34**(3):276-285.

Amalvy, J. I., E. J. Wanless, Y. Li, V. Michailidou, S. P. Armes and Y. Duccini (2004). "Synthesis and characterization of novel pH-responsive microgels based on tertiary amine methacrylates." Langmuir **20**(21): 8992-8999.

Ayres, N., S. G. Boyes and W. J. Brittain (2007). "Stimuli-Responsive Polyelectrolyte Polymer Brushes Prepared via Atom-Transfer Radical Polymerization." Langmuir **23**(1):182-189.

Azzaroni, O. (2012). "Polymer brushes here, there, and everywhere: Recent advances in their practical applications and emerging opportunities in multiple research fields." Journal of Polymer Science Part A: Polymer Chemistry **50**(16):3225-3258.

Bi, S., X. Wei, N. Li and Z. Lei (2008). "*In-situ* formation of Fe3O4 nanoparticles within the thermosensitive hairy hybrid particles." Materials Letters **62**(17-18):2963-2966.

Biesalski, M., D. Johannsmann and J. Ruhe (2002). "Synthesis and swelling behavior of a weak polyacid brush." Journal of Chemical Physics **117**: 4988-4994.

Bittrich, E., S. Burkert, M. Müller, K.-J. Eichhorn, M. Stamm and P. Uhlmann (2012). "Temperature-Sensitive Swelling of Poly(N-isopropylacrylamide) Brushes with Low Molecular Weight and Grafting Density." Langmuir **28**(7):3439-3448.

Bouchekif, H. and R. Narain (2007). "Reversible addition-fragmentation chain transfer polymerization of N-isopropylacrylamide: a comparison between a conventional and a fast initiator." J Phys Chem B **111**(38):11120-11126.

Chang, C., M. He, J. Zhou and L. Zhang (2011). "Swelling Behaviors of pH- and Salt-Responsive Cellulose-Based Hydrogels." Macromolecules **44**(6):1642-1648.

Chen, K., D. Liang, J. Tian, L. Shi and H. Zhao (2008). "*In-Situ* Polymerization at the Interfaces of Micelles: A "Grafting From" Method to Prepare Micelles with Mixed Coronal Chains." J. Phys. Chem. B **112**(40):12612-12617.

Compagnoni, M. A., A. C. Pero, S. M. M. Ramos, J. Marra, A. G. Paleari and L. S. Rodriguez (2012). "Antimicrobial activity and surface properties of an acrylic resin containing a biocide polymer." Gerodontology. doi: 10.1111/ger.12031

Ding, S. J., J. A. Floyd and K. B. Walters (2009). "Comparison of Surface Confined ATRP and SET-LRP Syntheses for a Series of Amino (Meth)acrylate Polymer Brushes on Silicon Substrates." Journal of Polymer Science Part A: Polymer Chemistry **47**(23):6552-6560.

Feng, C., L. Gu, D. Yang, J. Hu, G. Lu and X. Huang (2009). "Size-controllable gold nanoparticles stabilized by PDEAEMA-based double hydrophilic graft copolymer." Polymer **50**: 3990-3996.

Fujiwara, H. (2007) "Data Analysis", in Spectroscopic Ellipsometry: Principles and Applications, John Wiley & Sons, Ltd, Chichester, UK. doi: 10.1002/9780470060193.ch5.

Feng, C., L. Gu, D. Yang, J. Hu, G. Lu and X. Huang (2009). "Size-controllable gold nanoparticles stabilized by PDEAEMA-based double hydrophilic graft copolymer." Polymer **50**(16):3990-3996.

Gil, E. S. and S. M. Hudson (2004). "Stimuli-reponsive polymers and their bioconjugates." Progress in Polymer Science **29**(12):1173-1222.

Hinrichs, K., D. Aulich, N. Esser, S. Minko, I. Luzinov, O. Hoy, et al.M. Stamm (2008). In situ infrared ellipsometry for the analysis of stimuli-responsive polymer brushes, American Chemical Society.

Kikuchi, A. and T. Okano (2002). "Intelligent thermoresponsive polymeric stationary phases for aqueous chromatography of biological compounds." Progress in Polymer Science **27**(6):1165-1193.

Kim, B., C. N. Lam and B. D. Olsen (2012). "Nanopatterned Protein Films Directed by Ionic Complexation with Water-Soluble Diblock Copolymers." Macromolecules **45**(11):4572-4580.

Kooij, E. S., X. Sui, M. A. Hempenius, H. J. Zandvliet and G. J. Vancso (2012). "Probing the thermal collapse of poly(N-isopropylacrylamide) grafts by quantitative *in situ* ellipsometry." J Phys Chem B **116**(30):9261-9268.

Laurienzo, P., M. Malinconico, G. Mattia, R. Russo, M. I. La Rotonda, F. Quaglia, D. Capitani and L. Mannina (2006). "Novel alginate-acrylic polymers as a platform for drug delivery." Journal of Biomedical Materials Research Part A **78A**(3): 523-531.

Lenoir, S., C. Pagnoulle, C. Detrembleur, M. Galleni and R. Jerome (2005). "Antimicrobial activity of polystyrene particles coated by photo-crosslinked block copolymers containing a biocidal polymethacrylate block." e-Polymers **74**:1-11. http://hdl.handle.net/2268/4303 accessed on March 2013.

Li, C. Y., W. Yuan, H. Jiang, J. S. Li, F. J. Xu, W. T. Yang and J. Ma (2011). "PCL Film Surfaces Conjugated with P(DMAEMA)/Gelatin Complexes for Improving Cell Immobilization and Gene Transfection." Bioconjugate Chem. **22**: 1842-1851.

Li, J. B., J. Ren, Y. Cao and W. Z. Yuan (2009). "Preparation and characterization of thermosensitive and biodegradable PNDH-g-PLLA nanoparticles for drug delivery." Reactive & Functional Polymers **69**(12):870-876.

Li, W., H. Kong, C. Gao and D. Yan (2005). "PH-responsive poly(2-diethylaminoethyl methacrylate)-functionalized multiwalled carbon nanotubes." Chin. Sci. Bull. **50**(20):2276-2280.

Liu, L., C. Wu, J. Zhang, M. Zhang, Y. Liu, X. Wang and G. Fu (2008). "Controlled polymerization of 2-(diethylamino)ethyl methacrylate and its block copolymer with N-isopropylacrylamide by RAFT polymerization." J. Polym. Sci., Part A: Polym. Chem. **46**(10):3294-3305.

Liu, S., J. V. M. Weaver, M. Save and S. P. Armes (2002). "Synthesis of pH-Responsive Shell Cross-Linked Micelles and Their Use as Nanoreactors for the Preparation of Gold Nanoparticles." Langmuir **18**(22):8350-8357.

Marra, J., A. G. Paleari, L. S. Rodriguez, A. R. P. Leite, A. C. Pero and M. A. Compagnoni (2012). "Effect of an acrylic resin combined with an antimicrobial polymer on biofilm formation." J Appl Oral Sci **20**(6): 643-648.

Matyjaszewski, K. (2012). "Atom Transfer Radical Polymerization (ATRP): Current Status and Future Perspectives." Macromolecules **45**(10):4015-4039.

Matyjaszewski, K., B. Göbelt, H.-j. Paik and C. P. Horwitz (2001). "Tridentate Nitrogen-Based Ligands in Cu-Based ATRP: A Structure−Activity Study." Macromolecules **34**(3):430-440.

Mendonça, P. V., A. C. Serra, J. F. J. Coelho, A. V. Popov and T. Guliashvili (2011). "Ambient temperature rapid ATRP of methyl acrylate, methyl methacrylate and styrene in polar solvents with mixed transition metal catalyst system." European Polymer Journal **47**(7):1460-1466.

Morse, A. J., D. Dupin, K. L. Thompson, S. P. Armes, K. Ouzineb, P. Mills and R. Swart (2012). "Novel Pickering Emulsifiers based on pH-Responsive Poly(tert-butylaminoethyl methacrylate) Latexes." Langmuir **28**(32):11733-11744.

Munoz-Bonilla, A., M. Fernandez-Garcia and D. M. Haddleton (2007). "Synthesis and aqueous solution properties of stimuli-responsive triblock copolymers." Soft Matter **3**(6):725-731.

Naini, C. A., S. Franzka, S. Frost, M. Ulbricht and N. Hartmann (2011). "Probing the Intrinsic Switching Kinetics of Ultrathin Thermoresponsive Polymer Brushes." Angew. Chem. Int. Ed., 50: 4513–4516.

Nath, N. and A. Chilkoti (2002). "Creating “Smart” Surfaces Using Stimuli Responsive Polymers." Advanced Materials **14**(17):1243-1247.

Paleari, A. G., J. Marra, A. C. Pero, L. S. Rodriguez, A. Ruvolo-Filho and M. A. Compagnoni (2011). "Effect of incorporation of 2-tert-butylaminoethyl methacrylate on flexural strength of a denture base acrylic resin." J Appl Oral Sci **19**(3):195-199.

Queffelec, J., S. G. Gaynor and K. Matyjaszewski (2000). "Optimization of Atom Transfer Radical Polymerization Using Cu(I)/Tris(2-(dimethylamino)ethyl)amine as a Catalyst." Macromolecules **33**(23):8629-8639.

Rahane, S. B., J. A. Floyd, A. T. Metters and S. M. Kilbey (2008). "Swelling behavior of multiresponsive poly(methacrylic acid)-block-poly (N-isopropylacrylamide) brushes synthesized using surface-initiated photoiniferter-mediated photopolymerization." Advanced Functional Materials **18**(8):1232-1240.

Rakhmatullina, E., T. Braun, T. Kaufmann, H. Spillmann, V. Malinova and W. Meier (2007). "Functionalization of gold and silicon surfaces by copolymer brushes using surface-initiated ATRP(a)." Macromolecular Chemistry and Physics **208**(12):1283-1293.

Richter, A., G. Paschew, S. Klatt, J. Lienig, K. F. Arndt and H. J. P. Adler (2008). "Review on hydrogel-based pH sensors and microsensors." Sensors **8**(1): 561-581.

Rowe-Konopacki, M. D. and S. G. Boyes (2007). "Synthesis of Surface Initiated Diblock Copolymer Brushes from Flat Silicon Substrates Utilizing the RAFT Polymerization Technique." Macromolecules **40**(4):879-888.

Shah, R. R., D. Merreceyes, M. Husemann, I. Rees, N. L. Abbott, C. J. Hawker and J. L. Hedrick (2000). "Using Atom Transfer Radical Polymerization To Amplify Monolayers of Initiators Patterned by Microcontact Printing into Polymer Brushes for Pattern Transfer." Macromolecules **33**(2): 597-605.

Sanjuan, S., P. Perrin, N. Pantoustier and Y. Tran (2007). "Synthesis and swelling behavior of pH-responsive polybase brushes." Langmuir **23**(10):5769-5778.

Schädel, M., K. F. Jeltsch, P. Niyamakom, F. Rauscher, Y. Zhou, M. Krüger and K. Meerholz (2012). "Determination of volume fractions and ligand layer thickness of polymer/CdSe quantum dot blend films by effective medium approximations." Journal of Polymer Science Part B: Polymer Physics **50**(1):75-82.

Suchao-in, N., S. Chirachanchai and S. Perrier (2009). "pH- and thermo-multi-responsive fluorescent micelles from block copolymers via reversible addition fragmentation chain transfer (RAFT) polymerization." Polymer **50**(17):4151-4158.

Sui, X., Q. Chen, M. A. Hempenius and G. J. Vancso (2011). "Probing the Collapse Dynamics of Poly(N-isopropylacrylamide) Brushes by AFM: Effects of Co-nonsolvency and Grafting Densities." Small **7**(10):1440-1447.

Sun, J.-T., C.-Y. Hong and C.-Y. Pan (2010). "Fabrication of PDEAEMA-Coated Mesoporous Silica Nanoparticles and pH-Responsive Controlled Release." J. Phys. Chem. C **114**(29):12481-12486.

Sutani, K., I. Kaetsu, K. Uchida and Y. Matsubara (2002). "Stimulus responsive drug release from polymer gel. Controlled release of ionic drug from polyampholyte gel." Radiation Physics and Chemistry **64**(4): 331-336.

Tagliazucchi, M., M. G. Blaber, G. C. Schatz, E. A. Weiss and I. Szleifer (2012). "Optical Properties of Responsive Hybrid Au@Polymer Nanoparticles." ACS Nano **6**(9):8397-8406.

Thomassin, J.-M., S. Lenoir, J. Riga, R. Jerome and C. Detrembleur (2007). "Grafting of Poly[2-(tert-butylamino)ethyl methacrylate] onto Polypropylene by Reactive Blending and Antibacterial Activity of the Copolymer." Biomacromolecules **8**(4):1171-1177.

Tompkins, H. G. and W. A. McGahan (1999). Spectroscopic ellipsometry and reflectometry : a user's guide. New York, Wiley.

Truong, N. P., Z. Jia, M. Burges, N. A. J. McMillan and M. J. Monteiro (2011a). "Self-catalyzed degradation of linear cationic poly(2-dimethylaminoethyl acrylate) in water." Biomacromolecules **12**(5):1876-1882.

Truong, N. P., Z. Jia, M. Burgess, L. Payne, N. A. J. McMillan and M. J. Monteiro (2011b). "Self-Catalyzed Degradable Cationic Polymer for Release of DNA." Biomacromolecules **12**(10):3540-3548.

Twaites, B. R., C. de las Heras Alarcon, D. Cunliffe, M. Lavigne, S. Pennadam, J. R. Smith, et al.C. Alexander (2004). "Thermo and pH responsive polymers as gene delivery vectors: effect of polymer architecture on DNA complexation in vitro." Journal of Controlled Release **97**(3):551-566.

Vamvakaki, M., L. Papoutsakis, V. Katsamanis, T. Afchoudia, P. G. Fragouli, H. Iatrou, et al.S. H. Anastasiadis (2004). "Micellization in pH-sensitive amphiphilic block copolymers in aqueous media and the formation of metal nanoparticles." Faraday Discuss. **128**(Self-Organising Polymers):129-147.

van de Wetering, P., E. E. Moret, N. M. E. Schuurmans-Nieuwenbroek, M. J. van Steenbergen and W. E. Hennink (1999). "Structure−Activity Relationships of Water-Soluble Cationic Methacrylate/Methacrylamide Polymers for Nonviral Gene Delivery." Bioconjugate Chemistry **10**(4):589-597.

Wandera, D., S. R. Wickramasinghe and S. M. Husson (2010). "Stimuli-responsive membranes." Journal of Membrane Science **357**(1–2):6-35.

Wu, Y., W. Yang, C. Wang, J. Hu and S. Fu (2005). "Chitosan nanoparticles as a novel delivery system for ammonium glycyrrhizinate." International Journal of Pharmaceutics **295**(1-2):235-245.

Xue, C., N. Yonet-Tanyeri, N. Brouette, M. Sferrazza, P. V. Braun and D. E. Leckband (2011). "Protein Adsorption on Poly(N-isopropylacrylamide) Brushes: Dependence on Grafting Density and Chain Collapse." Langmuir **27**(14):8810-8818.

Yoon, K. R., S. M. Lee, B. Ramaraj and D.-P. Kim (2008). "Surface initiated-atom transfer radical polymerization of a sugar methacrylate on gold nanoparticles." Surface and Interface Analysis **40**(8):1139-1143.

Yu, W. H.; Kang, E. T.; Neoh, K. G.; Zhu, S. *J*. *Phys*. *Chem*. *B* **2003**, *107*, 10198.

Zhang, M., L. Liu, C. Wu, G. Fu, H. Zhao and B. He (2007). "Synthesis, characterization and application of well-defined environmentally responsive polymer brushes on the surface of colloid particles." Polymer **48**(7):1989-1997.

Zhou, F., H. Hu, B. Yu, V. L. Osborne, W. T. S. Huck and W. Liu (2007). "Probing the Responsive Behavior of Polyelectrolyte Brushes Using Electrochemical Impedance Spectroscopy." Anal. Chem. **79**(1):176-182.

Zhou, J., B. Wang, W. J. Tong, E. Maltseva, G. Zhang, R. Krastev, C. Gao, H. Mohwald and J. C. Shen (2008). "Influence of assembling pH on the stability of poly(L-glutamic acid) and poly(L-lysine) multilayers against urea treatment." Colloids and Surfaces B-Biointerfaces **62**(2): 250-257.

CHAPTER V

ANALYSIS OF PARTICLE TRANSPORT AND DEPOSITION OF MICRON-SIZED PARTICLES IN A 90˚ BEND USING LAGRANGIAN AND MODIFIED-EULERIAN APPROACHES

5.1 Abstract

Two-phase flows involving dispersed continuous phases are of scientific interest because they are commonly encountered in a variety of natural and industrial processes, such as aerosols, blood flow, emulsions and gas-catalyst system. Particle size is an important variable to consider for computational simulations because each necessitates a different modeling approach. In this chapter, a new Eulerian modeling approach for coarse particles (> 1 μm) solved for particle concentration, deposition, and velocity, where particle-continuity and -momentum equations are independent of the air flow velocity, is described. Eulerian simulation results were obtained on a laminar flow regime (Re 100 and Re 1000) for two different 90˚ bend grids, and results were compared with experimental data available in literature. Lastly, gravity effects are considered for both Re cases, additionally, a gravity directional study on the y-component (+/-) is discussed for Re 100. A major finding of this work is the use of modified Eulerian particle phase modeling, resulting in accurate prediction of both near-wall particle tracking and wall deposition, allowing faster simulation run times compared to the typical Lagrangian approach for coarse particles.

5.2 Introduction

Micro- and nanoparticles have been widely studied due to some unique properties arising from their size and high surface area to volume ratio (Nalwa, 2004; Best et al., 2012; Torres Galvis et al., 2012). These types of particles are also catalogued according to its size as coarse particles (> 1 μm), fine particles (1 μm - 100 nm) and ultrafine particles (< 100 nm), and are involved in a variety of transport processes such as drug delivery mechanisms, gas-particle flow in ducts, food processing industry, and blood flow. As an example, novel biomedical technologies include micron-sized particles that can be used as a drug delivery carriers for insulin and DNA transported by particular inhalation mechanisms (Jurgons et al., 2006; Pathak and Thassu, 2009). Conversely, dust, combustion exhaust, manufacturing toxins (e.g. dioxins), and many other environmental contaminants exist in the form of micron-sized particles. When inhaled, these particles can create health issues such as emphysema and cancer (Pope III et al., 2002). Particle inhalation can result in deposition on the mucus lining, where such particles may then be absorbed into the blood stream and transported to a variety of organs (Xia et al., 2009). Consequently, predicting deposition and impaction of micro- and nanoparticles is of interest to determine the effects and fate of these particles in a predetermined structure/process.

Several applications and prior studies for particle fate/deposition in human lungs are available in the literature, and some include drug delivery mechanisms (Hofmann, 1996), prediction of dust, diesel or coal particle deposition (Pope III et al., 2002), particle deposition in bronchial airway bifurcations, having crucial role in lung cancer induction (Balashazy et al., 2007), and atmospheric pollutants—both natural and anthropogenic

sources— as health hazardous materials (Oldham et al., 2000; Hesterberg et al., 2009). Exploring the mechanisms that drive particle deposition can lead to further understanding of deleterious particle deposition and the design of improved drug delivery mechanisms. However, modeling the human lung with complete accuracy, even with methods such as CT scans, is nearly impossible due to differences in lungs among individuals, surface roughness on the tracheobronchial trees, and variation on breathing rates. Moreover, experimental particle deposition studies are difficult because physical experimentation is limited and methods are still being developed. Thus, new experimental and/or modeling tools are needed to further understand particle transport and deposition in the human lung

Computational modeling to predict the transport and deposition of inhaled particles represents key enabling technologies for improved drug delivery methods and mitigation of detrimental health effects due to pollution. CFD programs and models are needed to confirm the mechanisms used for air flow and particle deposition and to compare results with available experimental data. A comparison of CFD data with experimental results can provide confidence that modeled deposition mechanisms and efficiencies are accurate representations of real-case scenarios. Additionally, CFD simulations can help to predict and understand the effects on local deposition patterns. Detailed model characteristics can begin after the basic computational needs are satisfied in comparison with experimental data. After model validations, improving computational methodologies can focus on the effects of grid size versus accuracy, variation of inlet velocity profiles, turbulence, thermophoretic forces, non-spherical and non-homogeneous particles, and other critical parameters.

Simplified models such as 90˚ bends and/or elbows are used for computational modeling due to the availability of experimental data in literature. Elbows/90˚ bends are well-known for experimental studies performed as fluid flows through rectangular or circular cross-sectional regions. Recently, a series of experiments were performed to determine the velocity profiles under a turbulent flow using a square cross-section area duct (Mandal et al., 2010). Square duct cross-sectional areas have also been analyzed to predict the turbulent flow behavior using a coupled Eulerian-Eulerian approach to estimate the deposition percentage of 50 micron-sized particles (Mohanarangam et al., 2008). Similarly, circular cross-sectional area and industrial duct bends have also been studied for different flow- and particle Reynolds-number, bend angle, curvature, and orientation (Peters and Leith, 2004a; Peters and Leith, 2004c). Different CFD models have reported problems, for example, the model by Pui et al (1987) and McFarland et al. (1997) was found to be inaccurate due to the high radial velocity that large droplets experienced in industrial bends. Models for particle deposition in industrial ducts (Peters and Leith, 2004a) and 90° bends of exhaust ventilation systems (Peters and Leith, 2004b) were then proposed in an effort to obtain better results with experimental data. Therefore, cross-sectional area, experiment variables, and simulation components become critical parameters as CFD models are implemented to predict particle transport and deposition, even on simple grids.

Eulerian-particle transport methodologies have been implemented to improve particle-tracking and -deposition in simplified grids. For example, two-phase flow CFD study of air-water mixtures in a 90˚ elbow, at different grid sizes and velocities, has been developed obtaining good agreement with the effects of stability and predictions of

particle transport and deposition (Mazumder and Siddique, 2011). Pilou and coworkers (Pilou et al., 2011) investigated particle deposition in a 90˚ bend using an Eulerian approach with a modified convective diffusion equation based on a velocity correction effect for the drift flux equation (Longest and Oldham, 2008). In addition, physiologically realistic bifurcations created by generations G3-G4 of the human lung were studied and particle deposition was predicted (Pilou et al., 2013). Data were then compared with previous modeling and experimental data published by Pui et al. (Pui et al., 1987). In fact, the experimental work of Pui and coworkers has been extensively compared with CFD results that use either Eulerian or Lagrangian simulations for particle tracking. For instance, over the same grid, Breuer et al. (Breuer et al., 2006) tracked particle deposition using a Lagrangian approach for laminar and turbulent flow; however, a large number of individual particles were considered affecting deposition results. Another study, over the same grid, used an Eulerian coupled method for solving particle deposition (Armand et al., 1998). However, kinematic viscosity was set to zero and particle acceleration due to gravity was neglected. Moreover, data from the experimental work performed by Pui et al. (1987) was compared with the analytical work of Cheng and Wang (1981), that had the limitation of considering a fully developed flow in a finite bend. A different publication later found out that the inlet profile and Dean (Dn) number are parameters that affect the deposition efficiency in the 90˚ elbow (Tsai and Pui, 1990). Here, Pui's et al. experiment is also analyzed and used to evaluate the performance of the Eulerian particle tracking methodology developed in this study.

Different modifications to Eulerian methods for particle tracking and deposition have been recently reported in the literature in distinctive meshes. A study by Longest

and Oldman (2008) developed a new method with velocity corrections close to grid wall on which the drift flux Eulerian equations are coupled with a Lagrangian approach near the wall. The newly developed method has been studied by Xi and Longest (2008) in a tracheobronchial three representative grid and compared with experimental data in a nasal cavity replica cast for various particles sizes ranging from 1 to 1000 nm. One of the primary advantages of their method is that the Drift flux equation accounts for particle inertia and diffusion terms to determine the total deposition of the particles on the two different grids of the study. This hybrid combination of Eulerian and Lagrangian methods was then used by Pilou et al. (2011) in the 90˚ bend previously explained. Additionally, it has been shown that the computational time was significantly reduced as the simulations were carried out using the newly drift flux velocity correction method as compared with typical Lagrangian simulations. Another advantage of this model was the improvement in particle deposition percentage values, as compared with experimental results and the generalized chemical species (CS) Eulerian equations (Longest and Oldham, 2008). Thus, improving Eulerian methods for particle tracking is a key component to obtain good agreement with experimental results, and validate any CFD model.

Lagrangian particle-tracking and turbulence models improving particle-tracking performance have also been reported in literature. For example, studies of a Lagrangian particle-tracking model with a particle-wall collision modification to predict flow movement and deposition of particles (1, 3, 5, 9, and 16 μm) in a 90^{o} ventilation duct have been previously conducted (Sun et al., 2011). In a different report, turbulent renormalized Group (RNG) k-ε model was used adopting a Lagrangian particle tracking

model to predict turbulent air and particle flow (Jiang et al., 2011). The particle penetration rates were validated in a test duct at 6 different Stokes numbers. Reynolds–Averaged Navier–Stokes (RANS) –Lagrangian methods for dust (ranging from 10 to 200 μm) deposition in square shaped duct bends with different ways of placement were also recently developed (Gao and Li, 2012). Different effects such as drag, lift force, gravity, inertia force, and turbulent diffusions were considered in the work mentioned above. A particular discovery was the effect of gravity and inertia force increasing particle deposition as relaxation time increases. Turbulent particulate-laden flows in curved pipes using a RANS approach in Ansys Fluent has been studied with different bend angles, bend curvature ratios, and various Re numbers (Zhang et al., 2012). An Enhanced Wall Treatment (EWT) combined with an RSM method was proposed for modeling particle deposition in flows with curved streamlines.

In this chapter, a new Eulerian method that solves independent particle – continuity and –momentum equations is presented and discussed over the 90˚ bend experimental results by Pui et al (1987) within the laminar flow regime. Findings in this work are then compared with experimental data and previous published Eulerian methods for the 90˚ bend at two different laminar flow conditions (Re 100 and Re 1000). Additionally, a grid refinement study for the Eulerian simulations at the two different Re numbers is discussed (APPENDIX F) and results are compared to each other to observe any effects on grid refinement levels. Lastly, gravity effects, such as magnitude and direction, are also discussed.

The main objectives of this section are to (1) develop an Eulerian approach to simulate particle flow and deposition with independent continuity and momentum

particle transport equations, (2) compare the particle Eulerian results with experimental results and previously published data to validate the CFD model, (3) analyze the Eulerian-Eulerian particle-tracking approach in a hybrid mesh (rectangular and tetrahedral cells) to account for the near-wall interactions and deposition of particles and (4) analyze two laminar flow cases (Re 100 and Re 1000) using the methods of this work, comparing gravity components, and grid dependence.

5.3 Methods

Simulations were carried out in the commercial software Ansys Fluent version 14 and grids were constructed in Gambit version 2.4. First, the governing transport equations and boundary conditions for the airflow velocity are described. Then, the particle tracking methodology used in this work is discussed. Finally, a summary of the simulation details and the two different computational elbow grids with the different levels or refinement are discussed.

5.3.1 Fluid phase: Airflow velocity

The airflow velocity was initially solved using a parabolic velocity profile as suggested by Tsai and Pui (1990). For this purpose, steady state and incompressible flow are considered for solving the Navier-Stokes equations. Re number was kept at values within a laminar flow regime as recently 90˚ bend studies suggest on this particular grid (Pilou et al., 2011). A SIMPLE pressure-velocity coupling scheme was utilized to find the pressure within the system using a second order finite approximation. Momentum equations were also solved using a second order upwind approximation to find the three

velocity components u_j where j=1,2,3 for each velocity component as shown in equation 5.1.

Governing equations for the airflow within the 90˚ bend grid are the conservation of mass and momentum equations displayed below:

$$\frac{\partial u_i}{\partial x_i} = 0 \tag{5.1}$$

$$\frac{\partial}{\partial x_i}(u_j u_i) = -\frac{1}{\rho}\frac{\partial P}{\partial x_j} + \nu \frac{\partial^2 u_j}{\partial x_i \partial x_i} \tag{5.2}$$

Where, *u* is the air velocity vector, *P* is the pressure, ρ is the density and *v* is the dynamic viscosity.

A Green-gauss node based gradient was used as the discretization scheme to solve for the momentum equation components. The obtained air-flow velocity profile was later used as the initial velocity profile for the particles within the elbow grids. Therefore, the effect of the fluid motion is considered separately from the particle motion as discussed later. For the inlet fluid velocity boundary condition, a fully developed parabolic velocity profile was chosen at the entrance of the bend. Stationary walls and a no slip boundary conditions are also considered for solving the velocity profile.

5.3.2 Particle phase analysis

Particle transport was modeled using an Eulerian approach. Drag force (F_d) is calculated based on low Re numbers and is represented by:

$$F_D = \frac{18\mu}{d_p^2}\frac{C_D Re}{24} \tag{5.3}$$

,where μ is the viscosity of the air, Re is the Reynolds number for the air flow, d_p is the diameter of the particle and C*d* is the drag coefficient that is obtained as described

elsewhere (Morsi and Alexander, 1972). This model is based on smooth and spherical particles and values for the constants a_i (APPENDIX F) can be calculated for different Re numbers:

$$C_D = a_1 + \frac{a_2}{Re} + a_3 * Re \quad \text{(Heistracher and Hofmann, 1995)} \tag{5.4}$$

Other forces such as thermophoresis, particle acceleration due gravity, lift and drag, and Brownian motion (negligible diffusion coefficient) are not considered for solving the drag force equation. Eulerian particle phase transport equations were solved using a second-order discretization method; additionally, the air flow was solved simultaneously within the solution of the particle tracking. A user-defined function (UDF) was used for the discretization of the equations utilized for the particle phase volume fraction and momentum equations using a second-order discretization scheme. These discretization schemes were applied on equations 5.5 and 5.6:

$$\frac{\partial}{\partial t}\left(\rho_p \alpha\right) + \frac{\partial}{\partial x_j}\left(\rho_p \alpha u_j\right) = 0 \tag{5.5}$$

$$\frac{\partial}{\partial t}\left(\rho_p \alpha u_i\right) + \frac{\partial}{\partial x_j}\left(\rho_p \alpha u_i u_j\right) = \rho_p \alpha g_i + \frac{\alpha}{V_p} F_{i,d} \tag{5.6}$$

,where α is a probability function of finding a particle in a particular point in space and time that resembles a volume fraction, and u_i is the particle velocity. The modified-Eulerian approach treats particles with a near-wall approximation if the distance between the particles and the wall is at a maximum level of half the diameter of the particles. Then the particle is treated with a slip velocity with a characteristic drag force using an iteration process until there is no slip velocity at the wall.

A uniform particle concentration (equal to one) was set at the airway inlet. Wall boundary conditions for particle momentum equations allow non-zero wall normal velocities to represent inertial impaction.

5.3.3 Grid style, topology and refinement studies

A 90˚ bend grid was constructed based on the description provided by Pilou (Pilou et al., 2011) and Pui experimental results(Pui et al., 1987). Two different grids were generated for two Laminar flow cases using Gambit v. 2.4. First, a grid was generated for a Re 100 (Dn 38) and a grid for the laminar flow case of Re 1000 (Dn 419) , both illustrated in Figure 5.1a. Each grid was constructed with hybrid mesh cells (tetrahedral and hexahedral cells). Tetrahedral cells were investigated near the walls in order to better resolve deposition Figure 5.1b shows the hybrid mesh style that is utilized in the center of the 90˚ bends.

A total of 3,351,529 cells were used to analyze the deposition values at Re 1000. A second grid used for simulations of laminar flow with Re 100 has approximately 1,000,000 cells. For Re 100 direction of gravity was not specified (Pui et al., 1987) and some runs were performed switching gravity from –y to +y direction. As a result, the Eulerian approach has been run to determine the efficiency of the novel proposed methodology. Details for the construction of the grids were followed as directed by Pui et al. (1987) and Pilou et al. (2011).

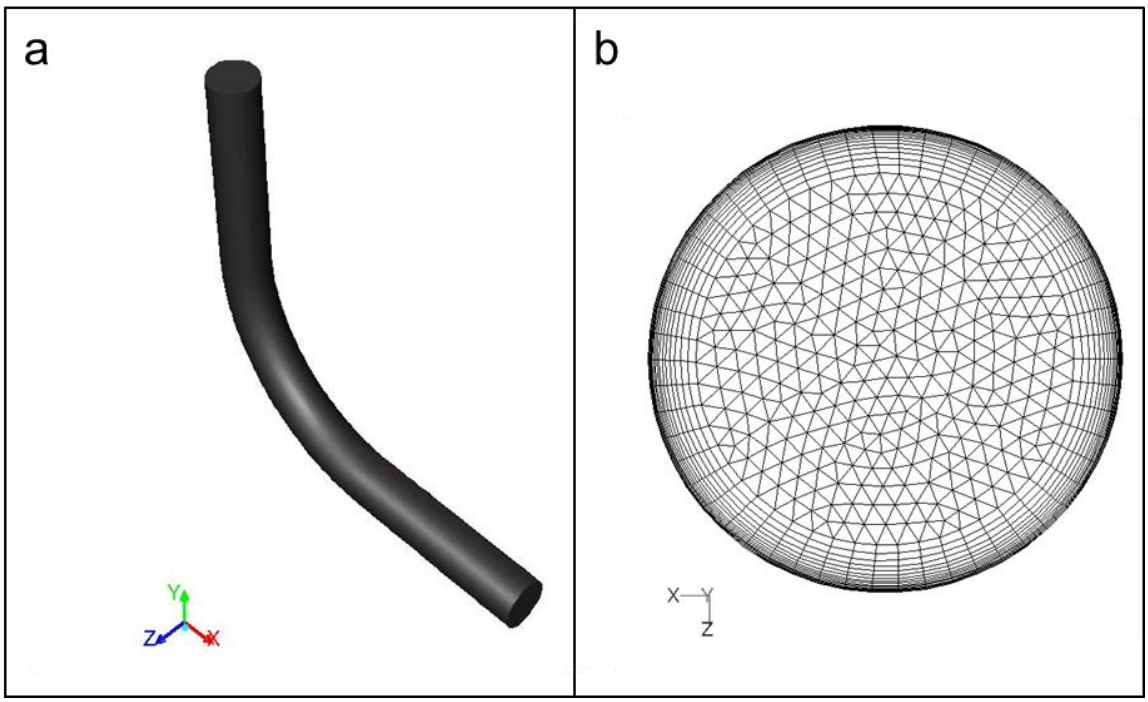

Figure 5.1 a) Grid utilized for 90˚ bend at Re 1000 and b) hybrid mesh style for a cross-section of the 90˚ bend

5.3.4 Simulation details

In this work, laminar flow was considered within the two different elbow grids. Airflow Re of 100 and 1000 were utilized for the two different grids explained in the last section. Parabolic inlet velocities profiles were established with maximum velocities of 3.37 m/s (Re =100) and 7.72 m/s (Re =100) at the center lines of the entrance of the grid. A uniform pressure value was applied at the outlet of the elbow grids. Different particle sizes were analyzed for each Re number of study and later compared with Stokes number as previous studies suggested. Details can be found in Table 5.1. Particle density was specified to be 895 kg/m^3 as described by Pui et al. (1987). Particles are also considered homogeneous in size with spherical shape. An initial inlet concentration for the particle

phase volume fraction was specified at the inlet – typically, 1 % volume fraction was utilized. The particle velocity was determined with a user-defined function for the Eulerian cases. Additionally, specified fluxes for the particles were established at the elbow walls.

Table 5.1 Particle size (in meters) for two different laminar flow cases

Re 100	Re 1000
5.36E-06	5.69E-06
5.91E-06	7.30E-06
6.87E-06	7.92E-06
7.65E-06	8.39E-06
8.83E-06	9.15E-06
9.23E-06	1.04E-05
9.77E-06	1.15E-05
1.15E-05	1.31E-05
1.22E-05	1.46E-05
	1.54E-05

5.4 Results and discussion

5.4.1 Fluid phase: airflow velocity profiles

Eulerian simulations were performed first to find the air velocity profile. At the entrance, a parabolic velocity profile was utilized using a maximum velocity of 7.72 m/s for a Re 1000 and 3.37 m/s for Re 100 (Figure 5.2). The center-plane velocity profile for the air flow for a Re 1000 is shown in Figure 5.2(b). The curvature of the 90˚ bend has a dramatic impact on the velocity profile for Re 1000. A region of low velocity is found at the bend curvature as the velocity increases at the bottom wall. Therefore, clearance of particles and less deposition can be expected in the high air velocity regions. Previous studies (Zhang et al., 2004) have shown the effects of curvature to have a useful mouth–

throat model for predicting the transport and deposition of particles using as comparison the 90˚ elbow discussed here. In this work, a similar velocity profile was obtained in the curved region. Additionally, Tsai and Pui (1990) also predicted the effect of an increase in the Dn number (high Re number) and the change in the axial flow behavior as shown in this work.

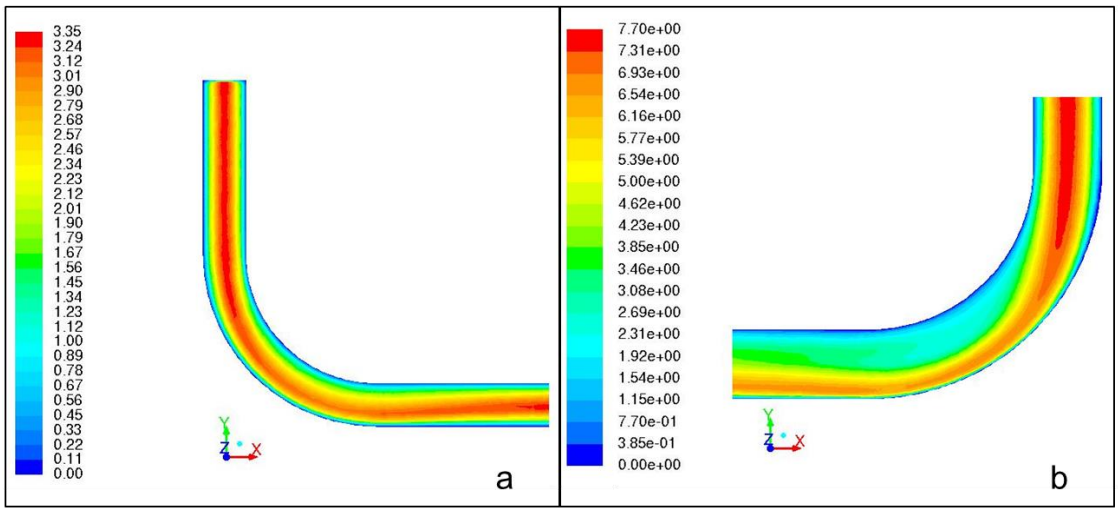

Figure 5.2 Air velocity profile for 90˚ bend for a Re number of a) 100 (Dn =38) and b) 1000 (Dn =419).

The center-plane velocity profile for Re 100 is shown in Figure 5.2a. The observed airflow appears to change in profile as the parabolic inlet profile changes to a more blunt profile due to curvature effects. However, as the airflow moves out of the bend a region of maximum velocity occurs again at the centerline. For Re 100 it is important to observe that the velocity profiles near the wall appear to be constant and have lower velocity values, being a result of the non-slip boundary condition. However, the particular effects seen at the curvature need to be considered for the analysis of the

particle deposition. Airflow for both grids was left to converge until the residuals for each discretization scheme were stable for each velocity component.

5.4.2 Particle transport and deposition

This section will discuss the results obtained for the different particle tracking techniques explored in this work. Particle phase and transport analysis were undertaken after obtaining an Eulerian solution for the air-flow. The Eulerian method employed in this work is compared for two laminar flow cases. A discussion on the first laminar flow case (Re 1000, Dn 419) is presented first. Then, results for the second case (Re 1000, Dn 38) are summarized and discussed next.

5.4.2.1 Eulerian–Eulerian particle phase transport and gravity effects comparison: Case I (Re 1000, Dn 419)

An increase in computational time and number of particles injected at the inlet in a particular grid are required to reach an accurate particle deposition percentage using a Lagrangian approach as discussed by Xi and Longest (2008a,b). This work is mainly focused on obtaining independent air-flow simulations for the Eulerian particle phase velocity field as the method differs from air phase due to particle inertia effects, including wall normal component at the bend. To analyze this effect, the y-component of the particle velocity is discussed and shown in Figure 5.3. As observed for a Re 1000, the impaction of particles at the curvature is very significant. It is expected that particle deposition analysis using an Eulerian approach is very sensitive at the near-wall region zone. The particle concentration field is relatively complex as presented earlier in equations 5 and 6; thus, comparison with other simulation methods is analyzed next.

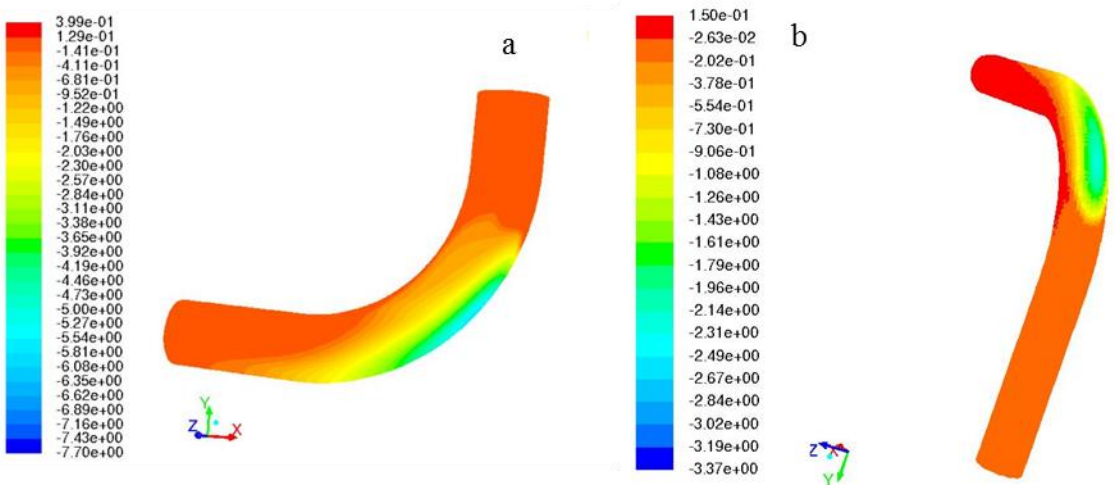

Figure 5.3 Y–component of the particle velocity for a) Re = 1000 and b) Re = 100

Quantitative results for the Eulerian modified numerical approximation with a numerical wall correction are shown in Figure 5.4. A significant outcome is that a better estimate for the deposition percentage was obtained with the modified Eulerian method as compared and contrasted with previous studies. The most recent results (Pilou et al., 2011) showed a particular trend on which underestimation of the particle deposition occurred at large Stokes number. Eulerian results of this work (Figure 5.4) showed better agreement for particle deposition percentage at high Stokes number. Therefore, a closer agreement with experimental data as Stokes number (particle size) increased is obtained. The results of this work were also compared with previous studies, such as the analytical work of Cheng and Wang (1981), Tsai and Pui (1990), Breuer et al. (2006) and the two-phase flow analysis of Armand et al. (1998), showing good agreement between them and the experimental data. Armand et al. (1998) over-predicted the deposition percentage for high Stokes number; whereas, the Eulerian modeling in this work is in closer agreement with the experimental data. Significant improvement is then shown for particle

deposition fractions in this 90˚ bend compared with previous methods. Three different levels of grid refinement were also compared for particle deposition efficiency.

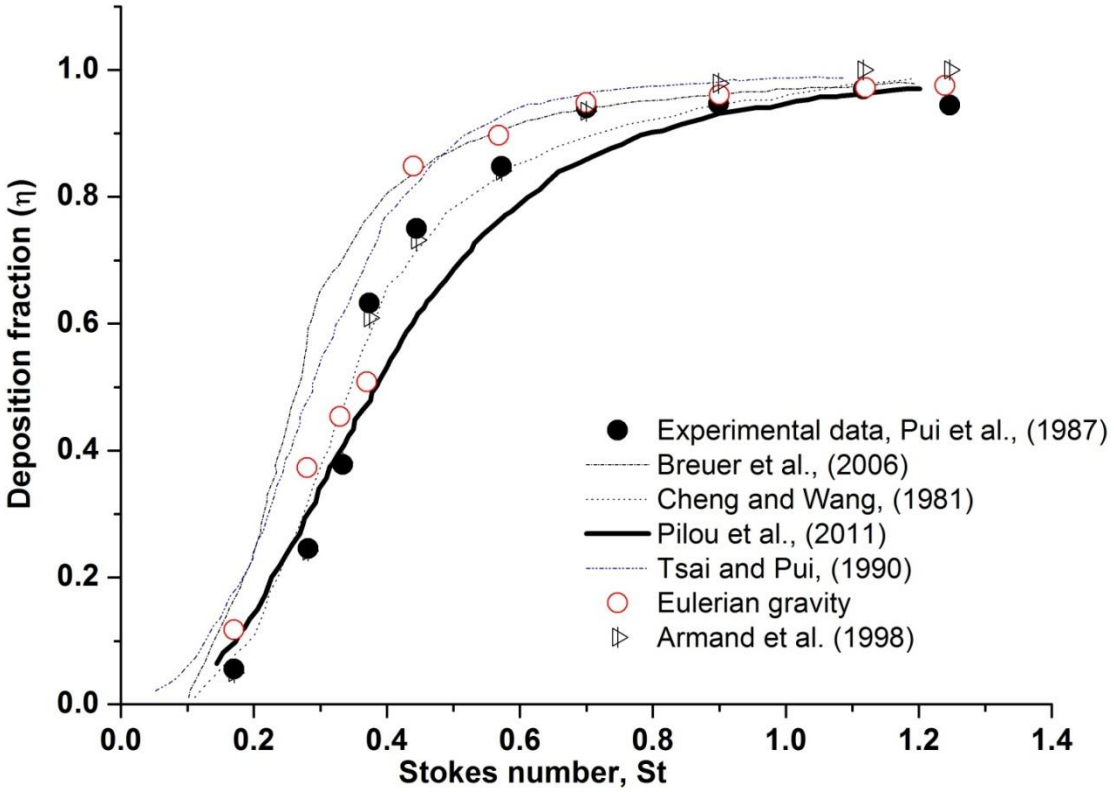

Figure 5.4 Comparison of Eulerian, Lagrangian and experimental deposition percentage for different particle sizes at Re 1000.

A comparison of the effect of gravity on the Eulerian deposition percentage results was also performed in this work (Figure 5.5). Interestingly, as gravity is input in the solution, the particle deposition efficiency values are not affected for Stokes number larger than 0.6. However, results for small Stokes values showed a decrease in the deposition percentage of particles at the elbow as compared with the experimental results. The main difference resides in the fact that gravity is taken into consideration when the

Eulerian model utilized in this work is solved. Thus, gravity force affects particle deposition for this particular 90˚ bend and the two-phase Eulerian model developed for CFD at Re 1000.

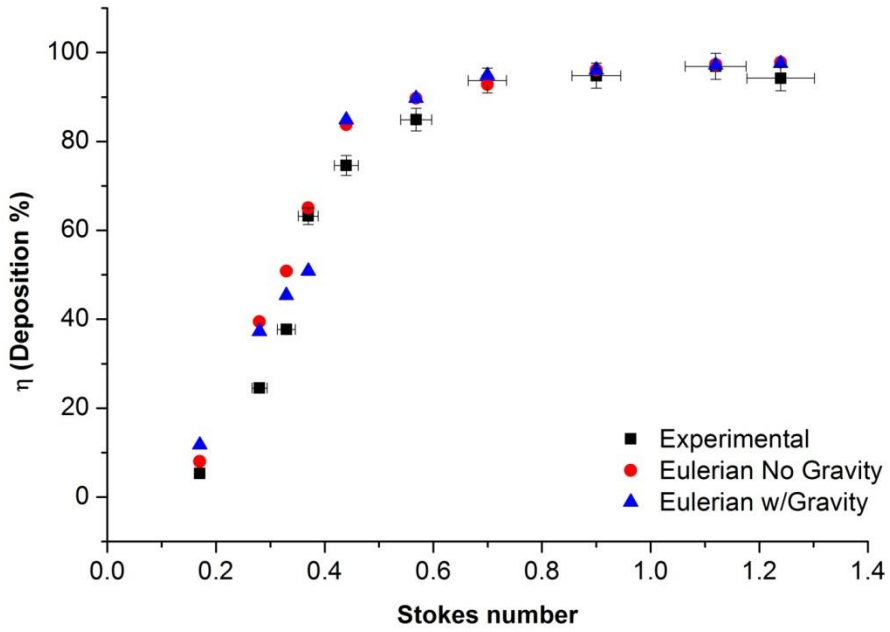

Figure 5.5 Comparison of Eulerian runs (with and without gravity) for Re = 1000 vs. Experimental results obtained by Pui et al. (1987)

Illustration of qualitative similarity in airway wall deposition patterns for 15.8 micron in elbow grid for the same Re (1000) are shown in Figure 5.6. Particle deposition patterns are observed near the curvature of the 90˚ bend where greater impaction of particles in the y-direction occurred, as previously discussed. However a high concentration of particles is also observed. Interestingly, this high-gradient line was present for all the different particle sizes which are larger than 9.15 microns.

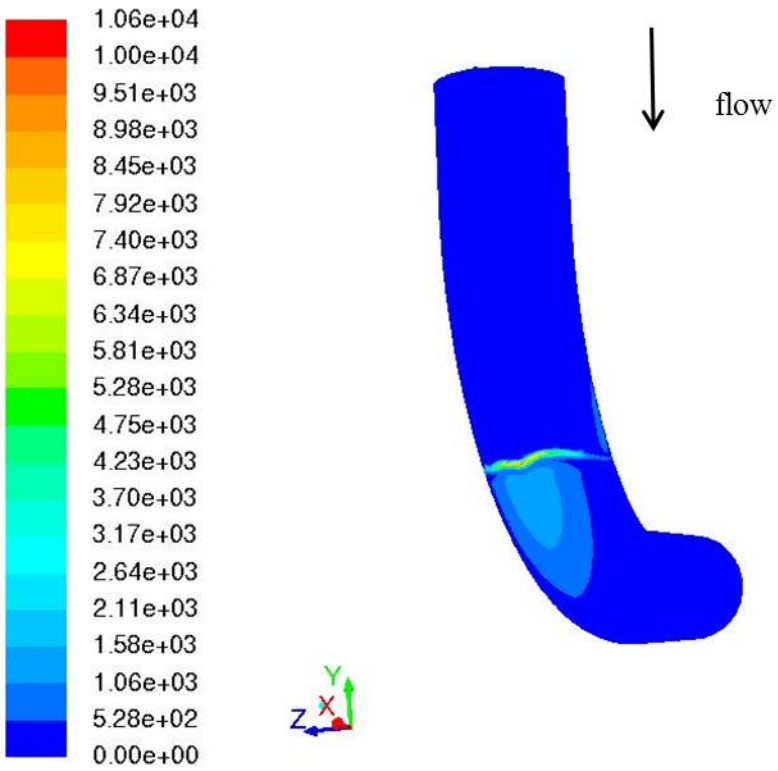

Figure 5.6 Illustrative particle deposition pattern for Re 1000 and 9.15 micron particles

5.4.2.2 Eulerian–Eulerian particle phase transport and gravity effects comparison: Case II (Re 100, Dn 38)

The agreement between the Eulerian particle transport/tracking simulations and experimental data is investigated using a second 90˚ bend case. This second laminar flow case was run at Re 100 (Dn 38). Results were also compared to experimental data by Pui et al. (1987), and the recent study performed by Pilou et al (2011). Eulerian simulations and experimental data for this case are presented in a quantitative particle deposition plot in Figure 5.7. It is observed that by increasing the Stokes number (particle size); the deposition percentage was over-predicted by the developed Eulerian method as compared with the experimental data.

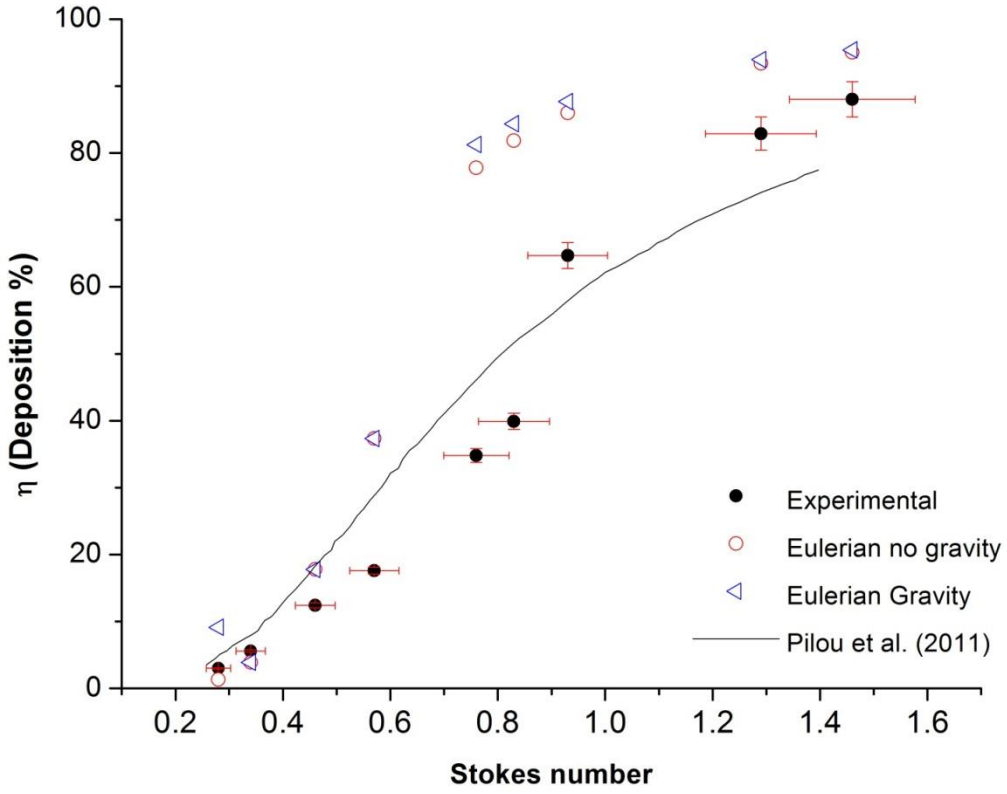

Figure 5.7 Eulerian and experimental (cumulative) deposition percentage for different particle sizes in the 90˚ bend elbow (Re = 100).

Conversely, previous simulations made by Pilou et al. (2011) showed under-predicted results with respect to the experimental data for high Stokes numbers. Therefore, the results shown in this work are still close to the expected values. The accounted gravity effects and the two-phase flow Eulerian method are the main difference between the results shown here and the results previously reported in literature. For this particular case (Re 100/ Dn 38) within the laminar-flow region solutions were also obtained neglecting gravity effects – continuity and momentum equations were solved. Pilou's et al. work (2011) and Armand et al. (1998) determined that gravity did not have any particular effects on their results. However, the equations

utilized in this work showed gravity dependence terms for Re 1000. For case II (Re 100), gravity effects and the deposition percentage are not as significant as compared to the 90° bend discussed in case I (Re 1000). Eulerian simulations for particle tracking and deposition analysis without gravity were also shown in Figure 5.7. Interestingly, under this regime at low Stokes numbers, a better fitting with the experimental data and the work of Pilou et al. (2011) was obtained. Thus, an important conclusion of this work is that gravity effects can be neglected at low Re, St and Dn number.

Figure 5.8 highlight specific points that show the main section of the 90˚ bend were the particle deposition occurred as Stokes number were varied for Re 100 considering gravity effects. In addition, the experimental results were calculated only for the bend region. Results show that deposition patterns occurred primarily close to the curvature on the elbow bottom walls and were affected by particle size. This effect is clearly observed for small Stokes numbers (small particle diameter). Additionally, size has an effect and it affects the impaction and particle deposition fraction around the elbow walls. Larger particles will impact faster just below the 90° bend; smaller particles impact after the curvature ends in fewer amounts. As the Stokes number increases (larger particles), deposition occurred closely to the entrance of the curvature where a high y-velocity component was shown and described early in Figure 5.3. As expected, large particles will impact faster as they encounter the curved region in the grid due to the gravitational and inertial effects.

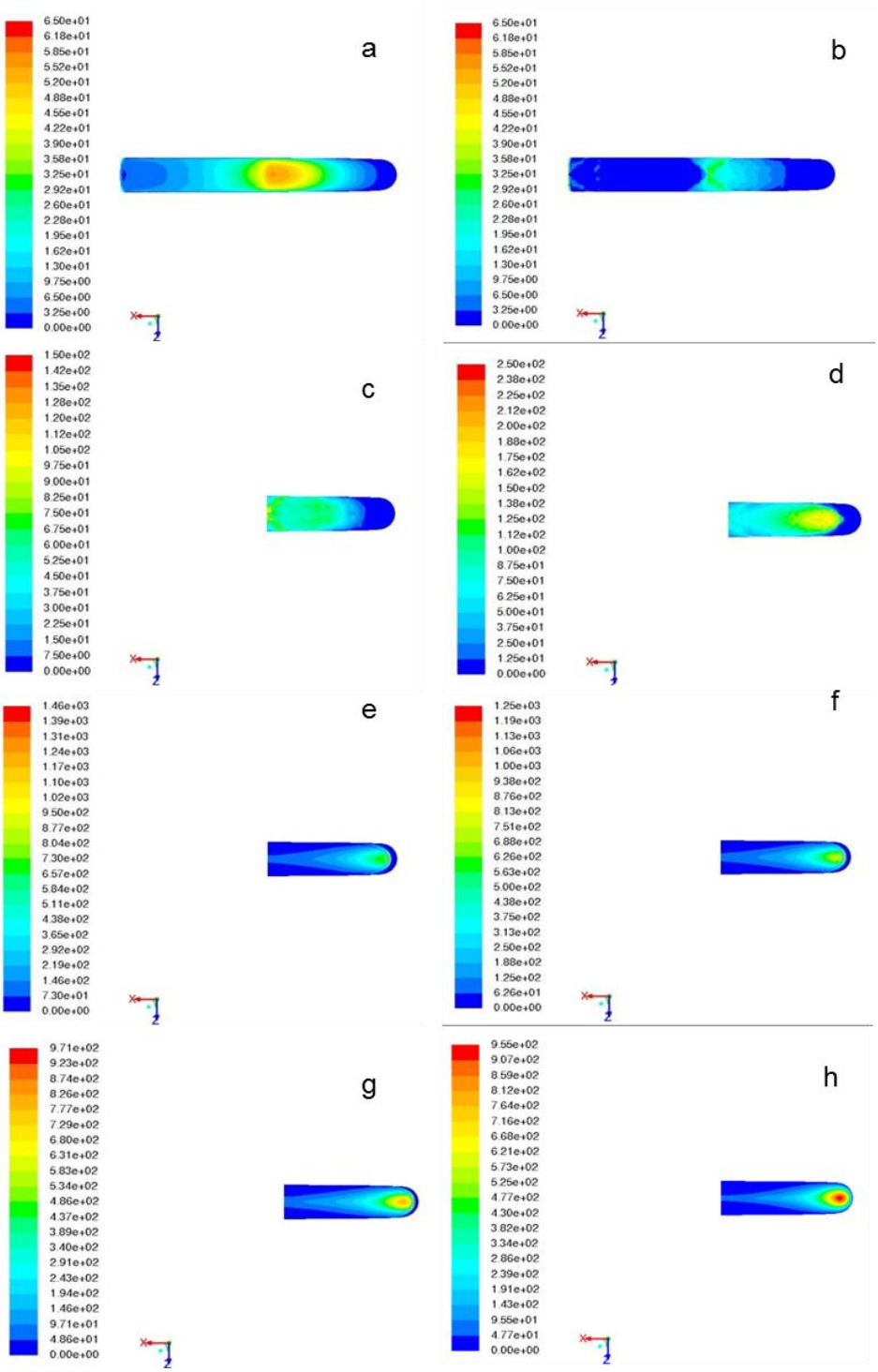

Figure 5.8 Particle deposition patterns for refined grid at low Re number (100) and Dn (38) number for different particle sizes

a) 5.36 microns, b) 5.91 microns, c) 6.87 microns, d)7.65, e) 8.83 microns, f) 9.23microns, g) 9.77 microns and h) 12.2 microns (bottom view).

The effects of particle deposition comparing gravity effects for low Stokes number are also analyzed. Figure 5.9(a,b and d) considered the effects of gravity in a positive y-direction, as a result, deposition patterns were clearly distinct when gravity is considered in opposite directions. Deposition fraction for 5.39 microns as gravity pointed in a positive y-direction changed drastically. Figure 5.9b illustrates how the particles were pulled by the effect of gravity after the curvature. Nonetheless, as particle diameter was increased to 12.24 microns, gravity did not affect the deposition percentage. As fine-particle tracking is one of the eventual goals of this effort, the Eulerian particle tracking method shows potential to successfully predict transport and deposition of even smaller particles than those studied in this work considering gravity for smaller particles.

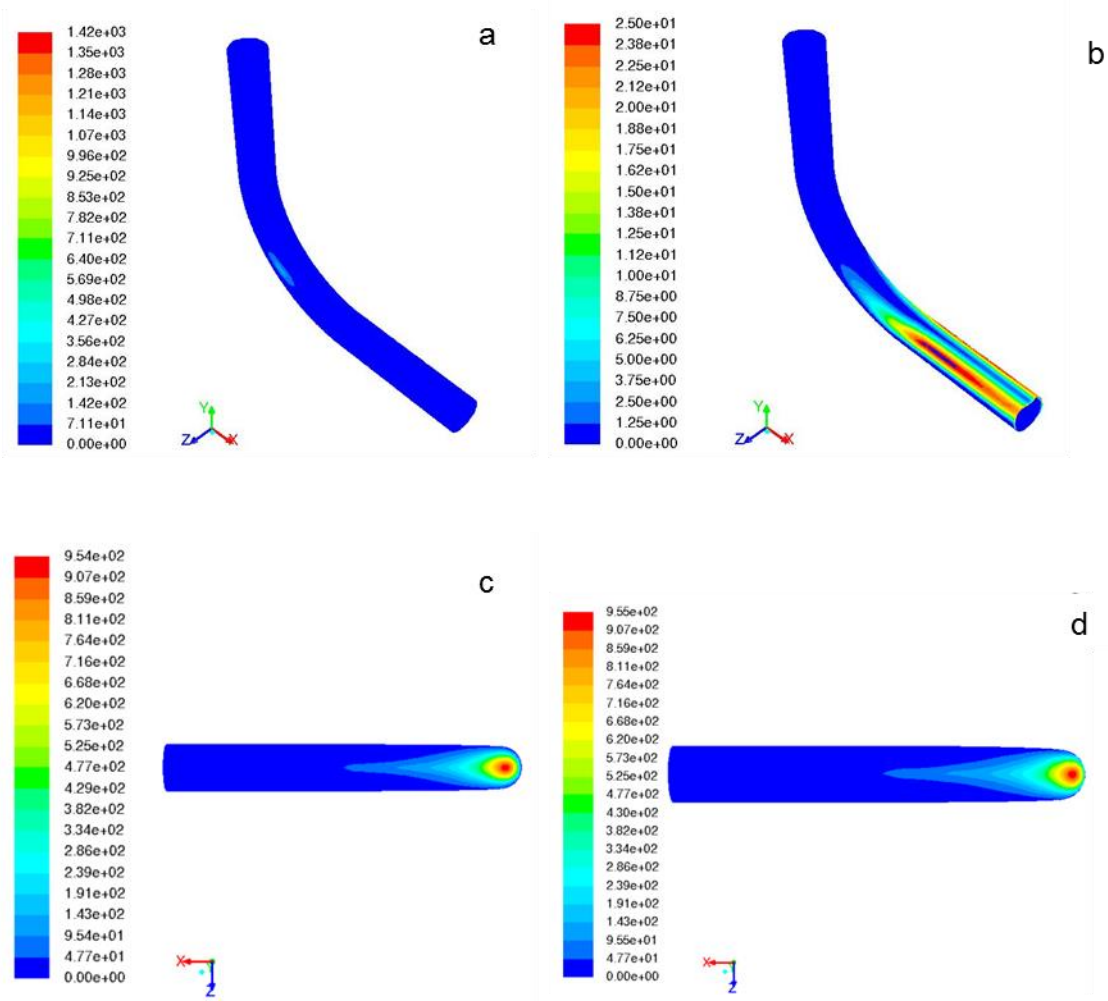

Figure 5.9 Comparison of gravity effects for different particle sizes: gravity going in positive y direction

a) 9.77 and b) 5.39 microns. No gravity effects (c) are shown for particle size of 12.24 microns and gravity going up is shown for the same particle size (d). All the images are for Re 100 and Dn 38.

Results suggest that Eulerian simulations predictions with experimental values better for small particle sizes (~ 5 micron) are in good agreement for Re 100. However, as the particle size increased particle deposition percentage was over-predicted. The two-phase coupled Eulerian particle solution approach for the two cases of study (Re 100 and Re 1000) seems to agree well with respect to previous models and experimental data.

Considering smaller particles will lead to consideration of other forces (e.g., thermal) or physical properties of the particles, such as surface roughness (Shi et al., 2007) and particle aggregation.

5.5 Conclusions

Analysis of the particle tracking and deposition predictions and comparison with experimental data for 5-12 micron-sized particles (Stokesian regime) has led to several important findings. The two-phase coupled Eulerian method, run in hybrid meshes, provided good agreement with the experimental data for the deposition of small particles (< 5 microns) despite the Re number of study. Moreover, particles are affected by the gravitational component as they deposit close to the curved surface in the 90° bend. As a result, gravity affects deposition results at low Stokes number for low Reynolds and Dn numbers. In general, the two-phase Eulerian particle approach has proved to be as successful as other methods previously published in literature and is in good agreement with experimental data for different laminar flow and Stokesian regimes. Future work will extend these analyses to more complex grids that better represent human lung airways.

5.6 References

Armand, P., D. Boulaud, M. Pourprix and J. Vendel (1998). "Two-fluid modeling of aerosol transport in laminar and turbulent flows." Journal of Aerosol Science **29**(8): 961-983.

Balashazy, I., B. Alfoldy, A. J. Molnar, W. Hofmann, I. Szoke and E. Kis (2007). "Aerosol drug delivery optimization by computational methods for the characterization of total and regional deposition of therapeutic aerosols in the respiratory system." Current Computer-Aided Drug Design **3**(1): 13-32.

Best, J. P., Y. Yan and F. Caruso (2012). "The Role of Particle Geometry and Mechanics in the Biological Domain." Advanced Healthcare Materials **1**(1): 35-47.

Breuer, M., H. T. Baytekin and E. A. Matida (2006). "Prediction of aerosol deposition in 90˚ bends using LES and an efficient Lagrangian tracking method." Journal of Aerosol Science **37**(11): 1407-1428.

Dehbi, A. (2011). "Prediction of extrathoracic aerosol deposition using RANS-random walk and les approaches." Aerosol Science and Technology **45**(5): 555-569.

Gao, R. and A. Li (2012). "Dust deposition in ventilation and air-conditioning duct bend flows." Energy Conversion and Management **55**(0): 49-59.

Heistracher, T. and W. Hofmann (1995). "Physiologically realistic models of bronchial airway bifurcations." Journal of Aerosol Science **26**(3): 497-509.

Hesterberg, T. W., W. B. Bunn, R. O. McClellan, A. K. Hamade, C. M. Long and P. A. Valberg (2009). "Critical review of the human data on short-term nitrogen dioxide (NO2) exposures: Evidence for NO2 no-effect levels." Critical Reviews in Toxicology **39**(9): 743-781.

Hofmann, W. (1996). "Modeling techniques for inhaled particle deposition: the state of the art." Journal of Aerosol Medicine-Deposition Clearance and Effects in the Lung **9**(3): 369-388.

Jiang, H., L. Lu and K. Sun (2011). "Experimental study and numerical investigation of particle penetration and deposition in 90° bent ventilation ducts." Building and Environment **46**(11): 2195-2202.

Jurgons, R., C. Seliger, A. Hilpert, L. Trahms, S. Odenbach and C. Alexiou (2006). "Drug loaded magnetic nanoparticles for cancer therapy." Journal of Physics-Condensed Matter **18**(38): S2893-S2902.

Longest, P. W. and M. J. Oldham (2008). "Numerical and experimental deposition of fine respiratory aerosols: Development of a two-phase drift flux model with near-wall velocity corrections." Journal of Aerosol Science **39**(1): 48-70.

Mandal, A., S. Bhattecharjee, R. Debnath, R. Debasish and S. Majumder (2010). "Experimental Investigation of Turbulent Fluid Flow through a Rectangular Elbow " International Journal of Engineering Science and Technology **2**(6): 1500-1506.

Mazumder, Q. H. and S. A. Siddique (2011). "CFD analysis of two-phase flow characteristics in a 90 degree elbow." Journal of Computational Multiphase Flows **3**(3): 165-175.

McFarland, A. R., H. Gong, A. Muyshondt, W. B. Wente and N. K. Anand (1997). "Aerosol Deposition in Bends with Turbulent Flow†." Environmental Science & Technology **31**(12): 3371-3377.

Mohanarangam, K., Z. F. Tian and J. Y. Tu (2008). "Numerical simulation of turbulent gas-particle flow in a 90° bend: Eulerian-Eulerian approach." Computational Chemical Engineering **32**: 561-571.

Morsi, S. A. and A. J. Alexander (1972). "An investigation of particle trajectories in two-phase flow systems " Journal of Fluid Mechanics **55**(2): 193-208.

Nalwa, H. S. (2004). Encyclopedia of nanoscience and nanotechnology. Stevenson Ranch, Calif., American Scientific Publishers.

Oldham, M. J., R. F. Phalen and T. Heistracher (2000). "Computational fluid dynamic predictions and experimental results for particle deposition in an airway model." Aerosol Science and Technology **32**(1): 61-71.

Pathak, Y. and D. Thassu (2009). Drug delivery nanoparticles formulation and characterization. New York, Informa Healthcare.

Peters, T. M. and D. Leith (2004a). "Measurement of particle deposition in industrial ducts." Journal of Aerosol Science **35**(4): 529-540.

Peters, T. M. and D. Leith (2004b). "Modeling Large-Particle Deposition in Bends of Exhuast Ventilation Systems." Aerosol Science and Technology **38**(12): 1171-1177.

Peters, T. M. and D. Leith (2004c). "Particle deposition in industrial duct bends." Ann Occup Hyg **48**(5): 483-490.

Pilou, M., V. Antonopoulos, E. Makris, P. Neofytou, S. Tsangaris and C. Housiadas (2013). "A fully Eulerian approach to particle inertial deposition in a physiologically realistic bifurcation." Applied Mathematical Modelling **37**(8): 5591-5605.

Pilou, M., S. Tsangaris, P. Neofytou, C. Housiadas and Y. Drossinos (2011). "Inertial particle deposition in a 90 laminar flow bend: An eulerian fluid particle approach." Aerosol Science and Technology **45**(11): 1376-1387.

Pope III, C. A., R. T. Burnett, M. J. Thun, E. E. Calle, D. Krewski, K. Ito and G. D. Thurston (2002). "Lung Cancer, Cardiopulmonary Mortality, and Long-term Exposure to Fine Particulate Air Pollution." The Journal of the American Medical Association **287**(9): 1132-1141.

Pui, D. Y. H., F. Romay-Novas and B. Y. H. Liu (1987). "Experimental study of particle deposition in bends of circular cross section." Aerosol Science and Technology **7**(3): 301-315.

Shi, H., C. Kleinstreuer and Z. Zhang (2007). "Modeling of inertial particle transport and deposition in human nasal cavities with wall roughness." Journal of Aerosol Science **38**(4): 398-419.

Slater, S. A. and J. B. Young (2001). "The calculation of inertial particle transport in dilute gas-particle flows." International Journal of Multiphase Flow **27**(1): 61-87.

Sun, K., L. Lu and H. Jiang (2011). "A computational investigation of particle distribution and deposition in a 90° bend incorporating a particle–wall model." Building and Environment **46**(6): 1251-1262.

Torres Galvis, H. M., J. H. Bitter, C. B. Khare, M. Ruitenbeek, A. I. Dugulan and K. P. de Jong (2012). "Supported Iron Nanoparticles as Catalysts for Sustainable Production of Lower Olefins." Science **335**(6070): 835-838.

Tsai, C.-J. and D. Y. H. Pui (1990). "Numerical Study of Particle Deposition in Bends of a Circular Cross-Section-Laminar Flow Regime." Aerosol Science and Technology **12**(4): 813-831.

Xia, T., N. Li and A. E. Nel (2009). "Potential Health Impact of Nanoparticles." Annual Review of Public Health **30**: 137-150.

Zhang, P., R. M. Roberts and A. Bénard (2012). "Computational guidelines and an empirical model for particle deposition in curved pipes using an Eulerian-Lagrangian approach." Journal of Aerosol Science **53**: 1-20.

Zhang, Y., W. H. Finlay and E. A. Matida (2004). "Particle deposition measurements and numerical simulation in a highly idealized mouth–throat." Journal of Aerosol Science **35**(7): 789-803.

CHAPTER VI

TRANSPORT MODELING OF MICRON- AND NANOMETER-SIZED PARTICLES IN A HUMAN LUNG GEOMETRY

This chapter examines a unified, two-fluid Eulerian-Eulerian modeling approach, where a concentration equation was solved for micron-sized particles in human lung-type geometry. A particle phase momentum equation was solved to determine the particle bulk velocities, separate from the air velocity. These results were compared to the more traditional approach of Lagrangian particle-tracking and to experimental data to evaluate the accuracy of the Eulerian method in a more complex geometry than the 90-degree elbow presented in Chapter 5. Steady state flow was considered through a representative idealized lung airway model consisting of three physiologically realistic airway branch bifurcations (PRB). Simulations were performed using the commercial computational fluid dynamics (CFD) code FLUENT, and the particle phase equations were implemented using user-defined function (UDF) subroutines. The effects of mesh resolution, mesh topology, particle size, and velocity inlet profile were investigated. Results suggest that the unified Eulerian-Eulerian method is an effective approach for particle transport simulations in the human lung airway, and total particle deposition percentages are in better agreement with experimental data as compared to the Eulerian-Lagrangian particle tracking method.

6.1 Introduction

Significant research efforts have been directed towards the use of micro- and nanoparticles for drug delivery to specific organs in the human body. General applications and previous approaches analyzing particle transport and deposition of particles inside human lung have used simplified geometry models, such as the 90° bend, previously described in Chapter 5. Bronchial airway bifurcations are the most common examples of simplified models for the analysis of particle transport and deposition in human lungs. For example, the physiological realistic bifurcation (PRB) model has been studied with the objective to obtain simplified geometries with realistic asymmetry comparable to human bronchial airways (Heistracher and Hofmann, 1995a; Hofmann et al., 1996; Oldham et al., 2000a). A mathematical description for the generation of the PRB grid is available in the open literature (Heistracher and Hofmann, 1995b) which allows for an accurate recreation of the PRB geometry and for this geometry to serve as a model geometry to use to assess CFD methods for physiological systems.

Several simulation studies conducted on a PRB grid have been compared with experimental data for validation. One of the first studies on a PRB grid demonstrated general agreement between experimental and CFD data; however, some differences were observed between the CFD and experimental data particularly in local deposition patterns (Oldham et al., 2000b). A different approach focused on the formation of secondary flows and irregular deposition patterns, demonstrating the effects of convective transport processes of the fluid influence particle deposition (Hofmann et al., 2001). Further investigations analyzed different parameters such as the effect of laminar or turbulent flow, upstream flow, and entrance effects for particles as small as 1 micron (Longest and

Oldham, 2006). Recently, a drift flux-velocity correction method (DVCM) was employed to determine the particle deposition on the walls of a PRB geometry utilizing a new Lagrangian solution near the wall that was solved in conjunction with the drift flux equation (Longest and Oldham, 2008). This method allowed for the calculation of aerosol particle inertia near the wall using a two-phase separated model to independently solve the air flow from the particle flow. In this work, the Eulerian model has been shown to yield good agreement with experimental data for a simple 90° bend grid. Therefore, the effect of parameters such as mesh type, velocity inlet profile, and grid refinement with the Eulerian-Eulerian model are now investigated using a PRB grid.

The effects of mesh type (unstructured vs. structured) and style (hexahedral, tetrahedral, prismatic cells) have a significant impact on particle tracking and deposition on PRB grids. In particular, previous studies have evaluated mesh style independence using hybrid, tetrahedral and prismatic meshes, both structured and unstructured-type. Hybrid meshes were found to overpredict particle deposition, and hexahedral cells, despite mesh type, had the best performance (Vinchurkar and Longest, 2008). The efficacy of a hexahedral mesh style on a PRB was first evaluated using a grid convergence index (CGI), resulting in accurate predictions with respect to experimental data (Longest and Vinchurkar, 2007). The studies previously described strongly suggest utilization of different hybrid/hexahedral cells for a better estimate on particle deposition percentages. Additionally, new experimental studies are now emerging for micron-sized particles where effects of surface roughness, pressure, particle size, and deposition fractions are parameters that need to be consistent between the experiments and CFD grids generation (Holbrook and Longest, 2013). Therefore, mesh style and type affect the

evaluation of particle tracking models, such as Eulerian-Lagrangian (E-L) and Lagrangian-Lagrangian (L-L) particle tracking methods. Both methods and mesh style effects on an unstructured grid at different levels of refinement are evaluated.

Recent efforts in particle transport modeling in the lung airway have focused on three-dimensional CFD simulations. Typically, the airflow in the lung is obtained from numerical solution of the single-phase Navier-Stokes equations, with the particles treated as a passive phase in a dilute mixture. Deposition of microparticles is typically calculated using a E-L approach, and statistical measurements of particle transport and fate are obtained by averaging over a large number of trajectories. Nanoparticles are often treated using a one-fluid Eulerian approach, in which a concentration equation is solved for the particle phase, and the phase (bulk) particle velocity is assumed to be equal to the air velocity. As an example, experiments to calculate magnetic deposition of coated and uncoated aerosol dispersion have been carried out in simplified geometries (Xie et al., 2010b) and *in vivo* experiments using rats (Xie et al., 2010a), and these experimental results have been compared with corresponding CFD simulations. 3D *in-silico* modeling has also been studied and compared with imaging analysis in an effort to obtain better particle deposition predictions (Martonen et al., 2007; Longest and Holbrook, 2012). In fact, advancements in 3-D particle tracking models is a need for nanoparticle drug delivery applications, as specific epithelial cells can be targeted in future drug-design advancements (Phalen et al., 2010). Therefore, this work focuses on the implementation of a coupled E-E particle tracking model, that later could be extended for the analysis of the human lung.

The main objectives of this chapter are to (1) implement a coupled E-E solution that is solved simultaneously for both the air flow and the particle flow velocities on a PRB grid, (2) compare the E-E solution with a E-L approach in which the air flow velocity is solved independently of the particle velocity, (3) compare a hybrid mesh (rectangular and tetrahedral cells) with a tetrahedral cell mesh and determine any improvement in particle deposition accuracy, and (4) compare and analyze the results of a simultaneous solution E-E at two different levels of grid refinement. These results can be used to guide new CFD simulations and to compare with future computational and/or experimental data for particle deposition in the lung. First, the governing transport equations and boundary conditions for the airflow velocity are described. Then, the particle tracking methodologies used in this work— E-E and E-L —are discussed. Finally, a summary of the simulation details and the effects of grid refinement are discussed.

6.2 Methods

Simulations were carried out using the commercial software Ansys Fluent version 12 and grids were constructed in Gambit version 2.4. PRB geometry is a third generation branch based on model A of Weibel (Weibel, 1963). Different parameters such as branching angle were modified to be more physiologically accurate as described elsewhere (Heistracher and Hofmann, 1995b; Heistracher and Hofmann, 1997). Results in this work were compared with experimental results available for particle diameter (Dp = 9.97 microns) and a particle density of 1060 kg/m^3 (Oldham et al., 2000b).

6.2.1 Fluid phase: Airflow velocity

The air flow velocity was initially solved using parabolic and blunt velocity profiles. For this purpose, the Navier-Stokes equations were considered, and steady state and incompressible flow conditions were also assumed, obtaining an Eulerian air flow velocity. Reynolds number was kept at values within the laminar flow regime, and an approximate value of Re 1800 was maintained at the inlet (parent branch) with an average velocity of 5.08 m/s to match the experimental work of Oldham et al. (2000). Air flow conditions were solved independently of particle phase (dilute particle assumption). Second-order discretization schemes were used to solve the momentum equations and a simple pressure correction scheme (PRESTO!) was used to discretize the pressure equation. Pressure outlet conditions were set to ensure equal flow at each outlet (Oldham et al., 2000b). Convergence for the air flow simulations was verified by reduction in residuals of over six orders of magnitude.

6.2.2 Mesh style and topology

Two different mesh styles were evaluated and compared for particle tracking and deposition studies. The tetrahedral (TET) mesh style consists of tetrahedral throughout the bifurcation, whereas the hybrid (HYB) mesh style consist of hexahedral cells close to the walls of the PRB geometry and tetrahedral cells away from the walls as shown in Figure 6.1. Additionally, the level of refinement was evaluated for both mesh styles. A coarse mesh and a refined mesh were considered for each mesh style. The changes in the level of refinement lead to a change in the number of cells in the geometry. The TET coarse mesh had 718,453 cells and TET refined mesh had 1,607,000 cells, with the refined case having more than double number of cells as the course mesh. The HYB

coarse mesh had a total of 1,325,282 cells and the HYB refined mesh had a total 5,863,693 cells. Analysis of the results is focused on the impact of refinement level, and therefore the number of cells, on the particle deposition and momentum equations.

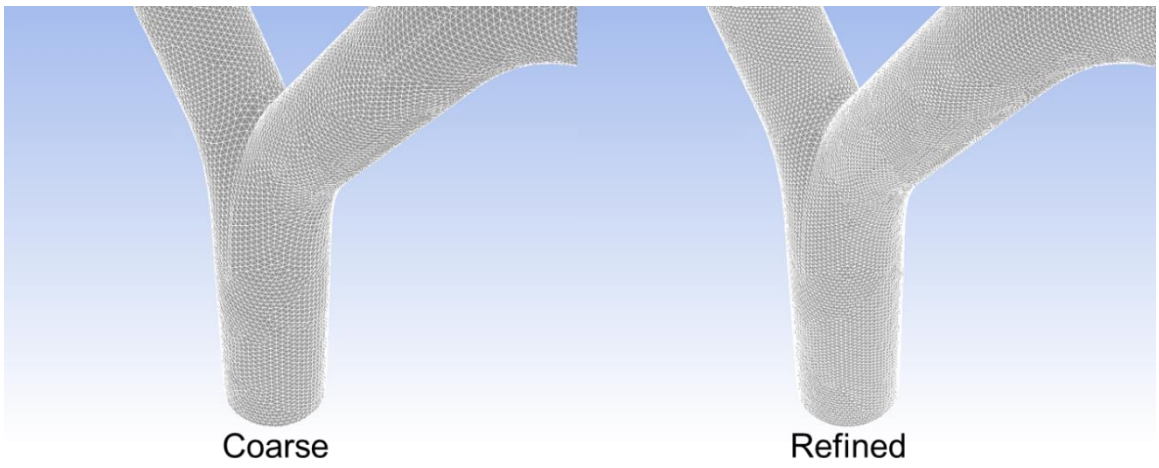

Figure 6.1 Unstructured grid for PRB showing two levels of refinement, coarse and refined.

6.2.3 Particle tracking: Lagrangian approach

The Lagrangian particle tracking scheme available in Fluent v12 was used to calculate the deposition fraction. The governing individual particle equations are

$$\frac{dx}{dt} = u \tag{6.1}$$

$$\rho_p V_p \frac{d\boldsymbol{u}}{dt} = \rho_p V_p \boldsymbol{g} + \boldsymbol{F}_D \tag{6.2}$$

where ρ_p is the density of the particle and is assumed to be much larger than the air density, V_p is the particle volume, g is gravitational acceleration, u the velocity vector and F_D is the drag force, as is described in Chapter 5. For these simulations, Brownian

motion was neglected. For this particular scenario, 100,000 randomly distributed particles were injected at the inlet with velocity equal to the fluid carrier (air). As an assumption, any particle striking an airway wall was assumed to adhere to the surface of the wall, and particle-particle interactions were also neglected.

6.2.4 Particle tracking: Eulerian approach

Eulerian particle phase transport equations were implemented in Fluent using User-Defined Function (UDF) subroutines. The same equations described in Chapter 5, Section 5.3.2 were used. Wall boundary conditions were used for the particle momentum equations which allow non-zero wall normal velocities to represent inertial impaction. Results shown in this section are for first order discretization schemes for the particle phase velocity.

6.3 Results and discussion

Results were compared to experimental data in terms of particle deposition patterns and cumulative deposition distribution within the PRB geometry. First, results for the airflow velocity are shown. Then, Lagrangian particle deposition patterns and Eulerian deposition patterns are discussed. Lastly, cumulative deposition percentages calculated from the main entrance tube in a positive y-direction until the last two branches were reached are discussed. The total length of the PRB is ~40 mm and the total cumulative deposition considered this length. As an example, at 20 mm, the first bifurcation has already been passed and the cumulative deposition percentage has considered all the particles that have been deposited previously to that point.

6.3.1 Fluid phase: Airflow velocity profiles

Eulerian simulations were first performed to find the air velocity profile. At the entrance, a parabolic velocity profile was utilized using a maximum velocity of 10.15 m/s for a Re ~1800 as shown in Figure 6.2. The most striking result was a stagnation point observed at the first bifurcation; thus, regions with relatively low velocity close to the outer walls of the PRB region were also observed. Velocity profiles at the outlet of the tube seem to be homogeneous. Regions of high velocity occurred close to the inside walls of the grid, and the particle phase velocity is compared next with these results.

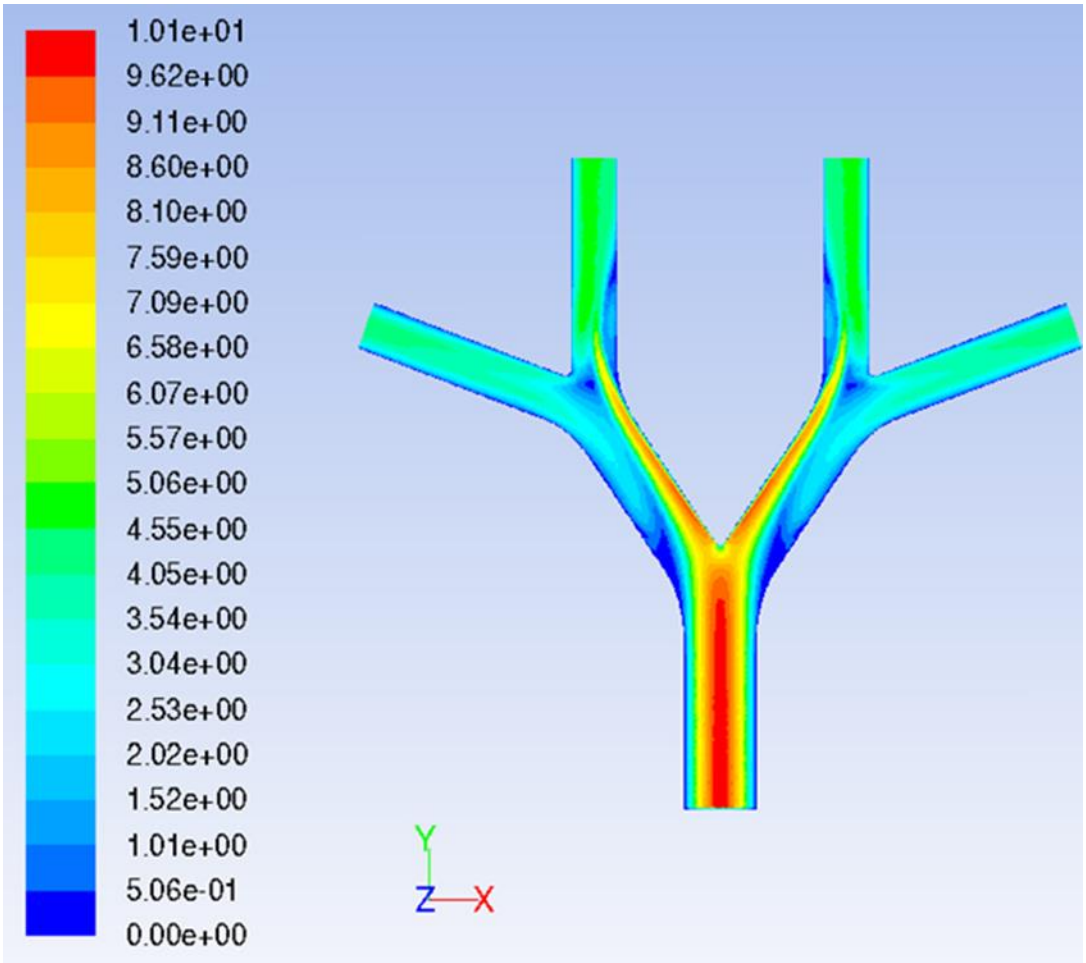

Figure 6.2 Center plane contours of air velocity magnitude for tetrahedral coarse mesh with a maximum inlet velocity of 10.15 m/s.

6.3.2 Particle transport: Lagrangian contours

Lagrangian simulations were used to track individual particles in each mesh. Some examples are shown for the tetrahedral mesh where individual paths can be observed for different particles injected at the entrance. Similar total deposition percentages were obtained for 100,000 of more injected particles. Qualitative results are shown in Figure 1.3 for 50,000 and 80,000 particles injected at the main branch, respectively. As observed, particles followed a path until and very few particles particles

exit the grid. This case was run for 15 micron-sized particles, and deposition percentages are a function of particle size (St) as explained and discussed in Chapter 5. When particles impact the grid walls, then those particles were assumed to deposit on the PRB wall and were included in the total deposition percentage calculation.

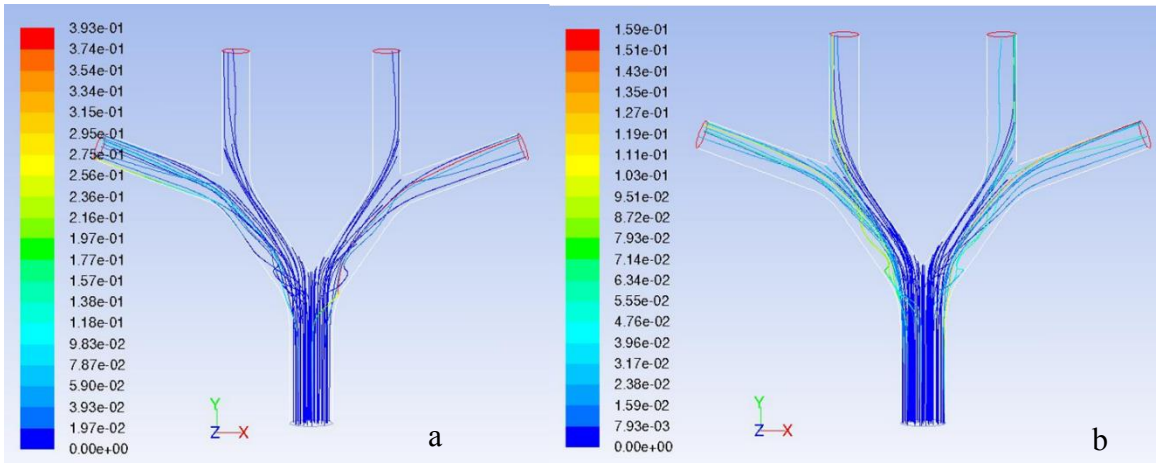

Figure 6.3 Lagrangian particle tracking

a) a 50,000 particle injection and b) a 80,000 particle injection.

6.3.3 Particle transport and deposition: Eulerian contours

Particle phase velocity was compared to the air flow velocity at the center plane of the PRB geometry. Similar results were obtained as compared with the air flow velocity profiles. However a particular difference is shown in Figure 6.4. As observed, particle phase velocity field differs from air phase due to particle inertia effects, including wall normal component at the bifurcation locations. The particle flow showed no stagnation point at the first bifurcation. Thus, particle phase considered inertial effects and particles theoretically can flow "out" through the walls, which is a symbolic representation of particle impaction and deposition on the walls.

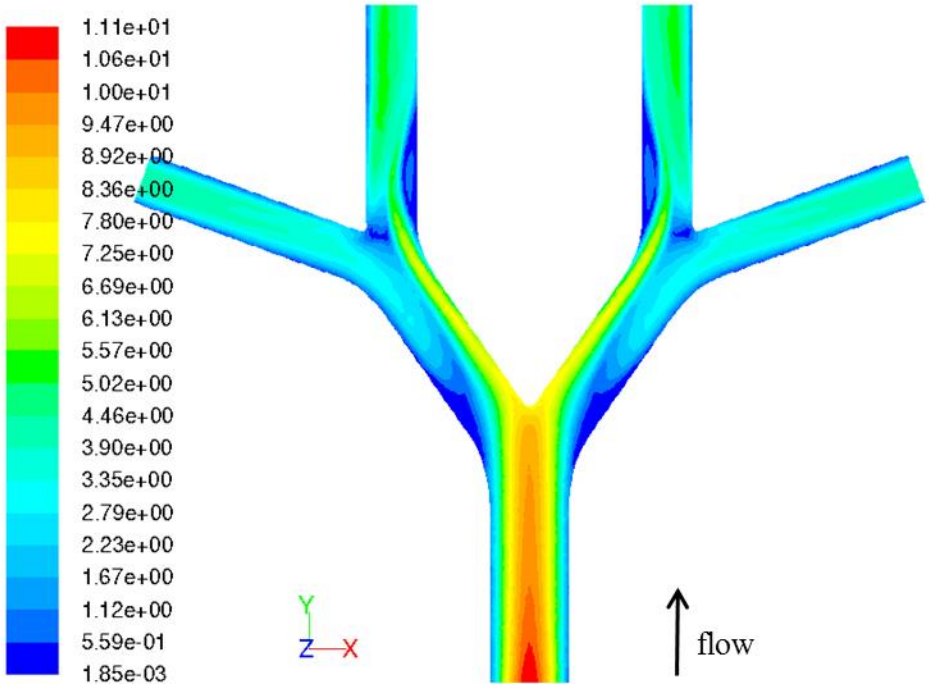

Figure 6.4 Particle phase velocity magnitude calculated using the Eulerian approach at the center plane.

Particle concentration contours can help to relate particle phase velocity and deposition on the PRB walls. Figure 6.5 shows the particle concentration profiles on which large concentration of particles (red regions) can be observed where particles had low velocities. These results were confirmed by observing the total deposition pattern on the 3-D PRB structure.

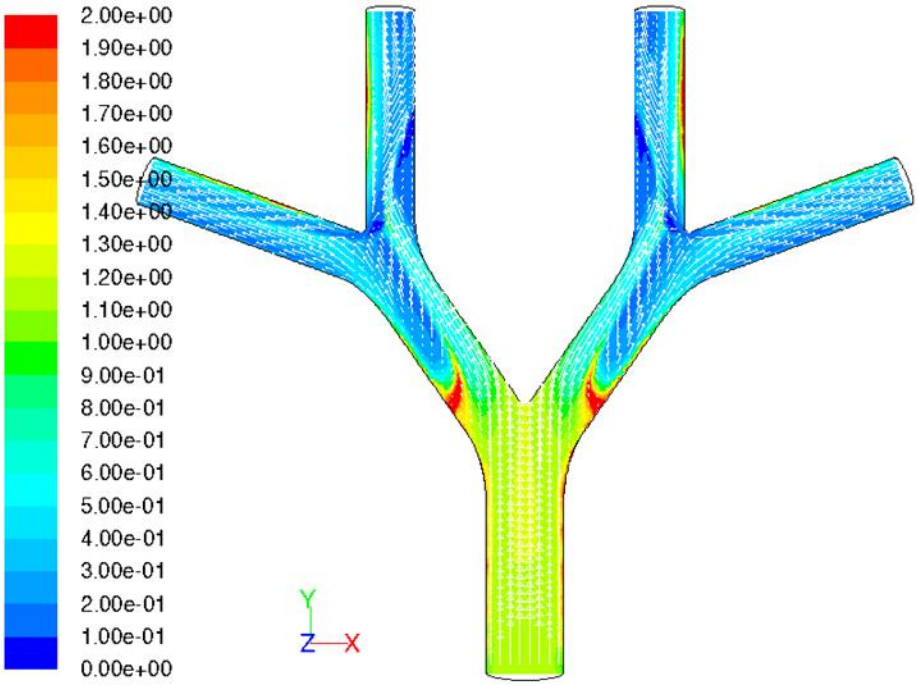

Figure 6.5 Final particle concentration profile at the center plane for an initial concentration of 1 at the inlet tube.

Qualitative results for the deposition patterns resemble the experimental results obtained elsewhere, showing high amount of particles deposited particularly in the bifurcation regions (Oldham et al., 2000b). These results can be observed in Figure 6.6 where a high concentration of particles was observed impacting the first and second bifurcations. In addition, some particles were deposited on the edges of the exit tubes. These results are in good agreement with the experiment previously discussed in literature.

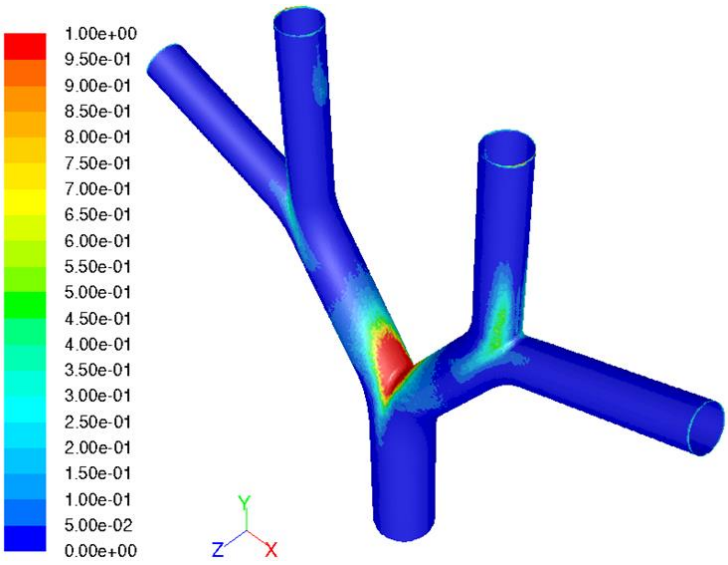

Figure 6.6 Qualitative deposition results for 9.97 micron particle diameter in a PRB unstructured grid.

6.3.4 Quantitative analysis: Comparison of experimental, Lagrangian and Eulerian results

This section compares quantitatively the deposition percentage occurring in the PRB by plotting cumulative deposition percentage vs. distance for different case scenarios. Previously, an explanation for the cumulative deposition percentage calculation was presented; thus, this parameter is plotted as a function of distance starting from the inlet tube until it reaches the last sections of the PRB geometry. Comparisons of mesh refinement, mesh topology, solution methods, inlet velocity profile, and particle diameter are discussed next.

6.3.4.1 Mesh refinement and topology: Eulerian and Lagrangian

Cumulative deposition percentage results are shown for the tetrahedral (TET) mesh, both for the coarse and refined levels of cell number. Interestingly, Lagrangian

and Eulerian simulations showed negligible differences between the two levels of refinement analyzed in this work, confirming grid independence for the cumulative deposition fraction.

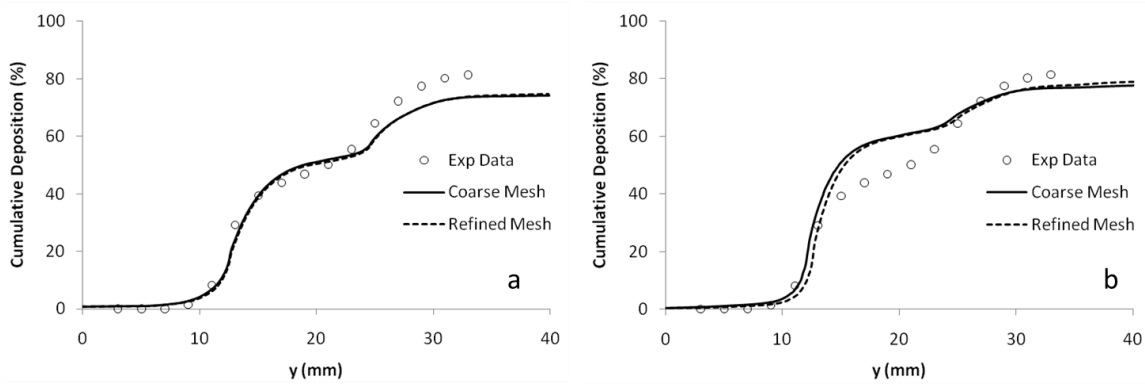

Figure 6.7 Effect on mesh refinement

a) Lagrangian and b) Eulerian simulations in the TET cell geometry.

Different analyses can be performed on the results shown previously (Figure 6.7). For example, Lagrangian results were independent of refinement level and the same trends were observed for both meshes. In addition, Lagrangian results were also in excellent agreement with the experimental results from the inlet until through the first bifurcation. After the second bifurcation, the Lagrangian data diverged from the experimental data, and the total cumulative deposition percentage was underpredicted. The Eulerian results also showed grid independence. The Eulerian results overpredicted the cumulative deposition percentage over the first bifurcation. However, the total cumulative deposition for the Eulerian method matches the experimental results better than the Lagrangian simulations.

The level of refinement was shown to be negligible for the PRB tetrahedral grid in the previous section. In this section, analysis is focused on the mesh topology. Tetrahedral and hybrid meshes were considered. The tetrahedral mesh is uniform throughout the PRB geometry with only tetrahedral cells used throughout the grid. The hybrid mesh has hexahedral cells close to the walls—where particle deposition occurs—and tetrahedral cells in the center of the PRB geometry.

Cumulative deposition percentage depicted to analyze the effect of mesh topology (Figure 6.8). For the Lagrangian method, cumulative deposition results on a tetrahedral mesh were in better agreement with the experimental data that the results obtained when using the hybrid mesh. The opposite trend was observed for the Eulerian method where the total deposition percentage was better predicted using a hybrid mesh.

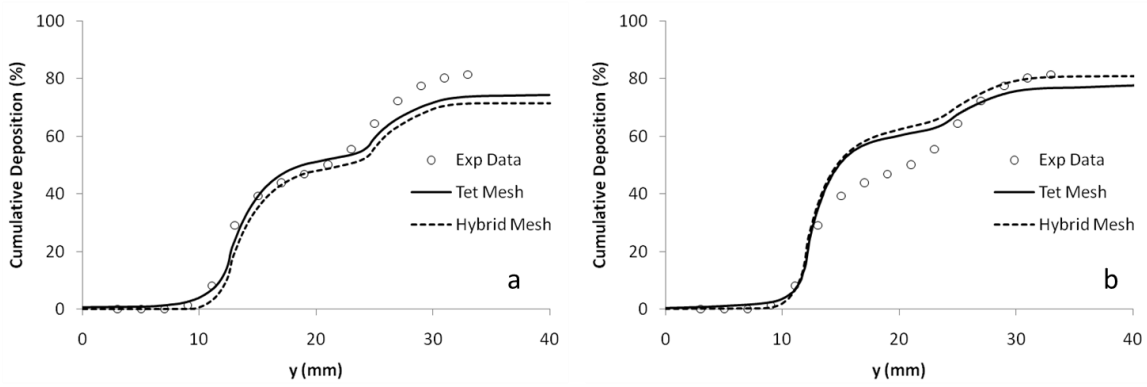

Figure 6.8 Comparison of mesh topology

a) Lagrangian and b) Eulerian simulations on the PRB geometry.

6.3.4.2 Comparison of simulation methods: Lagrangian vs. Eulerian

The most striking differences are probably better observed comparing both simulation methods on the two different mesh topologies (hybrid and tetrahedral). Figure

6.9 shows the simulation results for both methods on both meshes, and a comparison with the experimental data. Clearly, the total deposition percentage was very close for both methods on a tetrahedral mesh. But, Eulerian results seemed to overpredict the experimental values. On a hybrid mesh, Eulerian total cumulative deposition percentage was in agreement with the total experimental deposition percentage value. However, results overpredicted the cumulative deposition percentage for the first bifurcation. At this point, the methods are inconclusive with respect to understand which method is superior. Nonetheless, it has been shown that the new Eulerian method for particle deposition is in good agreement with the typical Lagrangian approach and experimental values.

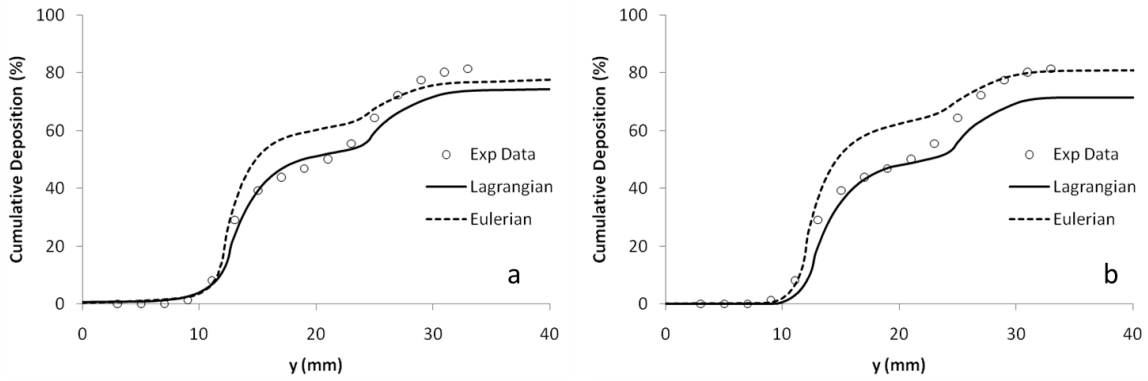

Figure 6.9 Comparison of simulation methods on a) tetrahedral mesh and b) hybrid mesh at the coarse level of refinement for Lagrangian and Eulerian simulations.

6.3.4.3 Effect of velocity inlet profile: Lagrangian vs. Eulerian

Velocity inlet profile can have a significant impact of particle deposition based on literature recommendations (Vinchurkar and Longest, 2008). Thus, the effects of a

change on velocity inlet profile are discussed. The different results previously analyzed considered parabolic inlet velocity profile at the main entrance. In this section, a flat/blunt homogeneous velocity value was considered at the inlet for the tetrahedral refined mesh. Mainly, the average velocity was considered uniform and calculated at the entrance of the PRB grid. Quantitative results are shown in Figure 6.10, and the results obtained with a blunt inlet velocity profile underpredicted the experimental results as compared with a parabolic inlet velocity profile. However, the fit at the first bifurcation had great improvements as compared with a parabolic inlet velocity profile. Thus, the effect of inlet velocity profile is as significant as the particle phase simulation method. Moreover, a critical parameter to evaluate and validate an inlet velocity profile is the comparison with the experimental work. Detailed experiments are needed to fully confirm the validity of a CFD model; until then, simulation approaches, as observed in this case, can be adjusted to match experimental results; but not applicable for usage on more complex grids, such as the human lung.

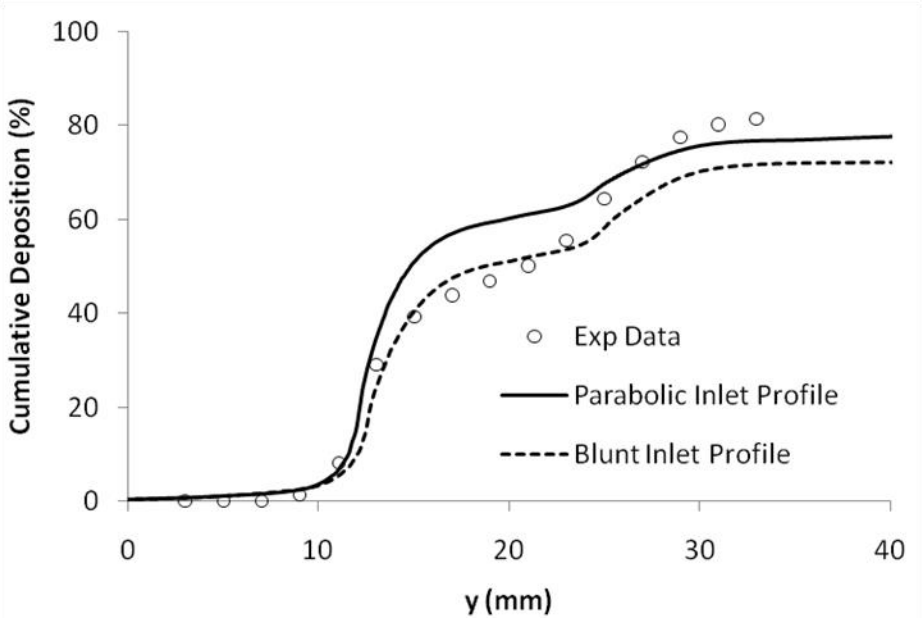

Figure 6.10 Inlet blunt velocity profile comparison with parabolic inlet velocity profile for Eulerian simulations.

6.3.5 Deposition rate and particle size dependence: Eulerian method

Different particle diameters have also been analyzed using an Eulerian approach. These experiments were performed due to possible utilization of Eulerian results on human lung geometries and/or larger and complex systems. Three different particle sizes (5, 10 and 20 microns) were analyzed using TET refined mesh; however, comparison with experimental data is only possible for 10 micrometers particle size. Figure 6.11 shows the cumulative deposition percentage for the different particles, and as expected as the particle size increases a higher deposition percentage was obtained. Moreover, the particular shape for each bifurcation observed in the last section was also observed for particles of different sizes. Results for 20 micron sized particles were 98.9% meaning

that almost all the particles were deposited on the surface of the PRB geometry. For 5 micron sized particle, only 31.6% of the particles deposited.

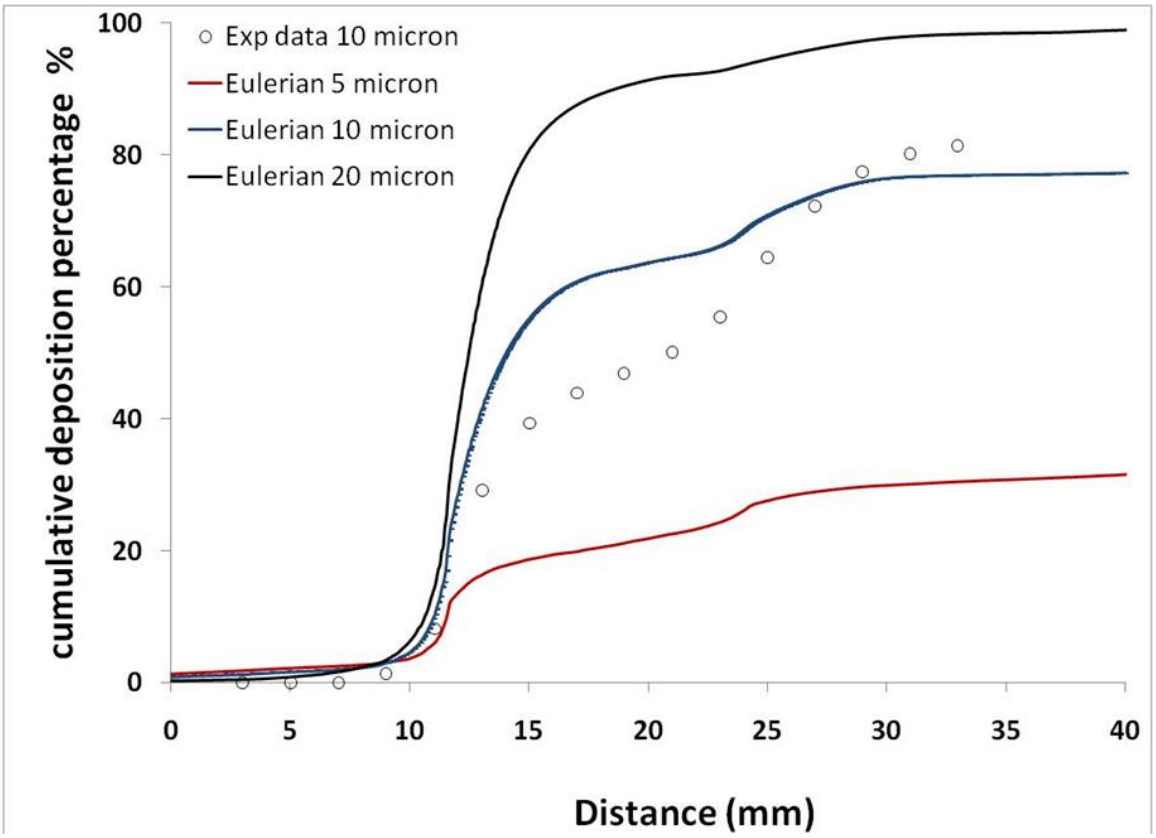

Figure 6.11 Cumulative deposition percentage for different particle size diameters using Eulerian simulation methods.

Particle volume fraction increased dramatically at the first bifurcation. This effect was clearly observed at the center planes of the PRB geometry. High concentration spots were obtained as the particle size increases, reducing the total amount of particles leaving the PRB. Figure 6.12 shows a representation of the different patterns obtained. These

results confirmed the cumulative deposition rate percentage obtained before due to the high amount of particles that were deposited after the first bifurcation.

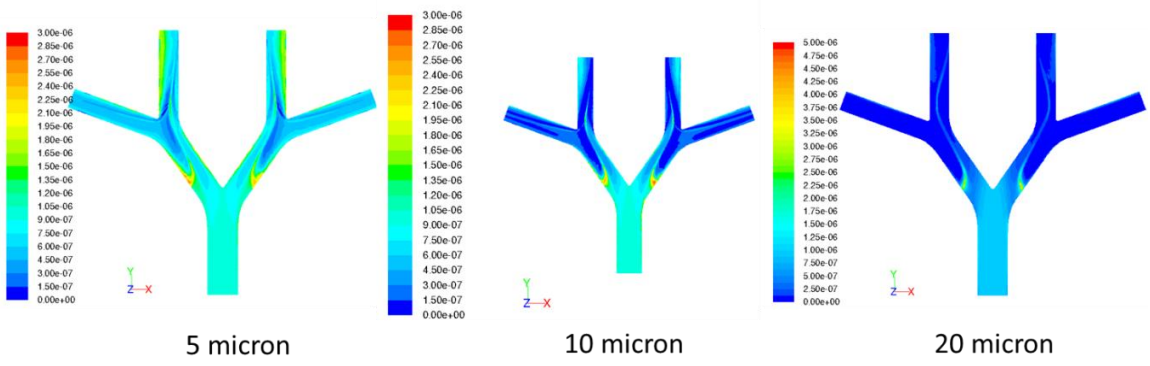

Figure 6.12 Particle volume fraction for different particle sizes at the center plane of the PRB geometry.

6.4 Conclusions

Analysis of the particle tracking and deposition predictions and comparison with experimental data for 10 micron, and 5 and 20 micron particles in a PRB human lung morphology model has been evaluated using an Eulerian and a Lagrangian approach. The two-phase coupled Eulerian method was in good agreement with Lagrangian and experimental data for 10 micron particles. The level of refinement used for the simulations was found to have negligible impact, despite a relatively large increase in cells between coarse and refined simulations. The effect of grid topology, hybrid vs. tetrahedral cells, showed small but non-negligible differences in the cumulative deposition fractions. A comparison of Eulerian-Eulerian and Eulerian-Lagrangian simulation methods shows that the Eulerian-Eulerian approach gives values for total deposition percentage closer to the experimental data, but agreement with the data

worsens after the first bifurcation and then the Eulerian-Lagrangian method is in better agreement. Conversely, a Lagrangian approach better captures the distribution of deposition as compared with experimental data using a parabolic inlet profile. The effect of the velocity inlet profile distribution had an impact on the results obtained; however, experimental details need to be confirmed to validate the assumptions performed in this study, as previously explained. More complex geometries and/or newer experimental sets of data should be used to validate the Eulerian particle tracking and deposition method presented and discussed in this chapter.

6.5 References

Heistracher, T. and W. Hofmann (1995a). "Physiologically realistic models of bronchial airway bifurcations." Journal of Aerosol Science **26**: 497-509.

Heistracher, T. and W. Hofmann (1995b). "Physiologically realistic models of bronchial airway bifurcations." Journal of Aerosol Science **26**: 497-509.

Heistracher, T. and W. Hofmann (1997). "Flow and deposition patterns in successive airway bifurcations." Ann Occup Hyg **41**: 537-542.

Hofmann, W., I. Balashazy and T. Heistracher (2001). "The relationship between secondary flows and particle deposition patterns in airway bifurcations." Aerosol Science and Technology **35**: 958-968.

Hofmann, W., T. Heistracher and I. Balashazy (1996). "Deposition patterns of inhaled radon decay products in human bronchial airway bifurcations." Environ. Int. **22**: S935-S940.

Holbrook, L. T. and P. W. Longest (2013). "Validating CFD predictions of highly localized aerosol deposition in airway models: In vitro data and effects of surface properties." J. Aerosol Sci. **59**: 6-21.

Longest, P. W. and L. T. Holbrook (2012). "In silico models of aerosol delivery to the respiratory tract - Development and applications." Adv. Drug Delivery Rev. **64**: 296-311.

Longest, P. W. and M. J. Oldham (2006). "Mutual enhancements of CFD modeling and experimental data: A case study of 1-micron particle deposition in a branching airway model." Inhalation Toxicology **18**: 761-771.

Longest, P. W. and M. J. Oldham (2008). "Numerical and experimental deposition of fine respiratory aerosols: Development of a two-phase drift flux model with near-wall velocity corrections." Journal of Aerosol Science **39**: 48-70.

Longest, P. W. and S. Vinchurkar (2009). "Inertial deposition of aerosols in bifurcating models during steady expiratory flow." Journal of Aerosol Science **40**: 370-378.

Martonen, T. B., J. D. Schroeter and J. S. Fleming (2007). "3D in silico modeling of the human respiratory system for inhaled drug delivery and imaging analysis." Journal of Pharmaceutical Science **96**: 603-617.

Oldham, M. J., R. F. Phalen and T. Heistracher (2000). "Computational fluid dynamic predictions and experimental results for particle deposition in an airway model." Aerosol Science and Technology **32**: 61-71.

Phalen, R. F., L. B. Mendez and M. J. Oldham (2010). "New developments in aerosol dosimetry." Inhalation Toxicology **22**: 6-14.

Vinchurkar, S. and P. W. Longest (2008). "Evaluation of hexahedral, prismatic and hybrid mesh styles for simulating respiratory aerosol dynamics." Computers & Fluids **37**: 317-331.

Weibel, E. R. (1963). Morphometry of the human lung. Berlin,, Springer.

Xie, Y., P. W. Longest, Y. H. Xu, J. P. Wang and T. S. Wiedmann (2010a). "In vitro and in vivo lung deposition of coated magnetic aerosol particles." Journal of Pharmaceutical Science **99**: 4658-4668.

Xie, Y., P. Zeng, R. A. Siegel, T. S. Wiedmann, B. E. Hammer and P. W. Longest (2010b). "Magnetic Deposition of Aerosols Composed of Aggregated Superparamagnetic Nanoparticles." Pharmaceutical Research **27**: 855-865.

CHAPTER VII

CONCLUSIONS

7.1 Conclusions

Computational simulations and experimental efforts have been carried out to obtain a better understanding of the transport, deposition, and surface modification of micron- and nano-sized particles. Experimental work was performed on magnetic nanoparticles ranging from 50 nm to 200 nm, resulting in the successful surface-confined polymerization of two different stimuli-responsive polymers: PNIPAM and PMAA. A novel methodology for the formation of biphasic Janus magnetic nanoparticle (JP) composites was developed, and the method can be expanded to nanoparticles with other functional groups and with or without a magnetic core. For all chemical modification, each reaction step was confirmed using FTIR. TEM and AFM imaging revealed the morphologies of the neat and surface modified nanoparticles, as well as the associations that occurred between the nanoparticles.

The pH- and thermo-responsiveness of different SRP-NP nanocomposite systems were evaluated using *in-situ* AFM, ellipsometry, and DLS. AFM was utilized to study the thermo-responsiveness behavior of a series of amino(meth)acrylate polymer brushes. Ellipsometry measurements were performed to evaluate the pH-responsiveness of these polymers by implementing a new GENOSC model. DLS was used to evaluate the responsiveness of surface-modified nanoparticles as a function of temperature. The

methods utilized in this work can be expanded to enable the synthesis of a wide range of nanocomposites and to evaluate in situ responsiveness.

Computational efforts include the development of a new Eulerian-Eulerian model, evaluated to confirm particle-transport and deposition in two different grids: a 90° bend and a physiological realistic bifurcation (PRB). Results obtained from this new model showed great agreement with experimental data and other models, including typical Lagrangian particle tracking methods. This Eulerian-Eulerian model is a new tool, improving computational time while effectively capturing particle deposition efficiencies, that could potentially be utilized for particle tracking inside the human lung and/or any other morphological structure.

New insights are presented through a focus on experimental and computational methods for micron- and nano-sized particles and surfaces. Nanotechnology and microtechnology have proven to be promising fields despite their infancy, and this work is expected to be complimentary for future studies, applications, and ventures. A summary of this work's main conclusions is presented next.

7.1.1 Surface modification of micron- and nano-sized particles

Chemical and morphological analyses confirmed the successful polymerization of different monomers on the surface of magnetic nanoparticles for three different scenarios: homopolymers, block copolymers, and biphasic polymers (resulting in Janus magnetic nanoparticles).

7.1.1.1 Chemical analyses

Surface modification of magnetic nanoparticles with different end-functionalized groups (–OH and $–NH_2$) and nominal diameters (50 nm, 100 nm, and 200 nm) was successfully performed, as was confirmed by XPS and FTIR. Different ATRP steps, such as initiation, homo- and block copolymer formation, and biphasic Janus nanoparticle production were all investigated with the techniques listed above.

ATR-FTIR analysis on Janus nanoparticle systems showed that post-polymerization steps confirmed the N-H peaks associated with primary amines of the 'bare' Fe_3O_4/NH_2 nanoparticles were no longer observed. In addition, characteristic carbonyl absorbances for PNIPAM (1650 cm^{-1}), and doublet peaks for the carboxylate anion from PMAA (1540 cm^{-1} and 1710 cm^{-1}) were clearly observed for the PMAA-Fe_3O_4-PNIPAM JP system. ATR-FTIR spectroscopy confirmed successful polymerization of homo- and block-copolymers on the surface of magnetic nanoparticles by monitoring chemical functionality changes at each reaction step.

Changes in surface chemistry were also monitored using XPS. For this purpose, the biphasic-Janus magnetic-nanoparticles were characterized, confirming the successful surface modification of the particles. XPS survey scans revealed average atomic percentage for "as received" magnetic nanoparticles of: carbon 55.37 ± 1.51%, oxygen 27.96 ± 17%, nitrogen 2.67 ± 2.5%, silica 3.79 ± 1.95%, and iron 5.23 ± 9.23%. XPS survey scan results for the Janus nanoparticles showed only carbon and oxygen after formation of PMAA-Fe_3O_4-PNIPAM JPs. Average atomic compositions obtained for Janus nanoparticles were carbon 73.77 ± 1.59%, oxygen 21.75 ± 1.79%, and nitrogen 4.48 ± 0.37%. Therefore, it is concluded that the entire surface of the magnetic

nanoparticle has been successfully surface-modified with polymer brushes on both hemispheres. For comparison purposes, a 50/50 mix of PNIPAM and PMAA will have a theoretical atomic percentage of carbon 70.8%, oxygen 22.9%, and nitrogen 6.3%. Elemental composition for carbon and oxygen measured by XPS are close to this theoretical mixture (C 74.4%, O 25.6%), however, nitrogen was not observed in the XPS measurements collected. Additionally, high resolution scans confirmed different changes for carbon atoms.

7.1.1.2 Morphological characterization

The production of hemispherical ("half-moon") structures for the generation of a biphasic Janus magnetic nanoparticles was confirmed by TEM. Additional AFM studies were then conducted to further confirm the half-moon morphology of these Janus nanoparticles. AFM topography images were used to observed the hemispherical shape of PNIPAM-Fe_3O_4/NH_2. After confirming the desired morphology, the second monomer (MAA) was grown on the opposite side of PNIPAM-Fe_3O_4/NH_2 via ATRP. TEM and AFM images confirmed the changes in the morphological structure after these steps. Moreover, TEM was primarily used to confirm the presence of block-copolymers on the surface of magnetic nanoparticles.

7.1.2 pH- and thermal-response characterization of stimuli-responsive polymers grafted on different substrates.

DLS, *in-situ* ellipsometry, and AFM were used to evaluate the performance of different responsive polymers while grafted on a specific surface. DLS was used to evaluate the thermo-responsive behavior of PMAA-PNIPAM-Fe_3O_4 nanocomposite system. Results confirmed the expected contraction of the polymer chains as temperature

was increased. The lower critical solution temperature (LCST) of the system was obtained over a certain range of temperatures, due to the fact that PNIPAM was combined with PMAA forming a heterogeneous polymer brush grafted on the surface of MNPs.

Different amino(meth) acrylate polymer brushes were also grafted on silicon wafers and evaluated as potential pH sensitive materials. A new model that includes a general oscillator layer (GENOSC) was implemented and used to obtain thickness and the optical properties of these polymer brushes as pH changed. However, parameters such as non-uniform thicknesses, roughness, and low grafting density negatively impacted the results due to data collection. Despite these results, PDMAEA and PTBAEMA proved to be pH responsive materials due to the protonation of the amine groups at low pH values. Similarly, PDEAEMA and PDMAEMA are affected in pH ranges of 4-10. In these conditions, the polymer chains swell rather than contract, producing the opposite effect reported in literature (swell as pH decreases). Thus, it is concluded that phosphate buffer solutions (PBS) interact with the polymer chains, opening new applications and possible studies with salt interactions and charges within the polymer backbone. Temperature changes were observed but not statistically conclusive at this point. Future work will analyze other types of polymers to confirm the results obtained by the GENOSC modeling in this work.

7.1.3 Analysis of particle-transport and –deposition of micron-sized particles in different grids

Two different cases: a 90° bend and physiological realistic bifurcation (PRB) were used to evaluate the performance of a Eulerian-Eulerian model for particle tracking and deposition studies. The results are reviewed next.

7.1.3.1 Case I: 90° bend

Particle tracking and deposition predictions were compared with experimental data for particle size ranging from 5-12 micrometers (Stokesian regime). Results in this work have led to several important findings. The two-phase coupled Eulerian method, ran in hybrid meshes, provided good agreement with the experimental data for the deposition of small particles(< 5 microns) despite the Re number of study. Moreover, particle deposition percentages were affected by the gravitational component as they deposited close to the curved surface in the 90° bend. As a result, gravity affects deposition results at low Stokes number for low Reynolds and Dean Numbers. In general, the two-phase Eulerian particle approach proved to be as successful as other methods previously published in literature, and is in good agreement with experimental data for different laminar flow and Stokesian regimes.

7.1.3.2 Case II: Physiological realistic bifurcation (PRB) grid

Eulerian-Eulerian simulations were also conducted for the prediction of the particle tracking and deposition patterns for 10 micron-sized particles in a human lung morphology (PRB), compared with experimental data, and compared with a Lagrangian approach. The two-phase coupled Eulerian method is in good agreement with Lagrangian and experimental data for 10 micron sized particles. Different factors were

analyzed to evaluate the results. First, the level of refinement used for the simulations was found to have negligible impact, despite a relatively large increase in cells between coarse and refined simulations. Second, the effect of grid topology—hybrid vs. tetrahedral cells—showed small but non-negligible differences in the cumulative deposition fractions. A comparison with both simulation methods leads to an Eulerian approach that provides better values for total deposition percentage but worse agreement with data through first bifurcations. Conversely, a Lagrangian approach captures better the distribution of deposition as compared with experimental data using a parabolic inlet profile. Additionally, the effect of the inlet velocity profile distribution had an impact on the results obtained; however, experimental details need to be confirmed to validate the assumptions utilized in this study. This may be a contribution of experimental error on the results obtained, as available experimental data confirmed confident intervals. Lastly, different particle sizes were also evaluated using the new Eulerian method. More complex geometries and/or newer experimental sets of data should be used to confirm the validation of the results presented and discussed in this chapter.

APPENDIX A

EXAMPLE ON THE SURFACE MODIFICATION OF SILANOL COATED MAGNETIC MICROPARTICLES>

A.1 Summary

In addition to 'as-received' Fe_3O_4/NH_2 magnetic nanoparticles, silanol coated microparticles, hereafter Fe_3O_4/OH, were also modified with ATRP to demonstrate the reaction process. Diffuse reflectance infrared spectroscopy(DRIFTS) was performed on this particles to obtain the chemical analysis of the sample as PMAA was grown on the surface.

A.2 Equipment

A Nicolet 6700 FT-IR with a mercury cadmium telluride (MCT) detector and dry gas purging was used to collect the DRIFT spectra. Thermo Scientific Ommic 8.1.10 software was used for data acquisition and analysis. Fe_3O_4/OH and surface-modified Fe_3O_4 nanoparticles were mixed with KBr powder (3 % w/w) for sampling and pure KBr was used as a background for DRIFTS analyses. Scans were collected from 400 cm^{-1} to 4000 cm^{-1} with a minimum of 256 scans collected at a 4 cm^{-1} resolution.

A.3 Materials and ATRP methodology

A.1.1 Materials

Fe_3O_4-OH (Chemicell), 1 micron nominal diameter, copper (I) chloride (Aldrich, 97%), triethylamine (Aldrich, 99.5%), Me_6TREN (Aldrich), methacrylic acid (Aldrich, 99%), water (Aldrich, HPLC grade), 2-bromoisobutyril bromide (Aldrich, 98%), toluene (Acros, 99.8%), tetrahydrofuran (THF; Fisher Sci., 99.9%), propanol (Aldrich, 99.7%).

A.1.2 Synthesis of Fe_3O_4-initiator

Modified Fe_3O_4-NH_2 nanoparticles were placed in 0.12 M triethylamine/THF solution for 10 seconds at ~ 0 °C. Then, a 0.1 M 2-bromopropionyl bromide/THF

solution was added to the reaction tube. This initiation reaction was allowed to proceed as it reached room temperature overnight and was performed under an inert nitrogen atmosphere using a steady flow of nitrogen to sparge the solution.

A.1.3 Synthesis of Fe_3O_4-PMAA

ATRP of MAA, either as a homopolymer or the second block, was conducted at a neutral pH. A 2 M solution of MAA/HPLC water was prepared, 1 M NaOH was added to neutralize the solution to a pH of 7, and then the solution was placed under a stream of nitrogen for ~1 h. To start the polymerization of MAA, a 0.1 mM solution of Me_6TREN and Cu(I)Cl was added to the monomer solution. This reaction was performed for 5 mg microparticles

A.4 Results and discussion

Si-O-Si bond, with a sharp double peak 1080 cm^{-1} is observed in the as received silanol particles (Alba et al., 1996). In addition a broad OH group can be seen at 3300 cm^{-1}. These result confirmed the presence of silica and an OH group on the surface of the as-received silanol particles (Figure A.1a)

FTIR spectroscopy was performed on PMAA-Fe_3O_4 and the spectra (Figure A.1b) showed chemical functionality expected for PMAA.. In particular, Figure 3 shows absorption peaks in the wavenumber region from 2900-3000 cm^{-1} that corresponds to -CH_2 and -CH_3 stretching vibrations, and a broader -O-H stretch (3300 cm^{-1}) as a result of the acid alcohol group present in the PMAA structure (Day and Underwood, 1991). Carbonyl (C=O) C-O stretching peaks from the carboxylate anion (C(=O)-O-) and acid (C(=O)OH) group observed at 1414 cm^{-1} and 1710 cm^{-1}, respectively, corresponding to a

PMAA structure (Matyjaszewski and Davis, 2002). Thus, PMAA was also coated on the surface of 'as-received' magnetic nanoparticles.

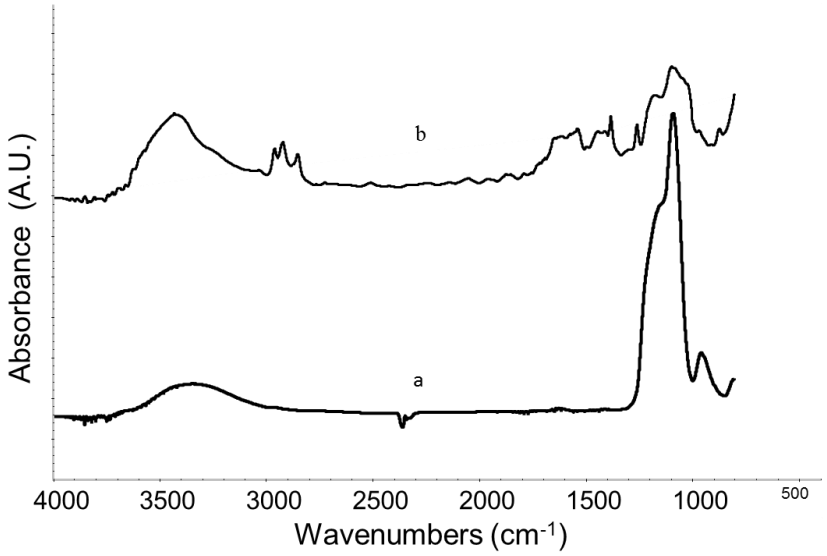

Figure A.1 DRIFT spectra of a) 'as received' silanol functionalized magnetic nanoparticles (Fe_3O_4/OH), and b) PMAA-modified magnetic nanoparticles (Fe_3O_4-PMAA).

A.5 References

Alba, M. D., Z. Luan, et al. (1996). "Titanosilicate Mesoporous Molecular Sieve MCM-41: Synthesis and Characterization." The Journal of Physical Chemistry **100**(6): 2178-2182.

Day, R. A. and A. L. Underwood (1991). Quantitative analysis : laboratory manual. Englewood Cliffs, N.J., Prentice-Hall.

Matyjaszewski, K. and T. P. Davis (2002). Handbook of radical polymerization (p. 523). New York: Wiley-Interscience.

APPENDIX B

SURFACE MODIFICATION OF MAGNETIC NANOPARTICLES: SONICATION EFFECTS

B.1 Summary

This section provides a brief summary of suggested work for future studies that will perfectly compliment the results and conclusions obtained from this study as a whole. The following sections describe modifications that could be considered for the surface modification of nanoparticles and two different characterization techniques that will allow for further explanation of *in-situ* effects of nanoparticle composites.

B.2 Analysis of preliminary results and future work

Sonication can improve nanoparticle dispersions and produce more homogeneous coating on its surface. The suggested configuration is shown in Figure A.2. Nitrogen is fed through a line to guarantee an inert atmosphere at all times. A thermocouple is also connected to the system, while the reactor is inside a controlled temperature bath to ensure homogeneous temperature. An injection port is used to introduce solution at any particular time; this port also helps to connect two external pumps. An external magnet is placed beside or below the reactor as depicted in Figure A.2

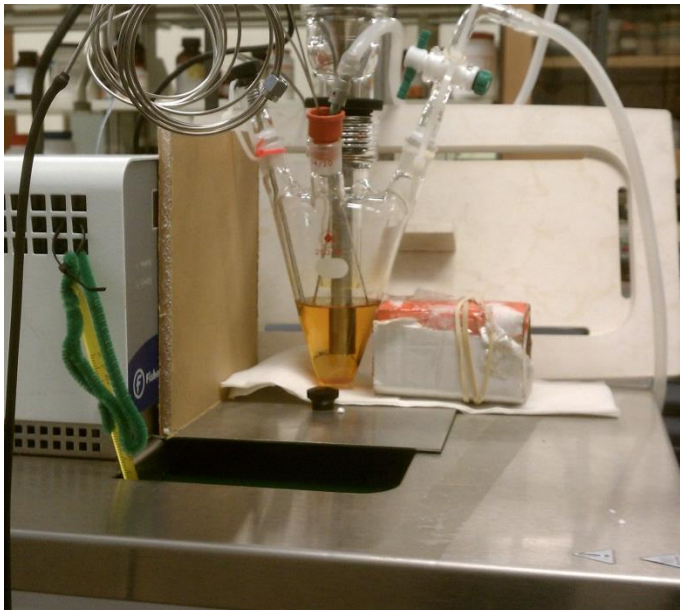

Figure A.2 Nanoparticle reactor equipped with a sonicator probe to mix magnetic nanoparticles.

Magnetic separation and particle washing is suggested to be inside the reactor to avoid any contact of the sample with air or oxygen. After allowing the particles to interact with the magnet for a certain amount of time (~2 hours), a peristaltic pump is connected to remove the unnecessary solvent, then another pump is used to flow anhydrous ethanol to the reactor to wash the particles. This procedure is repeated three times or until a clean ethanol solvent is observed inside the reactor as pictured in Figure A.3.

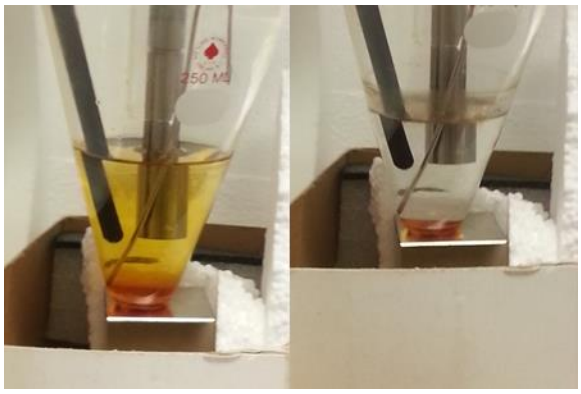

Figure A.3 Nanoparticle wash with anhydrous ethanol.

Nanoparticles were separated with the aid of magnet after bromine initation (left image). At least two washes are needed to obtain clean solvent on top of the magnet (right image).

'as-received' Fe_3O_4/NH_2 magnetic nanoparticles with two different nominal size: 200 and 50 nm, respectively, have been already tested using the sonicator reactor, thus, only preliminary data is presented in this work. Conditions for both studies include a monomer/catalyst/ligand ratio of 100/1/1 and 2.5 mg of magnetic nanoparticles. Nanoparticles were initially separated using an external magnet. Once the particles were separated, anhydrous toluene was added and the solution transferred to the sonicator reactor. Then, initiation was performed using two methods. 200 nm 'as-received' Fe_3O_4/NH_2 particles were initiated using a 0.12 M solution of triethylamine and 0.1 M 2-bromo-isobutyryl bromide on toluene. This reaction was performed for 6 h at 5 °C. 50 nm 'as-received' Fe_3O_4/NH_2 particles were initiated using a 3% v/v 2-bromoisobutyl bromide/toluene overnight under sonication effects. Sonication was tested at 20% power for two different cycles. 200 nm particles were sonicated at an on/off ratio of 2:10 seconds; whereas, 50 nm particles were sonicated at an on/off ratio of 2:5 seconds. All these experiments were performed in a thermo-controlled bath, guaranteeing reaction

temperatures to be at 20 °C at all times—an advantage over the results shown in Chapter 2.

Few results were obtained for this particular series of experiments; nonetheless, it can become a new field of study, because to the author's knowledge no surface modification studies on the surface of magnetic nanoparticles have been conducted with the aid of sonication. Parameters such as temperature, and sonication power and on/off ratio, can be controlled and provide new directions for research. As an example, berry-type magnetic nanoparticles were obtained in TEM measurements as shown in Figure A.4.

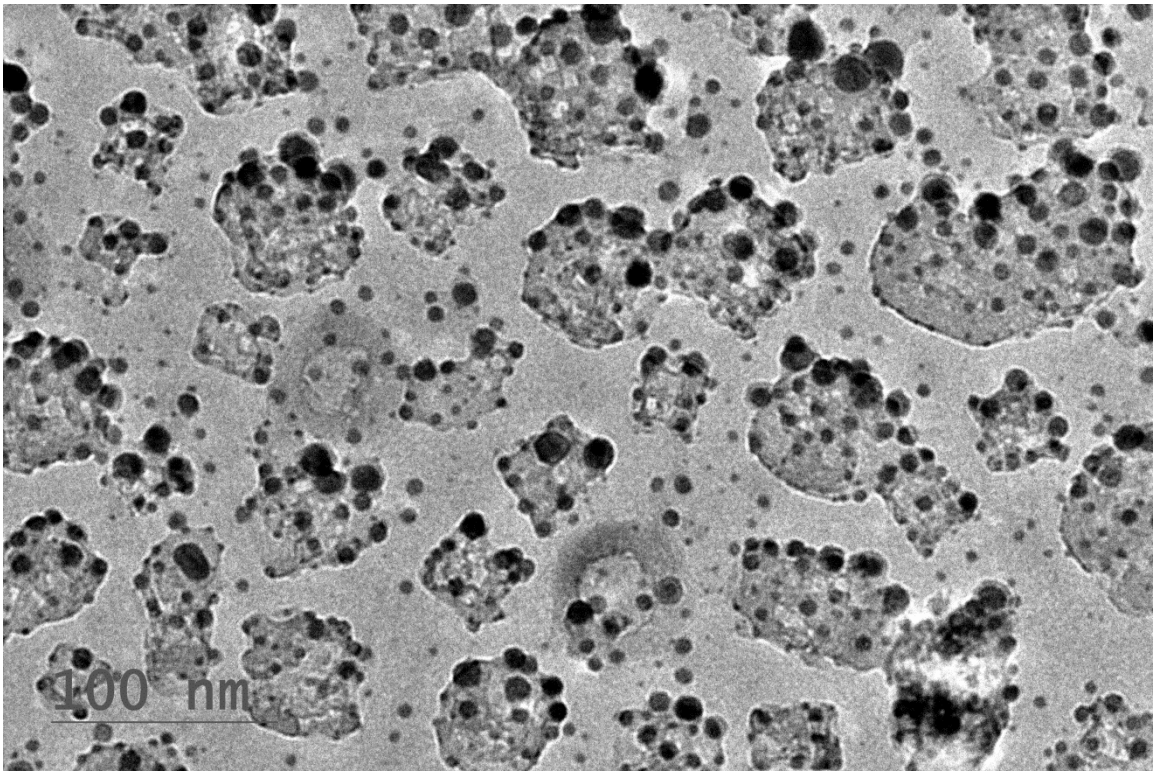

Figure A.4 TEM picture showing PNIPAM-Fe_3O_4 magnetic nanoparticles after a sonication reaction using a 2:10 sonication "on/off".

Interestingly, the nominal particle size of the nanoparticles pictured above was 200 nm; however, smaller composite structures were observed. "As-received" Fe_3O_4/NH_2 magnetic nanoparticles are depicted in Figure A.5. Only recently did the vendor (Chemicell) announce that their particles with nominal diameters larger than 100 nm were indeed multicore agglomerate structures. This is clearly seen in Figure 1.4. In fact, nanoparticles are not perfect "spheres" and their asymmetry will affect experiments such as DLS and UV/Vis spectroscopy. After observing this particular behavior, a second trial was performed on 50 nm Fe_3O_4/NH_2 and the results to date are included in this section as the basis of a future work discussion. Moreover, questions regarding the berry-type nanocomposite formation arise due to their unexplainable formation as it could be an effect of the sonicator probe or the TEM beam (200 kV).

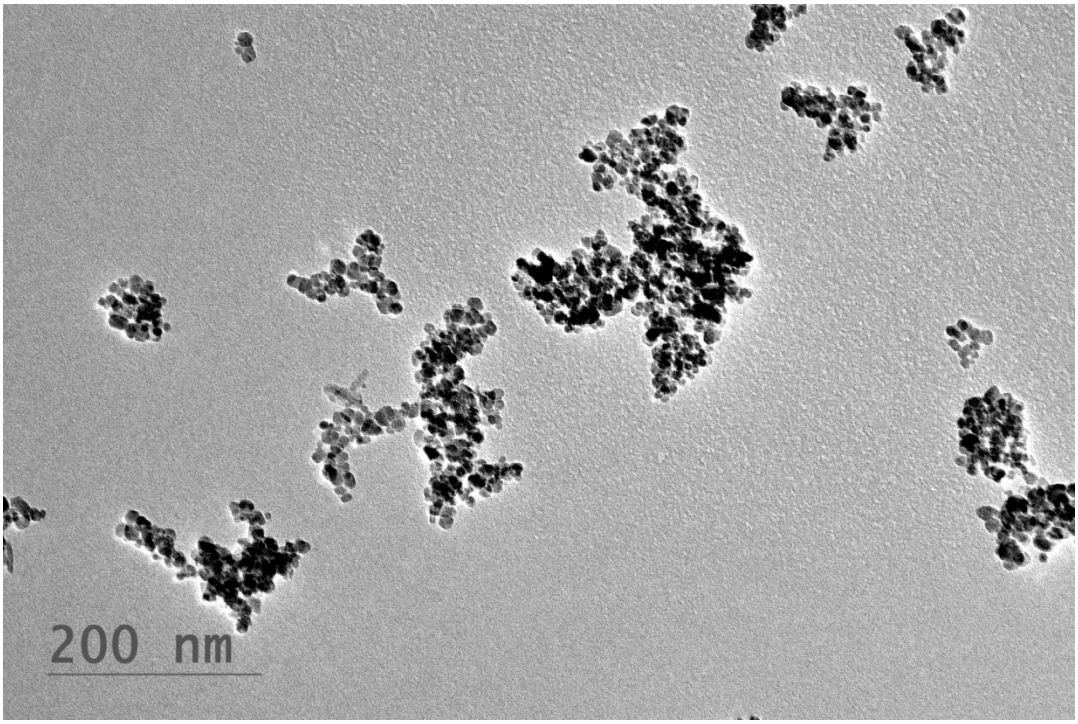

Figure A.5 Illustration of "as-received" 200 nm nominal diameter Fe_3O_4/NH_2 magnetic nanoparticles showing a silica core on the outside of an agglomerate of particles.

APPENDIX C

ENERGY DISPERSIVE X-RAY SPECTROSCOPY (EDS) STUDY ON A COPPER GRID

C.1 Summary

EDS was collected on a new 300 mesh copper grid with carbon film support coating. Results display a high percentage of carbon (86.5%) with respect to Copper (11 %) and oxygen (2.6) as depicted in Figure A.6. In fact, scans were collected on some surface-modified samples (results not shown) and high variability was observed, especially when close to the edges of each mesh.

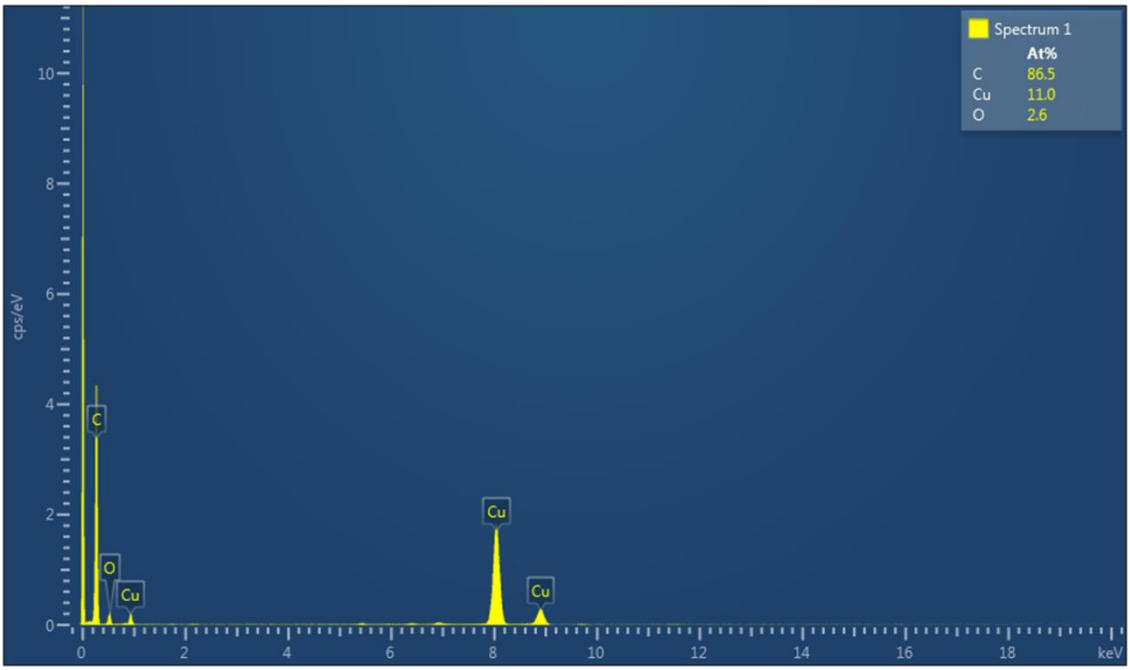

Figure A.6 EDS spectra of a clean/'as-received' copper/carbon coated grid that was used to deposit the surface-confined magnetic nanoparticles

APPENDIX D

DLS ANALYSIS OF ‘AS-RECEIVED’ MAGNETIC NANOPARTICLES

D.1 Objective

DLS was used to study the effects of heating on 'as-received' Fe_3O_4/NH_2 magnetic nanoparticles, and to compare with the surface modified Fe3O4@-PNIPAM-*b*-PMAA nanoparticles.

D.2 Equipment

The equipment used to characterize the 'as-received' nanoparticles was:

a. Brookhaven DLS: Dynamic light scattering measurements were collected at different temperatures with a ZetaPALS analyzer at a laser wavelength of 659 nm, Polystyrene cuvettes. A continuous model was used to obtain a hydrodynamic diameter by number using Particle Solutions (v 2.0) software from Brookhaven.

b. Wyatt DLS: A Dynapro Nanostar manufactured by Wyatt was used for DLS measurements, and Wyatt's Dynamics (v7.0.0) software was used to fit the data. Hydrodynamic radius was fitted by intensity using a Raleigh spherical model.

D.3 Results

Figure A.7 shows the response obtained for as-received MNPs as temperature was increased. In order to confirm that the particles did no extend while heating, two different equipment, and two different models were tested. As expected no response was obtained on the as-received magnetic nanoparticles. First, Brookhaven instruments are shown for a hydrodynamic diameter (thickness) obtained using a continuous model and analyses were performed by number analysis. In contrast, Wyatt results are shown for

intensity analysis and Rayleigh sphere models. Both, models and equipment, showed similar results. Thus, results previously discussed in Section 2.5.3 are confirmed, and temperatures variations on the hybrid nanoparticle system are mainly caused by the polymers grafted on the surface of the 'as-received' nanoparticles.

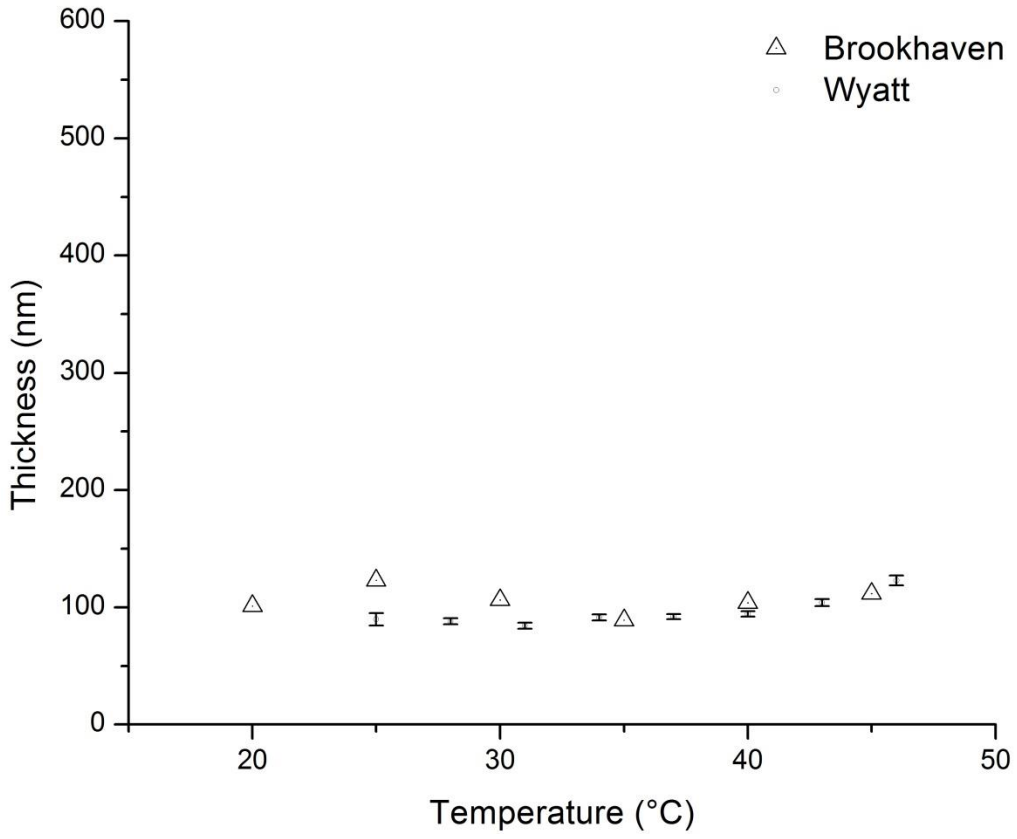

Figure A.7 Thickness response of 'as-received' Fe_3O_4/NH_2 at different temperatures using two different equipments.

Brookhaven instruments shows the hydrodynamic diameter for 100 nm 'as-received' nanoparticles, whereas Wyatt results are hydrodynamic radius.

APPENDIX E

SUPPORTING INFORMATION FOR THE ANALYSIS OF THE PH- AND THERMO-RESPONSIVENESS BEHAVIOR OF AMINO(METH)ACRYLATE POLYMER BRUSHES

E.1 Ellipsometry data collection: Modeling Psi and Delta

Ellipsometry measurements provide two parameters: Psi and Delta. In fact, these parameters are then fitted to a model; traditionally, a Cauchy layer model is used to obtain a thickness value at a single wavelength. Here, spectroscopic ellipsometry combined with a GENOSC model provides an enhancement in data modeling and characterization of thin films while grafted at a surface. As an example, Figure E.1 shows Psi an Delta for PDMAEMA and the model , dash lines, chosen to fit the data. As observed, selected regions of the spectrum, below 325 nm, are very noisy. This is due to the absorption of the pH solutions at these low wavelength values. Those, model was fit only to stable and non-noisy data as depicted in the same figure.

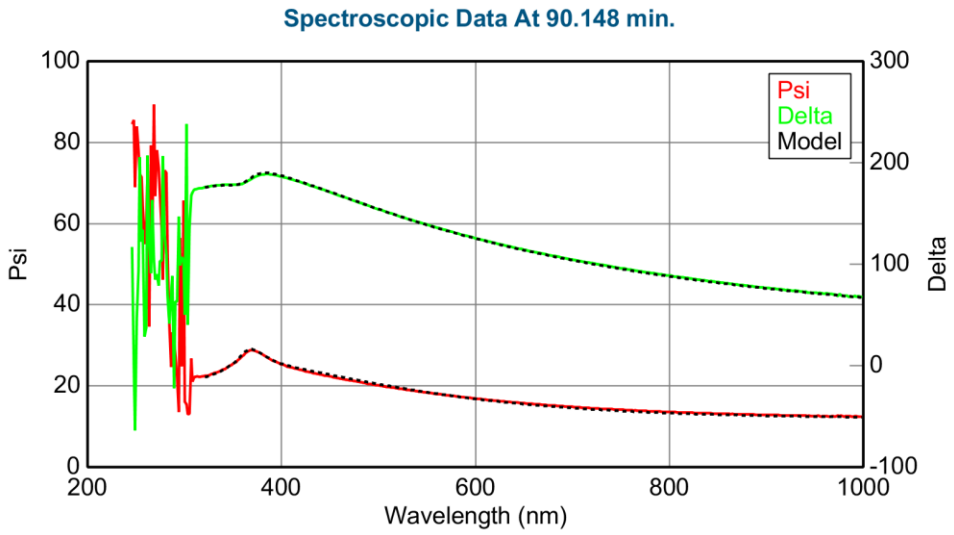

Figure E.1 Psi and Delta collected for PDMAEMA at ph 6 after 90 minutes of data collection

E.2 PBS buffer solutions

Different pH PBS solutions were utilized to characterize the pH-responsiveness of the different amino(meth)acrylate polymers presented in this work. Table E1, presents a summary of these pH buffer solutions

Table E.1 PBS buffer solutions utilized for the characterization of the pH-responsiveness of amino(meth)acrylate polymer brushes

pH	salts
2	Potassium hydrogen phthalate
3	Potassium Acid Phthalate, Sodium Hydroxide
4	Potassium hydrogen phthalate
5	Potassium Acid Phthalate, Sodium Hydroxide
6	Potassium Phosphate Monobasic, Sodium Hydroxide
7	Potassium Phosphate Monobasic/Sodium Hydroxide
8	Potassium Phosphate Monobasic/Sodium Hydroxide
9	Boric Acid/Potassium Chloride/Sodium Hydroxide
10	Boric Acid/Potassium Chloride/Sodium Hydroxide

E.3 Monomer/catalyst/ligands ratios used for ATRP and reactions schemes

A SAM was first deposition by treating the wafers in piranha solution (-OH end functionalized group), after attachment, 3-aminopropyldimethyl ethoxysilane was used to create the SAM ($-NH_2$). A bromine initiator, 2-bromoisobutyryl bromide, was reacted in a 3 % v/v toluene solution overnight. Lastly, monomers were polymerized using surface-confined ATRP/SET polymerization (Ding et al. 2009). An example is depicted for DEAMEA (Figure E.2), and ratios utilized for each monomer are also displayed in .

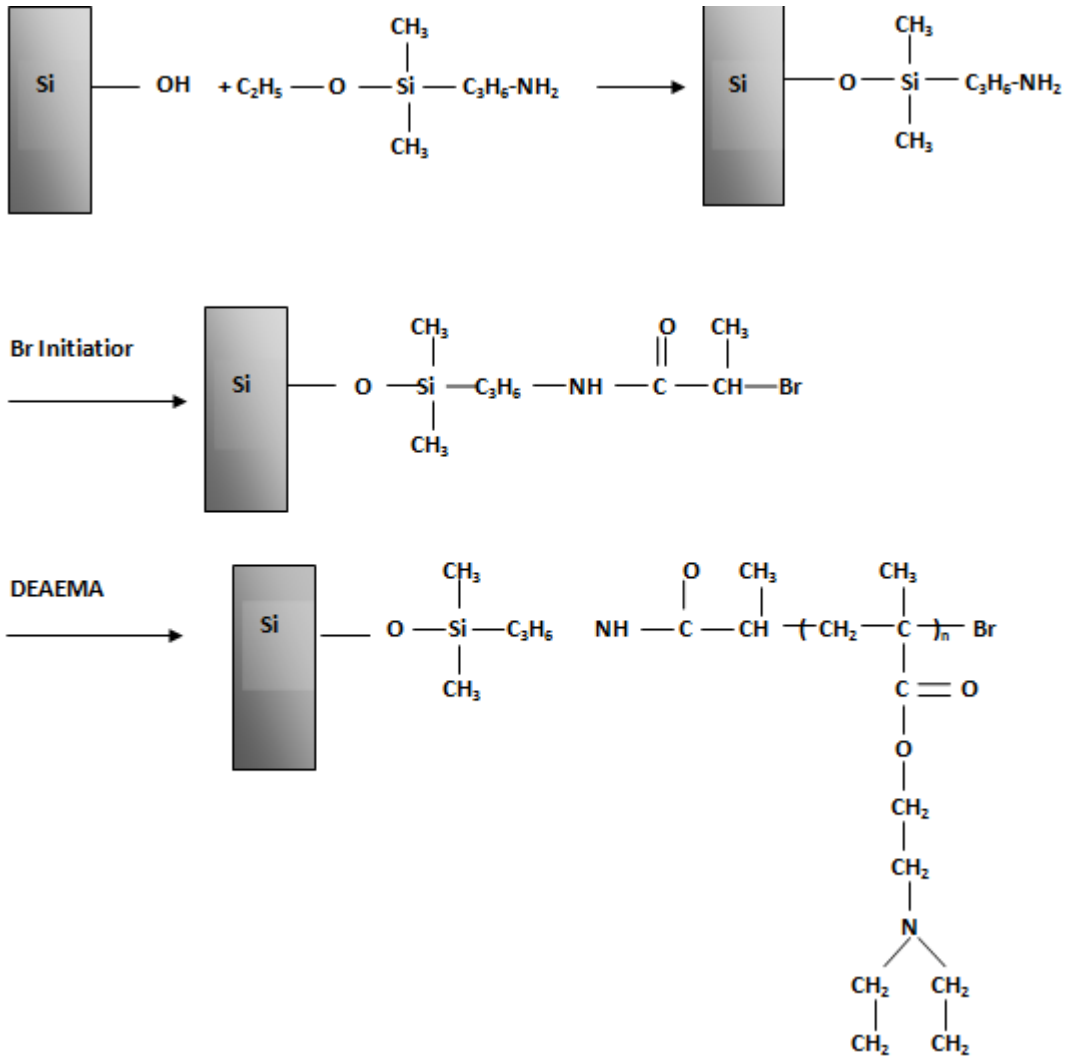

Figure E.2 Schematic showing the ATRP of amino(meth)acrylate monomers on Si wafers.

First, Si-wafers were treated in piranha solution. Then, 3-aminopropyldimethyl ethoxysilane was used as the SAM. A bromine initiator 2-bromoisobutyryl bromide was added to scheme. Lastly, monomers were polymerized using surface-confined ATRP/SET polymerization (Ding et al. 2009). Example is shown for DEAEMA.

A typical monomer/ligand/catalys/catalyst ratio was 100/4/10/1/. A summary of the different solvents and conditions of study are shown in Table E.2.

Table E.2 Monomer/catalyst/ligand utilized at different solvent, temperatures and times for the ATRP reactions of amino(meth)acrylate polymer brushed.

Monomer	Catalyst(S)	Ligand	Solvent	Temp (°C)	ATRP time (h)
DMAEMA	$CuBr/CuBr_2$	Bypiridine	IPA/water	40	48
DEAEMA	$CuCl/CuCl_2$	HMTETA	Methanol	60	72
DMAEA	$CuCl/CuCl_2$	Me_6TREN	Bulk	90	72
TBAEMA	$CuCl/CuCl_2$	HMTETA	Bulk	90	72

E.4 Static water contact angle measurements

The hydrophobic/hydrophilic characteristic of polymers grafted on a surface can be characterized using static water contact angle measurements (WCA). In order to obtain more information about surface properties, WCA was performed on each sample, and results are summarized in Table E.3.

Table E.3 Static water contact angle measurements for different amino(meth)acrylate polymer brushes grafted on the surface of Si wafers.

Polymer	WCA
PDMAEMA	77.8° ± 13.7°
PDEAEMA	64° ± 11.9°
PDMAEA	62.9° ± 8.4°
PTBAEMA	62.2° ± 8.42°
Si-SAM	79.6° ± 3.75°

E.5 AFM: A tool to evaluate the thermo-responsiveness properties of polymer brushes

Here, an individual plot for the different average thicknesses obtained for each polymer brush of study is presented. **Error! Reference source not found.** shows the height obtained at each pH PBS solution. Interestingly, PDMAEMA has a greater swelling than the rest of the polymers.

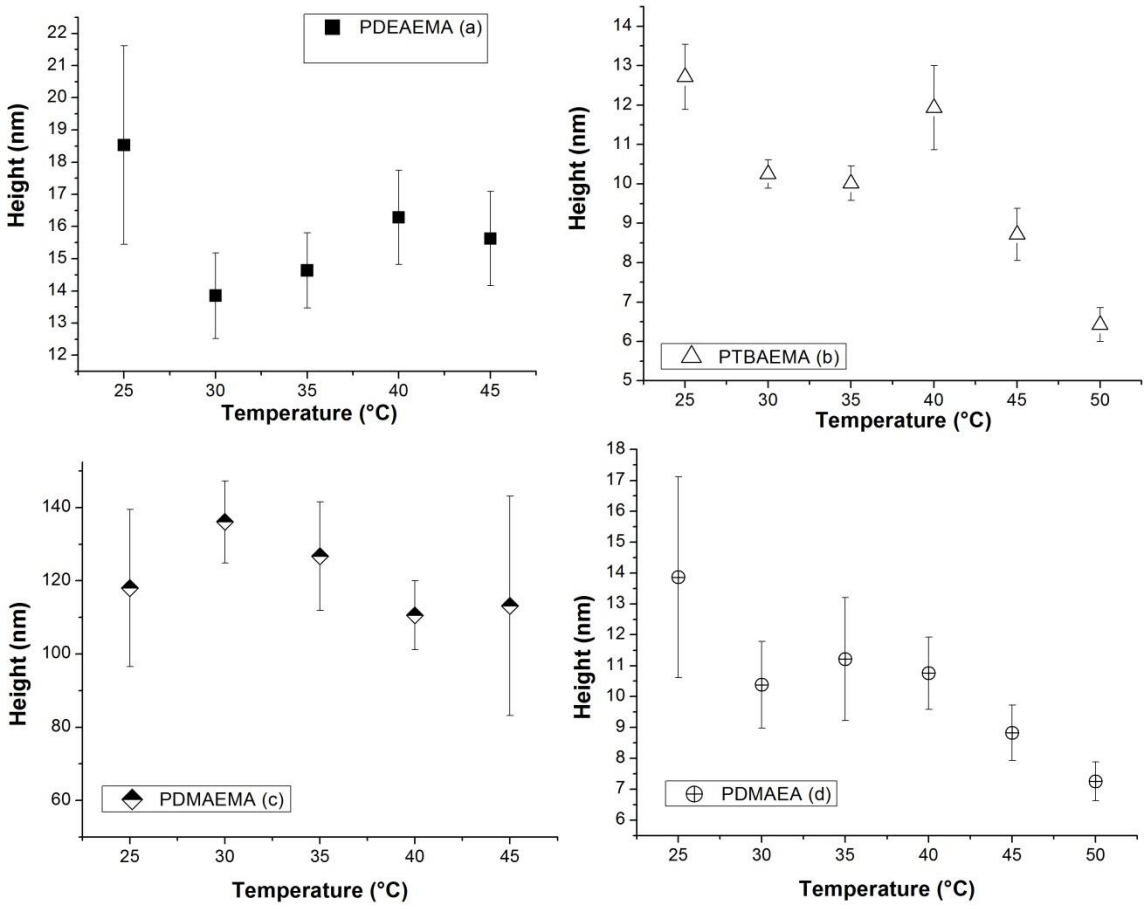

Figure E.3 Thermo-responsiveness behavior study using AFM for a) PDEAEMA, b) PTBAEMA, c) PDMAEMA, and d) PDMAEA.

E.6 Effects of pH changes during *in-situ* measurements

pH solutions were switched between 4 and 6 while the liquid cell was not in recirculating mode. For example (Figure E.4), pH 4 was kept constant for the first cycle, as observed, the thickness remain the same for both trials. However, when the pH was switched to 4, the thickness on the non-stable measurement was lower than on the stable run. This effect was caused due to the recirculation time of the new pH solution inside the liquid cell. A total of 3 volumes (~ 20 mL) were taken out of the recirculating bath after switching to pH 4 during the stable trial. Conversely, during the non-stable measurement only 1 volume (~ 5 ml) was removed before switching back to the recirculating pump. This study guarantees that the observed increase/decrease in thickness with respect to time is caused by slight changes in pH rather than a hysteresis effect. During the stable measurement, thickness always returned to the expected swollen value making it a reliable measurement. Future efforts should be addressed to remove enough pH solution of the recirculating bath before reaching a stable value.

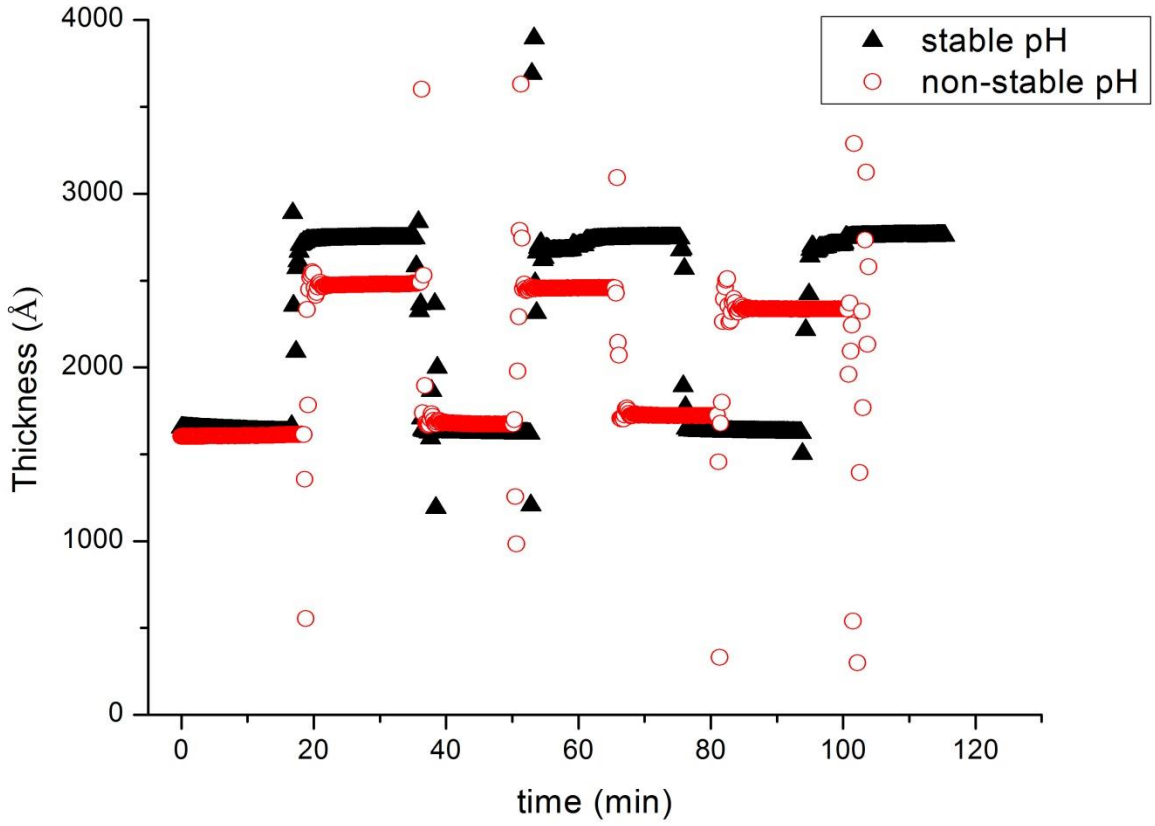

Figure E.4 pH switching cycles between 4 and 6 for PDMAEMA, and analysis of the variation on recirculation times.

APPENDIX F

DRAG FORCE CALCULATION CONSTANTS FOR DIFFERENT RE NUMBERS

F.1 Drag coefficient calculations

Different constants are needed to calculate drag force based on the Re number. Here a summary for each constant is presented in Table F.1

Table F.1 Drag force coefficient values for different Re numbers.

Re range	a_1	a_2	a_3
< 0.1	1		
< 1	0.94708	0.0037625	0.15375
< 10	1.2153	-0.16204	0.050917
< 100	1.9375	- 4.86125	0.025696
< 1000	4.0971	- 115.75	0.015183
< 5000	6.1925	- 1979.17	0.014875
< 10000	-20.4394	24112.5	0.019167
> 10000	-69.2708	225695.8	0.5191

APPENDIX G

EFFECT OF GRID REFINEMENT ON PARTICLE DEPOSITION PERCENTAGE FOR RE 100 AND RE 1000

G.1 Case I: Effects of grid refinement on Re 100 on an elbow grid

The effects of grid refinement were also evaluated in a coarse mesh with approximately 155,000 cells for Re 100. For St above 0.8, results showed that for Re 100 grid refinement is negligible. However, for stokes numbers below 0.8, there is a significant effect on deposition percentage, as observed in Figure G.1,**Error! Reference ource not found.** over-prediction on deposition percentage occurred in a coarse grid as compared with the refined grid. Thus, grid refinement levels are significant, in particular, for low stokes number. Moreover, at a low grid refinement, gravity effects are more noticeable.

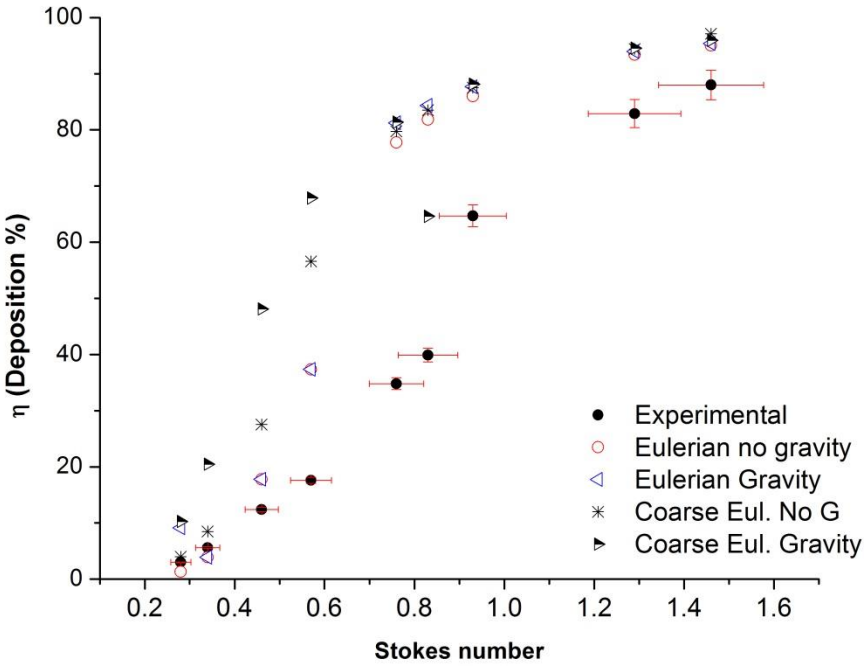

Figure G.1 Analysis of grid refinement levels for Re 100 using a coarse mesh with gravity and without gravity, compared with the refined grid results and the experimental values

G.2 Case II: Effect of grid refinement on Re 1000 on an elbow grid

Eulerian-Eulerian particle tracking is not affected by grid refinement as Re increases. These effects can be observed in Figure G.2. Moreover, at higher St number, deposition percentage seems to be independent of gravity and grid refinement level. However, at this point (St > 0.8) , most of the particles could not escape even at low Re number. No difference in deposition percentage are interesting results observed for small particles (low St). This confirms that the Eulerian model works good for at least 500,000 cells which was the size of the coarse grid run.

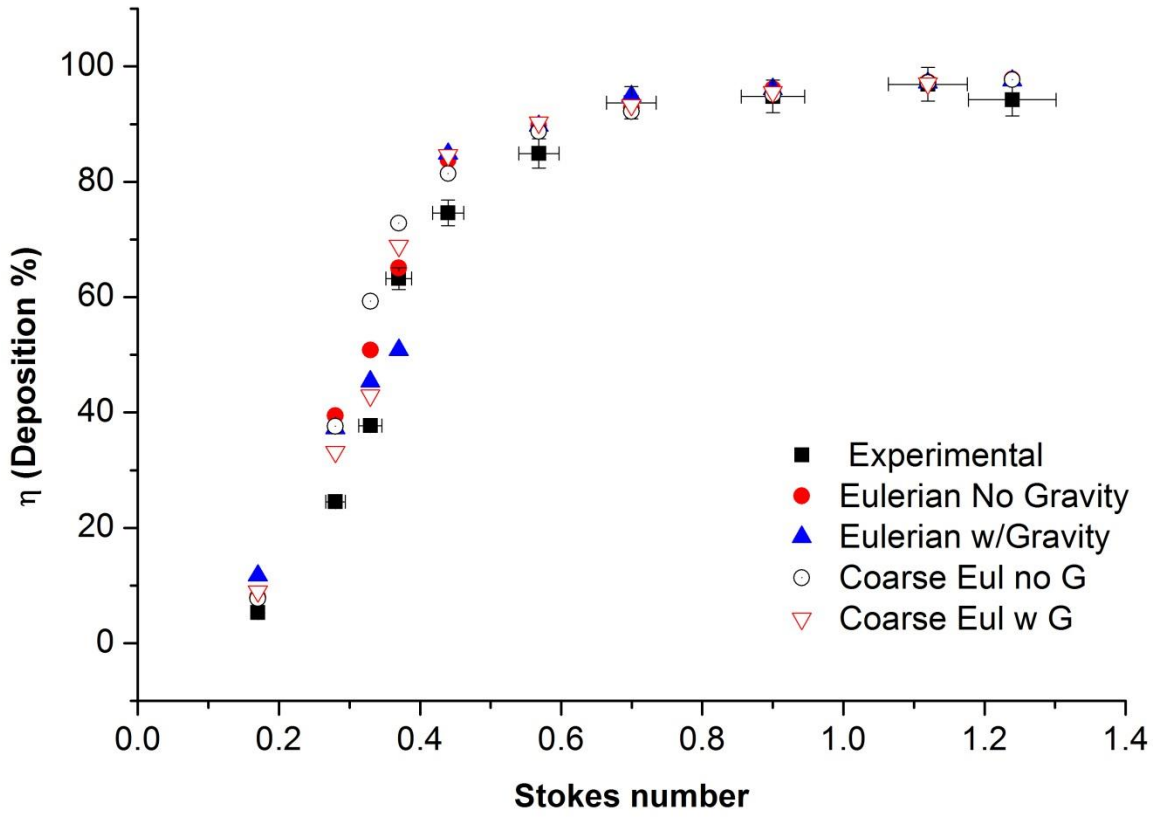

Figure G.2 Grid refinement study for Re 1000, no significant effects are observe on deposition percentage efficiency as St number changes.

APPENDIX H

STEPS FOR THE SURFACE MODIFICAITON OF AU-COATED SILICON WAFERS

H.1 Materials and chemical reagents

Different materials are required for the surface modification of a flat substrate. A list with some of the main material is presented (Table H.1). These procedures can be extended to the surface modification of other materials including magnetic nanoparticles, gold nanoparticle or silicon wafers. However, the end-functionalized group present on a surface must be known to proceed correctly. This appendix provides an overview on how to proceed on each particular case and has been adapted from different references in literature (Kim et al., 2000; Kim et al., 2002; Rakhmatullina et al., 2007).

Table H.1 Different materials required for the deposition of self-assembled monolayers (SAMs) and bromine initiators on a flat substrate

Substrates	Solvents	Chemicals
Au coated silicon wafers 10 mm x 10 mm	Ethanol 200 proof, anhydrous	11-mercapto-1-undecanol (MUD) [SAM forming thiol]
	Water, deionized milipore system	2-bromoisobutyryl bromide [initiator]
	THF , anhydrous	2-bromopropionyl bromide (bpb) [initiator]
		Tryethylamine
		Bis[2-(2′-bromoisobutyryloxy) ethyl] disulfide (initiator) (bbbd)

H.2 Au-SAM preparation

SAM preparation is very sensitive to contaminants on the surface; thus, it is necessary to clean the wafer first. After cleaning the wafer, SAM deposition and Br-initiation can be performed as discussed in the next sections.

H.2.1 Cleaning the wafer

These steps should be followed before any surface modification of the substrates. These step will guarantee a clean surface:

- Sonicate the wafer for 1-3 minutes in ethanol
- Dry the wafer using an N_2 stream (N2 'gun')
- Place the gold wafer in a UV ozone chamber for 15 minutes

H.2.2 SAM preparation:

SAM preparation should be performed overnight (at least 12 hours) to allow the thiol compound to react enough with the clean Au surface. Different parameters such as shaking the solution, dark room and concentration have been evaluated. Nonetheless, the chemistry worked fine in a non-anhydrous environment and no external agitation was required. The simple step carried out in this reaction is shown (Figure H.1) where an –OH end functionalized group will be available on the surface of the substrate.

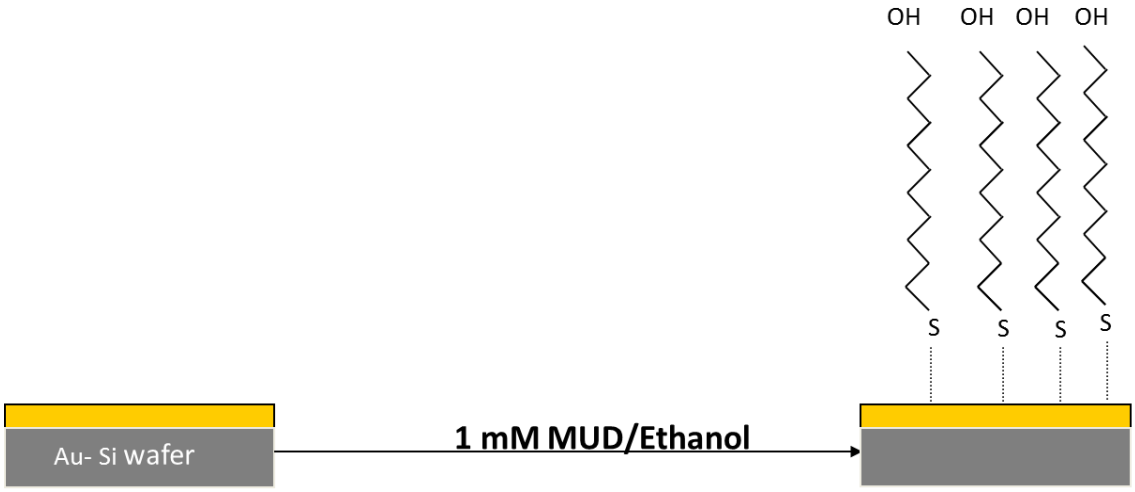

Figure H.1 Self-assembled monolayer deposition of a clean gold coated silicon wafer.

As previously discussed, SAM preparation should be carried out in 200-proof ethanol. Otherwise possible contaminants may interfere with the self-assembled monolayer deposition.

- Place the cleaned gold wafer in 1 mMol , 1.5 mMol or 5 mMol MUD/ethanol solution overnight under continuous N_2 purging
- Wash extensively (three times) with ethanol
- If to be characterized (typical$_l$y: IR, ellipsometry), dry with a stream of N_2. Otherwise, immediately store in a vial with clean ethanol

H.3 Br initiator preparation from Au-SAM

- Dry the Au-SAM wafer using a N_2 flow and place in a nitrogen atmosphere
- Under a nitrogen atmosphere perform the following steps:
- Place the Au-SAM previously prepared in 5 mL of 0.12 M triethylamine/ anhydrous THF solution for 10 seconds at ~ 0 ºC
- Gently, add 5 mL of 0.1 M 2-bromopropionyl bromide/anhydrous THF solution (2bpb). Constant agitation is required. If possible, the wafer should be in a flat position to ensure the reaction surface is well exposed to the 2 bpb solution.
- Total time for the reaction with 2bpb is about 3 minutes. After the reaction, remove the Au-SAM-Br sample from the 2-bpb soln and rinse sequentially with: THF and ethanol. Finally, dry using a nitrogen stream

H.4 Br initiator preparation from clean Au wafer

Br- can be directly attached as the end-functionalized group of a surface as described below. The main difference is that a disulfide with end brominated chains is

utilized as the SAM. This procedure is recommended due to the effective bromine initiated surface obtained in a single step avoiding organic wet chemistry; however, these wafers must immediately be used after this reaction and proceed with ATRP to form polymer brushes. This is due to the instability of brominated compounds on air. The next steps summarize how to prepare an Au-Br initiated surface:

- Wafer must be cleaned using the same steps previously described (H.2.1)
- Place wafers in a bbbd 1.5 mM ethanolic solution (200 proof) and allow to react overnight.
- After completion, Wash extensively (three times) with ethanol

H.5 References

Kim, J. B., M. L. Bruening and G. L. Baker (2000). "Surface-initiated atom transfer radical polymerization on gold at ambient temperature." Journal of the American Chemical Society **122**: 7616-7617.

Kim, J. B., W. X. Huang, M. L. Bruening and G. L. Baker (2002). "Synthesis of triblock copolymer brushes by surface-initiated atom transfer radical polymerization." Macromolecules 35: 5410-5416.

Rakhmatullina, E., T. Braun, T. Kaufmann, H. Spillmann, V. Malinova and W. Meier (2007). "Functionalization of gold and silicon surfaces by copolymer brushes using surface-initiated ATRP(a)." Macromolecular Chemistry and Physics **208**: 1283-1293.

APPENDIX I

EXPERIMENTAL PROCEDURES

I.1 FTIR spectrum collections for nanoparticles and powders

Attenuated Transmittance Reflectance (ATR) using a Miracle-IR attachment has been demonstrated to be the best IR technique for nanoparticle spectrum data collection. Limitations are found on this method as a result of solvent evaporation/contamination when the nanoparticles are in a solvent. It is suggested to try different solvents and analyze particular differences on the expected IR peaks as solvents are switched. This procedure contains a detailed description of the three different methods which could potentially be used for nanoparticle IR data collection. First, Transmission FTIR is described for data collection. Second, Diffused Reflectance Infrared Fourier Transform spectroscopy (DRIFTs) steps and sample preparation are explained. Third, ATR-FTIR general description is described

I.1.1 Transmission FTIR

Transmission crystals are made of Potassium Bromide (KBr). These crystals must be completely cleaned prior usage. A clean crystal is vital for good data collection, thus, it is expected to follow steps of section A. Additionally, the crystals are water-sensitive. Therefore, usage of other solvents is strongly preferred.

I.1.1.1 Crystal cleaning

1. Spray methanol on cotton balls using a squeeze bottle and clean both sides of the crystal
2. Using a nitrogen gun spray both sides of the crystal with methanol followed by continuous drying using a N2 gun. Repeat this step twice

3. Make sure to hold the crystal so it won't fall – crystals are very sensitive and they can scratch or break if dropped.
4. The KBr crystal is ready to be used if no spots are seen. Steps 1-4 should be repeated until no spots are seen. In case spots don't get removed use the crystal cleaning kit located below the FTIR accessories.

I.1.1.2 Sample preparation

(Make sure a vacuum oven/manifold line can be used to pull vacuum prior sample deposition)

1. Use a disposable micro-pipette to deposit an amount of nanoparticles suspension on one side of the KBr crystal.
2. Typically, a concentration of 0.5 miligrams/mL should be enough to get data with this method, however, particle concentration and results will depend on the size of the particles
3. The substrates with the solvent must immediately be placed in a vacuum oven for at least 15 minutes to guarantee solvent evaporation. A thin film should be observed on the surface of the crystal prior data collection. A thick film will flow vertically and won't allow the user to collect data
4. Identification of samples is critical at all times. Labeled petri dishes must be used to identify each KBr crystal – do not write on the KBr.
5. Make sure the transmission accessory is placed on the FTIR
6. Use a clean KBr crystal to collect the background
7. Save the background and use this new file in the data collection window to collect your sample.

8. Place the KBr crystal with your sample on the transmission accessory. The beam goes from right to left. Make sure your sample faces on the direction of the beam
9. Observe spectrum collection and when done save the experimental file
10. Clean the crystal(s) as previously discussed in section H.1.1.1.

I.1.2 Diffuse reflectance infrared Fourier transform spectroscopy (DRIFTs)

KBr is also used in DRIFTs. The main difference is that KBr is in a powder form for DRIFTs. Sample weight percent concentrations should be 3-8 % when running DRIFTs. A 5 % sample concentration is ideal. EasyDiff Accessory (Pike Technologies) is used for data collection. The following steps are required for this method:

1. KBr should be crushed using the DRIFTs kit and a razr blade prior any measurement. Additionally, clean KBr should always be used. Avoid cross-contamination
2. A basis of 1 gram sample weight is used. Weight 0.005 g of sample. Then, add 0.095 g of KBr weighted out on a different container. Mix both in a tube
3. There are two metal cups inside the DRIFTs kit. Use one for the prepared sample and the second one for clean KBr. Clean KBr helps as the background for data collection
4. Prior depositing the KBr or the sample on each cup, crush and make a homogeneous mixture of your sample with the blade and the two black holders. A flat surface is necessary for good data collection

5. Place both, the sample and the clean KBr, crushed powders on each metal cup.
6. DRIFTs holder should be placed against a surface. This is done to avoid your sample to fall down
7. Place the holder inside the FTIR and wait for 25 minutes before data collection. This is done to avoid water/CO_2 contamination.
8. Make sure to identify which cup contains the clean KBr and the sample
9. For DRIFTs Kubelka-munk corrections should be used. This is located in the experimental setup. Set sample compartment to main, Detector MCT or DTGS, Beam splitter to XT-KBr and IR source.
10. Collect the background after 25 minutes have passed on the clean KBr crystal
11. Open the top door of the FTIR and move the metal cup to the one containing your sample
12. Collect the sample with the saved background (clean KBr) crystal after waiting 5-8 minutes.
13. Store the sample back and dispose the KBr powder.

I.1.3 ATR-FTIR measurements using Miracle-ATR®

Miracle-ATR consists of a 45° diamond/ZnSe crystal with a fixed angle. This accessory can be used for powders and liquids. For flat substrates ER or ATR using Veemax is recommended.

I.1.3.1 Collecting powder samples

1. Use methanol to clean the crystal surface. Gently spray methanol on cotton balls and clean the surface. Wait until all the methanol has evaporated
2. Place your powder sample on top of the diamond/ZnSe crystal using a spatula
3. Look for the pressure tip with a concave bottom surface. Locate this tip on the instrument by rotating counterclockwise the top holder. When a tip is located on the instrument, remove first and then store in the FTIR sample kit.
4. Collect Sample first
5. Remove your powder sample and clean the crystal with methanol sprinkled cotton balls.

I.1.3.2 Collecting liquid samples

1. Liquid samples spectra are expected to take longer collection times due to the need of solvent evaporation. If possible, try to use a volatile solvent when preparing your sample (e.g. methanol, ethanol…)
2. The crystal should have a gray o-ring and the upper metallic plate to hold the liquid. This is done to avoid any liquid entering the instrument.
3. Place one drop of your solvent on top of the crystal and wait for total evaporation
4. Collect the sample spectrum once the solvent has evaporated.

5. Clean the surface of the crystal with methanol sprayed cotton balls and collect the background for your sample. It is suggested to collect the background after the sample in case the solvent takes a long time to evaporate.
6. Make sure all the system is clean before you leave

I.2 Experimental plan for the synthesis of amphiphilic Janus nanoparticles

I.2.1 Acronyms:

ATRP: Atom transfer radical polymerization

MNPs: Magnetic nanoparticles

SAM: self-assembled monolayer

MAA: methacrylic acid

MMA: methylmethacrylate

Fe_3O_4: iron oxide

MNPs to be used in this work will be:**FluidMAG-Amine (200 nm)**, with amine-NH_2 functional group as illustrated in Figure I.1.

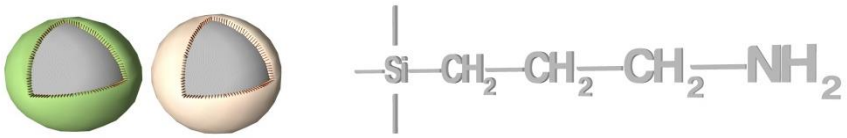

Figure I.1 Fe_3O_4/NH_2 substrate for Surface modification of MNPs

I.2.2 Procedure

The general procedure to obtain PMAA-Fe_3O_4-PNIPAM is as follow:

1. Fe_3O_4-NH_2 nanoparticles were used as received (suspended in water) and a drop of this material was deposited on the surface of mica, waiting until water evaporated completely. Aproximately, 30 minutes were needed. Electrostatic interactions between the nanoparticles and Mica – the substrate –will cause a physisorption of the MNPs on the surface of mica as depicted in Figure I.2

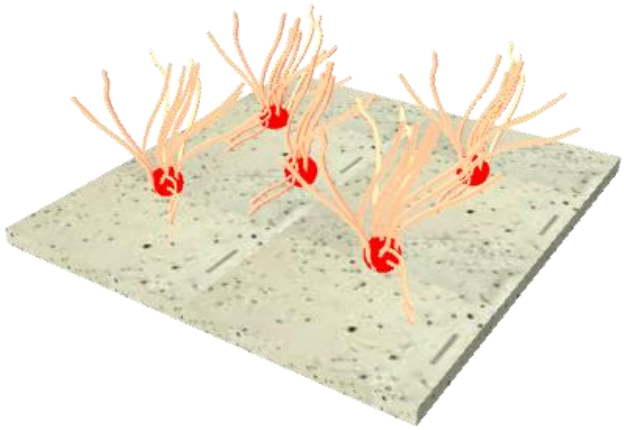

Figure I.2 Electrostatic interaction of MNPs with a mica substrate

2. surface modified MICA with MNPs was then placed in a Br-solution (~ 10 mmol 2-Bromo-isobutyril bromide/toluene) under a nitrogen atmosphere for about 12 hrs. This step will allow the free NH2- groups – non attached to the mica surface - to react with the initiator.
3. After attachment of the initiator, monomer + catalyst + ligand (MAA, Cu(I)Cl and Me6TREN) was added in excess to the solution - under an

inert atmosphere all the time. This reaction will proceed for at least 12 hours.

4. Every hour, an aliquot of the solution will be taken for later studies of molecular weight of any polymer that could be obtained in solution
5. After completion of the polymerization, a pH buffer of 2 was added to the solution to detach the magnetic particles from the MICA surface. Sonication was required at this point.
6. Particles in the pH buffer solution of 2 were then extracted using a needle and a syringe and the solution was placed in at least one centrifuge tube (15mL). Centrifugation, then decantation of solvent was conducted for at least two times. One with the remaining buffer solution and the other one with HPLC grade water to clean the NPs as much as possible. After the second centrifugation, particles were stored in HPLC grade water at 4^{o}C (fridge) until DRIFTS, DLS or TEM were used to characterize the sample.
7. Particles that remained will now be polymerized again in solution with another monomer (NIPAM or MMA). Steps 2 and 3 will now proceed but no MICA will be used at these steps. These reactions will proceed under sonication all the time to guarantee appropriate mixing within the solution. The resulting nanoparticles are illustrated in Figure I.3

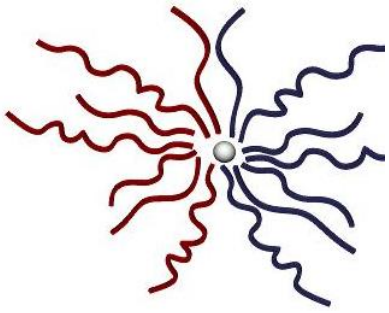

Figure I.3 Biphasic Janus nanoparticle (PMAA-Fe_3O_4-PNIPAM) with a magnetic nanoparticle carrier

I.3 The sandwich method: TEM: Sample/grid preparation for nanoparticles

I.3.1 General comments

1. Make sure to identify box lot number (lot_____) and the grids that you will be using for sample deposition
2. Materials: For each grid use two washers (~ 3 mm inside diameter hole), filter paper, tweezers for Grids, Tweezers, two caps, one 50 mL test tube, one septa cap, one needle (18 G) and one needle (22 G), Parafilm, scissors

I.3.2 Instructions

1. Place the filter paper on top of one washer (you can use glue to paste the paper)
2. Place the second washer on top of the filter paper (sandwich-configuration)
3. Use parafilm to wrap around the two washers
4. Insert the TEM 300 mesh copper grid until the non-shiny part stay in contact with the filter paper

5. Place the sandwich-grid configuration into a cap. Schematics of these steps can be observed in Figure I.4 and Figure I.5.
6. A second cap will be needed to be introduced in the test tube. If it is loose, use parafilm so it can be easily stopped at about ¾ from the bottom
7. Once, this cap is located and held steadily. Introduce the second cap with the TEM grid on it
8. Use 18G needle for vacuum and 22G for nitrogen
9. Connect these two needlees to different splits in the manifold
10. Put the needles (Black and pink) in a separate septa cap
11. Cover the test tube with the septa cap and start flowing nitrogen and pulling vacuum for 30 minutes as shown in Figures 1 and 2.
12. Carefully, remove the needles and the septa cap from the test tube
13. Remove the sandwiched-grid configuration
14. Remove Parafilm with scissors or a razor blade
15. Remove the top washer
16. Use the small tweezers to grab the Grid and place it in the respective box position (i.e. A1)
17. Make labels to identify each sample on the box grid
18. Write on your lab notebook the sample names, id and lot grid
19. Clean and wash the test tubes

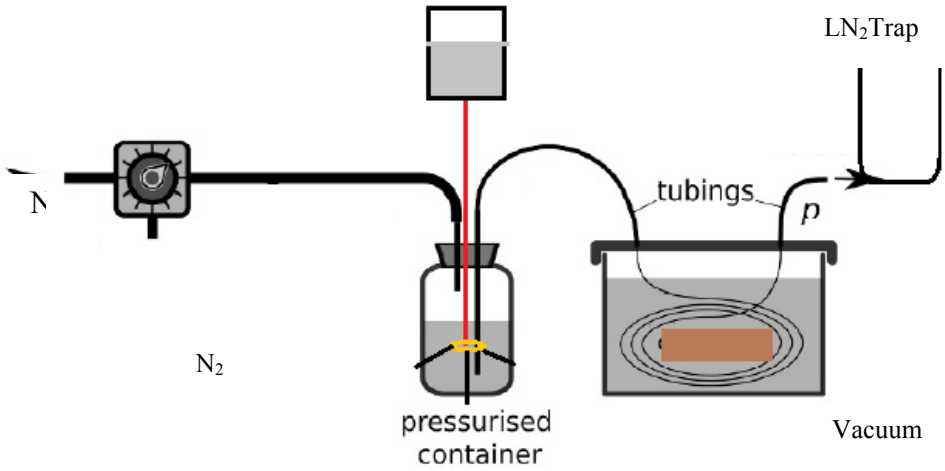

Figure I.4 Nitrogen/pressurized system for Au-NPs deposition on TEM grids

Figure I.5 Experimental design for the vacuum/nitrogen flow experiment performed in the lab

I.4 Ellipsometry Procedure: Aligning the liquid cell for *in-situ* measurements

1. Turn on the lamp power supply
2. Turn on the EC-400

3. Computer should be on (if Not, turn on at this point)
4. Open the completEASE program
5. The *measurement-system status*, should say “Waiting to acquire data”.
6. Select Hardware , then controls and click on “Install New Sample Stage”
7. Remove current stage and install New stage
8. Disconnect vacuum lines
9. Loose the four screws on the base
10. Remove the dry-sample stage
11. Place the liquid cell sample stage and tight the 4-screws
12. Select “Yes” to configure the software for the liquid cell
13. Sample Stage Secure. Hit, OK
14. Translation stage will move to the (0,0) position. Select OK. NOTE> Make sure there is nothing interfering with the beam
15. Select OK to initiate the change in angle to 75 degrees or 70 degrees, depending on the size of the liquid cell that you are using
16. Mounting the sample and aligning the cell
17. Make sure that the cell is not mounted
18. Place sample on mounting plane
19. Hand tighten four-captive screws evenly (USE Only enough torque to avoid leaking), check Figure I.6 for more details.
20. Aligning the 5 mL liquid cell by Selecting: Hardware>controls>general tab> “Align sample “ Or Measurement >Measurement controls> “align sample”

21. SELECT “NO” for full sample alignment. The tilt alignment will open in manual mode
22. Vertically Align the entrance window by adjust z-axis. Using page up and page down until you reach the center
23. Horizontally align entrance window by rotating cell
24. Loose the rotation locking screws
25. Adjust the tilt screws
26. Lock the rotation lock screws once the sample is aligned

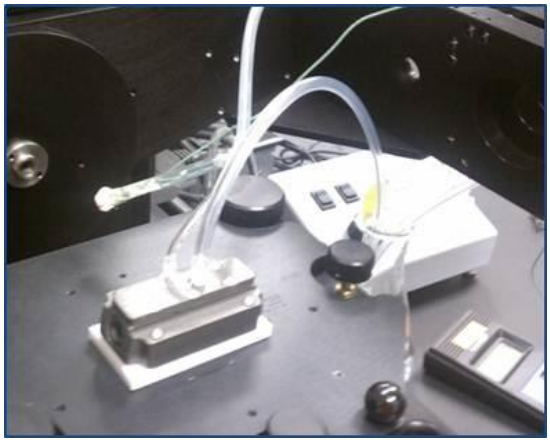

Figure I.6 General view of the liquid cell mounted on the ellipsometer

27. When done, select cancel sample tilt alignment or the Esc button
28. As a general check, turn-off the lights and see the aligned beam reflecting on the aperture of the detector

I.5 Modeling bare metal surfaces (substrates) using CompletEASE

1. Open CompletEASE software

2. Go to the Analysis Tab
3. Select Data: Open → Now, look for your data set in your preferred storage folder
4. Go Model: Select Open, now, choose Basic models on the left window
5. Select Blank model and select open (A window as seen below will pop up). Refer to Figure I.7

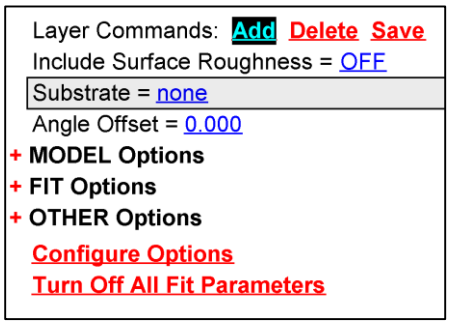

Figure I.7 CompletEASE model window

6. The model is constructed depending on the optical constants of the material.
7. Typical examples includes: seminconductors, metals , alloys ,etc.
8. For a Si substrate:Click "none" on the substrate tab. Then, select "Si_Jaw" from the library menu (Semiconductor tab) to enter the material optical properties of the semiconductor. In this case, Silica.
9. Different layers can be added to the substrate. Press "Add" in layer commands to add different layers to your model.

10. Add “INTR_JAW” from the semiconductor tab. This represents the interface between Silica and SiO_2. Typically one nanometer.
11. Now, For the Thermal Oxide, select SiO2_JAW (Semiconductor TAB) and approximate as much as you can a value for the thickness of the film.
12. If you have difficulties approximating a specific value for the thickness. Select Fit options and Perform Thickness Pre-fit: ON. This will help to determine the value for the expected thickness
13. Roughness can be included or not in the model. Check MSE for the results. Negative roughness does not add anything to the model and is not-realistic.
14. Si wafer with a transparent film (polymer). Open the blank model, click “none” on the substrate tab. Then, select “Si_Jaw” from the library menu (Semiconductor tab) into model substrate
15. Open Cauchy.mat into model film
16. Turn on Cauchy A,B, C and thickness
17. Pre-fit for thickness
18. Global fit for A parameter
19. Fit
20. Verify normal dispersion (view Cauchy layer optical constants)
21. SHORTCUT: Select the following model: “Si with Transparent Film.mod”
22. Add Roughness and grading
23. Roughness: Turn on the parameter for fitting

24. Grading. Right click on grade layer
25. One option is always to check for alternative fittings. For this purpose, try other options. Then hit Try alternate models. Automatically, the following will take place:
26. Ideal model
27. With roughness
28. With simple index grading
29. With both roughness and simple index grading

I.6 Procedure to run *in-situ* AFM measurements

I.6.1 Summary

This Experimental plan summarizes different steps that need to be followed using scanasyst mode in Dimension Icon AFM equipment as depicted in Figure I.8. Tips that are used for this experiment are: Scanasyst-fluid made of nitride tip and nitride lever. The cantilever has a T: 05-0.7 micrometer. And the frequency varies from 120-180 Khz. K: 0.7 N/m.

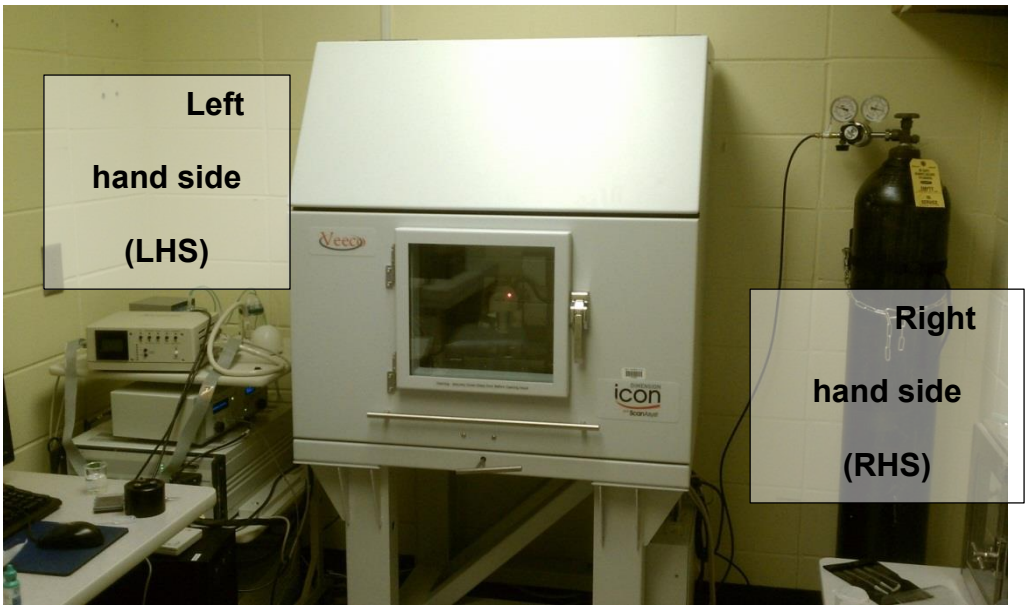

Figure I.8 AFM Icon front view

I.6.1.2 Procedure

I.6.1.2.1 Equipment startup

Turn on the computer and monitor for the Dimension Icon Equipment

Hit Ctrl+Alt+Del as it prompts on the monitor and introduce the password for the computer: emcenter

Connect the heater/cooler cable on the right hand side of the ICON instrument:

Turn on the equipment (using power strip on the left hand side of the instrument) and turn on the heater/cooler accessory. Note the turn on/off button is at the left on the back of this panel

I.6.1.2.2 Experimental setup

1. Use the fluid cell cantilever holder located in the cabinet on top of the computer.

2. Place the cantilever holder on the special setup (the one that has a spring)
3. Then, place one of the scanasyst-fluid tips on the cantilever as the spring lift the small wire/clamp to hold in place the tip.
4. The tip can be seen using the optical microscope in the adjacent lab.
5. Check that the cantilever is not tilted or not vertically positioned with respect to the gray clamp. By experience, if the cantilever is a barely tilted, beam alignment will be complicated and/or unsuccessful.
6. Open Nanoscope v.8.15.
7. Initialize the equipment
8. Select New experiment: Scanasyst in fluid and change the microscope setup to H/C Temperature.
9. Hit OK
10. Place the cantilever holder with the tip on the Bruker scanning head
11. Place the Teflon gasket at the bottom of the cantilever holder. This is used to protect the scanning head from any spill that might occur as the scanning in liquid takes place. **Be Careful!. When setting up the plastic sleeve/gasket as it might damage your tip.**
12. Go to setup and align the beam on the tip by:
13. Adjusting the laser intensity on the tip. Multiple reflections are observed on this particular cantilever/tip holder. Thus, location of the real beam must be performed to obtain a good result. First locate the laser on the screen by moving the **top-screws** on the scanning head until you see the beam on the computer screen as shown below (Figure I.9).

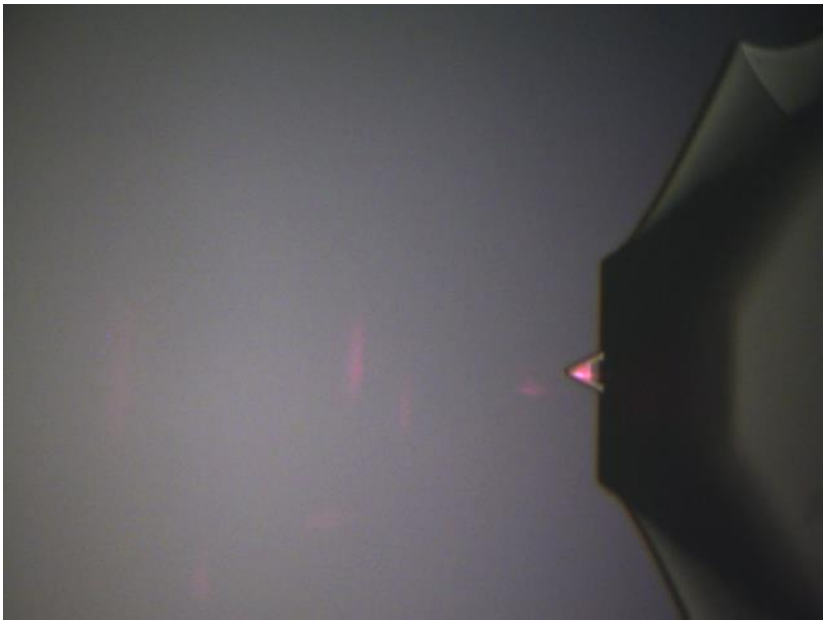

Figure I.9 Beam alignment while *in-situ* measurements are conducted

14. Adjust the side buttons of the scanning head, until the maximum intensity is obtained for the particular tip.
15. Typical values for intensity varies:

    No liquid: ~ 2.1 – 2. 5 V

    Liquid: 3.1- 3.5 Va
16. Place your wafer on one magnetic holder (utilized for this particular samples). Use copper tape to guarantee no movement and to be able to release the wafer after you are done with the experiment. If you use double side tape or any other tape most likely the wafer won't be able to come out of the surface and your sample will be unusable if it breaks.

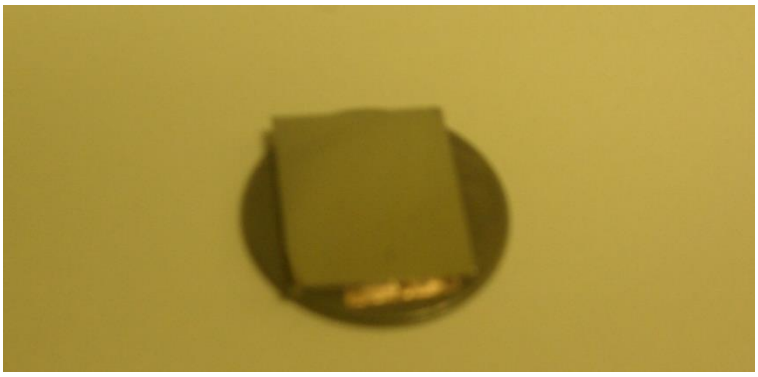

Figure I.10 Wafer holder while measurements are conducted *in-situ*

17. Place the wafer on the magnetic holder. Then add a drop of water (or the liquid you are trying to use on top of the wafer)
18. After correctly aligning the tip on the scanning head. Carefully, add 1-2 microdrops on the tip (This is extremely difficult and be aware/cautious of the laser).
19. Align the vertical position and red cross for the displacement due to the water refraction effect on the tip
20. Go to navigate and start lowering the scanning head until you see both drops (the one in the scanning head and the other one on the wafer) start coming closer. Reduce the speed to about 20%, then the two drops will crash and eventually the software will "suppose" that there is a misalignment.
21. Realign the tip with the laser. Also, make sure to "check" the box that says, alignment was performed on the fluid.
22. Go back to setup and check that the maximum intensity was reached

23. Go to navigate and detect a spot that you wish to scan by moving the side and top arrows on the computer screen.
24. Once you locate a spot, check your parameters. Mainly, scanning size and scans per line. It is suggested to use 512 scans/line. Additionally, at the beginning a very large area (15 -10 microns) should be scanned to setup a particular point , then you can move easily around your sample and/or point of interest.
25. Check parameters once again, and make sure that the maximum intensity has not changed. Go to scan and select the following screens:
    Height sensor
    peakforce error
    inphase
    quadrature
26. NOTE: This must be done before starting your scan. Otherwise, data will not be collected/saved.
27. Select the directory that you want to save your data by clicking on the folder with the camera on the rhs of the screen.
28. After selecting your folder, you can go to it by clicking on the small camera beside the directory on the top rhs of the screen
29. Type the name of your sample and hit enter
30. Hit engage
31. Wait until the sample data is starting to collect and hit the bottom arrow to start scanning from the top to the bottom

32. Select capture now for the image to save automatically
33. If by any reason your image is not saved. Stop the capture now and hit Capture last. This should save your file.
34. After the image has been collected click withdraw. Go back to the navigate button and select a new point of interest for your scan.
35. Once you are finished. Withdraw once again. Adjust the lifting speed to 20 % and slowly remove the tip from the water/liquid drop. The signal intensity should decreased dramatically as the tip comes out of contact with the water. Here, try to realing to be able to move the stage.
36. Once realigned, move the sample stage to the front. Dry the drop that is located on your sample with a kimwipe, and remove/store the sample.
37. Remove the scanning head (Be Careful with the laser). Now, remove the plastic gasket (Careful as it might break your tip). Then, remove the tip holder and place it on the special support. Place back the scanning head on the equipment. Use a kimwipe to dry any liquid. If a liquid different that water was used, make sure to use a couple of drops of waters to clean the tip. Dry on a side with kimwipes. This can be done in the optical microscope in the adjacent lab.
38. Once the tip has been cleaned, remove it with the tweezers and store in the box.
39. Clean and dry the fluid cell cantilever holder and store it back in the bag and put it in the drawer located on top of the computer.

40. Turn off the heater and go to the software and remove the heater/cooler H/C option.
41. Turn off the equipment using the power strip on the LHS of the instrument
42. Turn off the computer